

**SELF-COMPACTING CONCRETE:
DESIGN, PROPERTIES AND
SIMULATION OF THE FLOW
CHARACTERISTICS IN THE L-BOX**

Muna Mohammed Kareem AL-Rubaye

B.Sc., M.Sc.

A thesis submitted in fulfilment of the requirement for the degree of
Doctor of Philosophy



School of Engineering

Cardiff University, UK

November 2016

In the Name of God
The Most Compassionate and the Most Merciful

DECLARATION AND STATEMENTS

DECLARATION

This work has not previously been accepted in substance for any degree and is not concurrently submitted in candidature for any degree.

Signed (Muna AL-Rubaye) Date.....

STATEMENT 1

This thesis is being submitted in partial fulfilment of the requirements for the degree of Doctor of Philosophy (PhD).

Signed (Muna AL-Rubaye) Date.....

STATEMENT 2

This thesis is the result of my own independent work/investigation, except where otherwise stated. Other sources are acknowledged by explicit references.

Signed (Muna AL-Rubaye) Date.....

STATEMENT 3

I hereby give consent for my thesis, if accepted, to be available for photocopying and inter-library loan, and for the title and summary to be made available to outside organisations.

Signed (Muna AL-Rubaye)

Date.....

DEDICATION

This thesis work is dedicated to my loved country Iraq represented by the Ministry of Higher Education and Scientific Research, and my family who has been a constant source of support and encouragement during the preparation of this research.

ACKNOWLEDGEMENTS

I want to take this opportunity to express my immeasurable appreciation and deepest gratitude for the help and support extended to me by all those who gave me the chance to accomplish this thesis. I deeply appreciate my loved country Iraq represented by the Ministry of Higher Education and Scientific Research / Babylon University for their support during the study period.

My sincere gratitude is to my supervisor, Professor Karihaloo is more than I can express in words. It has been an honour to be his PhD student. I appreciate his support, suggestions, valuable discussions and continuous provisions that benefited me much in completion and success of this study. He helped me in numerical computations and analysis of the results. Without his support, I could not have finished my dissertation successfully.

I would like also to express my gratitude to my co-supervisor Dr. Kulasegaram who has been always helpful. I am deeply grateful to him for valuable discussions we had during my research project.

My thanks also go to the staff of research office and the technical staff of concrete laboratory at Cardiff University / School of Engineering for their help and support.

Warm and special thanks are expressed to my parents, sisters and brothers for their support during the period of this research.

Finally, special thanks go to my friends, especially my office members who supported me.

Muna AL-Rubaye

SYNOPSIS

Self-compacting concrete (SCC) can flow into place and compact under its own weight into a uniform mass even areas of congested reinforcement. Compared to vibrated concrete (VC), SCC has enhanced qualities and improves the durability of concrete, productivity and working conditions due to elimination of external vibration. Although SCC has passed from the research phase into real application, the need to update the knowledge on the fresh and hardened characteristics of SCC increases to overcome the problems associated with such concrete and to improve its performance.

The research reported in this thesis divided into three parts. The first part concerns the proportioning of SCC mixes, a simple and rational mix design procedure based on the desired target plastic viscosity and compressive strength of the mix has been developed. Practical guidelines in the form of design charts are provided for choosing the mix proportions of SCC mixes. An extensive experimental program was carried out in order to provide experimental validation of this mix design procedure on a series of SCC mixes in both the fresh and hardened states. All these mixes were extensively tested in the fresh state using the slump cone, J-ring, L-box and V-funnel apparatus; and these tests proved conclusively the validity of the mix proportioning method in the sense that all the mixes satisfied the self-compacting criteria and achieved the desired target plastic viscosity and compressive strength.

In the second part of the thesis, the fracture properties of the SCC mixes have been determined. These mixes differ by coarse aggregate volume (CA), paste to solids ratios (p/s) and water to cementitious material (w/cm). The simplified boundary effect approach (SBE) and the non-linear fictitious crack model are used to determine the size-independent fracture energy (G_F) and to obtain a bilinear stress-crack opening relationship $\sigma(w)$, respectively. The results showed that the specific fracture energy (G_F) and the critical crack opening (w_c) are dominated by the coarse aggregate volume in the mix and the mix grade. The larger the coarse aggregate volume (or the smaller the paste to solids ratio) the larger are both the mix toughness (G_F) and the critical crack opening (w_c). However, the higher the mix grade the larger is the mix toughness (G_F) but the lower is the critical crack opening (w_c).

The last part consider the numerical simulation of the flow characteristics of the SCC mixes based on the mesh-free particle method. The three-dimensional lagrangian particle-based smooth particle hydrodynamics (SPH) methodology has been used to model the flow characteristics of the SCC mixes in the L-box test. A Bingham-type constitutive model has been coupled with the Lagrangian momentum and continuity equations to simulate the flow. The numerical simulation results are compared with the actual L-box tests carried out on several SCC mixes and the comparison reveals that this methodology is very well suited for predicting the flow behaviour of SCC in terms of passing and filling abilities and the distribution of large aggregates.

Table of Contents

<u>DECLARATION AND STATEMENTS</u>	III
<u>DEDICATION</u>	IV
<u>ACKNOWLEDGEMENTS</u>	V
<u>Chapter 1</u>	1
<u>Introduction</u>	1
<u>1.1</u> <u>Scope of the research</u>	2
<u>1.2</u> <u>Research objectives</u>	3
<u>1.3</u> <u>Research methodology</u>	4
<u>1.4</u> <u>Outline of the thesis</u>	6
<u>Chapter 2</u>	9
<u>Self-compacting concrete (SCC)-</u>	9
<u>Literature Review</u>	9
<u>2.1</u> <u>Introduction</u>	10
<u>2.2</u> <u>Development of self-compacting concrete (SCC)</u>	10
<u>2.3</u> <u>What is SCC?</u>	11
<u>2.4</u> <u>How does SCC differ from VC?</u>	12
<u>2.5</u> <u>Fresh properties of SCC</u>	13
<u>2.6</u> <u>SCC Categories</u>	15
<u>2.7</u> <u>Constituent materials of SCC mix</u>	16
<u>2.7.1</u> <u>Cement and cement replacement</u>	16
<u>2.7.2</u> <u>Aggregates</u>	17

2.7.3	<u>Mineral admixtures</u>	18
2.7.4	<u>Chemical admixtures</u>	18
2.7.5	<u>Water</u>	20
2.8	<u>Mix proportioning methods of SCC</u>	20
2.8.1	<u>Empirical design method</u>	21
2.8.2	<u>Compressive strength method</u>	22
2.8.3	<u>Aggregate packing method</u>	22
2.8.4	<u>Mix design method based on statistical factorial model</u>	23
2.8.5	<u>Mix design method based on rheology of paste model</u>	24
2.9	<u>Assessing the workability of SCC</u>	25
2.10	<u>Testing methods of Fresh SCC</u>	26
2.10.1	<u>Flow-ability tests</u>	26
2.10.2	<u>Passing ability tests</u>	29
2.11	<u>Fracture mechanics of Concrete</u>	33
2.11.1	<u>Introduction</u>	33
2.11.2	<u>Nonlinear fracture mechanics (NLFM)</u>	34
2.12	<u>Determination of specific fracture energy</u>	36
2.13	<u>Fracture behavior of the SCC</u>	37
2.14	<u>Rheology of SCC</u>	38
2.15	<u>Measuring the rheological parameters</u>	39
2.16	<u>Effects of concrete constituents on the Bingham constants</u>	41
2.17	<u>Concluding remarks</u>	42

Chapter 3	43
<u>Simulation of fresh self-compacting concrete (SCC) flow – A brief summary</u>	43
<u>3.1 Introduction</u>	44
<u>3.2 Rheological models describing the flow of SCC</u>	44
<u>3.2.1 Fluid classifications</u>	46
<u>3.3 Simulation of the flow of SCC</u>	47
<u>3.3.1 Simulation of concrete as a homogeneous medium</u>	48
<u>3.3.2 Simulation of concrete as a heterogeneous medium</u>	48
<u>3.4 2D and 3D simulations of SCC flow in the L-box</u>	49
<u>3.5 The governing equations of concrete flow</u>	51
<u>3.5.1 Continuity equation (the mass conservation)</u>	51
<u>3.5.2 The momentum conservation equations</u>	51
<u>3.6 Eulerian and Lagrangian approaches</u>	52
<u>3.7 Numerical approximation-Smooth particle hydrodynamics (SPH)</u>	53
<u>3.7.1 SPH concept</u>	54
<u>3.7.2 SPH support domain</u>	55
<u>3.7.3 Kernel approximation</u>	55
<u>3.7.4 Particle interpolation</u>	56
<u>3.7.5 Corrected SPH integration</u>	58
<u>3.7.6 Neighbouring search</u>	58
<u>3.7.7 Treatment of boundary conditions</u>	58
<u>3.7.8 Incompressibility (ISPH) and weak compressibility in SPH approach</u> .	59

3.8	<u>Simulation of SCC with ISPH</u>	59
3.8.1	<u>Prediction step</u>	59
3.8.2	<u>Correction step</u>	60
3.8.3	<u>Time step</u>	60
3.9	<u>SPH discretisation of the governing equations</u>	61
3.10	<u>Concluding remarks</u>	62
<u>Chapter 4</u>		64
<u>Proportioning of self-compacting concrete mixes based on target plastic viscosity and compressive strength: Mix design procedure</u>		64
4.1	<u>Introduction</u>	65
4.2	<u>Target compressive strength</u>	66
4.3	<u>Target plastic viscosity</u>	69
4.4	<u>Basic steps of the proposed mix design method</u>	72
4.4.1	<u>Examples of mix proportioning</u>	73
4.5	<u>Design charts for mix proportioning of normal and high strength SCC mixes</u> 77	
4.5.1	<u>Examples of the use of design charts</u>	86
4.6	<u>Concluding remarks</u>	92
<u>Chapter 5</u>		93
<u>Proportioning of self-compacting concrete mixes based on target plastic viscosity and compressive strength: Experimental validation</u>		93
5.1	<u>Introduction</u>	94

5.2	<u>Materials and mix proportions</u>	94
5.3	<u>Mix procedure</u>	96
5.4	<u>Tests on fresh SCC</u>	97
5.4.1	<u>Flow-ability</u>	97
5.4.2	<u>Passing and filling ability</u>	104
5.5	<u>Testing of hardened SCC</u>	111
5.6	<u>Concluding remarks</u>	112
<u>Chapter 6</u>		114
<u>Influence of mix composition and strength on the fracture properties of self-compacting concrete</u>.....		114
6.1	<u>Introduction</u>	115
6.2	<u>Theoretical background</u>	117
6.3	<u>Experimental programme</u>	123
6.3.1	<u>Test geometry and specimens</u>	123
6.3.2	<u>Materials</u>	127
6.3.3	<u>Mix design</u>	127
6.3.4	<u>Specimen preparation and test procedure</u>	129
6.4	<u>Results and discussion</u>	129
6.5	<u>Bilinear tension softening diagram</u>	135
6.6	<u>Concluding remarks</u>	143
<u>Chapter 7</u>		144

<u>Simulation of the passing and filling abilities of self-compacting concrete (SCC) using L-box and smooth particle hydrodynamics (SPH)</u>	144
7.1 <u>Introduction</u>	145
7.2 <u>Development of SCC mixes</u>	147
7.3 <u>Boundary conditions</u>	149
7.4 <u>Treatment of aggregates</u>	150
7.4.1 <u>Colour coding of coarse aggregates in the test SCC mixes</u>	150
7.4.2 <u>Treatment of particles in SPH modelling of the L-box test</u>	154
7.5 <u>Simulation results</u>	157
7.5.1 <u>Simulation of the flow times of SCC mixes in the L-box</u>	157
7.5.2 <u>Simulation of the free surface profile of SCC in the L-box</u>	158
7.5.3 <u>Simulation of the distribution of large aggregates during the SCC flow in the L-box</u>	161
7.6 <u>Concluding remarks</u>	164
<u>Chapter 8</u>	166
<u>Conclusions and recommendations for future research</u>	166
8.1 <u>Conclusions</u>	167
8.2 <u>Recommendations for future research</u>	168
<u>References</u>	170
<u>Appendix A</u>	197
<u>Appendix B</u>	203
<u>Appendix C</u>	216

<u>Appendix D</u>	220
<u>Appendix E</u>	228

Chapter 1

Introduction

1.1 Scope of the research

Concrete occupies a distinguished position among the building materials and it has been used in construction for more than a century as a main construction material. In the reinforced concrete structures, the formworks and reinforcement are becoming more complex and extremely dense; therefore, many problems can occur due to insufficient compaction of concrete and of the inappropriate filling of the formworks. As a consequence of this, the durability and performance of mature concrete can be lower. Improved durability of concrete and working conditions have had high preference in the development of concrete construction. Therefore, attention has been directed towards the use of concrete independent of the need for compaction, known as self-compacting concrete (SCC) which offers a better quality of concrete and improved durability. It brought a new insight into concrete technology by increasing productivity and making casting homogeneous concrete in congested structures possible.

SCC was first developed in Japan in 1986; it was designed to fill the formwork completely and to flow through complex geometrical configurations and heavily reinforced areas, which are otherwise difficult to access, without any need for external compaction during the pouring process (Okamura and Ouchi, 2003). Along with these advantages, SCC offers many benefits to construction practice: improvement of the efficiency and effectiveness on site by reducing the labour cost and construction time, elimination of the noise pollution and the health problems related to the use of vibration equipment and improvement of the surface finishes with less defects.

It is widely accepted that successful SCC needs a combination of three fundamental requirements: filling ability, passing ability and segregation resistance. In order to achieve such requirements, it is necessary to adopt an appropriate mix design method for proportioning SCC mixes, however, the conflict between high fluidity and stability make SCC more complex to design than vibrated concrete (VC). Worldwide, different mix-proportioning methods have been proposed by researchers to design SCC mixes (Shi et al., 2015); to date, no unique mix design method has been adopted for proportioning SCC mixes, it is therefore of importance to devise a mix design method

for proportioning SCC to obtain adequate properties of fresh concrete that meet the self- compactability requirements

It is well known that the fracture behavior of concrete controls the failure of concrete structures and provides a basis for evaluation of the strength of cracked structures. The fracture mechanics provides an energy based failure theory that could be used in designing cement-based structures, since it studies the response and failure of structures as a consequence of crack initiation and propagation (Karihaloo, 1995). The most important properties describing the fracture behavior of the concrete mix are its specific fracture energy and the stress-crack relationship. Due to the variations in the composition of the SCC from the VC, concerns are raised among researchers about the fracture behavior and consequently about cracking mechanisms of SCC. Besides, limited research has been conducted to study the fracture properties of SCC, so there is an acute need for a study of the fracture behavior of SCC.

The workability and performance of fresh SCC during placement that includes transportation and pumping is dominated by its rheological properties, which in turn are affected by the characteristics of the mix constituents, i.e. cement, cement replacement materials, fine and coarse aggregates, water and admixtures. The passing ability around and between obstacles and the filling of the formwork are important properties of the SCC; they determine how well the SCC mix can flow through confined and limited zones. Accordingly, it is important to understand and predict the flow characteristics of the SCC mix in restricted area or around obstacles such as in L-box to examine how SCC fills formwork as a homogeneous mass without the segregation of mix components. The most cost-effective way to gain such an understanding is by performing numerical simulations, which will enable us to fully understand the flow behaviour of SCC and to reveal the distribution of larger aggregate particles inside the formworks.

1.2 Research aim and objectives

The overall aim of this study is to develop a simple and rational mix design method for proportioning successful SCC mixes, to investigate the fresh and hardened

properties of some of these mixes to validate the method, and to simulate their flow characteristics in the L-box.

With this aim in mind, the following objectives have to be met:

- To develop a mix design method for proportioning SCC mixes based on the desired target plastic viscosity and compressive strength of the mix. The simplicity and usefulness of this method will be enhanced by the provision of design charts for choosing the mix proportions that achieve the target plastic viscosity and the target compressive strength.
- To provide an experimental validation of the proposed mix design method to examine whether the developed SCC mixes meet the SCC criteria in both the fresh and hardened states.
- To investigate in detail the role of several compositional parameters such as the coarse aggregate volume, paste to solids ratio (p/s) and water to binder ratio (w/cm) on the fracture properties of SCC mixes. The fracture properties are the size- independent fracture energy (G_F) and the corresponding stress-crack relationship $\sigma(w)$.
- To simulate the flow characteristics of the SCC mix in the L-box test configuration using the three-dimensional mesh less Lagrangian smooth particle hydrodynamics (SPH) approach, treating the SCC mix as a non-Newtonian Bingham fluid. This methodology aims to provide insight into how the SCC can satisfy the self- compactability criterion of filling and passing abilities.
- To compare the distribution of coarse aggregate particles in the mixes during the simulation with the distribution of the corresponding sizes of coarse aggregate particles of the L-box test specimen.

1.3 Research methodology

To achieve the above objectives research is undertaken in four stages:

- ❖ **Firstly**, the mix design method for proportioning SCC mixes will be developed based on the target plastic viscosity and compressive strength. The

plastic viscosity of the SCC mixes will be estimated using micromechanical procedure (Ghanbari and Karihaloo, 2009) from the known plastic viscosity of the cement paste. A regression analysis will be performed on the data collected from many published sources to obtain a formula between the water to cementitious materials (w/cm) and the compressive strength.

- ❖ **Secondly**, the validity of the proposed mix design method will be proved by preparing a series of SCC mixes of different compressive strength and different plastic viscosity. In order to ensure that all mixes met the flow and passing ability criteria without segregation (SCC requirements), slump flow, J-ring, L-box and V-funnel tests will be conducted.
- ❖ **Thirdly**, the effect of several compositional parameters of SCC mixes on their fracture behaviour will be investigated. These parameters include: coarse aggregate volume, paste to solids (p/s) and water to binder (w/cm) ratios. The size-dependent fracture energy (G_f) will be measured using the RILEM work-of-fracture test on three point bend. Then, the size-independent fracture energy (G_F) will be calculated using the simplified boundary effect approach (SBE). Finally, the corresponding bilinear approximation of the stress-crack relationship will be obtained using the procedure based on the non-linear hinge model.
- ❖ **Fourthly**, the three dimensional Lagrangian smooth particle hydrodynamics (SPH) method will be used to simulate the flow of SCC mix in the L-box. SCC is regarded as non-Newtonian incompressible fluid whose behavior is described by a Bingham model, this model contains two parameters: the yield stress and the plastic viscosity. The former is predicted by an inverse manner of the developed SCC mixes (Badry, 2016a) and the latter is estimated using the micromechanical procedure (Ghanbari and Karihaloo, 2009). Then, the simulated results of flow characterises will be compared with experimental test results.
- ❖ **Fifthly**, The large coarse aggregate particles in the size ranges ($g \geq 20$, $16 \leq g < 20$, $12 \leq g < 16$, $8 \leq g < 12$ mm, where g is the size range of the aggregate) of the test SCC mixes will be colour coded with non-toxic non-water soluble paints so that the outlines of the aggregate particles would be clearly visible in the cut sections of the L-box test specimen. The distribution of the coarse

aggregate ($g \geq 20$, $16 \leq g < 20$, $12 \leq g < 16$, $8 \leq g < 12$ mm) during the flow of SCC mixes in the SCC mix will be simulated along two longitudinal sections. Then, the results of the numerical simulation of the flow times, the profile of free surface and the distribution of the large coarse aggregates will be compared with the corresponding test data.

Outline of the thesis

Including this introductory chapter, this thesis is organised into eight chapters, followed by bibliographical references and Appendices. The layout of the chapters is as follows:

Chapter 1 presents an introduction to the study, the objectives as well as research methodology and an outline of the thesis.

Chapter 2 reviews and summarises the relevant literature on SCC, its properties, the influence of materials used and the mix design methods proposed for developing SCC mixes. A review of the methods for testing SCC in its fresh state is also presented. Then, a review of the fracture mechanics of concrete which will be useful in a subsequent chapter will be given.

Chapter 3 provides an overview of smooth particle hydrodynamic approach, its concept, particle interpolation, kernel functions, density and gradient evaluation will be also presented together with a corrected particle interpolation. The three-dimensional Lagrangian governing equations of flow used to model the flow of SCC namely, the mass and momentum conservation equations will be introduced.

Chapter 4 describes the proposed mix design method for proportioning of SCC mixes; this method is based on the desired target plastic viscosity and compressive strength of the mix. The lower target plastic viscosity limit of these mixes varied between 3.5-8 Pa s and the upper target plastic viscosity is 15 Pa s and the characteristic cube strength between 30 and 80 MPa at 28 days age. Clarification of the basic steps of such method, the construction of the design charts and several examples on the use of the design charts are presented. The plastic viscosity of the SCC mixes so developed will be estimated by the micromechanical procedure. This plastic viscosity, together with the yield stress of the mix, will be used in the numerical simulation of SCC flow.

Chapter 5 presents the experimental validation of the mix design procedure on a series of the SCC mixes in both the fresh and hardened states. A series of SCC mixes that contained different volumetric ratios of paste to solid phases were prepared using the design charts. All these mixes were tested in the fresh state using the slump cone, J-ring, L-box, and V-funnel apparatuses.

Chapter 6 reports in detail on the basic concepts of the fracture mechanics. This chapter also reports the materials used, the preparation of the specimens and the test method used. As well, the determination of size-dependent fracture energy (G_f) using the RILEM work-of-fracture test on three point bend (TPB) and the size-independent fracture energy (G_F) using the simplified boundary effect approach (SBE) are presented. Finally, the procedure based on the non-linear hinge model for determining the bilinear stress-crack relationship for SCC mixes corresponding to the size-independent fracture energy (G_F) are also reported.

Chapter 7 presents the results of the 3-dimensional simulation of the non-Newtonian viscous SCC mixes. Here, an incompressible Lagrangian SPH method is adopted. The simulated results are the SCC flow times, the profile of free surface and the distribution of the large course aggregates ($g \geq 20$, $16 \leq g < 20$, $12 \leq g < 16$, $8 \leq g < 12$ mm) during the flow. Then, the comparison between the simulated results and the corresponding test data is presented.

Chapter 8 summarises the main conclusions of the research work embodied in Chapters 4 to 7. Recommendations for future research will be also made.

The thesis concludes with an alphabetical list of references to the works in the literature, cited in the text, and several appendices. Some of the work described in this thesis has been published or is in the process of publication, and has been presented at four Conferences. For easy reference, the publications are listed below.

[1] M. AL-Rubaye, S. Kulasegaram and B. L. Karihaloo, 2016. Simulation of self-compacting concrete in the L-box using smooth particle hydrodynamics (SPH). Magazine of Concrete Research (accepted).

[2] Al-Rubaye, M.M., Karihaloo, B.L. and Kulasegaram, S., 2016. Simulation of the flow of self-compacting concrete in the L-box using smoothed particle hydrodynamics

(SPH) method. In: the 24th UK Conference of the Association for Computational Mechanics in Engineering. Cardiff University, UK, pp. 56-59.

[3] Al-Rubaye, M.M., Alyhya, W.S., Abo Dhaheer, M.S. and Karihaloo, B.L. 2016. Influence of composition variations on the fracture behaviour of self-compacting concrete. In: 21st European Conference on Fracture, ECF21, Catania, Italy.

[4] Abo Dhaheer, M.S., Al-Rubaye, M.M., Alyhya, W.S., Karihaloo, B.L. and Kulasegaram, S., 2016. Proportioning of self-compacting concrete mixes based on target plastic viscosity and compressive strength: Part I - mix design procedure. *Journal of Sustainable Cement-Based Materials*, 5, pp.199–216.

[5] Abo Dhaheer, M.S., Al-Rubaye, M.M., Alyhya, W.S., Karihaloo, B.L. and Kulasegaram, S., 2016. Proportioning of self-compacting concrete mixes based on target plastic viscosity and compressive strength: Part II - experimental validation. *Journal of Sustainable Cement-Based Materials*, 5, pp.217–232.

[6] Alyhya, W.S., Abo Dhaheer, M.S., Al-Rubaye, M.M. and Karihaloo, B.L., 2016. Influence of mix composition and strength on the fracture properties of self-compacting concrete. *Construction and Building Materials*, 110, pp.312–322.

[7] Alyhya, W.S., Abo Dhaheer, M.S., Al-Rubaye, M.M., Karihaloo, B.L. and Kulasegaram, S. 2015. A rational method for the design of self-compacting concrete mixes based on target plastic viscosity and compressive strength. 35th Cement & concrete science conference (CCSC35), Aberdeen, UK.

[8] Alyhya, W.S., Abo Dhaheer, M.S., Al-Rubaye M. M., Karihaloo, B.L. and Kulasegaram, S. 2016. A rational method for the design of self-compacting concrete mixes target compressive strength. In: Khayat, K. H. ed. *Proceeding of the 8th International RILEM Symposium on Self-Compacting Concrete*. RILEM Publications SARL, Washington DC, USA.

Chapter 2

Self-compacting concrete (SCC)-

Literature Review

2.1 Introduction

In recent years, reinforced concrete structures are facing increasing demands for new structural design ideas; the reason behind this increased need is the increasing population. Consequently, the structural design and steel reinforcement in the concrete structures have become more complex and denser, resistive to concrete flow and can raise problems of pouring and compacting of concrete. The heavily congested steel reinforcement bars also have led to increased blockage due to the bridging of the coarse aggregate at the proximity of the steel reinforcement. In addition, casting of VC involves placing and subsequent compaction may require prolonged periods, which may result in a loss of concrete workability and a lack of long term durability of concrete structures.

SCC opens the possibility to address many of the problems associated with using VC in the reinforced concrete structures because of its intrinsic workability, passing and filling abilities and resistance to segregation. SCC is a type of concrete which can fill the whole mould completely with a minimum of defects and which compacts under its own self-weight without vibration. The concrete so produced is sufficiently cohesive, flows without segregation or bleeding and is of more reliable quality.

In this chapter, a general overview of the development of SCC will be given, highlighting the constituents materials used in SCC and their influence on the SCC mix characteristics in the fresh and hardened states. Mix design methods used for development of SCC and testing methods of SCC in its fresh state will also be reviewed. Then a brief review of the fracture mechanics of concrete will be given. Finally, the rheological properties of SCC will be summarised.

2.2 Development of self-compacting concrete (SCC)

In the early 1980s, durability issues related to concrete structures were a main concern and topic of interest in Japan. It was recognised that full compaction was difficult to obtain due to the reduction in the number of skilled workers and the increase of reinforcement volume in the Japanese construction industry; these conditions were leading to poor quality concrete with subsequent knock-on effects on the durability of concrete structures (Okamura and Ouchi, 1999).

The Japanese researchers came up with the concept of SCC in order to overcome problems associated with VC, and to enable form filling even in the presence of congested steel reinforcement and complicated formworks. Professor Okamura at the University of Tokyo proposed a concept for a design of concrete independent of the need for compaction in 1986.

The technology spread then to Europe starting from Sweden to other Scandinavian countries at the end of the 1990s (Billberg, 1999). In Denmark, SCC has been adopted in both ready-mix and pre-cast industry with an annual production reaching approximately 20% and 30%, respectively of the total concrete production (Thrane et al., 2004). Other countries, such as UK, France, Germany, USA and the Netherlands have also been developing and using SCC (Ouchi et al., 2003) with a temporary stagnation. One reason for this stagnation appears to be the lower segregation resistance of SCC compared with VC (Thrane et al., 2004).

The development of SCC has implied important changes in both the conceptual approach and construction methods for reinforced concrete structures, and opened new opportunities for design. SCC is widely used and appreciated, especially for tunnel linings of heavily reinforced structures, where conventional concrete would not fill out the formwork. The precast industry has taken great advantage of the possibilities given by casting with SCC.

2.3 What is SCC?

SCC is an advanced type of concrete with high performance that can spread into place under its own weight and achieve good consolidation in the absence of vibration without exhibiting defects due to segregation and bleeding. SCC provides consistency properties such as excellent filling and passing abilities, and adequate segregation resistance. Because of these unique properties, the use of SCC can result in improved construction productivity, improved jobsite safety, and enhanced concrete quality (Khayat et al., 1999a).

The advantages and disadvantages of SCC technology must be evaluated for each producer and application. SCC has many proven **advantages** over VC, including:

- Improved flow ability of concrete into complicated spaces and between congested reinforcement bars.
- Improved surface finish and reduced need to repair defects such as bug holes and honeycombing.
- Eliminated the internal segregation between aggregates particles and the surrounding paste.
- Improved workplace environment by reducing the harmful effects of vibration.
- Reduced manpower and construction time by placing SCC at a faster rate without vibration.
- Improved the interfacial transitional zone between cement paste and aggregate or reinforcement
- Improved durability and strength of the hardened concrete.
- SCC brings new possibilities into architectural design of concrete structures.

The disadvantages of SCC may include:

- Increased costs of SCC constituents, especially for admixtures and cementitious materials.
- Increased formwork costs due to possibly higher formwork pressures.
- Increased technical expertise required to develop mix proportions and quality control.
- The need efficient mixing procedure.

Many of these disadvantages can be, and have been, overcome by modifying the production and construction procedures.

2.4 How does SCC differ from VC?

SCC consists of cement, aggregates (coarse and fine), water and admixtures which are quite similar to the composition of VC, however, the reduction of coarse aggregates, the large amount of fines, the incorporation of super-plasticizer, the low water to cement ratio, is what led to self-compactability. Figure 2.1 shows graphically typical percentages of ingredients in the SCC and VC mixes.

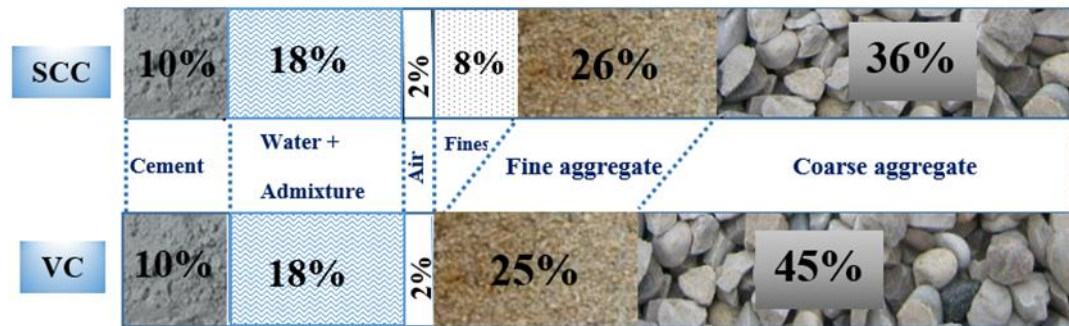


Figure 2. 1 Comparison between VC and SCC mixes (After: Okamura and Ouchi, 2003)

What makes SCC unique is the migration of air bubbles to the surface without any vibration which is mainly due to the dense matrix, mix proportion and the material characteristics. The smooth passing ability through reinforcement bars and the impressive filling ability of all the formwork without any segregation or bleeding are remarkable, even in narrow structural elements with complicated shapes and heavy reinforcement, thanks to the balance between high fluidity and moderate viscosity. All these properties in the fresh state lead to a high strength and durable concrete in the hardened state.

2.5 Fresh properties of SCC

The key characteristics of SCC are the properties in fresh state, and these characteristics should remain during transport and placing. When these characteristics are achieved properly, then the properties of SCC in hardened state such as durability and strength are also improved (Ouchi et al., 2003; EFNARC, 2005). The main characteristics of SCC in fresh state are:

Filling ability: filling ability reflects the deformability of SCC, i.e. the ability of fresh concrete to deform under its own weight and completely fill all parts of formwork horizontally and vertically while maintaining its homogeneity (Khayat, 1999; Okamura and Ozawa, 1995). There are two aspects of deformability: the deformation capacity is the maximum ability to deform; and deformation velocity refers to the time taken for the concrete to finish flowing. The high deformation capacity of SCC is related to the yield stress; thus, the yield stress must be decreased in order to ensure that SCC can flow around obstacles and achieve good filling ability. According to

Khayat and Tangtermsirikul (2000), the deformation capacity can be increased by lowering of interparticle friction between the solid particles, which include the paste, coarse aggregate, and fine aggregate.

Passing ability: the ability of fresh concrete to pass through high amount of reinforcement congestion without any separation of the constituents or blocking, whilst maintaining good suspension of coarse particles in the matrix. It depends on the risk of blocking which results from the interaction between constituent materials and obstacles. Blocking results from the interaction among aggregate particles and between aggregate particles and reinforcement. When concrete approaches a narrow space, the different flowing velocities of the mortar and coarse aggregate lead to a locally increased content of coarse aggregate (Noguchi and Tomosawa, 1999; Okamura and Ouchi, 2003). Figure 2-2 adapted from RILEM TC 174 SCC (2000) shows that some aggregates may bridge or arch at small openings which block the rest of the concrete. Therefore blocking mainly depends on the size, shape and content of coarse aggregate (Okamura, 1997). Likewise, paste volume is also an important factor on blocking (Billberg et al., 2004). Another conclusion of Billberg et al. (2004) is that blocking depends mainly on the yield stress, whereas plastic viscosity does not influence the passing ability of SCC. However, a paste with appropriate viscosity also prevents local increases in coarse aggregate and hence blocking is avoided.

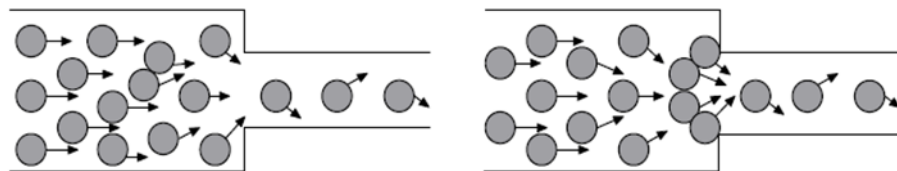


Figure 2. 2 Schematic of blocking (After: RILEM TC 174 SCC, 2000)

Segregation resistance: is sometimes called ‘stability’; it refers to the ability of concrete to remain homogeneous in fresh state without any migration or separation of its large aggregates. Segregation includes that between water and solid or between paste and aggregate or between mortar and coarse aggregate in both stationary and flowing states (RILEM TC 174 SCC, 2000). There are types of segregation; the first one is called dynamic segregation which happens during placing, the second one is

called static segregation which happens after placing, if coarse aggregate settles and the free water rises causing bleeding.

Segregation resistance is largely controlled by viscosity; therefore ensuring a high viscosity can prevent a concrete mix from segregation and/or bleeding. Bleeding is a special case of segregation in which water moves upwards by capillary action and separates from the mix. Some bleeding is normal for concrete, but excessive bleeding can lead to a decrease in strength, high porosity, and poor durability particularly at the surface (Douglas, 2004).

2.6 SCC Categories

Depending on the method of providing viscosity, SCC mix is classified as one of three types, powder, VMA or combined type (Dehn et al., 2000; Holschmacher and Klug, 2002).

- Powder-type SCC is characterised by a low water - powder ratio (W/P) and a high powder content, which are required to limit the free water content and increase the plastic viscosity. As a result of the high powder content, powder-type SCC mixes are sensitive to changes in constituent materials. Due to the low W/P ratio, such concretes are expected to have a high strength and shrinkage, and low permeability.
- VMA-type SCC is characterized by a high viscosity modifying agent (VMA) dosage, which is added primarily for increasing the plastic viscosity. To achieve flow-ability using this method a higher amount of super-plasticiser or higher W/P ratio is required compared with the powder-type.
- Combined – type SCC is developed to improve the robustness of powder-type SCC by adding a small amount of VMA. In this type of mixes, the VMA contents are less than those in the VMA-type SCC; the powder content and W/P ratio are less than those in the powder-type SCC. Viscosity is provided by the VMA along with powder. This type of SCC was reported to have high filling ability, high segregation resistance and improved robustness (Khayat and Guizani, 1997).

2.7 Constituent materials of SCC mix

Concrete is a mix of cement, aggregates (coarse and fine) and water, where cement acts as the binding material. SCC has the same constituent materials as those for VC but their relative proportions differ, and need to be precisely chosen. The reason behind that is the performance of SCC largely depends on the properties of its ingredients. Therefore, appropriate constituent materials should be selected and specifications must be given more enforcement to produce SCC. Generally speaking, a lower coarse aggregate content and higher amounts of additions and cement, mineral admixtures and chemical admixtures (particularly superplasticisers) are required to achieve self-compacting properties

SCC consists of cement (C) and cement replacement materials (CRMs), aggregates that include coarse and fine aggregates (CA & FA), mineral admixtures such as limestone powder (LP), chemical admixtures such as superplasticiser (SP) and Viscosity modifying agents (VMA), and water (W). The following sections briefly describe the constituent materials of SCC.

2.7.1 Cement and cement replacement

Portland cement is a common type of cement in general use around the world to produce various types of concrete. Portland cement is also a basic component of SCC; it is used alone or in combination with cement replacement materials (CRMs) to produce SCC.

Flow-ability and segregation resistance are achieved by limiting the content of coarse aggregate, the maximum aggregate size and reducing water–powder ratios (W/P) together with using super-plasticisers (SP) (Ouchi et al., 1998). Segregation and bleeding resulting from increased flow-ability during the transportation and placement of SCC can be overcome by enhancing the viscosity of SCC mix. This is usually supplied by using a high volume fraction of paste, limiting the maximum aggregate size or using viscosity modifying admixtures (VMA) (Khayat, 1999). However, chemical admixtures are expensive and may contribute to increasing the cost of concrete. On the other hand, achieving high powder content by increasing the cement content is not feasible, and may lead to a significant rise in material cost and some

negative impacts on concrete properties associated with the rise in temperature during hydration and higher drying shrinkage. Therefore, incorporating cement replacement materials (CRMs) in concrete can impart many advantages to concrete due to their effective physical and chemical effects on material packing and microstructure (Hassan et al., 2000; Khatri and Sirivivatnanon, 1995; Mehta, 1994). All CRMs have two properties; their particle size is smaller or the same as Portland cement particle and they become involved in the hydration reactions mainly because their ability to exhibit pozzolanic behaviour. The most common CRMs used are ground granulated blast furnace (ggbfs), micro-silica or silica fume (SF) and pulverised fuel ash or fly ash (FA).

2.7.2 Aggregates

Both fine and coarse aggregates are used in the production of self-compacting concrete. Coarse aggregate (CA) is a key component of concrete; it is granular material, such as gravel or crushed stone and is retained on the 4.75-mm (No.4) sieve. The properties and durability of concrete are affected by physical properties such as the size, shape, surface texture. Further, the well-graded coarse aggregates participate to produce the optimum mix with least particle interference (Shilstone, 1990), and hence improve the flowing ability and reduce the tendency of segregation in fresh concrete. As in VC, coarse aggregate affects the performance of SCC by influencing the properties of SCC in both fresh and hardened states (Noguchi et al., 1999; Okamura and Ozawa, 1995; Xie et al., 2002).

The second ingredient of aggregate is the fine aggregate (FA); it passes the 4.75 mm (No. 4) sieve but is retained on the 75 μm (No. 200) sieve. Similar to coarse aggregate, fine aggregate also influences the performance of SCC when it used in suitable amounts (Okamura and Ozawa, 1995; Su et al., 2002). For instance, fine aggregate influences the mortar flow and consequently the flowing ability of SCC (Okamura and Ozawa, 1995; Hu and Wang, 2005).

2.7.3 Mineral admixtures

Mineral admixtures are finely divided materials that are used in concrete in order to improve certain properties such as workability, strength, durability, economy, and to control the rate of hydration. Mineral admixtures are classified into two groups; the first group has pozzolanic properties and the second group does not have any pozzolanic properties and are also termed as fillers. One of the most commonly used fillers is ground limestone, normally known as limestone powder (LP). LP does not participate in cement hydration (Ye et al., 2007), and its action can be related to a change in the microstructure of the cement matrix associated with the small size of the particles, showing an enhancement in the packing density of powder, increasing the stability and the cohesiveness of fresh SCC. However, excessive amounts of fine particles can result in a considerable rise in the surface area of powder and an increase in inter-particle friction, due to solid-solid contact, which may affect the ability of the mixture to deform under its own weight, pass through obstacles and also a substantial rise in the viscosity (Yahia et al., 2005).

2.7.4 Chemical admixtures

2.7.4.1 Superplasticiser (SP)

Super-plasticisers, otherwise known as high range water-reducing admixtures (HRWRAs) contribute to the achievement of denser packing and lower porosity in concrete by increasing the flow-ability and improving the hydration through greater dispersion of the cement particles, and thus assisting in producing SCCs of high strength and good durability. Two aims can be achieved from using superplasticiser (SP): the first, the use of SP allows controlling the flow properties, which are of major importance for the design of e.g. SCC, and the second, SP allows the reduction of the water to cement ratio while maintaining workability in order to reach desirable strength and durability. The use of SP enhances the flow-ability of SCC by its liquefying and dispersing actions (Hu and de Larrard, 1996; Yen et al., 1999). In addition, a superplasticiser deflocculates the cement particles and frees the trapped water by its dispersing action and hence enhances the flow-ability of SCC as illustrated in Figure 2.3. However, a high amount could cause segregation and bleeding.



Figure 2. 3 Method of deflocculation and water liberation with use of Super-plasticiser, (After: Deeb, 2013)

The production of SCC and the achievement of required workability have become easier with the advent of superplasticisers and the developments in the admixture technology. There are four categories of SP, namely the sulfonated melamine formaldehyde condensates (plasticiser), sulfonated naphthalene formaldehyde condensates, modified lignosulfonates, and carboxylated acrylic ester co-polymers or poly-carboxylic ethers (Boukendakdji et al., 2012). The advances in admixture technology have played a substantial part in the development of SCC. Modern superplasticisers (based on poly-carboxylic ethers) promote good workability retention, contribute to the achievement of denser packing and lower porosity in concrete by increasing the flow-ability and improving the hydration through greater dispersion of the cement particles.

2.7.4.2 Viscosity modifying agents (VMA)

Viscosity modifying agents (VMA), also known as anti-washout admixtures, can be added to the concrete mixtures to improve segregation resistance, cohesiveness and reduce bleeding. In general these admixtures increase yield stress and plastic viscosity. They may be also used as an alternative to increasing the powder content or reducing the water content of a concrete mixture (Koehler et al., 2007).

Acrylic- or cellulose-based water-soluble polymers or polysaccharides of microbial sources, such as welan gum are the commonly used viscosity-modifying agents in concrete. Water-soluble polymers can imbibe some of the free water in the system, thus increasing the viscosity of the cement paste which, in turn, enables the paste to hold aggregate particles in a stable suspension.

When using VMAs in SCC mixtures it is important to take into account its compatibility with the super-plasticiser used. For instance, cellulose derivatives are incompatible with a naphthalene-based super-plasticiser, whereas welan gum is compatible (Khayat, 1995). Adding VMAs to SCC mixtures can alter cement hydration, resulting generally in a decrease in the compressive strength, flexural strength and modulus of elasticity of hardened concrete (Khayat, 1995).

2.7.5 Water

Water (W) has a profound impact on both the fresh and the hardened properties of SCC. W decreases both the yield stress and the plastic viscosity. Segregation is much more prone to happen in SCC if only W is added to increase the filling ability, therefore, SP should be incorporated in order to develop SCC mix with required properties. W in the fresh concrete includes freely movable water and the water retained by the powder (filler and cement), sand and VMA, but coarse aggregate does not confine water. Free W is one of the main factors determining the filling ability and segregation resistance (Ouchi et al., 1998).

2.8 Mix proportioning methods of SCC

Mix design is an essential first step for both research programmes and practical application of concrete and such step must start with the definitions of the applications of SCC. To ensure a good balance between the fresh properties of SCC such as deformability and segregation resistance, the proportion of the constituent materials must be carefully designed. Deformability can be accomplished by limiting the volume of the coarse aggregate while segregation resistance can be achieved by controlling the mortar rheology through reducing the W/cm, increasing the powder content, or adding VMA. Furthermore, the other properties of SCC like rheology, strength, shrinkage and durability are also affected by the mix design method, the characteristics of raw materials, incorporation of chemical and mineral admixtures, aggregate packing density, water to cement ratio (W/C) (Han et al., 2014; Esmaeilkhani et al., 2014; Siddique et al., 2012; Wang et al., 2014).

Although there are different mix proportioning methods used to develop SCC mixes, they do share some similarities. In reviewing of the proposed mix design methods, it is difficult to compare one method to another, because each method has been developed according to its own particular conditions and environment, and has its own special features and some inherent limitations. These methods can be categorized into different classes (Shi et al., 2015): empirical mix design method, compressive strength method, aggregate packing method, method based on statistical factorial model, and rheology of paste model. In the current study, the rational mix design method will be adopted for proportioning SCC. Even though there are a large number of publications on SCC mix design studies, there is no unique method that can be used for all SCC applications. The following sections detail the main concepts of these mix proportioning methods.

2.8.1 Empirical design method

According to empirical design method, the empirical data of the contents of coarse and fine aggregates (CA &FA), water (W) and cementitious materials (CMs) and superplasticizer dosage (SP) are included to determine the initial mix proportions. Okamura and Ozawa (1995) and Okamura (1997) proposed the early mix design method, and this method has also been used in many countries of Europe with some modifications (EFNARC, 2005). In this method, the contents of CA & FA are kept constant so that the self-compacting-ability can be achieved just by only modifying water to binder (W/B) ratio and superplasticiser (SP) dosage. Many researchers (Edamatsu et al., 1998; Edamatsu et al., 2003; Domone, 2009; Khaleel and Abdul Razak, 2014) have made modifications to the proposed method. This method was developed for general application and has the advantage of simplicity; however, its drawback is that the W/B ratio cannot be fixed based on the strength requirement because it has to be decided through achieving the self-compacting capacity, consequently, this ratio may not provide the desired strength. In addition, it may take many trial mixes to fix the suitable W/B ratio and SP dosage, as these two must be balanced to provide optimum flowing ability and segregation resistance.

2.8.2 Compressive strength method

This method is based on the required compressive strength to determine the contents of cement (C), mineral admixtures, water (W) and aggregate (CA& FA). Ghazi et al. (2010) have proposed a mix design method for SCC based on ACI 211.1-91 (1991) method for proportioning VC and EFNARC (EFNARC, 2002) method for proportioning SCC with certain modifications. The compressive strength of VC according to ACI 211.1-91 method was ranged from 15 to 40 MPa, while according to this proposed method the range of compressive strength expanded from 15 to 75 MPa, furthermore, the content of CA depended on the maximum aggregate size and fineness modulus of the fine aggregate. Dinkar et al. (2013) followed such an approach, and developed a mix design method for SCC containing granulated blast-furnace slag (ggbfs) based on the strength requirements and considered the efficiency of ggbfs. However, this method provides a clear and accurate procedure to obtain specific quantities of ingredients and reduces the need for trial mixes; but it demands adjustments to all ingredients like fine and coarse aggregate, superplasticizer and water, to achieve the best mix proportion.

2.8.3 Aggregate packing method

The essence of this method is to improve particle packing of the concrete system and reduce the high paste volumes sometimes associated with SCC. Moreover, this method determines mix proportions by minimizing the void content (maximum packing density) among aggregate particle to allow more paste to cover aggregate surfaces in a given concrete system.

Hwang and Tasi (2005) proposed a method based on the Densified Mixture Design Algorithm (DMDA). The DMDA method is developed from the hypothesis that the physical properties will be optimum when the physical density is high. The major difference from the other mixes design algorithms is that instead of partial replacement of cement, DMDA incorporates fly ash that is considered as part of the aggregate and not the paste to fill the void of aggregates and hence increase the density of the aggregate system. As a result, besides physically acting as filler, fly ash acts chemically as a pozzolanic material. Although the SCC designed by the DMDA is

highly flowable, cost-effective and durable, there is very little information concerning the passing ability through reinforcement and segregation resistance. Su et al., (2001, 2003), and Sedran and De Larrard (1999) have developed mix design methods for SCC, henceforward referred to as the Chinese method and the French method, respectively. The principal consideration of these methods is to optimize the particle size distribution of the fine and coarse aggregates, powders based on the packing considerations. As a basis for concrete proportioning, linear packing calculations were developed to calculate the packing of aggregates with varying particle size distributions. This was done by successively filling up the voids of aggregate with optimum amounts of binding paste to satisfy the required properties of concrete with regard to workability and strength. Sebaibi et al. (2013) and Kanadassan and Abdul Razzak (2014) have followed the aggregate packing approach, they have made modifications on this method to develop SCC mixes. The aggregate packing approach is simple and uses a smaller amount of binders, but it has limitations such as the determination of the optimum fine aggregate to coarse aggregate ratio or the packing factor are not explained, hence, these two values are assumed empirically to carry out the mix design.

2.8.4 Mix design method based on statistical factorial model

Statistical modelling approaches have been used to identify the relative significance of primary mix parameters and their effects on fresh and hardened properties of SCC. Khayat et al. (1999a, 2000) proposed a statistical factorial model by selecting five key mix parameters: the content of cement, water-to powder ratio, volume of coarse aggregate, and dosage of both SP & VMA to derive design charts. These design charts correlate the input mix-design variables to output material properties, mainly consisting of the measurements of fresh state properties as well as the compressive strength (Shi et al., 2015). According this approach, regression models are used to evaluate data and optimize proportions. Other authors Sonebi (2004), Ozbay et al. (2009) and Bouziani (2013) followed this design approach to design and optimize the mixes, to compare the responses obtained from various test methods, to analyze the effect of changes in mix parameters to evaluate SCC mix.

One of the advantages of using this approach is that it is valid for a wide range of mix proportions. Another advantage is that it provides an efficient means to determine the influence of key variables on SCC properties. However, the resulting regression models are specific to only the materials and range of proportions considered, therefore the establishment of statistical relationships needs intensive laboratory testing on available raw materials.

2.8.5 Mix design method based on rheology of paste model

Since the control of self-compacting abilities of SCC mix depends on controlling the flow properties of cement paste, it is necessary to understand the influence of each constituent on the flow behavior at paste scale.

Saak et al. (2001) have introduced a design methodology for SCC, assuming that the segregation resistance and workability of fresh concrete are affected largely by the rheology and density of the cement paste matrix, given a specified particle size distribution and volume fraction of aggregate. This methodology highlights how the segregation can be controlled in SCC, but it does not clearly explain how the aggregate properties and content influence the filling ability and passing ability of concrete. In addition, it does not provide any clear guidelines for obtaining high strength and improved transport properties or durability. Bui et al. (2002) extended Saak's concepts by including the effects of aggregate volume ratio, the paste volume ratio, particle size distribution of the aggregates and the ratio of the fine to coarse aggregate.

The paste rheology model and criteria related to aggregate spacing and average aggregate diameter can be applied for different coarse-to-total aggregate ratios, cement contents, and water-to binder ratios as well as different contents and types of fly ash. It can reduce the extent of laboratory work and materials used, and provide the basis for quality control and further development of new mineral and chemical admixtures. The limitation of this method is that restricted guidance is provided for selecting the average spacing between aggregates and for optimizing paste rheology.

Karihaloo and Ghanbari (2012) and Deeb and Karihaloo (2013) have proposed a mix design method for proportioning normal and high strength SCC mixes based on their plastic viscosity. It exploits the expression for the plastic viscosity of the SCC mix

developed by Ghanbari and Karihaloo (2009) using micro–mechanical principles. In this procedure, SCC is regarded as a two–phase suspension in which the solid phase is suspended in a viscous liquid phase. The increase in the plastic viscosity of the liquid phase as a result of the addition of the solid phase (filler, fine and coarse aggregates) is estimated in a stepwise manner from the two–phase suspension model.

2.9 Assessing the workability of SCC

The assessment of the workability of SCC mix can be divided into three categories as proposed by Tattersall (1991):

- Qualitative assessment; it is a general description of concrete behaviour such as workability, flow-ability, stability, compactability, pump-ability...etc. without any attempt to quantify.
- Quantitative empirical assessment to be used as a simple description of behaviour such as slump flow test, L-box test...etc.
- Quantitative fundamental assessment; it is a description related to rheological terms of concrete, e.g. plastic viscosity, fluidity and yield value.

Fresh SCC mix is a multi-phase system with non-linear time-dependent properties. The quantitative fundamental rheological tests can be performed on an SCC mix using rheometers of different types. However these tests suffer for some drawbacks; they are not suited for use at the working site, and they can be rather time-consuming (Utsi et al., 2003). Therefore, it is important to find suitable workability test methods for continuous use outside the laboratory, and to calibrate them with rheological parameters. For the SCC mix, a number of quantitative empirical workability assessment tests have been proposed and established in practice, such as slump flow test, J-ring test, L-box test, V-funnel test, U-box test and wet sieve stability...etc. In this section, the workability tests which are recommended by the British standard (BS EN 206-9, 2010) are discussed, namely the slump flow and V-funnel tests for flowing ability, L-box and J-ring tests for passing ability.

2.10 Testing methods of Fresh SCC

A concrete mix can only be classified as SCC if the requirements for fresh properties like filling ability, passing ability and segregation resistance are fulfilled. Each of these properties should be evaluated independently through an appropriate test method to determine its quality; filling ability should be evaluated with the slump flow test and V-funnel test, passing ability with the J-ring and L-box tests. A review of the test methods is presented in the following sections.

2.10.1 Flow-ability tests

2.10.1.1 Slump flow test

The slump flow test on SCC is in many respects similar to the slump test conducted on VC except that no compaction is included. The slump test is the most common and popular test used to assess the deformability capacity of SCC in the absence of obstacles because this test is simple and rapid (Takada and Tangtermsirikul, 2000). The segregation resistance in this test can be detected visually. Because of its simplicity procedure, the slump test can be done either on site or in the laboratory with inverted or upright Abram's cone. It is carried out in accordance with BS EN 12350-8 (2010).

The test procedure involves placing the cone on the centre of a non-absorbing levelled flat steel plate, filling with the sample without compaction and then lifting vertically. SCC flows out freely under the influence of gravity. After the sample has stopped flowing, the largest diameters of the deformed sample in two perpendicular directions are measured as d_1 , d_2 (mm) (Figure 2.4). The final spread is the average flow spread diameter SF calculated using Equation (2.1)

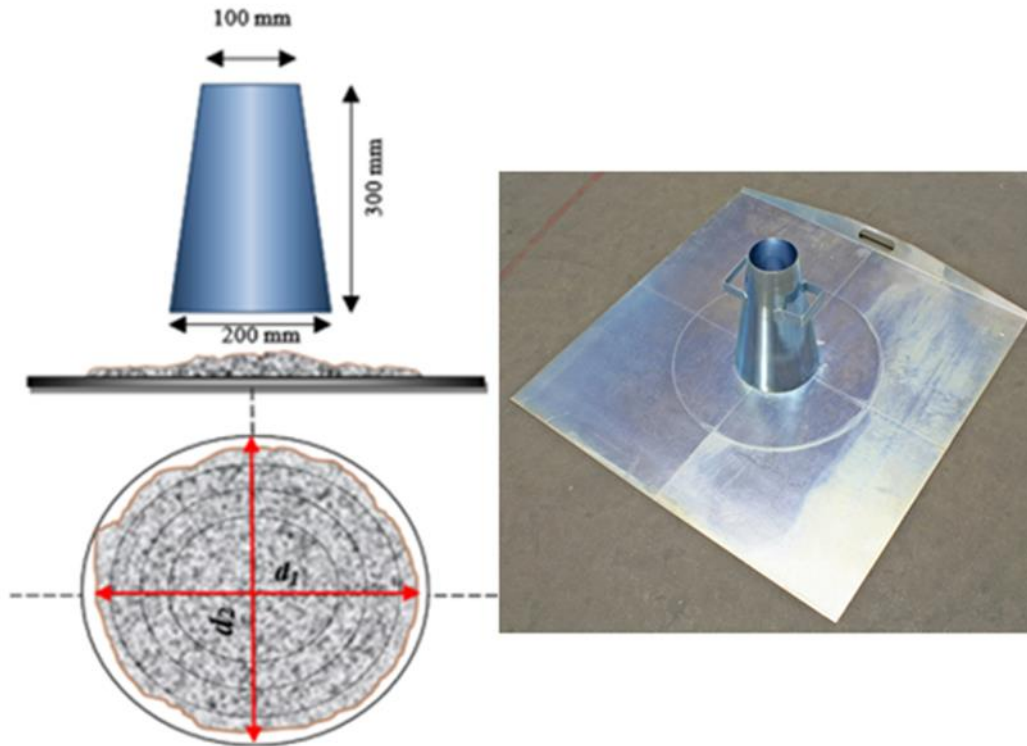


Figure 2. 4 Slump flow test approach

$$SF = \frac{(d_1 + d_2)}{2} \quad (2.1)$$

The criteria of acceptance are:

- ❖ Achieving a large diameter with no segregation indicates a good deformability and a low yield stress.
- ❖ t_{500} ‘the time needed for SCC to reach a diameter of 500 mm’ should be recorded.
- ❖ This test is not acceptable when the largest aggregate size is more than 40 mm.
- ❖ The difference between d_1 and d_2 should be less than 50 mm otherwise the test should be repeated.
- ❖ Segregation can be detected by visually inspecting a ring of cement paste/mortar in the edge of flow, and /or ensuring that no coarse aggregates and/or fibres have lifted in the centre of flow.

2.10.1.2 V-funnel test

The V-funnel test is used to assess deformation velocity of SCC flowing through a restricted area by measuring the time for SCC to flow out of the funnel under its own weight (Figure 2.5). It is carried out in accordance with BS EN 12350-9 (2010). This test is used to evaluate deformation velocity, which is affected by the passing ability and segregation resistance of concrete. A long V-funnel time can indicate either a low deformation capacity due to high inter-particle friction or blockage of the flow.

In this test a standard funnel is filled completely with SCC, and after a delay of (10 ± 2) s from filling the funnel, the bottom outlet is opened allowing the concrete to flow. The V-funnel time is the elapsed time (t) in seconds between the opening of the bottom outlet and the time when the light becomes visible from the bottom, when observed from the top (EFNARC, 2005).

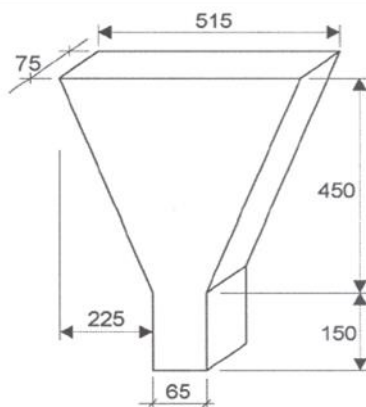


Figure 2. 5 V-funnel test approach

The criteria of acceptance are:

- ❖ The flow of concrete from the funnel shall be continuous;
- ❖ V-funnel flow time, $t_{V\text{-funnel}}$, should be recorded to the nearest 0.5 s;
- ❖ The test should be repeated if blockage occurs.

2.10.2 Passing ability tests

2.10.2.1 J-ring test

J-ring is a test used in conjunction with a slump test to assess the passing ability of SCC through gaps in the obstacles, e.g. reinforcement. For this test, the slump test apparatus is used with an open steel rectangular section ring with 16 steel rods ($\phi 16$ mm) and 100 mm height, as shown in the Figure 2.6. The gap between the bars is 42 mm ± 1 .

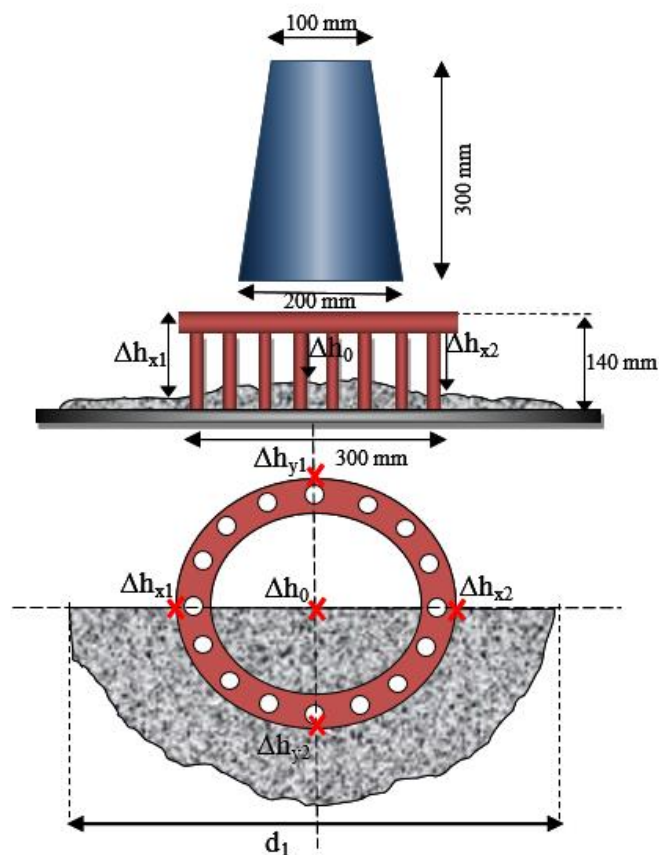


Figure 2. 6 J-ring test apparatus

After filling the cone with concrete without using any vibration or rodding, the cone is lifted perpendicular to the steel base plate allowing the concrete to flow freely. The time needed for the flow to reach 500 mm diameter is recorded as t_{500J} , and the flow allowed to stop before recording the remaining measurements (BS EN 12350 -12, 2010).

- Flow spread of the J-ring (SF_J) indicates the restricted deformability of SCC and can be expressed using Equation (2.2)

$$SF_J = \frac{(d_1+d_2)}{2} \quad (2.2)$$

- Flow time t_{500J} has been recorded.
- The J-ring passing ability PJ , measured by the blocking step, is calculated using Equation (2.3) and expressed to the nearest 1 mm.

$$PJ = \frac{\Delta h_{x1} + \Delta h_{x2} + \Delta h_{y1} + \Delta h_{y2}}{4} - \Delta h_0 \quad (2.3)$$

where:

Δh_0 : is the height measurement at the centre of flow.

Δh_{x1} , Δh_{x2} , Δh_{y1} , Δh_{y2} are the four measurement heights at positions just outside the J-ring.

The criteria of acceptance are:

- ❖ the flow spread (SF_J) of SCC, using the J-ring can be assessed relative to the flow spread (SF) of the same mix using the slump test as described in Table 2.1

Table 2. 1 Passing ability criteria

(SF-SF _J)	Passing ability rate	Notes
< 25 mm	0	No visible blocking
25 mm - 50 mm	1	Minimal to noticeable blocking
> 50 mm	2	Noticeable to extreme blocking

- ❖ The blocking step PJ should be less than 10 mm (BS EN 206-9, 2010).
- ❖ t_{500J} which is the time needed for SCC to reach a diameter of 500 mm should be recorded.

- ❖ This test is not acceptable when the largest aggregate size is more than 40mm.
- ❖ The difference between d_1 and d_2 should be less than 50 mm otherwise the test should be repeated.
- ❖ Segregation can be detected by visually inspecting a ring of cement paste/mortar in the edge of flow, and /or ensuring that no coarse aggregates or fibres have lifted in the centre.

2.10.2.2 L-box test

The L-box test is used to assess the filling and passing ability of SCC, or in other words the ability of concrete to pass through reinforced bars without blocking or segregation. The apparatus consists of a rectangular section box in shape of an “L” with a vertical and horizontal section separated by a movable gate as shown in Figure 2.7. After filling the vertical column of the L-box, the gate is lifted to allow SCC to flow into the horizontal part after passing through the rebar obstructions. Two measurements are taken, (H_1 , H_2) heights of concrete at the beginning and end of the horizontal section, respectively. The ratio H_2/H_1 represents the filling ability, and typically, this value should be 0.8~1, while the passing ability can be detected visually by inspecting the area around the rebar.

In L-box, 2 or 3 smooth steel bars with 12 mm diameter can be used to represent light or dense reinforcement with distance between them 59 and 41 mm, respectively.

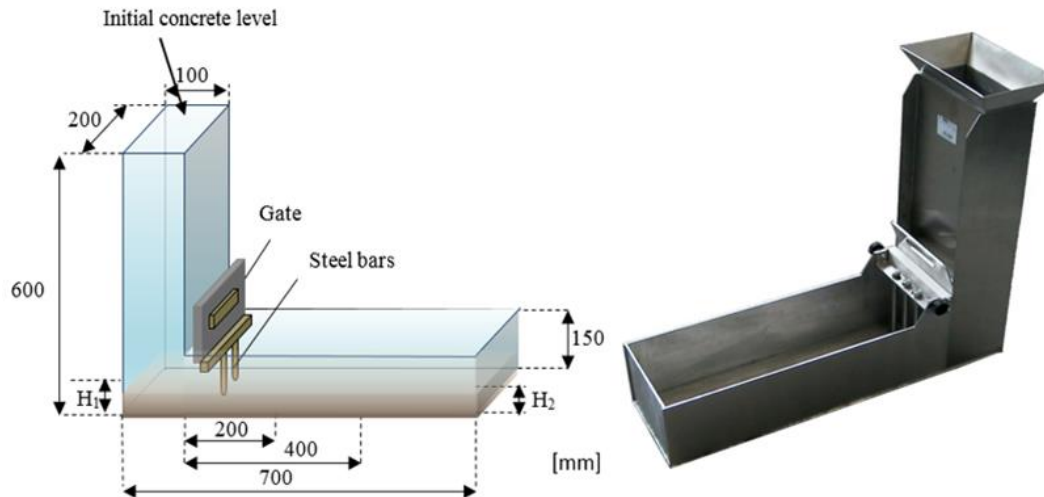


Figure 2. 7 L-box test apparatus

The passing ability ratio PL should be calculated:

$$PL = \frac{H_2}{H_1} \quad (2.4)$$

H_1 is the mean depth of concrete in the vertical section of the box

H_2 is the mean depth of concrete at the end of the horizontal section of the box.

t_{200} and t_{400} are also recorded which represent the time of SCC to reach 200 mm and 400 mm from the gate, respectively as illustrated in Figure 2.7.

According to BS EN 12350-10 (2010).The criteria of acceptance are :

- ❖ For this test, at least 14l of SCC should be prepared in accordance with (BS EN 12350-10, 2010).
- ❖ No signs of segregation or bleeding;
- ❖ Passing ability ratio PL should be between 0.8 and 1; a value more than 1 means an error.
- ❖ There is no recommendation for t_{200} and t_{400} values, but longer values represent higher viscosity.

It should be mentioned that this test is very sensitive to the operator in terms of the speed of lifting the gate. Slow lifting can result in an increase in t_{200} and t_{400} .

2.11 Fracture mechanics of Concrete

2.11.1 Introduction

“Plain and reinforced concrete structures are full of flaws, such as pores filled with water, air voids, lenses of bleed water under coarse aggregates and shrinkage cracks, even before they are mechanically loaded. These flaws, and especially the small cracks (microcracks), grow stably under external loading, coalesce with existing or newly-formed microcracks until large fractures are formed which cause the collapse of the structure. To date these structures are designed without regard to either the propagation of large cracking zones through them or an energy failure criterion. Fracture mechanics provides an energy based failure theory that could be used in designing cement-based structures against the consequences of crack initiation and propagation” (Karihaloo, 1995).

Based on their tensile stress-deformation response, most engineering materials can be categorized into three main classes;

- Brittle: stress suddenly drops to zero when a brittle material fractures.
- Ductile: stress remains nearly constant when a ductile material yields.
- Quasi-brittle: stress gradually decreases after the peak stress.

The linear elastic fracture mechanisms theory (LEFM) has been available since 1920 (Griffith, 1920; Griffith, 1924), but this theory is only applicable to elastic homogeneous brittle materials such as glass. Later modifications by Orowan (1949), and Irwin (1957), extended it to elastic-plastic homogeneous materials. Attempts were made in the 1950s (Breslar and Wollack, 1952) and 1960s (Kaplan, 1961; Glucklich, 1963) to apply LEFM to concrete, which was thought to be brittle, but these proved unsuccessful (Kesler et al., 1972). The lack of success of LFEM is because cement-based materials exhibit a totally different response. It was concluded that LEFM is not

applicable for concrete because it is not a brittle material, whereas the only exception to this general rule was the case of large concrete structures. Consequentially, due to the fact that concrete is a quasi-brittle material, nonlinear fracture mechanics (NLFM) for concrete was proposed.

2.11.2 Nonlinear fracture mechanics (NLFM)

As mentioned above, it was argued that the LEFM is not applicable to concrete due to the existence of the inelastic toughening mechanisms (i.e. fracture process zone) that appear around a crack when it propagates. Therefore, a fracture theory capable of describing the material softening process that takes place in the fracture process zone must be a nonlinear fracture mechanics (NLFM) theory.

The following section gives a brief description of the fictitious crack model (FCM) as one of the NLFM models.

2.11.2.1 Fictitious crack model (FCM)

The so-called fictitious crack model (FCM) proposed by Hillerborg et al. (1976) is the first nonlinear theory of fracture mechanics of concrete. It includes the tension softening fracture process zone through a fictitious crack ahead of the pre-existing crack whose faces are acted upon by certain closing stresses such that there is no stress concentration at the tip of this extended crack (Figure 2.8). In this model the crack is composed of two parts; a real traction-free crack of length a_0 (the true or physical crack through which no stresses can be transmitted) and a fictitious crack or fracture process zone (FPZ) ahead of the true crack.

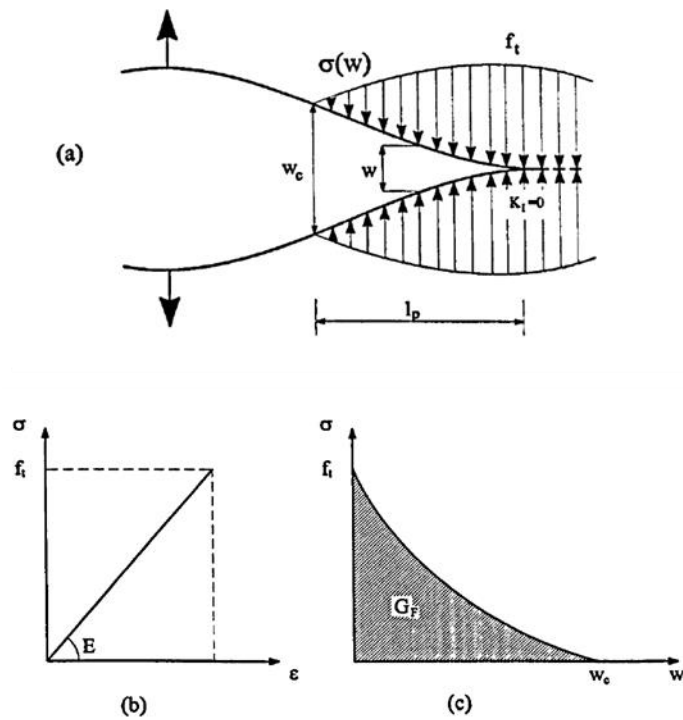


Figure 2. 8 (a) A real traction-free crack terminating in a fictitious crack with residual stress transmission capacity $\sigma(w)$. The material ahead of the fictitious crack tip is assumed to be linear (b), but the material within the fracture process zone is softening; the area under the softening curve equals fracture energy G_F (c) (After: Karihaloo, 1995).

In the fictitious crack model, it is necessary to have two material parameters. These are:

- The shape of stress-deformation relation $\sigma(w)$ in the softening zone;
- The area under the tension softening curve which is the specific fracture energy G_f (Figure 2.8c)

$$G_f = \int_0^{w_c} \sigma(w) dw \quad (2.5)$$

where, w_c is the critical crack opening at which the closing stress is equal to zero.

There is also another material parameter which can be obtained from the above information, namely the characteristic length of the material

$$l_{ch} = \frac{EG_f}{f_t^2} \quad (2.6)$$

2.12 Determination of specific fracture energy

According to the RILEM-50FMC recommendation (1985), the specific fracture energy (G_f) is the average energy given by dividing the total work of fracture with the projected fracture area. This parameter can be measured using a pre-cracked (notched) specimen. A commonly used specimen shape for the determination of (G_f) is a notched beam loaded in three-point bending (Figure 2.9). The specimen is loaded gradually and the variation of the load (P) is plotted against the mid-span deflection. The specific fracture energy (G_f) is then calculated using the formula

$$G_f = \frac{1}{(W-a)B} \int P d\delta \quad (2.7)$$

where W , B and a are the specimen depth, width and the notch length, respectively. The weight of the specimen can be considered, if necessary (i.e. large specimens).

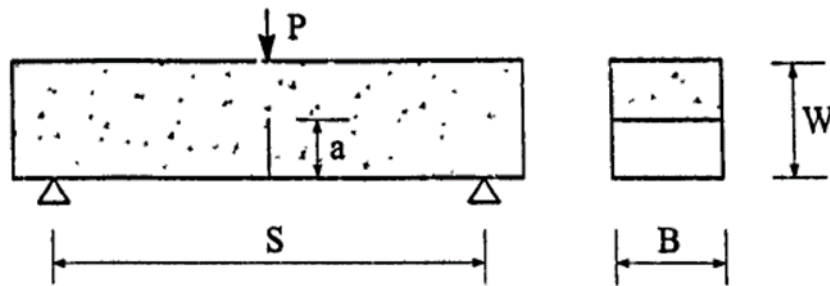


Figure 2. 9 General three-point bend test arrangement of a notched beam

The fracture energy defined by Equation (2.7), which may be size- or ligament-dependent, is denoted by $G_f(\alpha)$, to distinguish it from the size-independent G_F , with $\alpha = a/w$. The specific fracture energy (G_f) can also be determined using a local energy g_f concept described by Duan et al. (2003, 2007) as follows:

$$G_f\left(\frac{a}{W}\right) = \frac{1}{W-a} \int_0^{W-a} g_f(x) dx \quad (2.8)$$

Differentiating Equation (2.8) with respect to the crack length a gives the local fracture energy $g_f(x)$ at the crack tip:

$$g_f(x) = G_f(\alpha) - (W - a) \frac{dG_f(\alpha)}{d\alpha} \quad (2.9)$$

The size-dependence of the fracture energy can be explained by a non-constant distribution of the fracture energy along the crack growth path. The bilinear function used to approximate the non-constant local fracture energy distribution along a ligament is based on the assumption of the proportionality of the local fracture energy to the fracture process zone (FPZ) length and characterises the FPZ length reduction when approaching a specimen back boundary (Duan et al., 2003).

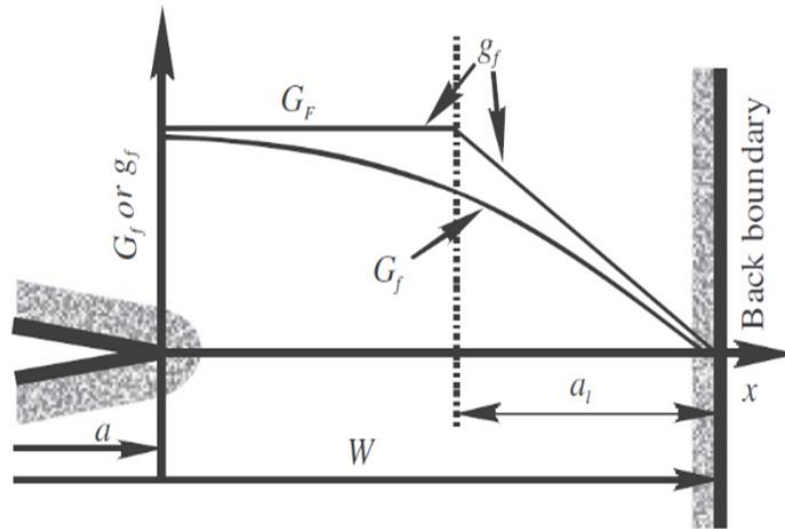


Figure 2. 10 The distribution of fracture energy (G_f and g_f) along the un-notched ligament of a notched specimen (After: Duan et al., 2001)

A relationship between the measured size-dependent fracture energy (G_f), the transition length (a_l) and the size-independent fracture energy (G_F) can be obtained by substituting the bilinear approximation for the local fracture energy variation (Figure 2.10) into Equation (2.8).

2.13 Fracture behavior of the SCC

The fracture behavior of concrete is an important aspect to be considered for analysis and design of engineering structures that provides a basis for evaluation of the strength of cracked structures (Bažant and Planas, 1998). It is greatly dependent on the properties of the particular components of the SCC and VC as well. In comparison with VC, SCC has different mix compositions due to the presence of higher fine particles and paste but lower coarse aggregate content (Okamura and Ouchi, 2003;

Okamura et al., 2000; Edamatsu and Nishida, 1998 and Su et al., 2001), which in turn lead to change in the pore structure of the SCC. Due to these differences, concerns are raised about the fracture behavior of the SCC. These concerns are primarily because a lower coarse aggregate content in the SCC mix relative to the VC mix of the same grade is likely to reduce its energy absorption capacity and thus its ductility (Beygi et al., 2014a; Domone, 2006).

Previous work (Beygi et al., 2014b; Beygi et al., 2014c; Nikbin et al., 2014c; Beygi et al., 2013b; Rozière et al., 2007) is reported on the fracture behavior of SCC based on the size-dependent specific fracture energy. Cifuentes and Karihaloo (2013) used the model of Hu and Wittmann (2000) and its simplified version proposed by Karihaloo et al. (2003) to study the fracture properties of the SCC. Since the fracture behavior of SCC has a direct influence on the durability of concrete structures, therefore it needs to be addressed by studying the effect of composition parameters of the SCC mixes. In this Chapter, a summarised overview of the fracture mechanics principles was presented. More details will be reported in Chapter 6.

2.14 Rheology of SCC

Rheology is ‘the science of deformation and flow of matter’ (Tattersall and Banfill, 1983). The important parameters of the rheology that describe the flow of SCC are the plastic viscosity and the yield stress. The rheological parameters provide a quantitative and fundamental way of characterizing the deformability, passing ability and stability of SCC, which are critical for concrete industry as they affect all the mechanical properties in the hardened state. The plastic viscosity is a measure of the resistance of SCC to flow due to internal friction. It is computed as the slope of the shear stress versus shear rate plot from rheometer flow curve measurements. Mixes with high plastic viscosity are often described as “sticky” or “cohesive”. Concrete with higher plastic viscosity takes longer to flow. It is closely related to t_{500} and v-funnel time (the higher the plastic viscosity, the longer the t_{500} and v-funnel time).

Yield stress can be considered as the minimum force required to initiate the flow. Flow initiates when the shear stress becomes higher than the yield stress, however, when its value becomes equal or lower than the yield stress, the flow stops. This suggests that

the yield stress must be the dominant factor that governs the slump flow spread. It is known however that the yield stress of SCC mixes is very low (in the order of tens of Pascal) in comparison with normal concretes (thousands of Pascal) and remains nearly constant over a large range of plastic viscosities as shown in Figure (2.11).

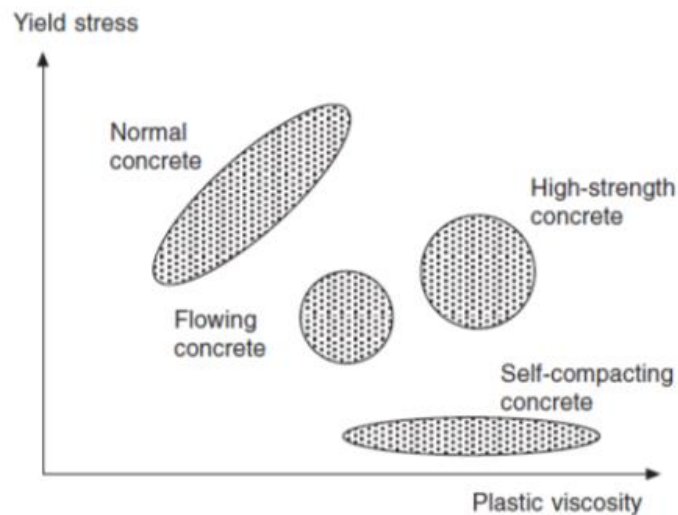


Figure 2. 11 Rheology of several types of concrete (After: Domone, 2003)

2.15 Measuring the rheological parameters

To measure the rheological parameters of general viscous liquids (such as cement pastes) and solid-liquid suspensions (such as self-compacting concretes), a rheometer is used. When choosing a rheometer, it should take into account the small size of aggregate used in self-compacting concrete compared with conventional vibrated concrete, the presence of yield stress, moderate plastic viscosity, the potential of segregation and the high sensitivity to small changes in materials and their proportions. It is difficult to account all these factors in one rheometer, however, two types of rheometer can be used, namely that which imposes a controlled shear rate on SCC and measures its shear stress, and that which does the opposite. A wide range of rheometers is commercially available such as the coaxial cylinder rheometers, parallel plate rheometers and impeller rheometers (Domone, 2003).

Domone (2003) reported that for a given concrete mix, logically, any rheometer should give the same values of these two fundamental parameters. But in practice that is not

the case. This was indeed proved by Banfill et al. (2000) using a series of comparative tests in which three instruments were taken to the same laboratory and used simultaneously to test a series of fresh concrete mixes with a wide different range of rheological characteristics. Figure 2.12 shows an example of how two different rheometers gave totally different responses for the same mix.

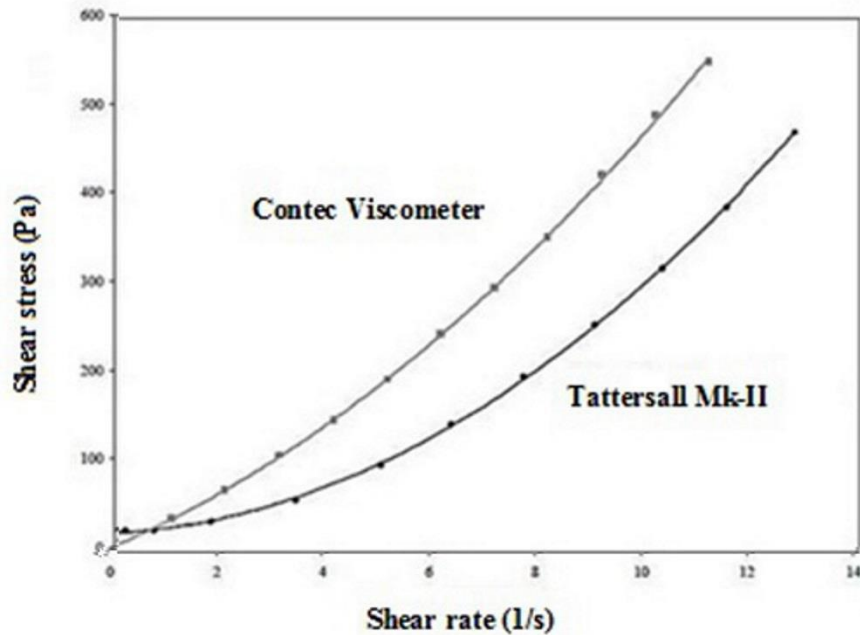


Figure 2. 12 Two different responses for a single SCC mix tested by two rheometers (After: Feys et al., 2007)

In both cases, the yield stress values were somewhat more consistent than those of plastic viscosity. These inaccurate results, which often have a large scatter with mixes containing long fibres, have triggered research in to alternative prediction techniques for plastic viscosity (Krieger and Dougherty, 1959; Struble and Sun, 1995).

Ghanbari and Karihaloo (2009) have developed a micromechanical procedure for estimating the plastic viscosity of SCC with or without steel fibres from the knowledge of the plastic viscosity of cement paste alone or of the cement paste with SP and/or VMA. Details of this micromechanical procedure will be explained in Chapter 4.

Many researchers (Grünewald, 2004; Roussel, 2006a; Thrane, 2007; Tregger et al., 2007) have investigated the potential of a relationship between the rheological characteristics of SCC mix (yield stress and plastic viscosity) and the measured

parameters in the slump flow test (namely, slump flow diameter and t_{500}). They all agreed that the time t_{500} can be related to the plastic viscosity but that the slump flow spread is a function of both the yield stress and the density of SCC.

2.16 Effects of concrete constituents on the Bingham constants

The SCC mix is strongly dependent on the composition and characteristics of its constituents in the fresh state. Figure 2.13 illustrates the effect of water, superplasticiser, cement replacement materials and the cement paste on the yield stress and plastic viscosity of concrete. Generally, addition of superplasticisers decreases the yield stress dramatically but does not change the viscosity very much. Compared with superplasticisers, increasing the water content results in decrease in both the yield stress and the plastic viscosity, but the side effect of the change in water content in concrete is that it may lead to segregation. Use of cement replacement materials such as ggbs or fly ash leads to a decrease in the yield stress of concrete, but their effects on viscosity are different: fly ash reduces the viscosity while ggbs increases it. The rheological properties of concrete are also affected by the paste; addition of paste can result in a decrease in yield stress and an increase in viscosity.

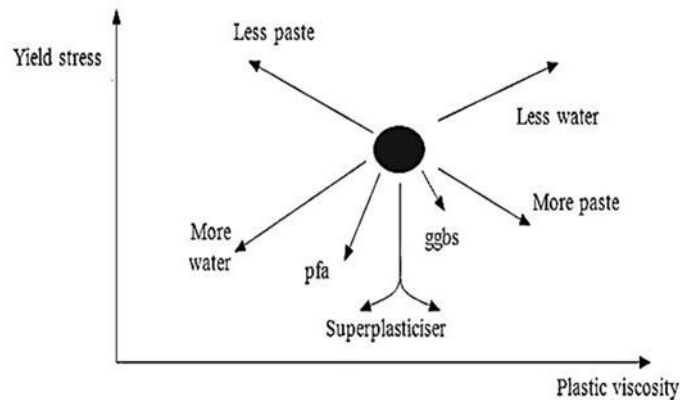


Figure 2. 13 General effects of concrete constituents on the Bingham parameters (After: Domone, 2003)

2.17 Concluding remarks

Self-compacting concrete (SCC) was created as a solution for the lack of enough skilled labors for placement of the concrete in construction industry and to achieve durable concrete structures by improving the quality in the construction process. It can be placed and consolidated under its own weight without any external vibration due to its excellent deformability, and which at the same time is cohesive enough to maintain its homogeneity without segregation or bleeding.

The mix design method for proportioning SCC mixes is a key issue in the development of SCC. Although, there are a large number of publications on SCC mix design studies, there is no unique mix design method for any given application because each mix design approach has its own special features and some inherent limitations. With regard to the mix method for proportioning normal and high strength SCC mixes proposed by Karihaloo and Ghanbari (2012) and Deeb and Karihaloo (2013), while this method is rigorous and based on sound physical principles, it produces a bewildering array of mixes that reach the target plastic viscosity. However, this method does not give any practical guidelines on how to choose the most appropriate mix. Moreover, it was developed on the basis of reference mixes of a range of known cube compressive strength, but the latter was not explicitly imposed as a design criterion. Modifications will be made in the present study (Chapters 4 and 5) to overcome the above shortcomings of this method for proportioning SCC mixes. These modifications included the explicit imposition of the target compressive strength of the SCC mix as a design criterion and the provision of practical guidelines on how to choose the most appropriate mix proportions.

Even though extensive work is reported on the fracture behavior of VC, limited information is available on the fracture parameters for the powder type SCC which is more brittle. The differences in the composition of SCC from VC raise concerns about its fracture behaviour; therefore, it is necessary to investigate in detail the role of several composition parameters such as coarse aggregate volume, paste to solids (p/s) and water to binder (w/cm) ratios of SCC mixes in their fracture properties such as the specific fracture energy and the stress-crack opening relationship.

Chapter 3

Simulation of fresh self-compacting concrete (SCC) flow – A brief summary

3.1 Introduction

The application of computational simulation tools in the field of concrete technology has increased for solving complicated engineering problems, replacing expensive experimental tests in order to save time, effort and materials. Numerical simulation can translate different physical problems into a discrete form of mathematical description, its wide importance owing to the increasing computer capabilities. For construction industry, modelling of the flow of fresh concrete increasingly becomes an important issue due to fact that rheological properties of concrete which mainly affect its flow behaviour have a great influence on its strength and durability. The modelling of fresh SCC could be used for simulation of flow of SCC mix e.g. total form filling and detailed flow characteristics as coarse aggregate particles migrate during the flow. Furthermore, computer modelling could be a helpful tool for understanding the rheological behaviour of SCC mix as it flows through formwork to identify a minimum workability of the fresh SCC that could ensure the appropriate filling of a given formwork.

This chapter provides a brief overview of the fundamentals of the SPH method and its implementation. More comprehensive details may be found in the PhD thesis of Deeb, (2013).

3.2 Rheological models describing the flow of SCC

The two common rheological models that describe the flow behaviour of concrete are the Bingham and Herschel-Bulkely. From a rheology point of view, self-compacting concrete is often modelled as a Bingham fluid (Ferraris, 1999; Banfill, 2006). This model contains two parameters: 1. yield stress τ_y , which is the minimum shear stress that an SCC mix has to overcome to start flowing, and 2. plastic viscosity: η the measure of the resistance of SCC to flow due to internal friction. Concrete with higher plastic viscosity takes longer to flow. It is closely related to t_{500} and v-funnel time (the higher the plastic viscosity, the longer the t_{500} and v-funnel time). Knowing the important rheological terms (yield stress and plastic viscosity) of a fluid provides a quantitative and fundamental way of characterizing the flowing ability, filling ability, passing ability and stability of SCC.

The Bingham constitutive model is described by the equations

$$\tau = \tau_y + \eta\dot{\gamma} \quad \tau > \tau_y \quad (3.1)$$

$$\dot{\gamma} = 0 \quad \tau \leq \tau_y \quad (3.2)$$

Most numerical simulations consider only the steady-state of the flow while the thixotropic state i.e. the loss of workability of concrete during the flow is not taken into account. However, SCC can exhibit shear thickening behaviour which means the plastic viscosity η increases with the shear rate $\dot{\gamma}$ (e.g. in pumping and mixing); in this case, SCC can be modelled by the Herschel-Bulkley model (Vasilic et al., 2010). The Herschel-Bulkley model is a generalization of the Bingham model in such a way that, upon deformation, the viscosity can be shear thinning or shear thickening. It is written as:

$$\tau = \tau_y + \eta\dot{\gamma}^n \quad \tau > \tau_y \quad (3.3)$$

$$\dot{\gamma} = 0 \quad \tau \leq \tau_y \quad (3.4)$$

For a shear thinning fluid, the index n may have any value between 0 and 1.0; the smaller the value of n , the greater is the degree of shear thinning. For a shear thickening fluid, the index n will be greater than unity.

From a computational point of view, it is expedient to represent the piecewise bi-linear Bingham constitutive relation with its associated discontinuity at zero shear rate by a smooth continuous function

$$\tau = \eta\dot{\gamma} + \tau_y(1 - e^{-m\dot{\gamma}}) \quad (3.5)$$

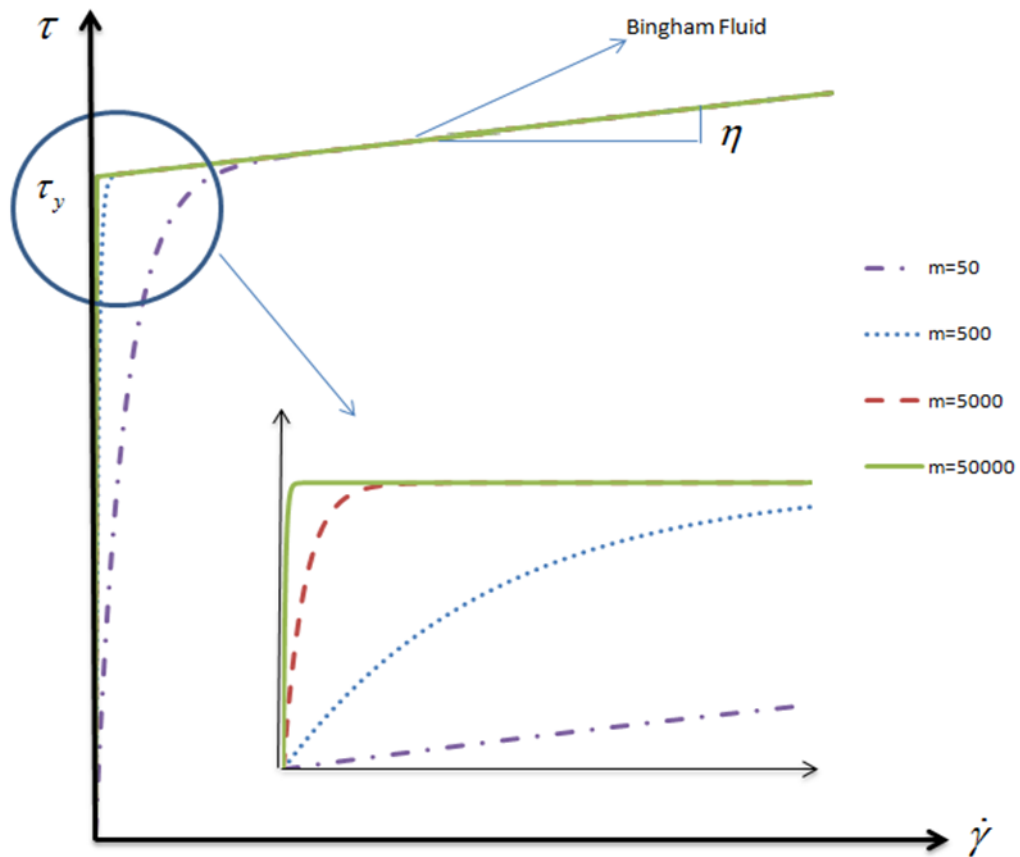


Figure 3. 1 A bi-linear Bingham fluid constitutive model replaced by the continuous function (3.3) (After: Ghanbari, 2011)

where m is a very large number. It can be seen from Figure 3.1 that the continuous function in Equation (3.5) approaches the bi-linear function for large m . On the scale of the Figure (3.1), the discontinuity at τ_y cannot be distinguished for $m = 5000$ and 50000 .

3.2.1 Fluid classifications

Fluids have been classified in the literature as Newtonian or non-Newtonian depending on whether their response to shear rate is linear or non-linear, or as compressible or incompressible depending on their response to pressure. In this thesis, we shall be dealing with a non-Newtonian, incompressible fluid.

3.3 Simulation of the flow of SCC

With the advent of SCC that can flow, fill the formwork completely and compact under its own self-weight without vibration, the numerical simulation may serve as a tool to model the SCC flow and to predict concrete workability. SCC is assumed to have the characteristic of viscous non-Newtonian fluid, best described by a bi-linear Bingham-type constitutive model where the flow only initiates once the shear stress has reached a critical value called the yield stress τ_y (Papanastasiou, 1987; Ghanbari and Karihaloo, 2009). Computer modelling which is usually used in literature can be divided into two main categories, grid and particle-based methods. Grid or mesh based numerical methods such as the finite difference method (FDM) and the finite element method (FEM) are used for solving problems in engineering and science by dividing the continuum domain into small discrete domains (discretization of domain) called mesh or grid related to each other by nodes. Although grid based methods are still considered as being the primary computational based methods, there are limitations in their application due to the difficulty of solving complicated problems namely free surfaces, large deformability, moving interfaces, difficult boundary conditions and complex geometry that make the computations costly and time consuming (Liu and Liu, 2010). Consequently, mesh-free methods have become a necessity to address problems where it is difficult to use grid based methods.

In mesh-free particle methods, the problem and boundary domains are represented by a set of arbitrarily distributed particles without using any mesh to connect those particles; therefore it is easy to handle very large deformations and free-surface fluid flows since the connectivity among particles is generated as part of the computation which can change with time. These particles possess material properties and interact with each other within the range controlled by a smoothing function (Fulk and Quinn, 1996; Liu and Liu, 2003). Due to the Lagrangian nature of the SCC flow and due to the fact that an SCC mix is essentially an aggregate of particles of different sizes and shapes, the use of mesh-less particle-based Lagrangian numerical techniques to simulate such flows is both more appropriate and simpler than the traditional mesh-based methods (Dufour and Pijaudier-Cabot, 2005; Roussel et al., 2007). An example of this category is the smooth particle hydrodynamics (SPH) method. The SPH is a mesh-less Lagrangian approach that offers considerable potential as a numerical

method for modelling problems involving large deformations. Its simplicity and Lagrangian nature have been exploited in the past to model many free-surface fluid flows and related engineering problems (Monaghan, 1994; Cummins and Rudman, 1999; Kulasegaram et al., 2004). The attractiveness of the SPH method is its early stage adaptability which allows to deal with very complicated deformation, moreover, “the harmonic combination between the Lagrangian formulation and particle approximation” (Liu and Liu, 2003) allows particles to carry material properties; therefore it becomes easier to model flows with complex geometry, free surfaces, discontinuity and large deformation.

The computational modelling methods of concrete flow can be divided into two main groups: 1. methods that treat concrete as a homogeneous medium, and 2. methods that treat it as a heterogeneous medium. Choosing the right technique depends on the purpose of the simulation and whether the solid components of concrete are considered as separate particles or are embedded inside the mortar.

3.3.1 Simulation of concrete as a homogeneous medium

In this simulation concrete is regarded as a viscous fluid without particle inclusions. It is the easiest and fastest way to simulate fresh concrete. The drawback of this method is that the particle blocking and segregation cannot be predicted (Roussel, 2007). This approach has been taken by many researchers, e.g. Mori and Tanigawa (1992), Thrane et al. (2004), Kitaoji et al. (1997), Kurokawa et al. (1997), Roussel and Coussot (2005), Roussel (2006b), Patzák and Bittnar (2009), and Gao and Fourie (2015). They used either specialised mesh-based finite element approaches or the standard computational fluid dynamics (CFD) approach.

3.3.2 Simulation of concrete as a heterogeneous medium

Self-compacting concrete (SCC) in fresh state can exhibit a fluid-like behaviour or a granular medium-like behaviour depending on whether the volume fraction of coarse aggregates in the viscous suspension is small or large.

Gram (2009) used the Discrete Element Method (DEM) commercial software PFC^{3D} to model the flow of SCC. Martys (2005) used the Dissipative Particle Dynamics method (DPD) which allowed for much larger time steps, as opposed to DEM.

Mori and Tanigawa (1992) used the so-called visco-plastic suspension element method (VSEM) where concrete is divided between mono-sized spherical coarse aggregates and mortar.

Švec et al. (2012) have modelled the free surface flow of suspension of rigid particles in a non-Newtonian fluid using the lattice Boltzmann method combined with Immersed Boundary Method and particle dynamics. This model is efficient and robust allowing simulations of tens of thousands of particles.

3.4 2D and 3D simulations of SCC flow in the L-box

This section briefly provides a general overview of the 2D and 3D simulations available in the literature to model the flow characteristics of fresh SCC in the L-box. The ability of passing around and between obstacles such as steel bars and the filling of the formwork are important properties of SCC; they determine how well the SCC mix can flow through confined and limited zones. For this reason, it is essential to simulate the SCC flow in restricted area or around obstacles such as in L-box to examine how SCC fills formwork as a homogeneous mass without the segregation of mix components.

Martys and Ferraris (2002) used dissipative particle dynamics (DPD) to model the flow of fresh concrete, the results showed agreement between simulation results and experimental data. A different approach was taken by Dufour and Pijaudier-Cabot (2005) to simulate the movement of SCC in the slump and the L-box tests with a Lagrangian finite element method (FEM). They considered concrete as a non-Newtonian fluid with a shear-strain rate curve of Bingham fluid. Simulation results revealed that the method somewhat correctly predicted the final SCC surface profile in the L-box. There were considerable errors in predicting the time when SCC reached the face wall. Patzák and Bittnar (2009) have simulated the 2D flow of concrete in the L-box using the finite element method (FEM) and the interface-capturing method to track the position of a free surface.

Baluch et al.(2011) have simulated the SCC flow in the slump test and the L-box test using 2D computational fluid dynamics (CFD) software ANSYS/FLUENT. They concluded that the results show a good correlation between the numerical simulation and the experimental result.

Thrane et al. (2004) have simulated the SCC as a single fluid flow with Bingham behaviour using the Galerkin FEM formulation of the Navier–Stokes equations with the code Fidap. The code did not have the means to treat discrete particles and hence couldn't assess the blocking resistance. They concluded that it is necessary to use a 3D model for simulating SCC in the L-box. It was found that there are differences between the obtained numerical flow times and the experimental data due to the time it takes to lift the gate in the experiment.

Kulasegaram et al. (2011) and Kulasegaram and Karihaloo (2012) used a 2D Lagrangian particle-based SPH method to simulate the flow of SCC with and without steel fibres in the slump and L-box tests and to determine how the fibres distribute and orient themselves during the ultra-high performance, self-compacting concrete (UHSPCC) flow. The comparison between the experimental data and the simulation results revealed that SPH method has suitable accuracy for predicting the flow properties. The 2D SPH method has also been used by Lashkarbolouk et al. (2013) to simulate the flow of two kinds of concrete in the L-box; SCC and high performance concrete (HPC). The comparison between the simulation results and the experimental data confirmed that SPH method has suitable accuracy for predicting the flow characteristics.

Deeb et al. (2014a) used the 3D SPH method in order to model numerically the flow of SCC with and without steel fibres inside formwork like the L-box. The simulation was focused on the distribution of large aggregate particles of different sizes throughout the flow of SCC mixes without fibres, whereas the simulation of high strength SCC mixes which contain steel fibres was focused on the distribution of fibres and their orientation during the flow. The capabilities of this methodology were validated by comparing the simulation results with the L-box test carried out in the laboratory.

The smooth particle hydrodynamics (SPH) will be used in the present research. Due to the fact that SCC undergoes large deformations during the flow and the fact that it contains particles of different sizes, SPH is an ideal computational method to represent with a good margin of accuracy its rheological behaviour. This method has been tested and proved to be efficient and accurate in modelling SCC without fibres by Kulasegaram et al. (2011) and Badry et al. (2016a; b) and SCC with fibres by Kulasegaram and Karihaloo (2012), and Deeb et al. (2014a; b; c)

3.5 The governing equations of concrete flow

The behaviour of SCC can be described using the governing equations of fluid: continuity and momentum equations which are based on the fundamental physical laws of conservation. However, when there is no change in the temperature during test and the heat flux in a continuum is absent, the energy can be assumed to be identically conserved. Also, as the viscosity and density are not affected by the temperature, the energy conservation equations can therefore be ignored.

3.5.1 Continuity equation (the mass conservation)

The continuity or mass conservation equation in the Lagrangian form is

$$\frac{D\rho}{Dt} + \rho \nabla \cdot \mathbf{v} = 0 \quad (3.6)$$

For an incompressible fluid, the density is constant, and therefore (3.6) becomes

$$\nabla \cdot \mathbf{v} = 0 \quad (3.7)$$

where ρ , t , and \mathbf{v} the fluid particle density, time, and particle velocity, respectively.

D denotes the substantial or material derivative.

3.5.2 The momentum conservation equations

If gravity g is the only body force acting on the continuum the momentum conservation equations in the Lagrangian form can be written in the compact vectorial form as

$$\frac{D\mathbf{v}}{Dt} = -\frac{1}{\rho} \nabla P + \frac{1}{\rho} \nabla \cdot \boldsymbol{\tau} + \mathbf{g} \quad (3.8)$$

where P , \mathbf{g} and $\boldsymbol{\tau}$ are pressure, gravitational acceleration, and shear stress, respectively.

3.6 Eulerian and Lagrangian approaches

There are two fundamental approaches to describe the physical governing equations: Eulerian and Lagrangian.

- **The Eulerian approach** is a spatial description such as Finite element method (FEM), Finite difference method (FDM) and Finite volume method (FVM); it is used to track a certain fixed position in the flow field and follows the change in properties, as different fluid elements pass through that location (Figure 3.2).

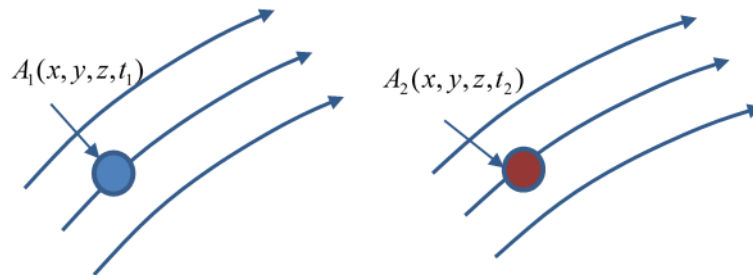


Figure 3.2 Different fluid elements at different times at a fixed location in the fluid flow (After Deeb, 2013)

- **The Lagrangian approach** such as vortex method, Finite Point set Method (FPM), and SPH method; it is used to track a material element of the fluid as it moves, and the changes in its properties, e.g. velocity are monitored (Figure 3.3).

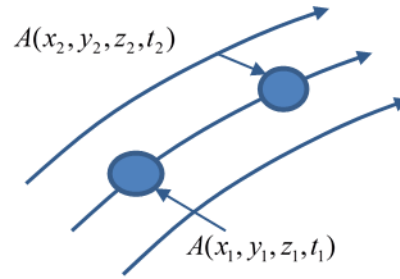


Figure 3.3 Fluid particle motion from time t_1 to time t_2 (After: Deeb, 2013)

The two derivatives, Lagrangian and Eulerian are related to each other, e.g. for velocity

$$\frac{D\mathbf{v}}{Dt} = \frac{\partial\mathbf{v}}{\partial t} + (\mathbf{v}\cdot\nabla)\mathbf{v} \quad (3.9)$$

where the term $\mathbf{v}\cdot\nabla$ is the convective derivative, which defines the time rate of change as the fluid element moves from one location to another in the flow field.

3.7 Numerical approximation-Smooth particle hydrodynamics (SPH)

The SPH is a Lagrangian particle-based numerical method (Figure 3.4). It was widely used for hydrodynamics and astrophysical applications, it was first independently proposed by Lucy (1977) and Gingold and Monaghan (1977) to solve particular astrophysical problems. The SPH was first conceived for compressible flow problems in confined flow simulations, until later Monaghan (1994) proposed and developed a modified SPH formulation to model free surface in viscous liquid flow. Other researchers have since solved various engineering problems including multi-phase problems (Monaghan and Kocharyan, 1995), quasi-incompressible flow (Monaghan, 1994; Morris et al., 1997), incompressible fluid flow (Shao and Lo, 2003; Solenthaler and Pajarola, 2009) flow through porous media (Zhu et al., 1999), viscous fluid flow (Takeda et al., 1994), shock simulations (Monaghan and Gingold, 1983), gravity currents (Monaghan, 1996), heat transfer (Chaniotis et al., 2002; Cleary et al., 2002), turbulent flows (Welton, 1998), interfacial flows, discontinuity and large deformability (Bui et al., 2008; Colagrossi and Landrini, 2003) and sloshing problems (Kelecyc and Pletcher, 1997; Koshizuka et al., 1995). The interaction between fluids,

free surfaces and many other applications can be also simulated using SPH (Amini et al., 2011).

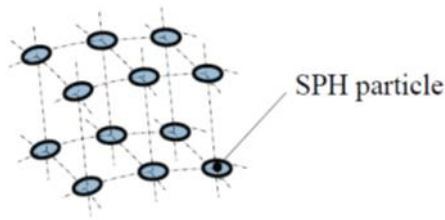


Figure 3.4 SPH model (After: Vesenjak and Ren, 2007)

Bonet and Kulasegaram (2000) applied SPH to simulate metal forming. Other notable modifications or corrections to the SPH method were made by Bonet and Kulasegaram (2000), and Dilts (1999, 2000). The Lagrangian nature of SPH allows the grid to be embedded in the material and thus reduces some of the material interface problems associated with Eulerian techniques.

3.7.1 SPH concept

SPH is an integral interpolation method to approximate values and derivatives of continuous field quantities by using discrete sample points (Gingold and Monaghan, 1977). The key characteristics of SPH as reported by Liu and Liu (2003) are: **1. Domain discretisation:** the entire problem domain in the physical space is discretised into a finite number of macroscopic volumes of fluid. Each macroscopic fluid volume is represented by a particle in SPH. These particles possess individual material properties and move according to the governing conservation equations. **2. Smoothing kernel approximation:** Each particle, say particle ‘ a ’ carries the field variables such as the mass m_a , density ρ_a , pressure P_a , velocity v_a , position r_a , temperature (T_a), internal energy (E_a), colour (c_a) which are represented by integral functions, the so-called kernel functions. **3. Particle approximation:** The kernel is further approximated using particles, by replacing the integration in the integral representation of the field variable and its derivatives with summation over all the corresponding values at the neighbouring particles in a local domain called the support domain. **4. Lagrangian:** The particle approximation is performed on all terms related to field

variables to produce a set of ordinary differential equations (ODEs) in a discretized form with respect to time.

3.7.2 SPH support domain

The support for a particle ‘ a ’ is the domain where all the information for all interior particles is used to determine the information at the point ‘ a ’ (see Figure 3.5). This means that any physical property of a particle ‘ a ’ can be obtained by summing the same property of particles that lie in the support domain Ω within a radius ch of the observed particle ‘ a ’ and multiplying the sum by a smoothing function, where c is a scaling constant related to the smoothing function (usually equal to 2).

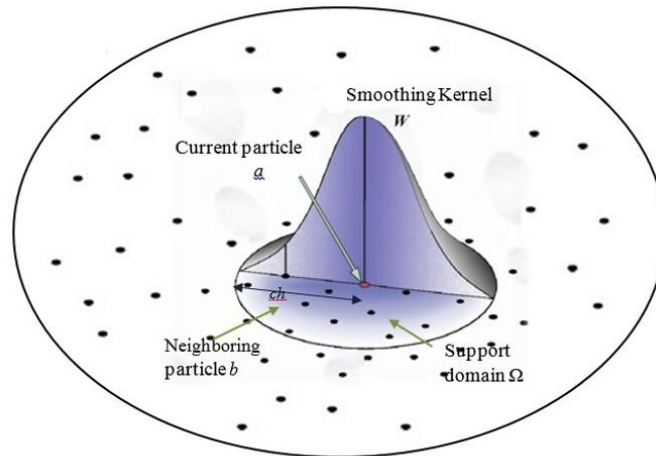


Figure 3.5 Distribution of physical properties of a particle (After: Deeb, 2013)

3.7.3 Kernel approximation

SPH provides a concept to approximate the spatial derivative using particles, which therefore makes computing the spatial derivatives in particle-based method as easy as in the grid-based methods. SPH is based on integral interpolation; for instance, a continuous quantity $f(\mathbf{x})$ over a space Ω can be written as the convolution of the quantity and Delta function

$$f(\mathbf{x}) = \int_{\Omega} f(\mathbf{x}') \delta(\mathbf{x} - \mathbf{x}') d\mathbf{x}' \quad (3.10)$$

where Ω is the volume of the domain, $d\mathbf{x}'$ an elementary volume, and $\delta(\mathbf{x} - \mathbf{x}')$ is the Dirac Delta function i.e.

$$\delta(\mathbf{x} - \mathbf{x}') = \begin{cases} 1 & \mathbf{x} = \mathbf{x}' \\ 0 & \mathbf{x} \neq \mathbf{x}' \end{cases} \quad (3.11)$$

The Dirac Delta function is approximated with the so-called smoothing kernel function W of limited support h

$$f(\mathbf{x}) \approx \int_{\Omega} f(\mathbf{x}') W(\mathbf{x} - \mathbf{x}', h) d\mathbf{x}' \quad (3.12)$$

W should be differentiable, normalised, and should converge to the Delta function.

The SPH approximation is highly dependent on the choice of the kernel function. The most common kernels are: Gaussian, cubic spline and quartic spline.

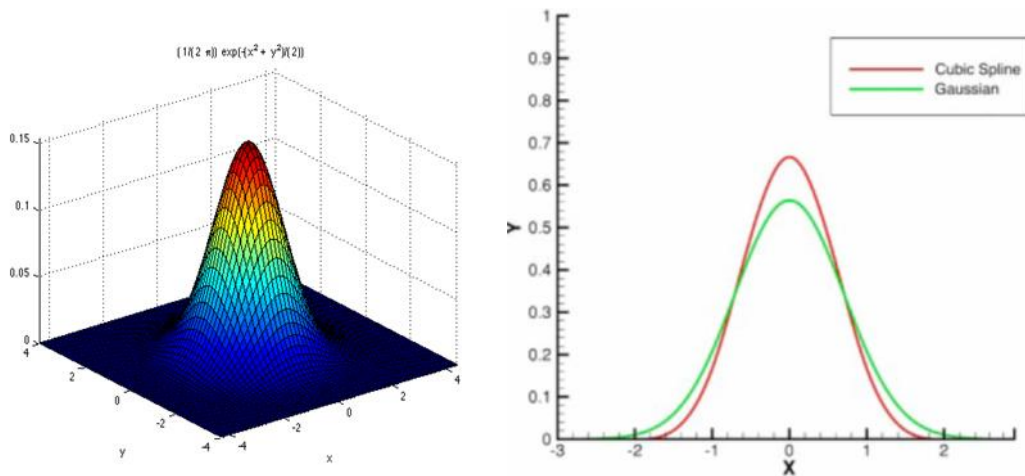


Figure 3.6 Gaussian and cubic spline shape functions (After: Li and Liu, 2002)

Figure 3.6 illustrates the Gaussian and the cubic spline functions; they look similar but the cubic spline has a more compact support as compared with the Gaussian function.

3.7.4 Particle interpolation

The entire domain of the problem is discretised into a limited number of particles N and then all the field variables are approximately calculated on these particles. First,

the infinitesimal volume dx' at the location of particle 'b' can be approximately replaced by the finite volume of the particle V_b where $V_b = \frac{m_b}{\rho_b}$. The inclusion of density ρ_b and mass m_b makes SPH the ideal numerical solution to simulate dynamic fluid flow such as the flow of self-compacting concrete. The continuous integral in Equation (3.12) can be converted to a discretized form of summation over all the particles N .

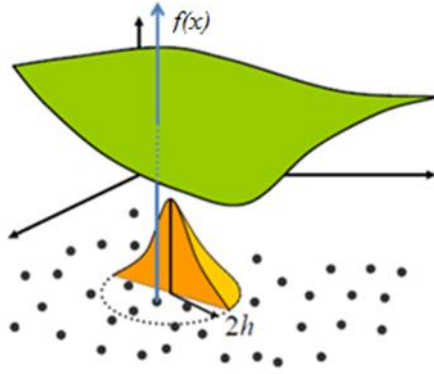


Figure 3.7 Particle approximation of function $f(\mathbf{x})$ (After: Deeb, 2013)

Therefore, the continuous integral in Equation (3.12) can be expressed in the equivalent forms of discretized particle approximation (Figure 3.7)

$$f(\mathbf{x}) = \sum_{b=1}^N m_b \frac{f(\mathbf{x}_b)}{\rho_b} W(\mathbf{x} - \mathbf{x}_b, h) \quad (3.13)$$

$$f(\mathbf{x}) = \sum_{b=1}^N V_b f(\mathbf{x}_b) W_b(\mathbf{x}) \quad (3.14)$$

The differential of this function is given by

$$\nabla f(\mathbf{x}) = \sum_{b=1}^N V_b f(\mathbf{x}_b) \nabla W_b(\mathbf{x}) \quad (3.15)$$

where the quantity $\nabla W_b(\mathbf{x})$ denotes the gradient of the kernel, which is taken as centred on the position of particle a (Figure 3.7). The application of Equation (3.14) to compute the approximate value for the density of a continuum leads to the classical SPH equation

$$\rho(\mathbf{x}) = \sum_{b=1}^N m_b W_b(\mathbf{x}) \quad (3.16)$$

3.7.5 Corrected SPH integration

The basic SPH approximations as given by Equation (3.14) and (3.15) do not accurately reproduce or approximate the function $f(\mathbf{x})$ and its derivative $\nabla f(\mathbf{x})$ because they do not conserve angular momentum. Therefore corrected SPH equations have been developed to address these issues (Bonet and Lok, 1999; Bonet and Kulasegaram, 2000). Using the corrected gradient of the corrected kernel, the SPH Equations (3.14) and (3.15) can be rewritten as

$$f(\mathbf{x}) = \sum_{b=1}^N V_b f(\mathbf{x}_b) \tilde{W}_b(\mathbf{x}) \quad (3.17)$$

$$\nabla f(\mathbf{x}) = \sum_{b=1}^N V_b f(\mathbf{x}_b) \tilde{\nabla} \tilde{W}_b(\mathbf{x}) \quad (3.18)$$

where $\tilde{W}_b(\mathbf{x})$ indicates that the kernel function is corrected to satisfy the linear consistency conditions, and ‘ b ’ is the neighbouring particle within the support domain.

3.7.6 Neighbouring search

Neighbouring search in the support domain is considered to be the most computational expensive part of the simulation. Many methods have been implemented to ensure an adequate way for neighbourhood search, e.g. Wróblewski et al. (2007), Monaghan and Lattanzio (1985), Liu and Liu (2003), and Bonet and Peraire (1991).

3.7.7 Treatment of boundary conditions

In SPH, boundary conditions should be imposed to satisfy balancing the inner particles’ forces thus preventing those particles from penetrating the wall. A range of methods is available in literature to impose boundary conditions in SPH method, e.g. repulsive forces (Monaghan, 1994), mirror particles (Takeda et al., 1994; Cummins and Rudman, 1999) and dummy particles (Dalrymple and Knio, 2001; Shao and Lo,

2003; Lee et al., 2008; Amini et al., 2011). The dummy particle approach will be used in this thesis (see Chapter 7).

3.7.8 Incompressibility (ISPH) and weak compressibility in SPH approach

Enforcing incompressibility in SPH can be pursued using two different approaches - the weakly or quasi-compressible SPH will be referred to as WCSPH (Monaghan, 1994; Lee et al., 2008) and the truly incompressible SPH as ISPH (Kulasegaram et al., 2011). In this thesis, the latter approach will be taken (Chapter 7).

3.8 Simulation of SCC with ISPH

For completeness of presentation, a brief description will be given of the incompressible SPH simulation method, as applied in this study to simulate the L-box flow test.

A projection method based on the predictor-corrector time stepping scheme is used to track the Lagrangian non-Newtonian flow (Chorin, 1968; Cummins and Rudman, 1999; Koshizuka et al., 1998) and the incompressibility condition is satisfied exactly through a pressure Poisson equation.

3.8.1 Prediction step

The prediction step ignores incompressibility and only the viscous stress and gravity terms are considered in the momentum Equation (3.8) to obtain an intermediate particle velocity \mathbf{v}_{n+1}^* and position by an explicit integration in time:

$$\mathbf{v}_{n+1}^* = \mathbf{v}_n + \left(\mathbf{g} + \frac{1}{\rho} \nabla \cdot \boldsymbol{\tau} \right) \Delta t \quad (3.19)$$

And

$$\mathbf{x}_{n+1}^* = \mathbf{x}_n + \mathbf{v}_{n+1}^* \Delta t \quad (3.20)$$

3.8.2 Correction step

The correction step is applied to enforce the incompressibility condition prior to incrementing the time by considering the pressure term in Equation (3.8)

$$\frac{\mathbf{v}_{n+1} - \mathbf{v}_{n+1}^*}{\Delta t} = -\left(\frac{1}{\rho} \nabla P_{n+1}\right) \quad (3.21)$$

where \mathbf{v}_{n+1} is the corrected particle velocity at the time step $n+1$. Computing Equation (3.21) requires the pressure P_{n+1} . This is obtained by imposing the incompressibility condition in the mass conservation Equation (3.6) (as the particle density remains constant during the flow).

$$\nabla \cdot \mathbf{v}_{n+1} = 0 \quad (3.22)$$

Equations (3.21) and (3.22) give

$$\nabla^2 P_{n+1} = \frac{\rho}{\Delta t} \nabla \cdot \mathbf{v}_{n+1}^* \quad (3.23)$$

where ∇^2 is the Laplacian.

Once the pressure is obtained from the Poisson Equation (3.23), the particle velocity is updated by the computed pressure gradient Equation (3.21), followed by the instantaneous particle position:

$$\mathbf{v}_{n+1} = \mathbf{v}_{n+1}^* - \left(\frac{1}{\rho} \nabla P_{n+1}\right) \Delta t \quad (3.24)$$

$$\mathbf{x}_{n+1} = \mathbf{x}_n + \mathbf{v}_{n+1} \Delta t \quad (3.25)$$

3.8.3 Time step

The time step Δt is chosen based on the relevant stability conditions for the given problem. In the case of Bingham-type SCC fluid flow, the time step is primarily

controlled by the effective plastic viscosity. Therefore, the time step size is generally decided by (Cummins and Rudman, 1999).

$$\Delta t = \min \left(\frac{\alpha_1 r_0}{v_{\max}}, \frac{\alpha_2 r_0^2 \rho}{\mu} \right) \quad (3.26)$$

where r_0 is the initial particle spacing, v_{\max} is the maximum particle velocity, α_1 and α_2 are the coefficients usually in order of 0.1. These coefficients depend on the choice of SPH kernel functions and the nature of the engineering application.

3.9 SPH discretisation of the governing equations

In the governing equations of SCC flow (Equations (3.6) and (3.8)), three terms need to be defined in the SPH formulation; these are the divergence of velocity field in the mass conservation Equation (3.6), the gradients of pressure and viscous terms in the momentum conservation Equation (3.8) and the Laplacian term $\nabla^2 P_{n+1}$ in the Poisson Equation resulting from enforcing the incompressibility (3.23).

The divergence of the velocity field can be obtained by identifying $f(x)$ in the Equation (3.18) with the velocity term

$$(\nabla \cdot \mathbf{v})_a = \sum_{b=1}^N V_b \mathbf{v}_b \cdot \tilde{\nabla} \tilde{W}_b(\mathbf{x}) \quad (3.27)$$

The gradient of pressure in the momentum equations can be obtained in the similar manner as above

$$(\nabla P)_a = \sum_{b=1}^N V_b P_b \tilde{\nabla} \tilde{W}_b(\mathbf{x}) \quad (3.28)$$

The viscous term, $\frac{1}{\rho} \nabla \boldsymbol{\tau}$ can be written in a similar manner as

$$\left(\frac{1}{\rho} \nabla \boldsymbol{\tau} \right)_a = \sum_{b=1}^N \frac{m_b}{\rho_b^2} \boldsymbol{\tau}_b \tilde{\nabla} \tilde{W}_b(\mathbf{x}) \quad (3.29)$$

The above incompressible SPH computational strategy described in Sections 3.6 and 3.7 will be implemented to simulate the flow of SCC mixes in the L-box in Chapter 7.

3.10 Concluding remarks

The necessity for the computational modelling of the flow characteristics of the fresh SCC has been recognized by the industry to ensure sufficient hardened properties and an appropriate durability of structures. The behaviour of concrete in its plastic form has a significant effect on the durability and strength of a structure and it is necessary to optimize the casting procedure, mix design through proportioning, predicting the passing behaviour, the proper filling of a given formwork and the distribution of large aggregates during the flow.

Different numerical models have been adopted to simulate the flow of SCC to provide a comprehensive understanding of the flow of SCC mix in the formwork. As an SCC mix consists of particles of different sizes and shapes, it is simpler and more appropriate to use mesh-less particle-based numerical techniques like the smooth particle hydrodynamics (SPH) method to simulate the flow characteristics of the SCC. The modelling of the flow of the SCC mix in the L-box using SPH method has been done previously by Deeb et al. (2014a), nevertheless, many aspects are needed to be taken into consideration in numerical simulation. These aspects include: the effect of friction of the L-box sides and of the steel bars, the effect of the time delay in the lifting of the L-box gate manually and the comparison between the simulated distribution of large coarse aggregates with the test distribution found in the laboratory specimens using colour coded aggregates. An appropriate computational strategy using SPH method will be presented in Chapter 7 to simulate the flow behaviour of SCC in the L-box configuration.

Chapter 4

Proportioning of self-compacting concrete mixes based on target plastic viscosity and compressive strength: Mix design procedure

4.1 Introduction

The proportioning of self-compacting concrete (SCC) mixes requires a balance between their flow and passing ability on the one hand and the resistance to segregation on the other (Corinaldesi and Moriconi, 2004; Wu and An, 2014; Okamura and Ouchi, 2003). The early mix proportioning approaches proposed by Okamura and Ouchi (1999); Domone (2000), and Okamura et al. (2000) and later developed by others (Ouchi et al., 1998) were all heuristic in nature requiring many trial mixes. However, the extensive research work carried out on the rheological properties of SCC (Roussel, 2006; Tregger et al., 2012; Saak et al., 2001; Chidiac and Mahmoodzadeh, 2009; Figueiras et al., 2014; Wallevik and Wallevik, 2011; Petersson and Billberg, 1999; Li and Kwan, 2011, 2013) has greatly improved the proportioning of SCC mixes. A summary of different mix proportioning approaches can be found in Shi et al. (2015). The European Federation of National Trade Associations (EFNARC) guidelines (2005) give typical ranges of primary ingredients (Table 4.1); the actual amounts depend on the desired strength and other performance requirements. Thus, the mix proportioning still involves considerable trial and error.

Table 4. 1 Typical range of SCC mix compositions according to EFNARC(2005)

Ingredients	Typical range by mass,kg/m ³	Typical range by volume, litres/m ³
Powder (cementitious materials + filler)	380–600	–
Water	150–210	150–210
Coarse aggregate	750–1000	270–360
Water to powder ratio by volume	0.85–1.10	
Fine aggregate	Typically 48–55% of the total aggregate	

A rigorous method for proportioning normal and high strength SCC mixes based on their plastic viscosity has been proposed by Karihaloo and Ghanbari (2012) and Deeb and Karihaloo (2013). It exploits the expression for the plastic viscosity of an SCC mix developed by Ghanbari and Karihaloo (2009) using micro–mechanical principles. This expression shows how the known plastic viscosity of the paste is increased by the addition of solid phase particles, i.e. filler, fine and coarse aggregates. The contribution

of each of the solid phases to the overall increase depends on its volume fraction and shape of its particles. As a result, the final expression for the plastic viscosity of an SCC mix is the product of the known plastic viscosity of the paste and contributions of each of the solid phases. Whilst the method for proportioning SCC mixes proposed in (Karihaloo and Ghanbari, 2012; Deeb and Karihaloo, 2013) is rigorous and based on sound physical principles, it produces a bewildering array of mixes that reach the target plastic viscosity but does not give any practical guidelines on how to choose the most appropriate mix. Moreover, the method was developed on the basis of reference mixes of a range of known cube compressive strength, but the latter was not explicitly imposed as a design criterion.

It is the aim of this study to overcome the above shortcomings of this method for proportioning SCC mixes. Practical guidelines in the form of design charts will be provided for choosing the mix proportions of SCC mixes, the lower target plastic viscosity limit of these mixes varying between 3.5-8 Pa s dependent upon the characteristic cubic strength in the range of 30-80 MPa, while the upper target plastic viscosity is 15 Pa s, irrespective of the compressive strength. Several mixes with differing paste to solids ratios by volume will be selected using these guidelines and prepared in the laboratory in order to confirm the simplicity and usefulness of this method. This will be reported in the next Chapter.

This chapter has been published in the journal ‘Journal of Sustainable Cement-Based Materials’ (see publication 4 in the list in Chapter 1).

4.2 Target compressive strength

The compressive strength of a concrete mix is mostly determined by the ratio of water to cementitious material (w/cm) under given curing conditions. A regression analysis was performed on the data collected from many published sources (Deeb and Karihaloo, 2013; Beigi et al., 2013a; Dinakar et al., 2013a; Panesar and Shindman, 2011; Felekoğlu et al., 2007; Rozière et al., 2007; Nikbin et al., 2014a; Boukendakdji et al., 2012; Persson, 2001; Dinakar et al., 2013b; Leemann and Hoffmann, 2005; Parra., 2011; Beygi., 2013b; Nuruddin et al., 2014; Zhu and Gibbs, 2005; Carpinteri et al., 2010; Rabehi et al., 2013; Beygi et al., 2014a; Dinakar et al., 2008; Collepardi et al., 2007; Nikbin et al., 2014b; Bui et al., 2002; Domone, 2007; Ferrara et al., 2007)

and on the data obtained in various studies in Cardiff University (Figure 4.1). It was found that the compressive strength of SCC (MPa) could be best fitted by an Abrams–type relation ($R^2 = 0.94$):

$$f_{cu} = \frac{195}{12.65(w/cm)} \quad (4.1)$$

where f_{cu} is the 28-day equivalent cube compressive strength (MPa) and w/cm is the ratio of water to cementitious materials (i.e. cement + cement replacement material, e.g. *ggbfs*). The large scatter in the surveyed data is no doubt a reflection of the differences in the curing conditions, the cement type, the type of cement replacement material and replacement levels up to 30%, the amount of coarse aggregate and the maximum size of coarse aggregate. The values have been adjusted for the size of the cube test specimens to that of 100 mm cubes. It was found however (see later) that formula (4.1) overestimates the cube compressive strength of low strength (30 – 40 MPa) SCC mixes. This is perhaps a result of the presence of high powder content in these mixes, as has also been stated by Nanthagopalan and Santhanam (2009). For 30 MPa mix, the w/cm predicted by (4.1) needs to be decreased by approximately 14% and that for 40 MPa mix by 8%.

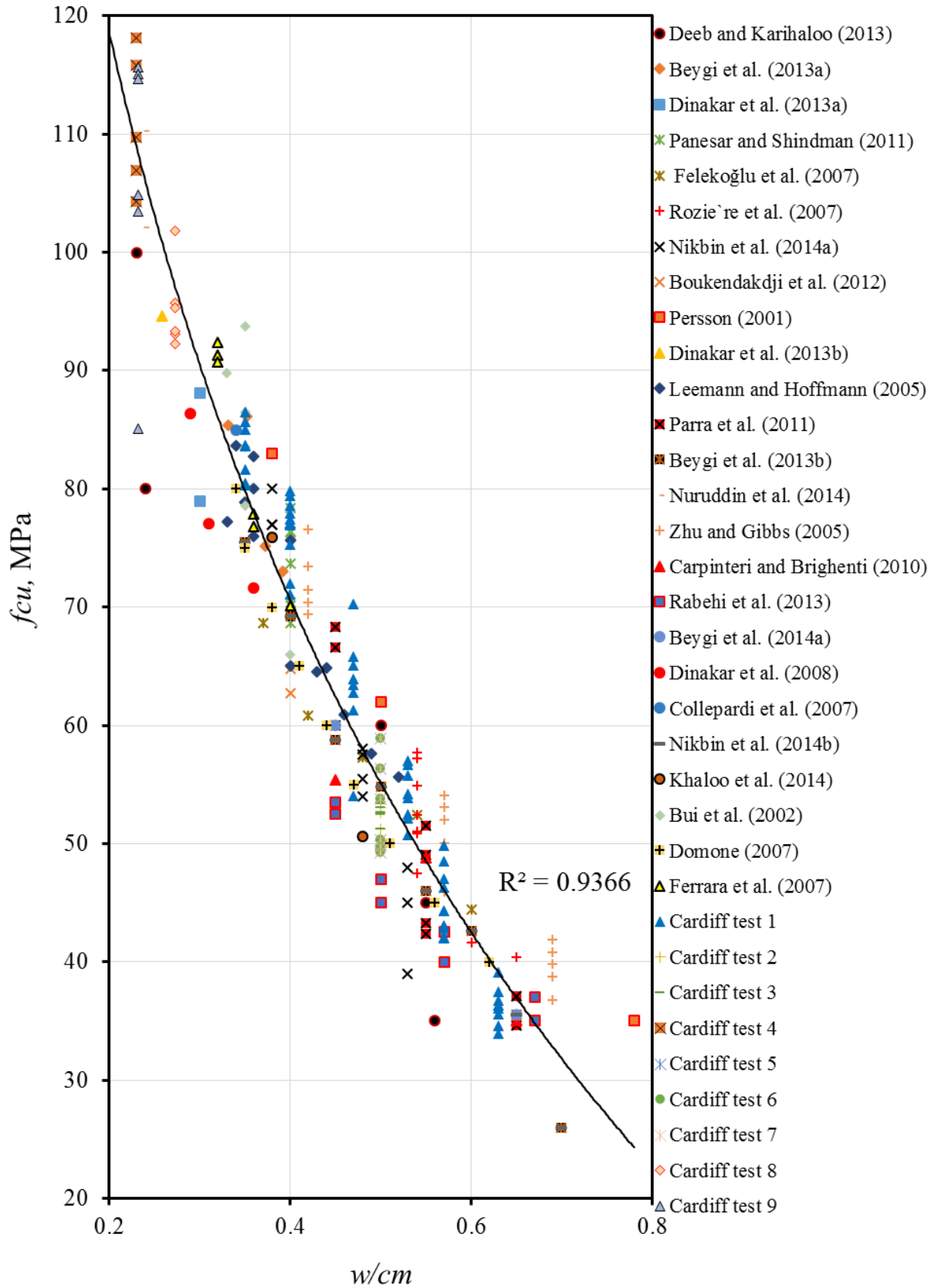


Figure 4. 1 Relation between compressive strength and water to cementitious material ratio

4.3 Target plastic viscosity

Fresh SCC is a non-Newtonian fluid best described by a Bingham-type model. This model contains two rheological parameters of SCC, namely its yield stress and plastic viscosity (Ferraris, 1999; Banfill, 2006). It is known however, that the yield stress of SCC mixes is low (in the order of tens of Pa) in comparison with vibrated concrete mixes and it remains so over a wide range of plastic viscosity (Dransfield, 2003). Thus the most important parameter is the plastic viscosity which changes with the plastic viscosity of the paste and the mix composition.

The plastic viscosity of a homogeneous viscous fluid, such as a paste (mixture of cement, cement replacement material, water and superplasticizer) can be measured rather accurately with a viscometer which is not possible for a non-homogeneous viscous fluid such as an SCC mix. There is a large scatter in the plastic viscosity of the same SCC mix measured with different rheometers, as has been noticed by many researchers (Banfill et al., 2000; Feys et al., 2007; Wallevik et al., 2011). Ghanbari and Karihaloo (2009) have therefore proposed a micromechanical procedure for estimating the plastic viscosity of an SCC mix knowing the plastic viscosity of the paste used in it. In this procedure, SCC is regarded as a two-phase suspension in which the solid phase is suspended in a viscous liquid phase. The increase in the plastic viscosity of the liquid phase as a result of the addition of the solid phase (filler, fine and coarse aggregates) is estimated in a stepwise manner from the two-phase suspension model. Figure 4.2 shows the hierarchy of these two-phase liquid and solid suspensions that are used for estimating the plastic viscosity of all SCC mixes based on the viscosity of the cement paste used in them.

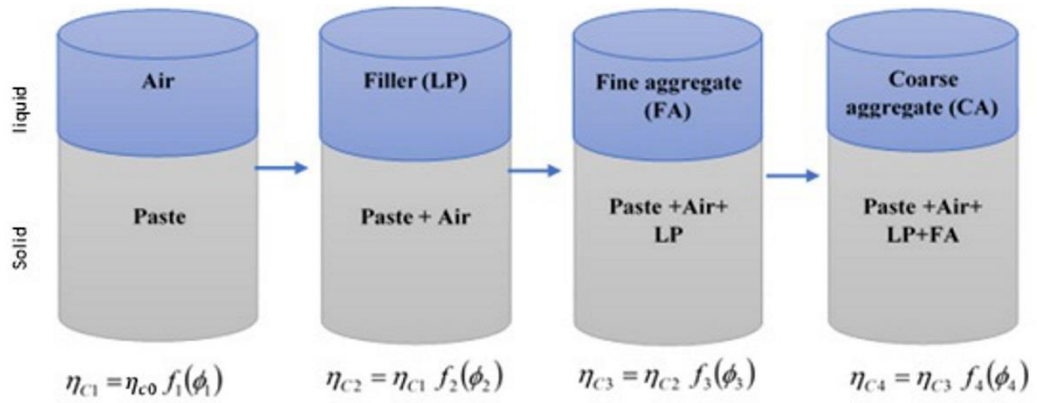


Figure 4. 2 Hierarchy of two-phase liquid-solid suspensions constituting an SCC mix (After: Deeb, 2013)

The plastic viscosity of the i -th liquid–solid suspension can be estimated from the plastic viscosity of the preceding $(i-1)$ th phase as

$$\eta_{ci} = \eta_{ci-1} * f_i(\phi_i) \quad (4. 2)$$

Here,

η_{ci} = plastic viscosity of the i -th liquid–solid suspension;

η_{ci-1} = plastic viscosity of the preceding $(i-1)$ th phase. In the first step $i = 1$, η_{c0} is the known plastic viscosity of the paste; $f_i(\phi_i)$ = a factor larger than unity that predicts the increase in the plastic viscosity induced by the solid phase with a volume fraction ϕ_i

$$\phi_i = \frac{v_i}{v_i + v_o} \quad (4. 3)$$

where

v_i : volume of solid phase i ; v_o : volume of the continuous matrix phase in which the solid phase i is suspended;

According to this procedure, the plastic viscosity of an SCC mix is given by:

$$\eta_{mix} = \eta_{paste} * f_1(\phi_1) * f_2(\phi_2) \dots * f_n(\phi_n) \quad (4. 4)$$

where n is the total number of solid phases in the mix. Besides the filler, fine and coarse aggregates, air voids can also be treated as a second phase in a viscous suspension (Figure 4.2). Einstein was the first to develop an expression $f_i(\phi_i)$ for dilute suspensions (second phase volume fraction less than 10%) containing randomly distributed rigid or hollow spheres with no hydrodynamic interactions (Koehler and Fowler, 2007) :

$$f_i(\phi_i) = 1 + [\eta]\phi_i \quad (4.5)$$

The numerical factor $[\eta]$ is equal to 2.5 for rigid spherical particles and to 1 for spherical air bubbles that are packed randomly in a hexagonal arrangement. Subsequent investigations have proved that the numerical factor 2.5 is quite accurate even for rigid ellipsoidal particles with an aspect ratio less than 3.

However, at higher concentrations of the solid phase (volume fraction >10% up to the maximum possible volume fraction, ϕ_m), the hydrodynamic interactions between the particles and the Brownian motions cannot be ignored. In this situation, Krieger–Dougherty (1959) formula (Equation 4.6) has been found to be appropriate for cement–based suspensions. The value of ϕ_m is 0.74 for hexagonal close packing, 0.63 for random hexagonal packing, and 0.524 for cubic packing.

$$f_i(\phi_i) = \left(1 - \frac{\phi_i}{\phi_m}\right)^{-[\eta]\phi_m} \quad (4.6)$$

The particle size distribution significantly affects ϕ_m . Furthermore, the numerical factor $[\eta]$ and ϕ_m depend upon the shear rate; the former tends to decrease with increasing shear rate, whereas the latter shows the opposite trend. However, $[\eta]$ and ϕ_m change in such a way that a decrease in the first leads to an increase in the second, but the product of the two changes remains practically the same and equal, on average, to 1.9 (de Kruif et al., 1985). In most SCC mixes, the volume fractions of the filler, fine and coarse aggregates generally exceed 10%, so that their contribution to the increase in the known plastic viscosity of the paste is given by Equation (4.6). The volume fraction of the trapped air bubbles is however low, around 2%, such that Equation (4.5) with the numerical factor equal to 1 is appropriate. For simplicity, this

2% increase due to trapped air is included in the plastic viscosity of the paste in Equation (4.7):

$$\eta_{mix} = \eta_{paste} * \left(1 - \frac{\phi_{Filler}}{\phi_{m1}}\right)^{-1.9} * \left(1 - \frac{\phi_{Fine Agg.}}{\phi_{m2}}\right)^{-1.9} * \left(1 - \frac{\phi_{Coarse Agg.}}{\phi_{m3}}\right)^{-1.9} \quad (4.7)$$

Note that the packing density (i.e. the maximum volume fraction, ϕ_m , $\phi_{m1} = 0.524$, $\phi_{m2} = 0.63$ and $\phi_{m3} = 0.74$) increases with the addition of solid phases. When the first solid phase is added to the paste, the packing is loose so that it is appropriate to assume cubic packing. When however, the last solid phase is added to the suspension, the packing is very dense and it is appropriate to assume hexagonal close packing.

4.4 Basic steps of the proposed mix design method

The basic steps of the proposed mix design method are summarised below.

1. Select the desired plastic viscosity of the mix with the lower limit of the target plastic viscosity in the range of 3.5–8 Pa s and the upper limit of the target plastic viscosity is 15 Pa s, and remembering that the slump cone t_{500} time increases with increasing plastic viscosity of the mix. The EFNARC guidelines (2005) may be helpful in the choice of the desired plastic viscosity depending on the application;
2. Calculate the ratio of water to cementitious materials (w/cm) that produces the target cube characteristic strength from Equation (4.1);
3. Choose the water content in the range of 150–210 kg/m³, following EFNARC guidelines (2005) (Table 4.1), and calculate the mass of cementitious materials (cm) in kg/m³. The amount of ggbs is assumed to be 25% of cementitious material (cm). It is known (Nehdi et al., 2004) that the replacement of 25% cement (c) by ggbs has little or no effect on the paste viscosity;
4. Assume a trial superplasticizer (SP) dosage as a per cent of the cementitious material mass in the range of 0.4–0.8 % for the MasterGlenium superplasticizer used in this work. For this superplasticizer the manufacturer's recommended dosage is 0.2 – 1.2 kg per 100 kg of cementitious material (BASF, 2014).
5. Estimate the plastic viscosity of the paste from the w/cm and SP/cm ratios (Sun et al., 2006) (see Table 4.2). It is known that SP/cm has little impact on the paste viscosity; the major impact is on the yield stress (Domone, 2003);

6. Calculate the mass of the solid phase ingredients (filler, fine aggregate and coarse aggregate) according to their volume fractions, as explained in the examples below;
7. Check if the total volume of the produced mix is equal to 1 m³. If not, scale the ingredient masses to achieve a total volume of 1 m³;
8. Calculate the plastic viscosity of the mix using Equation (4.7) and compare it with the desired one (step 1). If the difference is within $\pm 5\%$, adopt the mix proportions. If not, choose a different combination of the volume fractions of the solid phase ingredients (step 6) and repeat steps 7–8.

Table 4. 2 Estimated plastic viscosity of the paste (cement +ggbs + SP+ water+ air) (Sun et al., 2006)

Mix designation	w/cm	η_{paste} , Pa s	$\eta_{paste+air\ voids}$, Pa s
30	0.63	0.104	0.11
40	0.57	0.176	0.18
50	0.53	0.224	0.23
60	0.47	0.286	0.29
70	0.40	0.330	0.34
80	0.35	0.365	0.37

4.4.1 Examples of mix proportioning

As an example, let us proportion the mix of an SCC having a 28-day target cube compressive strength of 70 MPa. The procedure is as follows.

1. Suppose that the desired target plastic viscosity of the mix is equal to 11 Pa s;
2. Calculate the w/cm ratio from Equation (4.1) corresponding to strength grade C70. It works out to be 0.40;
3. Assume the water content, w to be 180 kg/m³, then the mass of cementitious materials (cm);

$$cm = \frac{w}{(w/cm)} = \frac{180}{0.40} = 450 \text{ kg/m}^3;$$
4. Assume a trial superplasticizer dosage (super – plasticizer mass, SP) as a per cent of mass of cementitious materials (say 0.65%) which equals 2.925 kg/m³ ;
5. Estimate the plastic viscosity of the paste $\eta_{paste} = 0.34$ Pa s (Table 4.2);

6. In order to estimate the volume fractions of filler LP , fine aggregate FA and coarse aggregate CA , we first rewrite Equation (4.7) as (note the use of different packing densities, as explained above);

$$\eta_{mix} = \eta_{paste} * \left(1 - \frac{\phi_{LP}}{0.524}\right)^{-1.9} * \left(1 - \frac{\phi_{FA}}{0.63}\right)^{-1.9} * \left(1 - \frac{\phi_{CA}}{0.74}\right)^{-1.9}$$

$$\text{Let } u = \left(\frac{\eta_{mix}}{\eta_{paste}} * 0.524^{-1.9} * 0.63^{-1.9} * 0.74^{-1.9}\right)^{\frac{1}{-1.9}}$$

so that the above equation becomes $u = (0.524 - \phi_{LP}) * (0.63 - \phi_{FA}) * (0.74 - \phi_{CA})$.

Substituting $\eta_{mix} = 11 \text{ Pa s}$ and $\eta_{paste} = 0.34 \text{ Pa s}$, gives

$$u = 0.03919 = (0.524 - \phi_{LP}) * (0.63 - \phi_{FA}) * (0.74 - \phi_{CA})$$

$$\text{Let } x = \sqrt[3]{u} = 0.3397,$$

then the values of ϕ_{LP} , ϕ_{FA} and ϕ_{CA} are given by

$$\phi_{LP} = 0.524 - t_1 * x$$

$$\phi_{FA} = 0.63 - t_2 * x$$

$$\phi_{CA} = 0.74 - t_3 * x$$

where, t_1 , t_2 , and t_3 are arbitrarily chosen factors such that $t_1 * t_2 * t_3 = 1$. Let us choose $t_1 = 1$, $t_2 = 1$ and $t_3 = 1$, in the first instance.

For this choice of t_1 , t_2 , and t_3 , the volume fractions of solid phases will be

$$\phi_{LP} = 0.524 - t_1 * x = 0.524 - 1 * 0.3397 = 0.1843$$

$$\phi_{FA} = 0.63 - t_2 * x = 0.63 - 1 * 0.3397 = 0.2903$$

$$\phi_{CA} = 0.74 - t_3 * x = 0.74 - 1 * 0.3397 = 0.4003$$

The amounts of solid phases, i.e. limestone filler LP , fine aggregate FA and coarse aggregate CA that are suspended in the liquid paste are calculated according to their volume fractions ϕ_i , knowing that the densities of cement, ggs , water, superplasticizer, limestone powder, fine aggregate and coarse aggregate are 2950, 2400, 1000, 1070, 2400, 2650 and 2800 kg/m^3 , respectively:

$$\phi_{LP} = \frac{\frac{LP}{\rho_{LP}}}{\left(\frac{c}{\rho_c} + \frac{ggs}{\rho_{ggs}} + \frac{w}{\rho_w} + \frac{SP}{\rho_{SP}} + 0.02\right) + \frac{LP}{\rho_{LP}}} \quad \rightarrow \quad LP = 197.4 \text{ kg/m}^3$$

$$\phi_{FA} = \frac{\frac{FA}{\rho_{FA}}}{\left(\frac{c}{\rho_c} + \frac{ggbs}{\rho_{ggbs}} + \frac{w}{\rho_w} + \frac{SP}{\rho_{SP}} + \frac{LP}{\rho_{LP}} + 0.02\right) + \frac{FA}{\rho_{FA}}} \quad \rightarrow \quad FA = 483.8 \text{ kg/m}^3$$

$$\phi_{CA} = \frac{\frac{CA}{\rho_{CA}}}{\left(\frac{c}{\rho_c} + \frac{ggbs}{\rho_{ggbs}} + \frac{w}{\rho_w} + \frac{SP}{\rho_{SP}} + \frac{LP}{\rho_{LP}} + \frac{FA}{\rho_{FA}} + 0.02\right) + \frac{CA}{\rho_{CA}}} \quad \rightarrow \quad CA = 1175 \text{ kg/m}^3$$

7. The total volume of the SCC mix that the above ingredients will yield (including the volume occupied by trapped air bubbles, 0.02)

$$\text{Total Volume} = \frac{c}{\rho_c} + \frac{ggbs}{\rho_{ggbs}} + \frac{w}{\rho_w} + \frac{SP}{\rho_{SP}} + \frac{LP}{\rho_{LP}} + \frac{FA}{\rho_{FA}} + \frac{CA}{\rho_{CA}} + 0.02$$

$$\text{Total Volume} = \frac{450 \cdot 0.75}{2950} + \frac{450 \cdot 0.25}{2400} + \frac{180}{1000} + \frac{2.925}{1070} + \frac{197.4}{2400} + \frac{483.8}{2650} + \frac{1175}{2800} + 0.02 = 1.049 \text{ m}^3$$

As the yield does not equal 1 m^3 , the amounts of materials are adjusted

$$cm = 450/1.049 = 429.1 \text{ kg/m}^3$$

$$w = 180/1.049 = 171.7 \text{ kg/m}^3$$

$$SP = 2.925/1.049 = 2.789 \text{ kg/m}^3$$

$$LP = 197.4/1.049 = 188.3 \text{ kg/m}^3$$

$$FA = 483.8/1.049 = 461.4 \text{ kg/m}^3$$

$$CA = 1175/1.049 = 1121 \text{ kg/m}^3$$

$$\text{Total Volume} = \frac{c}{\rho_c} + \frac{ggbs}{\rho_{ggbs}} + \frac{w}{\rho_w} + \frac{SP}{\rho_{SP}} + \frac{LP}{\rho_{LP}} + \frac{FA}{\rho_{FA}} + \frac{CA}{\rho_{CA}} + 0.02 = 1.000 \text{ m}^3$$

8. Check the plastic viscosity of the mix using Equation (4.7)

$$\eta_{mix} = \eta_{paste} * \left(1 - \frac{\phi_{LP}}{\phi_m}\right)^{-1.9} * \left(1 - \frac{\phi_{FA}}{\phi_m}\right)^{-1.9} * \left(1 - \frac{\phi_{CA}}{\phi_m}\right)^{-1.9}$$

$$\eta_{mix} = 0.34 * \left(1 - \frac{0.1839}{0.524}\right)^{-1.9} * \left(1 - \frac{0.2899}{0.63}\right)^{-1.9} * \left(1 - \frac{0.3999}{0.74}\right)^{-1.9} = 10.93 \text{ Pa s}$$

The mix masses before and after scaling to 1 m^3 are given in Table 4.3, together with the difference between the actual and target plastic viscosities.

Table 4. 3 Mix constituents and plastic viscosity of an SCC mix

	<i>Ingredient, kg/m³</i>							<i>η, Pa s</i>	<i>difference</i>
	<i>cement</i>	<i>ggbs</i>	<i>w</i>	<i>SP</i>	<i>LP</i>	<i>FA</i>	<i>CA</i>		
Before adjust	337.5	112.5	180	2.925	197.4	483.8	1175		
After adjust	321.9	107.3	171.7	2.789	188.3	461.4	1121	10.93	-0.68%
Density	2950	2400	1000	1070	2400	2650	2800	–	

As the difference of -0.68% in the plastic viscosity is well within the acceptable range, the mix would seem to be acceptable.

However, the amount of coarse aggregate exceeds the limit in the guidelines (EFNARC, 2005) (Table 4.1), so it is necessary to adjust the mix proportions, choosing different arbitrary values of t_1 , t_2 and t_3 for the same target plastic viscosity and strength:

Steps 1-5 are the same as described above.

6. In order to calculate the volume fractions of solid phases, let choose values of t_1 , t_2 , and t_3 different from those used above. Let $t_1 = 1.25$, $t_2 = 0.64$ and $t_3 = 1.25$ such that $t_1 * t_2 * t_3 = 1$. Accordingly, the volume fractions of solid phases work out to be $\phi_{LP} = 0.0994$, $\phi_{FA} = 0.4126$ and $\phi_{CA} = 0.3154$. The amounts of solid phases, i.e. limestone filler LP , fine aggregate FA and coarse aggregate CA that are suspended in the liquid paste are calculated according to their volume fractions ϕ_i ;

$$\phi_{LP} = \frac{\frac{LP}{\rho_{LP}}}{\left(\frac{c}{\rho_c} + \frac{ggbs}{\rho_{ggbs}} + \frac{w}{\rho_w} + \frac{SP}{\rho_{SP}} + 0.02\right) + \frac{LP}{\rho_{LP}}} \quad \rightarrow LP = 96.42 \text{ kg/m}^3$$

$$\phi_{FA} = \frac{\frac{FA}{\rho_{FA}}}{\left(\frac{c}{\rho_c} + \frac{ggbs}{\rho_{ggbs}} + \frac{w}{\rho_w} + \frac{SP}{\rho_{SP}} + \frac{LP}{\rho_{LP}} + 0.02\right) + \frac{FA}{\rho_{FA}}} \quad \rightarrow FA = 752.4 \text{ kg/m}^3$$

$$\phi_{CA} = \frac{\frac{CA}{\rho_{CA}}}{\left(\frac{c}{\rho_c} + \frac{ggbs}{\rho_{ggbs}} + \frac{w}{\rho_w} + \frac{SP}{\rho_{SP}} + \frac{LP}{\rho_{LP}} + \frac{FA}{\rho_{FA}} + 0.02\right) + \frac{CA}{\rho_{CA}}} \quad \rightarrow CA = 887.6 \text{ kg/m}^3$$

7. The total volume of the SCC mix that the above ingredients will yield (including the volume occupied by trapped air bubbles, 0.02);

$$\text{Total Volume} = \frac{c}{\rho_c} + \frac{ggb_s}{\rho_{ggb_s}} + \frac{w}{\rho_w} + \frac{SP}{\rho_{SP}} + \frac{LP}{\rho_{LP}} + \frac{FA}{\rho_{FA}} + \frac{CA}{\rho_{CA}} + 0.02 = 1.0 \text{ m}^3$$

As the yield does not equal to 1 m^3 , the amounts of ingredients are adjusted. The results are shown in Table 4.4.

8. The mix plastic viscosity is recalculated by using Equation (4.7), and shown in Table 4.4. As the difference between the target plastic viscosity and the actual mix plastic viscosity is within $\pm 5\%$, the mix proportions after adjustment are acceptable.

Table 4. 4 Mix constituents and plastic viscosity of an SCC mix

	<i>Ingredient, kg/m³</i>							<i>η, Pa s</i>	<i>difference</i>
	<i>cement</i>	<i>ggb_s</i>	<i>w</i>	<i>SP</i>	<i>LP</i>	<i>FA</i>	<i>CA</i>		
Before adjust.	337.5	112.5	180	2.925	96.42	752.4	887.6		-0.08%
After adjust	335.8	111.9	179.1	2.91	95.93	748.5	883.1	10.99	
Density	2950	2400	1000	1070	2400	2650	2800	–	

In view of the arbitrariness in the choice of t_i , it is clear that there are many (theoretically infinite) combinations of the volume fractions of the solid phases that can be chosen for an SCC mix and still reach the target cube compressive strength and mix plastic viscosity. It is however possible that some of these combinations may not yield a satisfactory SCC mix. It is therefore necessary to use other sources of information based on accumulated knowledge of SCC mixes, e.g. the EFNARC guidelines (2005) and survey report (Domone, 2006), as was done above. To aid the user in making a knowledgeable choice, a software program was developed from which design charts were constructed which are presented below.

4.5 Design charts for mix proportioning of normal and high strength SCC mixes

Thousands of solid phase volume fraction combinations (i.e. t_1 , t_2 , and t_3) were produced using a software program; this program is given in Appendix A. These

combinations covered wide ranges of target cube compressive strength and mix plastic viscosity (see Appendix B, Tables B.1-B.6). They have been collected in groups according to the target strength for ease of SCC mix proportioning. It was found convenient for presentation of a huge body of data to normalise the amounts of dry phases by the plastic viscosity and to present the amounts in separate plots, beginning with the cementitious materials (cm), and ending with the content of all dry phases ($cm + LP + FA + CA$). These design charts are given in Figures 4.3-4.9. The scatter reflects the multiplicity of possible combinations. It is however interesting to note that the scatter is the least in the bottom (cm) and the top ($cm + LP + FA + CA$) curves. This is because the amount of cm calculated from the target compressive strength is according to the water content which varies in the narrow range of 150-210 l/m³ (EFNARC, 2005), and the amounts of all dry ingredients contribute to the target plastic viscosity of the mix.

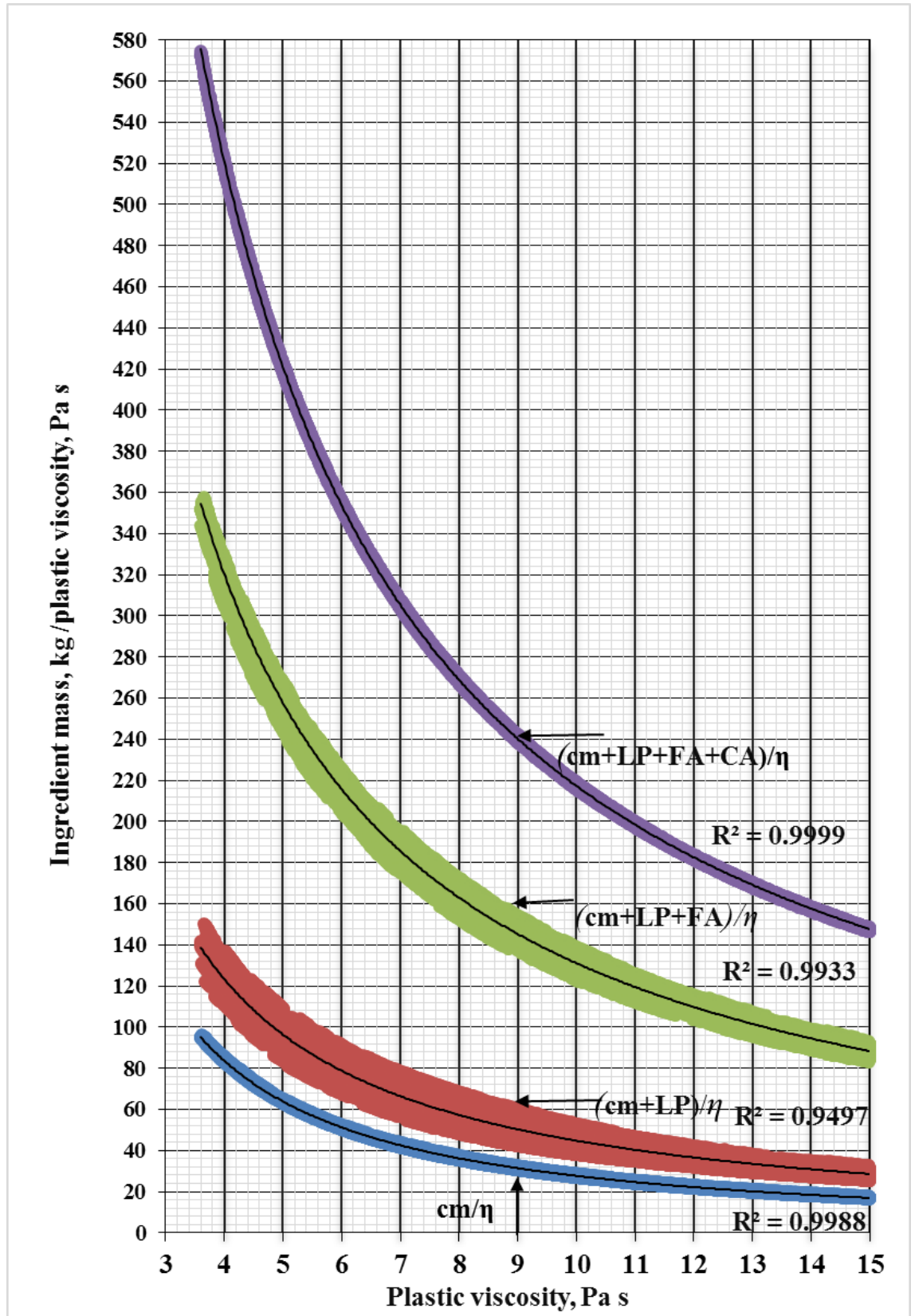


Figure 4. 3 Ingredient mass (kg) normalised by mix plastic viscosity vs plastic viscosity

for 30 MPa mix

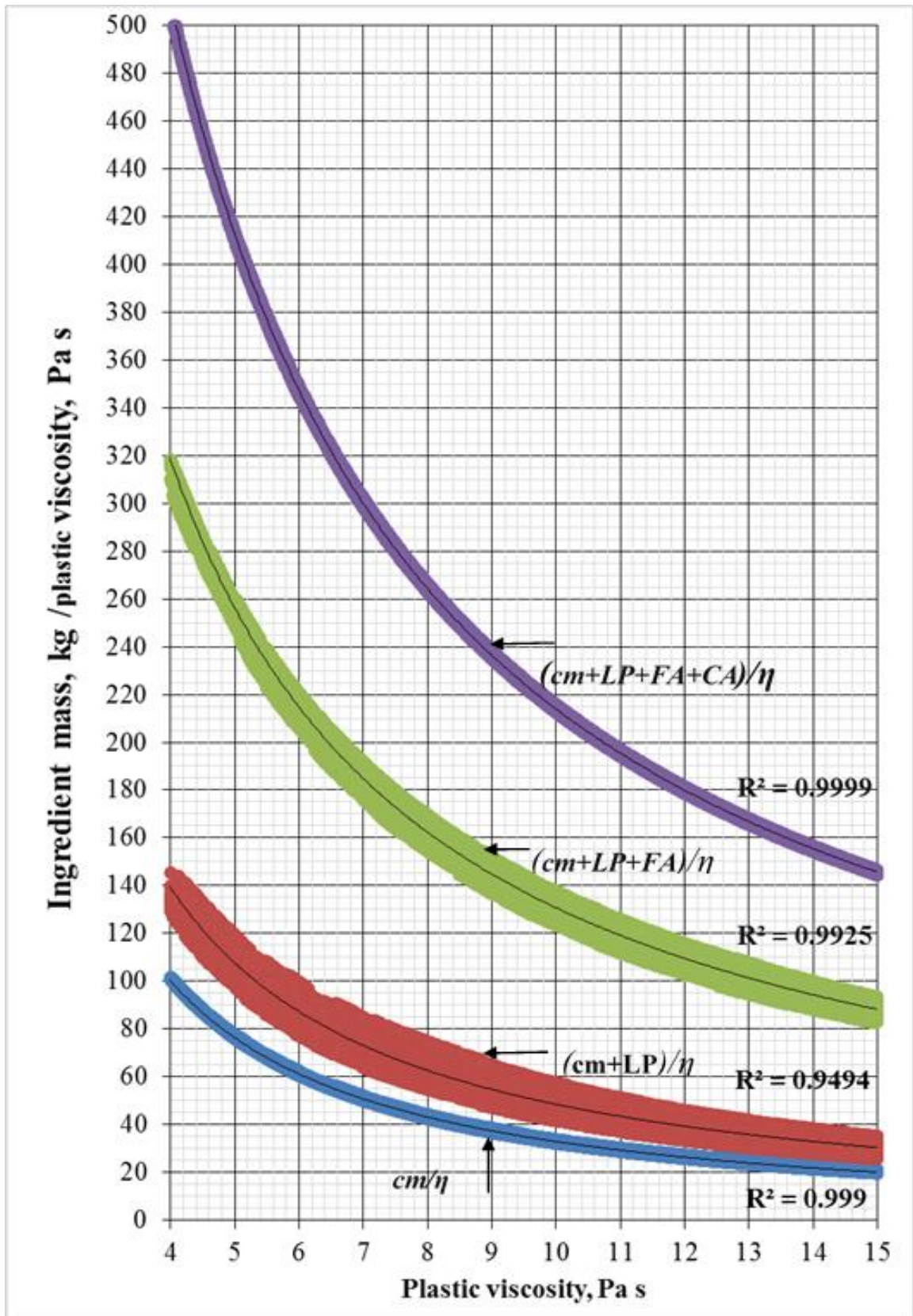


Figure 4. 4 Ingredient mass (kg) normalised by mix plastic viscosity vs plastic viscosity

for 40 MPa mix

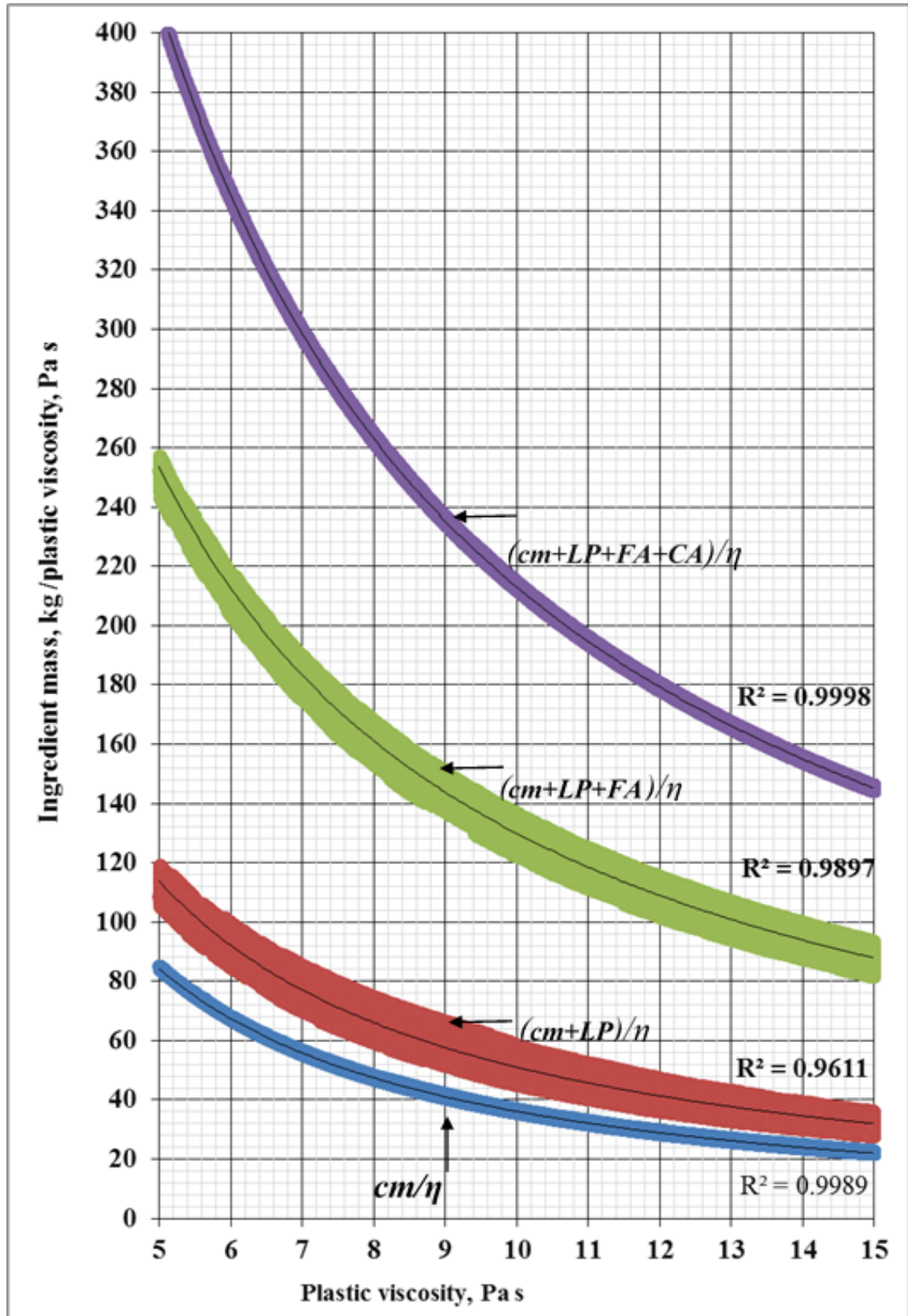


Figure 4. 5 Ingredient mass (kg) normalised by mix plastic viscosity vs plastic viscosity

for 50 MPa mix

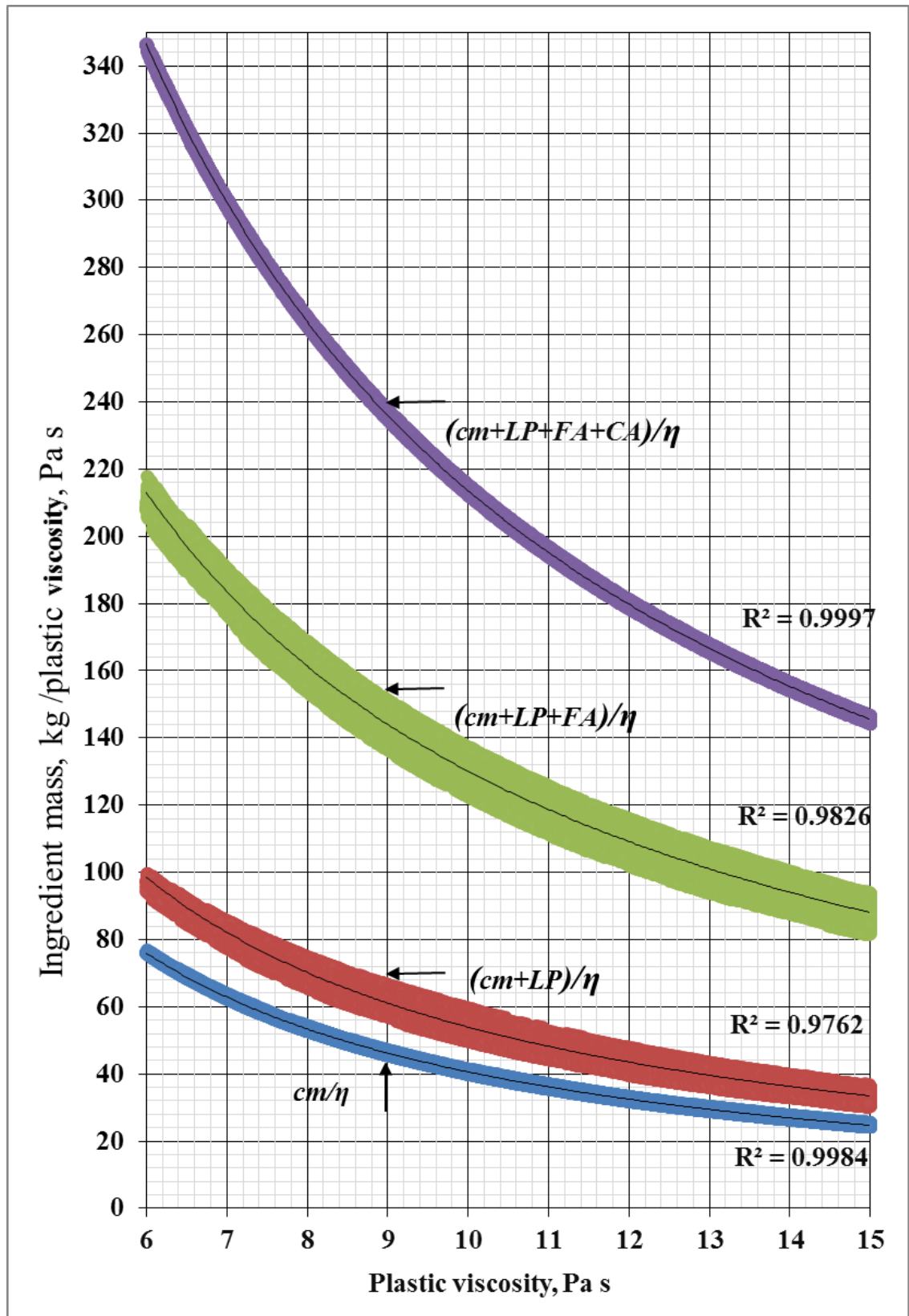


Figure 4. 6 Ingredient mass (kg) normalised by mix plastic viscosity vs plastic viscosity

for 60 MPa mix

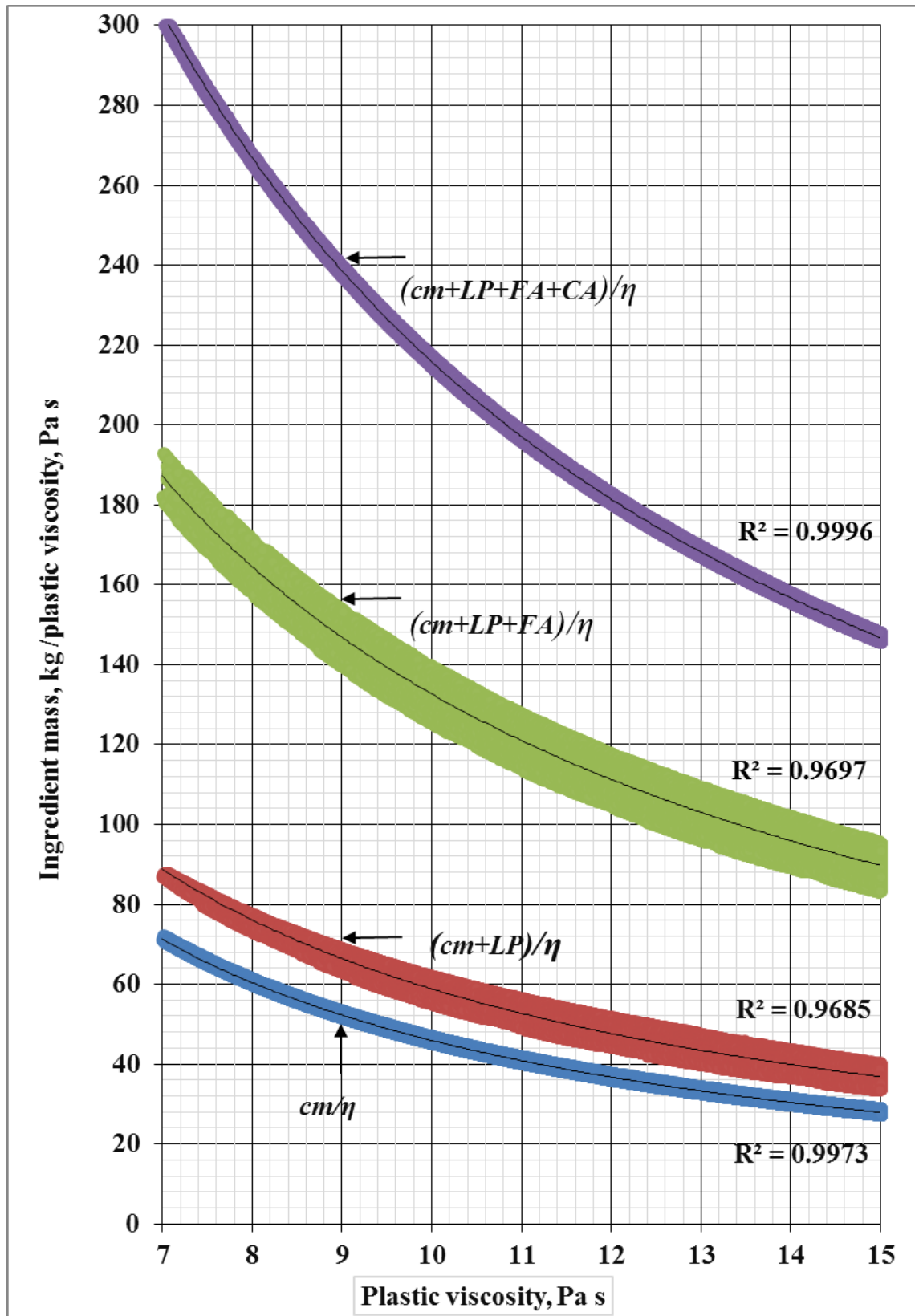


Figure 4. 7 Ingredient mass (kg) normalised by mix plastic viscosity vs plastic viscosity

for 70 MPa mix

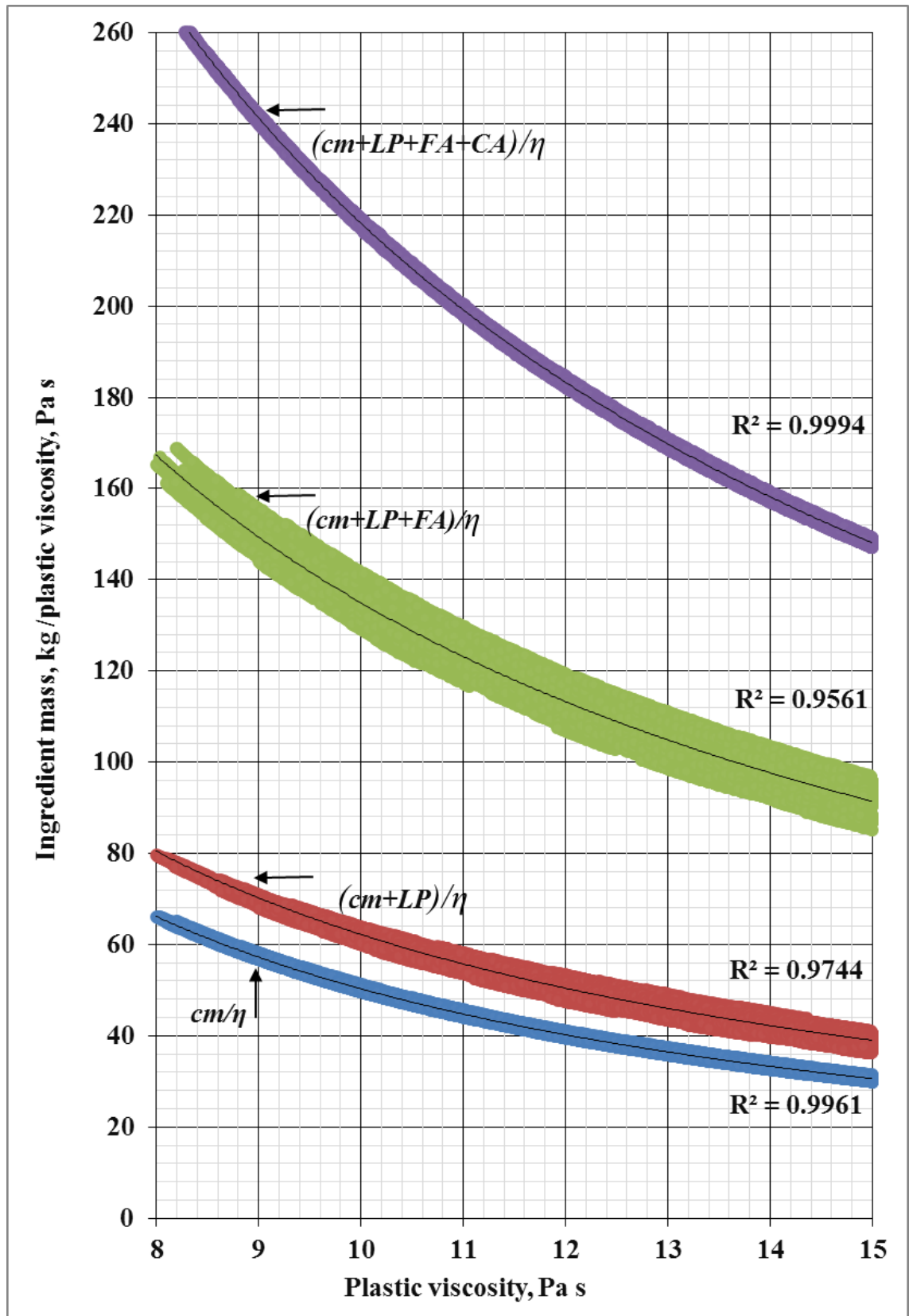


Figure 4. 8 Ingredient mass (kg) normalised by mix plastic viscosity vs plastic viscosity

for 80 MPa mix

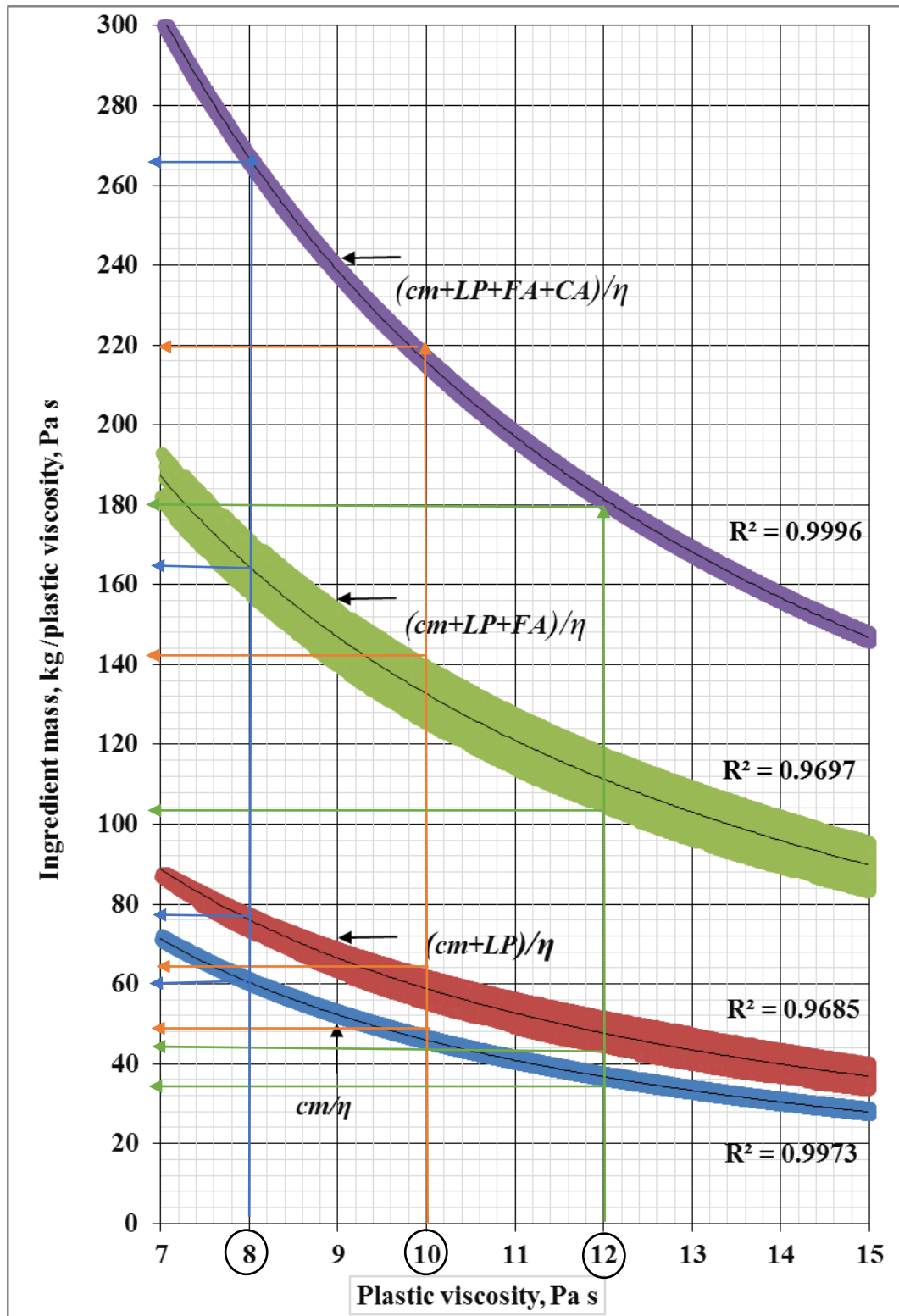


Figure 4. 9 Ingredient mass (kg) normalised by mix plastic viscosity vs plastic viscosity for 70 MPa for use in the explanatory examples below

4.5.1 Examples of the use of design charts

In order to demonstrate how easy it is to use the design charts (Figures 4.3-4.8), let us assume we wish to design an SCC mix with a target cube compressive strength of 70 MPa.

1. Suppose further that the desired target plastic viscosity of mix is 8 Pa s (Figure 4.9);
2. For the desired target strength= 70 MPa $w/cm= 0.4$ (Equation 4.1);
3. Calculate the cementitious material content (cm);

$$\text{For } \eta_{mix} = 8 \text{ Pa s} \longrightarrow \frac{cm}{\eta} = 61 \text{ (bottom curve)} \longrightarrow cm = 61 * 8 = 488 \text{ kg/m}^3;$$

$$c = 0.75 * 488 = 366 \text{ kg/m}^3, \text{ ggbs} = 0.25 * 488 = 122 \text{ kg/m}^3;$$

$$\text{As } w/cm = 0.40 \longrightarrow w = 0.40 * 488 = 195.2 \text{ l/m}^3$$

4. Assume a trial superplasticizer dosage (super – plasticizer mass, SP) as a per cent of mass of cementitious materials (say 0.65%) which equals to 3.17 kg/m³;
5. The plastic viscosity of the paste according to its w/cm and SP/cm ratios is equal to 0.34 (Table 4.2);
6. Calculate the solid phase ingredient contents (*LP, FA and CA*);

$$\text{For } \eta_{mix} = 8 \text{ Pa s};$$

$$\frac{(cm+LP)}{\eta} = 76 \text{ (second curve from bottom)} \quad (\text{Figure 4.9})$$

$$(cm+LP) = 76 * 8 = 608 \text{ kg/m}^3 \longrightarrow LP = 608 - 488 = 120 \text{ kg/m}^3$$

$$\frac{(cm+LP+FA)}{\eta} = 164 \text{ (second curve from top)}$$

$$(cm+LP+FA) = 164 * 8 = 1312 \text{ kg/m}^3 \longrightarrow FA = 1312 - 488 - 120 = 704 \text{ kg/m}^3$$

$$\frac{(cm+LP+FA+CA)}{\eta} = 266 \text{ (top curve)}$$

$$(cm+LP+FA+CA) = 266 * 8 = 2128 \text{ kg/m}^3 \longrightarrow CA = 2128 - 488 - 120 - 704 = 816 \text{ kg/m}^3.$$

7. Calculate the total volume of the mix;

$$\begin{aligned} \text{Total volume} &= \frac{c}{\rho_c} + \frac{\text{ggs}}{\rho_{\text{ggs}}} + \frac{w}{\rho_w} + \frac{\text{SP}}{\rho_{\text{SP}}} + \frac{\text{LP}}{\rho_{\text{LP}}} + \frac{\text{FA}}{\rho_{\text{FA}}} + \frac{\text{CA}}{\rho_{\text{CA}}} + 0.02 \\ &= \frac{366}{2950} + \frac{122}{2400} + \frac{195.2}{1000} + \frac{3.17}{1070} + \frac{120}{2400} + \frac{696}{2650} + \frac{824}{2800} + 0.02 = 1.0 \text{ m}^3 \end{aligned}$$

8. Check the plastic viscosity using Equation (4.7);

$$\eta_{\text{mix}} = \eta_{\text{paste}} * \left(1 - \frac{\phi_{\text{LP}}}{\phi_m}\right)^{-1.9} * \left(1 - \frac{\phi_{\text{FA}}}{\phi_m}\right)^{-1.9} * \left(1 - \frac{\phi_{\text{CA}}}{\phi_m}\right)^{-1.9}$$

$$\eta_{\text{mix}} = 0.34 * \left(1 - \frac{0.113}{0.524}\right)^{-1.9} * \left(1 - \frac{0.375}{0.63}\right)^{-1.9} * \left(1 - \frac{0.291}{0.74}\right)^{-1.9} = 7.69 \text{ Pa s}$$

$$\text{Viscosity diff.} = \frac{(\text{calculated } \eta_{\text{mix}} - \text{target } \eta_{\text{mix}})}{\text{target } \eta_{\text{mix}}} * 100 = \frac{(7.69 - 8)}{8} * 100 = -3.87\%$$

This is within the acceptable difference $\pm 5\%$.

It is interesting to observe that in this example we chose the mix combinations corresponding to the best-fit lines in the curves (see Figure 4.9). That is why the total mix volume worked out to be exactly 1 m^3 , so that the plastic viscosity of the mix is within the acceptable deviation from the desired target value. This would not have been so, had we chosen the mix combinations different from the best-fit lines within the scatter band. As a rule, the more the deviation from the best-fit lines, the more the total mix volume deviates from 1 m^3 and consequently the more the plastic viscosity of the resultant mix deviates from the target value. If the deviation is more than $\pm 5\%$, then as mentioned above the procedure would need to be repeated (see step 8 in the mix design procedure §4.4).

In order to demonstrate this we choose two examples with ingredient proportions away from the best fit-lines, and nearer the upper and lower limits of scatter. Let us design an SCC mix with a target cube compressive strength of 70 MPa and choose the starting ingredient amounts at the upper limits of scatter in the design chart (Figure 4.9).

1. Suppose the desired target plastic viscosity of mix is 10 Pa s;
2. For the desired target strength= 70 MPa $w/cm = 0.4$ (Equation 4.1);
3. Calculate the cementitious material content (cm);

$$\text{For } \eta_{\text{mix}} = 10 \text{ Pa s} \longrightarrow \frac{cm}{\eta} = 48 \text{ (bottom curve)} \longrightarrow cm = 48 * 10 = 480 \text{ kg/m}^3;$$

$$c = 0.75 \cdot 480 = 360 \text{ kg/m}^3, \text{ ggs} = 0.25 \cdot 480 = 120 \text{ kg/m}^3;$$

$$\text{As } w/cm = 0.4 \longrightarrow w = 0.4 \cdot 480 = 192 \text{ l/m}^3$$

4. Assume a trial superplasticizer dosage (superplasticizer mass, SP) as a per cent of mass of cementitious materials (say 0.65%) which equals to 3.12 kg/m^3 ;
5. The plastic viscosity of the paste according to its w/cm and SP/cm ratios is equal to 0.34 (Table 2);
6. Calculate the solid phase ingredient contents (LP , FA and CA);

$$\text{For } \eta_{mix} = 10 \text{ Pa s};$$

$$\frac{(cm+LP)}{\eta} = 64 \text{ (second curve from bottom) (Figure 4.12)}$$

$$(cm+LP) = 64 \cdot 10 = 640 \text{ kg/m}^3 \longrightarrow LP = 640 - 480 = 160 \text{ kg/m}^3$$

$$\frac{(cm+LP+FA)}{\eta} = 141 \text{ (second curve from top)}$$

$$(cm+LP+FA) = 141 \cdot 10 = 1410 \text{ kg/m}^3 \longrightarrow FA = 1410 - 480 - 160 = 770 \text{ kg/m}^3$$

$$\frac{(cm+LP+FA+CA)}{\eta} = 220 \text{ (top curve)}$$

$$(cm+LP+FA+CA) = 220 \cdot 10 = 2200 \text{ kg/m}^3 \longrightarrow CA = 2200 - 480 - 160 - 770 = 790 \text{ kg/m}^3$$

Calculate the total volume of the mix;

$$\text{Total volume} = \frac{360}{2950} + \frac{120}{2400} + \frac{192}{1000} + \frac{3.1}{1070} + \frac{160}{2400} + \frac{770}{2650} + \frac{790}{2800} + 0.02 = 1.026 \text{ m}^3$$

Owing to the total mix volume exceeding 1 m^3 , it must be scaled to 1.0, so the ingredient amounts will be:

$$cm = 480 / 1.026 = 467.8 \text{ kg/m}^3$$

$$w = 192 / 1.026 = 187.1 \text{ kg/m}^3$$

$$SP = 3.12 / 1.026 = 3.0 \text{ kg/m}^3$$

$$LP = 160 / 1.026 = 156 \text{ kg/m}^3$$

$$FA = 770 / 1.026 = 750.5 \text{ kg/m}^3$$

$$CA = 790 / 1.026 = 770 \text{ kg/m}^3$$

$$\text{Total volume} = \frac{467.8 \cdot 0.75}{2950} + \frac{467.8 \cdot 0.25}{2400} + \frac{187.1}{1000} + \frac{3}{1070} + \frac{156}{2400} + \frac{750.5}{2650} + \frac{770}{2800} + 0.02 = 1 \text{ m}^3$$

Check the plastic viscosity using Equation (4.7);

$$\eta_{mix} = \eta_{paste} * \left(1 - \frac{\phi_{LP}}{\phi_m}\right)^{-1.9} * \left(1 - \frac{\phi_{FA}}{\phi_m}\right)^{-1.9} * \left(1 - \frac{\phi_{CA}}{\phi_m}\right)^{-1.9}$$

$$\eta_{mix} = 0.34 * \left(1 - \frac{0.147}{0.524}\right)^{-1.9} * \left(1 - \frac{0.390}{0.63}\right)^{-1.9} * \left(1 - \frac{0.275}{0.74}\right)^{-1.9} = 9.52 \text{ Pa s}$$

$$\text{Viscosity diff.} = \frac{(\text{calculated } \eta_{mix} - \text{target } \eta_{mix})}{\text{target } \eta_{mix}} * 100 = \frac{(9.52 - 10)}{10} * 100 = -4.8\%$$

This is within the acceptable difference $\pm 5\%$.

The next example deals with the design of an SCC mix with a target cube compressive strength of 70 MPa. In this example, we choose the starting ingredient amounts at the lower limits of scatter in the design chart (Figure 4.9).

1. Suppose the desired target plastic viscosity of mix is 12 Pa s;
2. For the desired target strength = 70 MPa \longrightarrow $w/cm = 0.40$ (Equation 4.1);
3. Calculate the cementitious material content (cm);

$$\text{For } \eta_{mix} = 12 \text{ Pa s} \longrightarrow \frac{cm}{\eta} = 34 \text{ (bottom curve)} \longrightarrow cm = 34 * 12 = 408 \text{ kg/m}^3;$$

$$c = 0.75 * 408 = 306 \text{ kg/m}^3, \text{ ggbs} = 0.25 * 408 = 102 \text{ kg/m}^3;$$

$$\text{As } w/cm = 0.40 \longrightarrow w = 0.40 * 408 = 163.2 \text{ l/m}^3$$

4. Assume a trial superplasticizer dosage (super – plasticizer mass, SP) as a per cent of mass of cementitious materials (say 0.65%) which equals to 2.65 kg/m³ ;
5. The plastic viscosity of the paste according to its w/cm and SP/cm ratios is equal to 0.34 (Table 4.2);

6. Calculate the solid phase ingredient contents (*LP, FA and CA*);

For $\eta_{mix} = 12 \text{ Pa s}$;

$$\frac{(cm+LP)}{\eta} = 43 \text{ (second curve from bottom) (Figure 4.9)}$$

$$(cm+LP) = 44 * 12 = 528 \text{ kg/m}^3 \longrightarrow LP = 528 - 408 = 120 \text{ kg/m}^3$$

$$\frac{(cm+LP+FA)}{\eta} = 104 \text{ (second curve from top)}$$

$$(cm+LP+FA) = 104 * 12 = 1248 \text{ kg/m}^3 \longrightarrow FA = 1248 - 408 - 120 = 720 \text{ kg/m}^3$$

$$\frac{(cm+LP+FA+CA)}{\eta} = 180 \text{ (top curve)}$$

$$(cm+LP+FA+CA) = 180 * 12 = 2160 \text{ kg/m}^3 \longrightarrow CA = 2160 - 408 - 120 - 720 = 912 \text{ kg/m}^3$$

Calculate the total volume of the mix;

$$\text{Total volume} = \frac{306}{2950} + \frac{102}{2400} + \frac{163.2}{1000} + \frac{2.65}{1070} + \frac{120}{2400} + \frac{720}{2650} + \frac{912}{2800} + 0.02 = 0.979 \text{ m}^3$$

Owing to the total mix volume not being equal to 1 m^3 , it must be scaled to 1.0, so the ingredients amounts will be:

$$cm = 408 / 0.979 = 416.7 \text{ kg/m}^3$$

$$w = 163.2 / 0.979 = 166.7 \text{ kg/m}^3$$

$$SP = 2.65 / 0.979 = 2.7 \text{ kg/m}^3$$

$$LP = 120 / 0.979 = 122.6 \text{ kg/m}^3$$

$$FA = 720 / 0.979 = 735.4 \text{ kg/m}^3$$

$$CA = 912 / 0.979 = 931.5 \text{ kg/m}^3$$

$$\text{Total volume} = \frac{416.7 * 0.75}{2950} + \frac{416.7 * 0.25}{2400} + \frac{166.7}{1000} + \frac{2.7}{1070} + \frac{122.6}{2400} + \frac{735.4}{2650} + \frac{931.5}{2800} + 0.02 = 1 \text{ m}^3$$

Check the plastic viscosity using Equation (4.7);

$$\eta_{mix} = 0.34 * \left(1 - \frac{0.131}{0.524}\right)^{-1.9} * \left(1 - \frac{0.416}{0.63}\right)^{-1.9} * \left(1 - \frac{0.333}{0.74}\right)^{-1.9} = 14.07 \text{ Pa s}$$

$$\text{Viscosity diff.} = \frac{(\text{calculated } \eta_{mix} - \text{target } \eta_{mix})}{\text{target } \eta_{mix}} * 100 = \frac{(14.07 - 12)}{12} * 100 = +17.25\%$$

The difference exceeds the acceptable value, $\pm 5\%$, so different ingredient masses need to be chosen from the design chart (Figure 4.9), beginning with the cementitious materials ($\frac{cm}{\eta}$).

For $\eta_{mix} = 12 \text{ Pa s}$, choose

$$\frac{cm}{\eta} = 36 \text{ (bottom curve)} \longrightarrow cm = 36 * 12 = 432 \text{ kg/m}^3;$$

$$c = 0.75 * 432 = 324 \text{ kg/m}^3, \text{ ggbs} = 0.25 * 432 = 108 \text{ kg/m}^3;$$

$$\text{As } w/cm = 0.40 \longrightarrow w = 0.40 * 432 = 172.8 \text{ l/m}^3$$

$$\frac{(cm+LP)}{\eta} = 44 \text{ (second curve from bottom)} \longrightarrow LP = 528 - 432 = 96 \text{ kg/m}^3$$

$$\frac{(cm+LP+FA)}{\eta} = 104 \text{ (second curve from top)} \longrightarrow FA = 1248 - 432 - 96 = 720 \text{ kg/m}^3$$

$$\frac{(cm+LP+FA+CA)}{\eta} = 180 \text{ (top curve)} \longrightarrow CA = 2160 - 432 - 96 - 720 = 912 \text{ kg/m}^3$$

$$\text{Total volume} = \frac{c}{\rho_c} + \frac{\text{ggbs}}{\rho_{\text{ggbs}}} + \frac{w}{\rho_w} + \frac{SP}{\rho_{SP}} + \frac{LP}{\rho_{LP}} + \frac{FA}{\rho_{FA}} + \frac{CA}{\rho_{CA}} + 0.02 = 0.988 \text{ m}^3$$

The volume must be scaled to 1.0, so the ingredient amounts will be:

$$cm = 432 / 0.988 = 437.2 \text{ kg/m}^3$$

$$w = 172.8 / 0.988 = 174.9 \text{ kg/m}^3$$

$$SP = 2.65 / 0.988 = 2.68 \text{ kg/m}^3$$

$$LP = 96 / 0.988 = 97.2 \text{ kg/m}^3$$

$$FA = 720 / 0.988 = 728.7 \text{ kg/m}^3$$

$$CA = 912 / 0.988 = 923 \text{ kg/m}^3$$

$$\text{Total Volume} = \frac{c}{\rho_c} + \frac{\text{ggbs}}{\rho_{\text{ggbs}}} + \frac{w}{\rho_w} + \frac{\text{SP}}{\rho_{\text{SP}}} + \frac{\text{LP}}{\rho_{\text{LP}}} + \frac{\text{FA}}{\rho_{\text{FA}}} + \frac{\text{CA}}{\rho_{\text{CA}}} + 0.02 = 1 \text{ m}^3$$

$$\eta_{\text{mix}} = 11.61 \text{ Pa s from Equation (4.7).}$$

$$\text{Viscosity diff.} = \frac{(\text{calculated } \eta_{\text{mix}} - \text{target } \eta_{\text{mix}})}{\text{target } \eta_{\text{mix}}} * 100 = \frac{(11.61 - 12)}{12} * 100 = -3.25 \%$$

This is within the acceptable difference, so the mix design is complete.

4.6 Concluding remarks

The proposed method of proportioning SCC is simple as evidenced by the examples. This method was based on the rheological characteristics represented by plastic viscosity of the mix and the target compressive strength. Guidelines have been provided by way of design charts for choosing the mix proportions. Besides, several examples have been given explaining the use of these design charts. The important observation from the design charts is that the lower limit of target plastic viscosity of the SCC mix increases as the target compressive strength of the mix increases. This is due to the specified target spread of the SCC mix which depends on the superplasticizer (*SP*) dosage used as a per cent of the cementitious material mass in the range of 0.4–0.8%. To lower the limit further would require a larger dose of superplasticizer or a larger replacement of cement by ggbs than the 25% limit used in the present work.

The procedure and design charts can also be used when the mix ingredients have different densities (apart from type II cement) because the plastic viscosity depends only on the volume fractions (Equation 4.7). For designing a mix whose target compressive strength is different from those of design charts in Figures 4.3-4.8, for example, a mix with target compressive strength 55 MPa, the values of ingredient masses can be interpolated from charts for mixes with target compressive strengths 50 and 60 MPa (Figures 4.5 and 4.6).

Experimental validation of the mix design procedure will be provided on a series of SCC mixes in both the fresh and hardened states in the next Chapter.

Chapter 5

Proportioning of self-compacting concrete mixes based on target plastic viscosity and compressive strength: Experimental validation

5.1 Introduction

In Chapter 4, a mix design method for SCC was developed based on the desired target plastic viscosity and compressive strength of the mix. Design charts were provided as a guide for mix proportioning. The lower limit of the target plastic viscosity of these mixes varied between 3.5-8 Pa s and the upper limit is 15 Pa s and the characteristic cube strength between 30 and 80 MPa at 28 days age. Several examples on the use of the design charts were given.

In the present Chapter, we provide experimental validation of this mix design procedure on a series of SCC mixes in both the fresh and hardened states. A series of SCC mixes that contained different volumetric ratios of paste to solid phases were prepared using the design charts. All these mixes were extensively tested in the fresh state using the slump cone, J-ring, L-box and V-funnel apparatus (EFNARC, 2005; BS EN 206-9, 2010). These tests proved conclusively the validity of the mix proportioning method in the sense that all the mixes satisfied the self-compacting criteria and achieved the desired target plastic viscosity and compressive strength. This mix proportioning method reduces the number of trials, testing time and the materials needed to design SCC mixes.

This chapter has been published in the journal ‘Journal of Sustainable Cement-Based Materials’ (see publication 5 in the list in Chapter 1).

5.2 Materials and mix proportions

The verification of the proposed SCC mix design method using the design charts was carried out by testing many mixes of differing cube compressive strength. Mixes of strength 30, 40, 50, 60, 70, and 80 MPa and different target plastic viscosity were prepared with a paste to solids ratio (p/s by volume) in the range 0.72-0.79 and subjected to the slump flow, J-ring, L-box and V-funnel tests in the fresh state to ensure that they met the flow and passing ability criteria without segregation. These mixes are identified below with letter C. Mixes of the same grades but with smaller p/s were simultaneously investigated by two other PhD students (Abo Dhaheer, 2016; Alyhya, 2016). Their mixes are identified with letters A and B. Standard cubes (100

mm) were then cast, cured in water and tested for compressive strength at 7, 28 and 90 days of age. The amounts and details of the ingredients used in the test mixes are given in Tables 5.1 and 5.2. These were chosen using the design charts and the procedure described in Chapter 4. Locally available type II cement (cement II /B-V 32.5 R according to BS EN197-1 (2011) and ground granulated blast furnace slag (ggbs) with a specific gravity of 2.95 and 2.40, respectively were used. The super-plasticizer used was a polycarboxylic ether-based type with specific gravity of 1.07. Crushed limestone coarse aggregate with a maximum size of 20 mm and a specific gravity of 2.80 was used, while the fine aggregate was river sand having a specific gravity of 2.65. Limestone powder as filler with maximum particle size of 125 μm was used (specific gravity 2.40). A part of the river sand was replaced by an equivalent volume of the coarser fraction of limestone filler in the size range 125 μm - 2 mm.

Table 5. 1 Mix proportions of test SCC mixes, kg/m³

Mix designation	<i>cm</i> ^a		water	<i>SP</i> ^b	<i>w/cm</i>	<i>SP/cm</i>	<i>LP</i> ^c	<i>FA</i> ^d		<i>CA</i> ^e
	cement	<i>ggbs</i>						<i>FA</i> ^{**}	<i>FA</i> ^{***}	
30C*	240	80	201.6	2.3	0.63	0.72	194	291	504	756
40C	262.5	87.5	199.5	2.5	0.57	0.71	194	291	479	756
50C(50C)	281.2	93.8	198.8	2.8	0.53	0.75	186	279(0)	478(786)	756
60C	315	105	197.5	2.8	0.47	0.67	172	258	477	756
70C	345	115	184	[3.3]3.0	0.40	0.72	170	255	478	756
80C	367.5	122.5	171.5	[3.9]3.5	0.35	0.80	172	258	478	756

* The use of the designation C was explained above.

a: cementitious materials.

b: super-plasticizer. Figures in square brackets refer to increase in SP needed for satisfying passing ability.

c: limestone powder <125 μm .

d: fine aggregate < 2 mm (Note: a part of the fine aggregate is the coarser fraction of

the limestone powder, FA **125 μm –2mm, whereas FA *** refers to natural river sand < 2 mm).

e: coarse aggregate <20 mm.

Table 5. 2 Further details of test SCC mixes

Mix designation	Target plastic viscosity, Pa s	Actual plastic viscosity, Pa s	Paste vol. fraction	Solid vol. fraction	Paste/solid (by vol.)
30C	5.5	5.24	0.42	0.58	0.72
40C	7.5	7.44	0.43	0.57	0.75
50C(50C)	8.5(8.5)	8.52(8.52)	0.43	0.57	0.75
60C	9.5	9.00	0.44	0.56	0.79
70C	10.5	10.22	0.44	0.56	0.79
80C	11.5	11.52	0.44	0.56	0.79

As mentioned above, a part of the river sand was replaced by an equivalent volume of the coarser fraction of limestone filler in the size range 125 μm - 2 mm. However, tests were also done on a mix of strength 50 MPa (shown in parenthesis in Tables 5.1 and 5.2) in which no replacement of the river sand fine aggregate was made in order to check whether this replacement made any difference to the flow characteristics of the SCC mix in the fresh state or its compressive strength in the hardened state.

5.3 Mix procedure

The SCC mixes were prepared in a small planetary mixer by mixing the coarsest constituent (coarse aggregate up to 20 mm) and the fine one (ggbs), followed by the next coarsest (fine aggregate) and next finest constituent (limestone powder), and so on. Before each addition, the constituents were mixed for two minutes. To fluidize the dry mix, two-thirds of the super-plasticiser (*SP*) was added to the water. One-half of this water-(*SP*) mixture was added to the dry constituents and was mixed for two minutes. One-half of the remaining water-(*SP*) mixture was then added and was mixed

for two minutes. This process was continued until all water-(*SP*) was added. The remaining one-third of the (*SP*) was added and was mixed for two minutes just before transferring the SCC mix into the slump cone. The horizontal spread up to 500 mm was timed. If any segregation or bleeding was visible, the (*SP*) dosage was judiciously altered. This trial process was continued until the mix met the flow-ability criterion (BS EN 206-9, 2010) and was homogeneous with no visible segregation or bleeding. In this manner, all self-compacting mixes of different strength concrete mixes were developed.

5.4 Tests on fresh SCC

5.4.1 Flow-ability

Tests were conducted to determine the t_{500} and $t_{v\text{-funnel}}$ times of the fresh mixes. These are summarized in Table 5.3. The time taken by the fresh SCC mix to reach a 500 mm diameter spread in the slump cone flow t_{500} was determined from time sequencing a video recording of the test with an accuracy of a thousand of a second, while the time taken by the fresh SCC mix to flow out of the v-funnel (daylight appearing when viewed from above) was recorded as $t_{v\text{-funnel}}$ flow time (Figure 5.1). Within the chosen flow spread range of 650–750 mm, the t_{500} and $t_{v\text{-funnel}}$ varied between 0.81–2.09 s and 2.76–7.44 s, respectively. Figures 5.2-5.5 show the horizontal spread of different SCC mixes. All tested self-compacting mixes showed no signs of segregation or bleeding on thorough visual inspection.

Table 5. 3 Flow-ability test results, t_{500} and $t_{v-funnel}$ of SCC mixes

Mix designation	Slump flow test		V-funnel test
	Spread, mm	t_{500} , s	$t_{v-funnel}$, s
30C	655	0.81	2.76
40C	650	0.84	3.30
50C(50C)	750(740)	1.31(1.24)	4.04(3.90)
60C	655	1.40	4.04
70C	680	1.92	6.30
80C	670	2.09	7.44

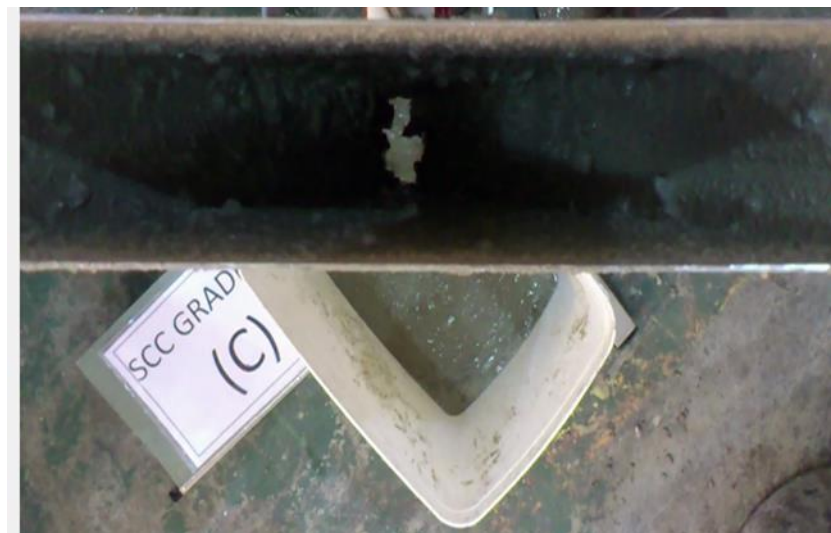
**Figure 5. 1 Recording V-funnel time (daylight appearing when viewed from above)**



Figure 5. 2 Horizontal spread of SCC mix: 30C (Left), 40C (Right)



Figure 5. 3 Horizontal spread of SCC mix: 70C (Left), 80C (Right)



Figure 5. 4 Horizontal spread of SCC mix: 70C (Left), 80C (Right)



Figure 5. 5 Horizontal spread of SCC mix (50C)

A comparison of the flow tests on 50 MPa mix in which a part of the river sand fine aggregate was replaced by the coarser fraction of limestone filler with the same grade mix but without the replacement (shown in parenthesis in Table 5.3) shows that the flow characteristics of the mixes are not significantly affected by this replacement. This is consistent with the small differences in the particle size distributions of the coarser fraction of limestone filler and river sand (Figure 5.6). Moreover, as the volume fractions (not the masses) of the fine aggregate (with or without replacement)

in the mixes are the same (Tables 5.1 and 5.2), their plastic viscosity will be the same (see Eq. 4.7 [Chapter 4]).

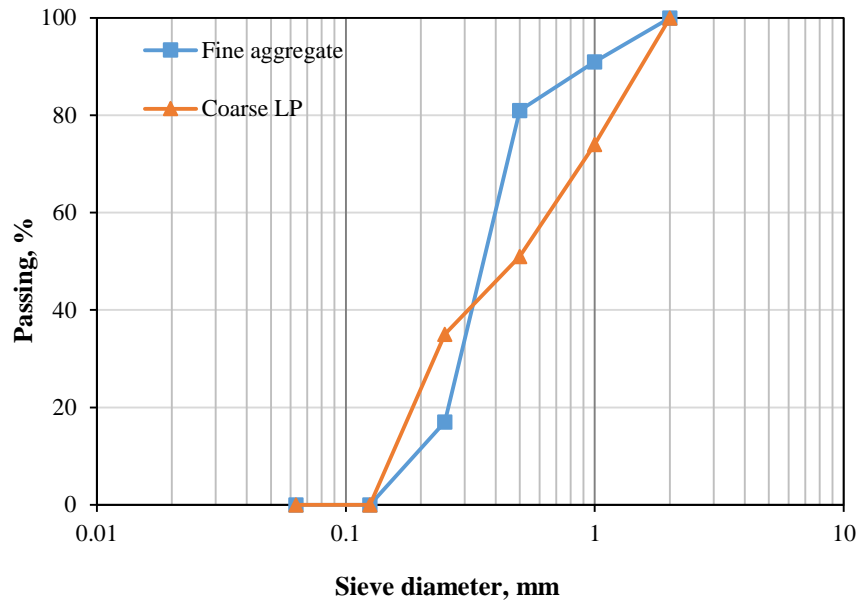


Figure 5. 6 Particle size distribution curves for coarser fraction of limestone filler and fine aggregate

Figure 5.7 shows a plot of the flow time of all mixes and the corresponding water to powder (i.e. cement + *ggbfs* + limestone powder < 125 μm) ratio (w/p). It is seen that a larger t_{500} requires a higher powder or lower water content. The w/p ratio has a considerable influence on both the fresh and hardened properties of SCC, with often its influence on the fresh properties limiting the selection of its value (Domone, 2006). It has been reported that a decrease in the water content and an increase in the amount of fine particles can increase cohesion and viscosity of the mix (Felekoğlu et al., 2007), resulting in a good distribution of the solid particles throughout the casting of SCC. However, mixes with low water content require relatively high dosages of superplasticizer, especially at low cm contents, to achieve the accepted requirements of SCC deformability (Khayat et al., 1999b).

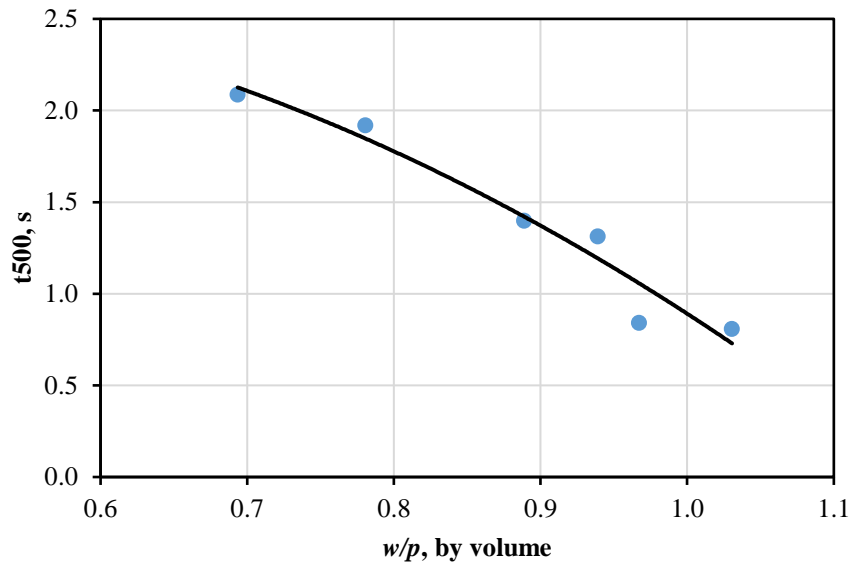


Figure 5. 7 Relationship between flow time (t_{500}) and water to powder ratio

The time needed to reach 500 mm diameter spread is related to the plastic viscosity of the mix. This is clearly seen in Figure 5.8 for a given target flow spread. Regarding the plastic viscosity, it is worth mentioning that it is very difficult if not impossible to measure it accurately. It is well known (Banfill et al., 2000; Feys et al., 2007; Wallevik and Wallevik, 2011) that for one and the same mix, different types of rheometer give different values of Bingham parameters (plastic viscosity and yield stress). Therefore, the micromechanical procedure proposed by Ghanbari and Karihaloo (2009) which calculates the plastic viscosity of an SCC mix from the known plastic viscosity of the paste (which can be accurately measured with a viscometer) has been recommended and used in this Chapter. This was already explained in Chapter 4 and indeed forms the basis of the proposed mix proportioning method

It should also be mentioned that the yield stress is well correlated with the slump flow spread (Fowler et al., 2007; Wallevik, 2003). That is why we have determined the target flow spread of our mixes within the range of 700 ± 50 mm. It is implied that these mixes have nearly the same yield stress and thus make the plastic viscosity as the controlling parameter which we have correlated with t_{500} in Figure 5.8. The following statement from Fowler et al. (2007) supports this implicit assumption “the plastic viscosity is often the main factor distinguishing the workability of one mix from another. Changes in plastic viscosity can directly reflect changes in materials or

mixture proportions, making the t_{500} measurement particularly valuable for quality control”. Of course, a different choice of target flow spread, say from the EFNARC guidelines (2005) will necessarily require different t_{500} .

The plastic viscosity has been plotted against $t_{v-funnel}$ and flow spread in Figure 5.9. It can be seen that the $t_{v-funnel}$ of mixes having the flow spread in the range of 650–750 mm increases with an increase in the mix plastic viscosity, despite an increase in the SP dosage. In other words, the flow time is dominated by the plastic viscosity rather than the super-plasticizer dosage. This has also been observed by Nepomuceno et al. (2014) and Takada and Tangtermsirikul (2000).

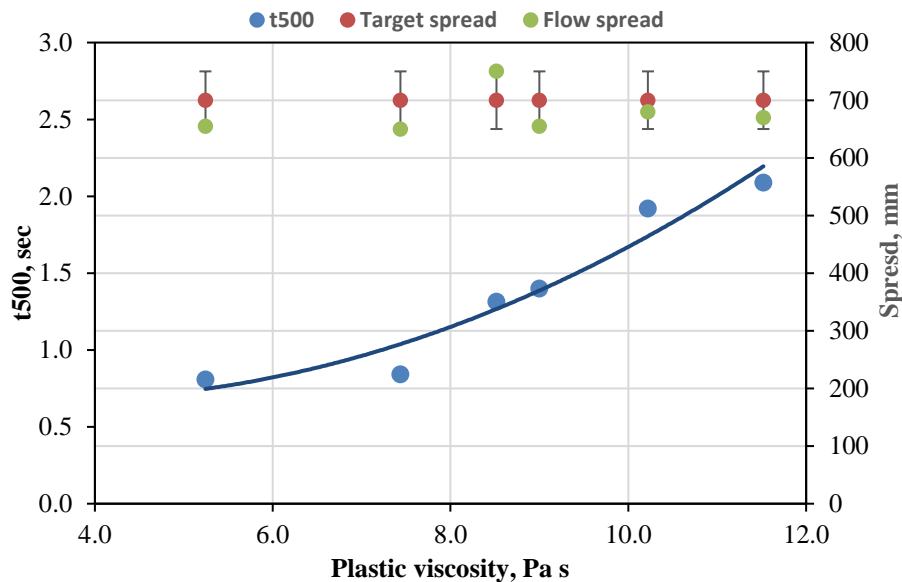


Figure 5. 8 Relationship between plastic viscosity and t500 for target flow spread $700 \pm 50\text{mm}$

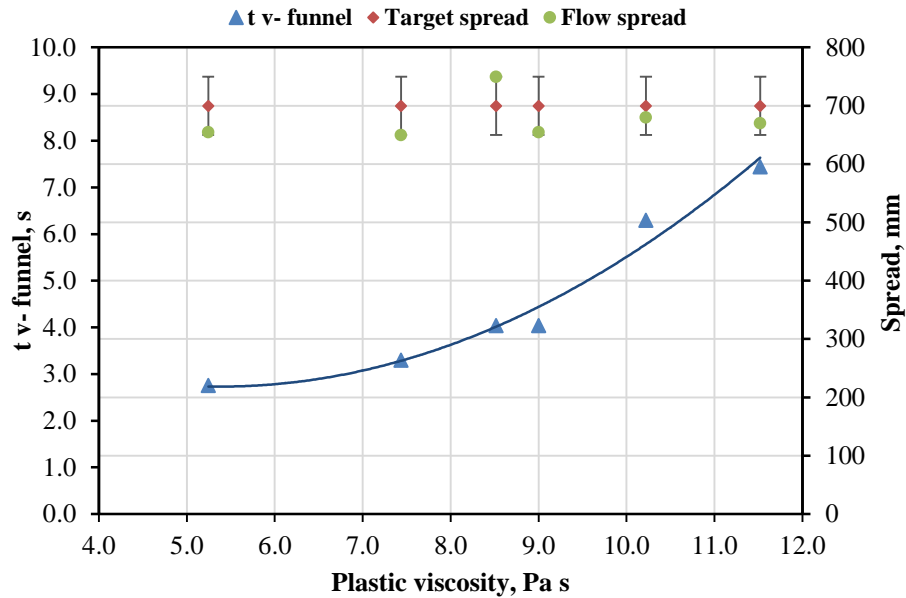


Figure 5.9 Relationship between plastic viscosity and tv–funnel time with a target flow spread ($700 \pm 50\text{mm}$)

5.4.2 Passing and filling ability

All the above test mixes that satisfied the flow-ability criterion and showed no signs of segregation were subjected to the passing and filling ability test using the J–ring and L–box to ensure that they were able to pass through the narrow gaps that exist between reinforcing bars in real reinforced concrete structural elements. For this purpose, a 300mm diameter J–ring apparatus with 10 steel rods (each of diameter 16 mm and 100 mm height) was used, as recommended by EFNARC (2005). The results are presented in Table 5.4. There were some mixes (especially those with a low flow spread, i.e. low dosage of *SP*) that had passed the flow–ability test but did not meet the passing ability criterion. In such instances, the *SP* dosage had to be increased (shown in square brackets in Table 5.1). The results indicated that (after the increase in *SP*) all mixes met the passing ability criterion and showed no blockage or signs of segregation (Figures 5.10 - 5.13). Again, the influence of the replacement of some river sand fine aggregate by the coarser fraction of limestone filler on the flow characteristics was minimal, as can be judged by comparing the entries for 50 MPa mixes within and without the parenthesis in Table 5.4. Figure 5.14 shows that t_{500j} time correlate well with the plastic viscosity for all the mixes.

Table 5. 4 Passing ability test results, J-ring and L-box

Mix designation	J-ring flow test		L-box test		
	Spread, mm	t_{500j} , s	t_{200} , s	t_{400} , s	H_2/H_1
30C	650	0.74	0.53	1.10	0.92
40C	635	0.88	0.67	1.40	0.89
50C(50C)	730(740)	1.48(1.36)	0.63(0.70)	1.33(1.30)	0.91(0.89)
60C	630	1.60	0.81	1.65	0.87
70C	680	2.39	1.15	2.46	0.92
80C	655	2.80	1.45	3.07	0.91



Figure 5. 10 Flow and passing ability of SCC mix: 30C (Left), 40C (Right)

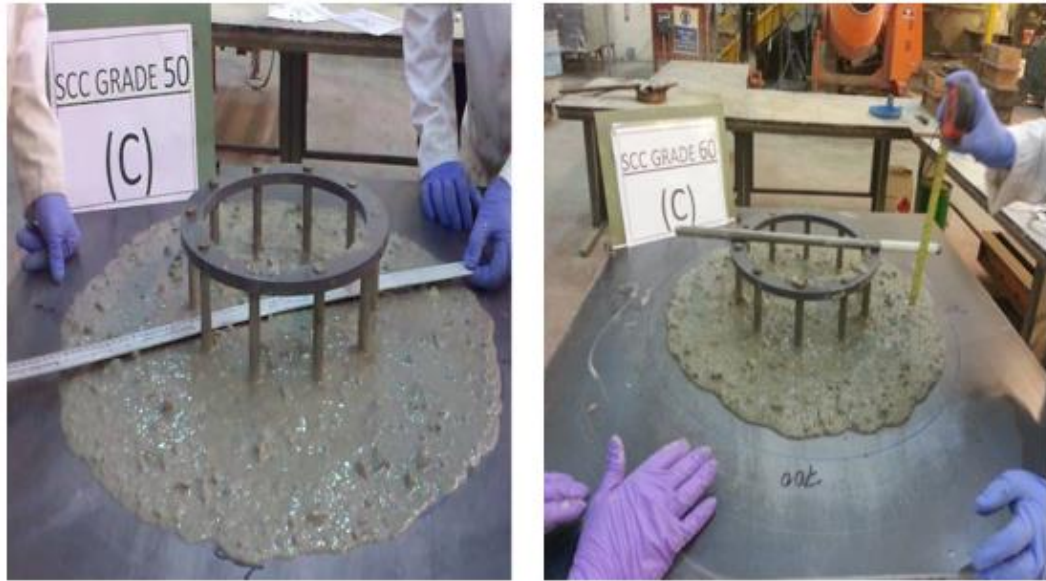


Figure 5. 11 Flow and passing ability of SCC mix: 50C (Left), 60C (Right)



Figure 5. 12 Flow and passing ability of SCC mix: 70C (Left), 80C (Right)



Figure 5.13 Flow and passing ability of SCC mix (50C)

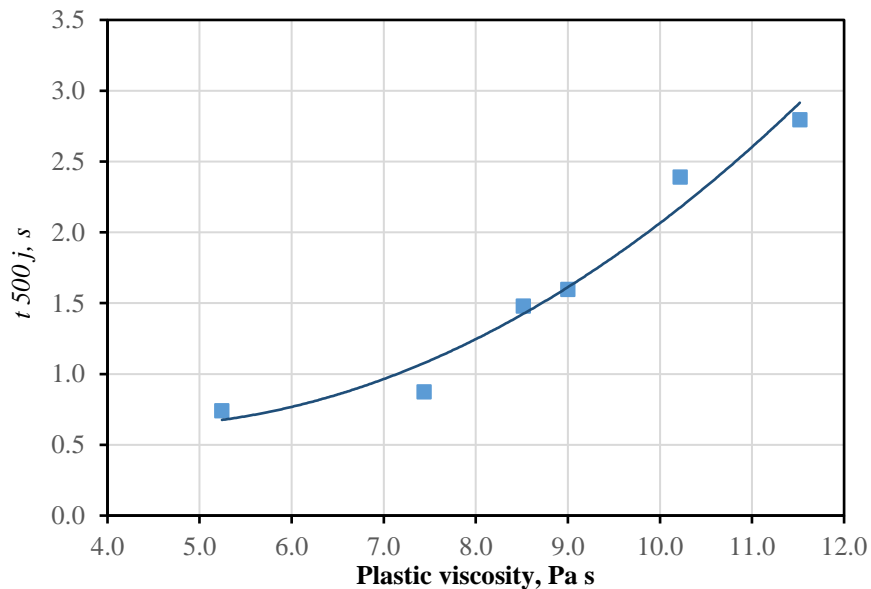


Figure 5.14 t_{500J} time versus plastic viscosity

The relationship between the parameters t_{500} of J-ring and slump flow of SCC was also taken into consideration in this study. The best-fit curve of t_{500} against the plastic viscosity is plotted alongside t_{500J} in Figure 5.15. It was found that the difference between these times is more pronounced for the higher plastic viscosities (9-12 Pa s) than the lower ones. A possible explanation for this increase is that the mixes become sticky taking more time to pass through the obstacles of the J-ring.

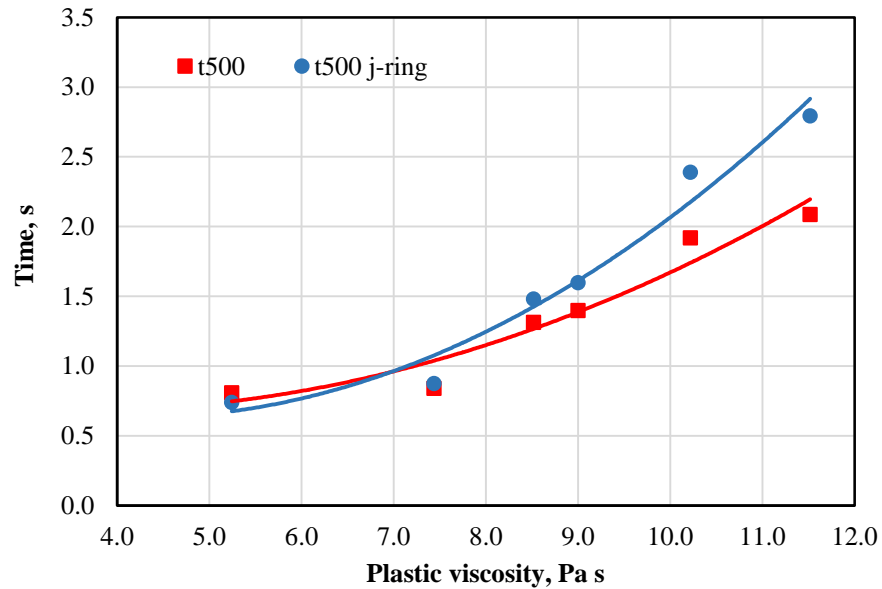


Figure 5. 15 Plastic viscosity versus t500 and t500J

According to the ASTM C 1621/ C 1621M (2008), the J-ring test can be used in combination with the slump flow test to assess the passing ability of SCC. If the difference between spread diameters ($D_{flow} - D_{J-ring}$) of the two tests is less than 25 mm then there is no visible blockage. If it is between 25 and 50 mm then there is minimal to noticeable blockage. Table 5.5 shows the difference from which it is clear that for all mixes there is minimal or no blockage.

Table 5. 5 Difference between flow and J-ring spread diameter

Mix designation	D_{flow} , mm	D_{J-ring} , mm	$D_{flow} - D_{J-ring}$, mm
30C	655	650	5
40C	650	635	15
50C(50C)	750(740)	730(740)	20(0)
60C	655	630	25
70C	680	680	0
80C	670	655	15

In order to test the ability of an SCC mix to fill the formwork containing reinforcement under its own weight, the L-box apparatus with two adjustable steel rods (each of

diameter 12mm) was used (BS EN 206-9 2010; EFNARC 2005). The times for the mix to reach 200 mm (t_{200}) and 400 mm (t_{400}) from the vertical leg as well as the blockage ratio (H_2/H_1) were recorded. All mixes that had passed the J-ring test also passed the L-box test without any alteration in SP or mix ingredients (Figures 5.16 and 5.19). Figure 5.20 shows that t_{200} and t_{400} times correlate well with the plastic viscosity for all the mixes. The results also showed that no large aggregate particles had segregated or been blocked by the rods. Also, it can be seen (Table 5.4) that the mixes exhibited a blockage ratio (BR) of more than 0.80, which reflects good filling ability.

Therefore, from the flow and passing ability perspectives, all the test SCC mixes satisfied the required criteria for viscosity class 1 to qualify them as SCC in accordance with BS-EN 206-9 (2010).



Figure 5. 16 Passing and filling of SCC mix: 30C (Left), 40C (Right)



Figure 5. 17 Passing and filling of SCC mix: 50C (Left), 60C (Right)



Figure 5. 18 Passing and filling of SCC mix: 70C (Left), 80C (Right)



Figure 5. 19 Passing and filling of SCC mix (50C)

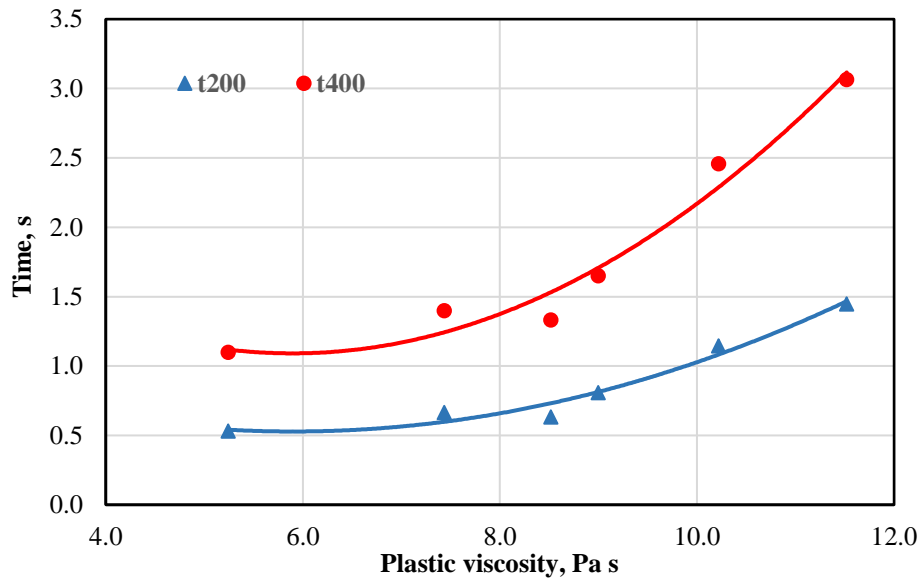


Figure 5. 20 t200 and t400 times in L-box versus plastic viscosity

5.5 Testing of hardened SCC

The accuracy of the proposed design method has been validated through compressive strength tests performed on 100mm cube specimens (three per mix and age), cured in water at ambient temperature. The results are presented in Table 5.6 and Figure 5.21. The test was carried out at 7, 28 and 90 days of age. The results confirm the well-known trends against the w/cm ratio and confirmed the reliability of the proposed mix-design approach. The effect of the replacement of a part of the river sand fine aggregate

by the coarser fraction of limestone powder is minimal also in the hardened state, as can be judged by the entries in the parenthesis in Table 5.6.

Table 5. 6 Cube compressive strength test results for SCC mixes

Mix designation	Compressive strength, MPa		
	7 days	28 days	90 days
30C	22.1	36.1	43.4
40C	31.6	45.2	56.4
50C(50C)	37.2	55.6(53.7)	64.0
60C	44.2	69.1	83.7
70C	47.5	78.6	87.9
80C	60.8	84.2	90.5

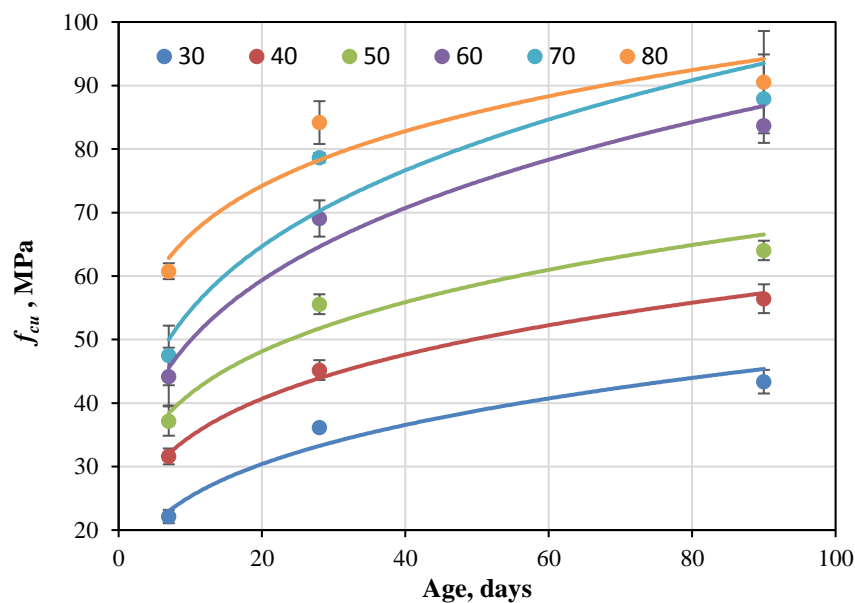


Figure 5. 21 Gain of compressive strength of mixes C with age

5.6 Concluding remarks

The method of proportioning proposed in Chapter 4 is simple and leads to mix proportions that indeed are self-compacting concrete. This is validated by tests on a series of mixes differing by the paste to solids volumetric ratios. These mixes were prepared in the laboratory and found to meet the necessary self-compacting criteria

and the target plastic viscosity and compressive strength. It may however be necessary to increase the *SP* content in order to meet the passing and filling ability tests, but the content will still be in the range 0.4-0.8% of the mass of cementitious materials, as assumed in the design procedure in Chapter 4. It is worth emphasizing that the plastic viscosity of the paste remains practically unaltered in this range; the *SP* content mostly affects the yield stress of the paste.

The coarser fraction of limestone filler ($125\mu\text{m} - 2\text{mm}$) can be used to replace an equivalent volume of river sand fine aggregate. Tests have showed that this replacement makes practically no difference to the properties of SCC in fresh and hardened tests. Such a replacement is environmentally friendly and economic, thus enhancing the sustainability of the SCC mixes.

The proposed mix proportioning method reduces considerably the extent of laboratory work, the testing time and the materials used.

Chapter 6

Influence of mix composition and strength on the fracture properties of self-compacting concrete

6.1 Introduction

Specific fracture energy and the stress-crack relationship of a concrete mix are the most important parameters describing its fracture behaviour. They form a basis for the evaluation of the load carrying capacity of cracked concrete structures (Karihaloo, 1995; Bažant and Plannas, 1998). According to RILEM recommendations (1985), the specific fracture energy (or toughness) can be obtained by the work-of-fracture method requiring tests on notched three-point bend specimens of different sizes and notch to depth ratios.

It is however widely recognised (Abdalla and Karihaloo, 2003; Bažant, 1996; Bažant and Kazemi, 1991; Carpinteri and Chiaia, 1996; Hu and Wittmann, 1992; Mindess, 1984; Nallathambi et al., 1985), that the specific fracture energy of concrete obtained using the RILEM method is dependent on the size of the test specimen and the notch to depth ratio. To eliminate this size dependency, Guinea and co-workers (Guinea et al., 1992; Planas et al., 1992; Guinea et al., 1994), and Hu and Wittmann (2000) proposed methods to correct the measured size-dependent specific fracture energy (G_F) in order to obtain a size-independent value (G_F). The methodology proposed by Guinea and co-workers involves adding the non-measured work-of-fracture due to the curtailment of the tail of the load-central deflection (P - δ) curve recorded in the three-point bend test. On the other hand, the methodology of Hu and Wittmann (2000) is based on the observation that the local specific energy along the initially un-cracked specimen ligament varies during the crack propagation, the variation becoming more pronounced as the crack approaches the stress-free back face of the specimen, the so-called free boundary effect.

Abdalla and Karihaloo (2003) and Karihaloo et al. (2003) simplified the free boundary effect formalism of Hu and Wittmann (2000). They proposed and validated extensively a simplified method by which the size-independent fracture energy can be determined by testing only geometrically identical specimens of the same size, half of which contain a shallow starter notch (notch to depth ratio = 0.1), while the other half contain a deep notch (notch to depth ratio = 0.6). Their method significantly reduces the number of specimens to be tested and eliminates the need for using the least squares

method to solve an overdetermined system of simultaneous equations, as required in the Hu and Wittmann (2000) method.

Besides the size-independent fracture energy (G_F), the analysis of cracked concrete structures using the non-linear fictitious crack model (Hillerborg et al., 1976) requires the stress-crack relationship $\sigma(w)$ of the concrete mix relating the residual stress transfer capability σ to the opening displacement w of the fictitious crack faces. As the determination of the tension softening diagram using the direct tension test is not a simple task (Karihaloo, 1995), it is often approximated by a bilinear relationship whose parameters are determined in an inverse manner by matching the experimental load-displacement curve of a notched three-point bend beam. For this an analytical model based on the concept of a non-linear hinge was proposed by Ulfkjaer et al. (1995), and further developed by Stang and Olesen (1998) and Olesen (2001). In this model, the flexural response of a notched beam is obtained by allowing the fictitious crack to develop from the pre-existing notch in the central region of the beam where the bending moment is the largest. The width of this region, proportional to the beam depth, fixes the width of the non-linear hinge. Outside of this region, the material is assumed to behave in a linear elastic manner. Abdalla and Karihaloo (2004), and Murthy et al. (2013a) showed how the non-linear hinge model can be adapted to construct the bilinear tension softening diagram of a concrete mix corresponding to its size-independent specific fracture energy.

The fracture behaviour of concrete is significantly influenced by the properties of the interfacial transition zone (ITZ) (Akçaoğlu et al., 2004), which in turn are governed by the mix ingredients in vibrated concrete (VC) and self-compacting concrete (SCC), as well. In comparison with VC, as we have in Chapters 4 and 5 SCC requires relatively high amounts of fine particles and paste, but low coarse aggregate content (Okamura and Ouchi, 2003; Okamura et al., 2000; Edamatsu and Nishida, 1998 and Su et al., 2001). Although SCC has passed from the research phase into real application, the differences in its composition from VC raise concerns about its fracture behaviour (Beygi et al., 2014a; Domone, 2006). The concern is primarily because a lower coarse aggregate content in an SCC mix relative to a VC mix of the same grade is likely to reduce its energy absorption capacity and thus its ductility. This needs to be addressed.

Previous work (Beygi et al., 2014b; Beygi et al., 2014c; Nikbin et al., 2014c; Beygi et al., 2013b; Cifuentes and Karihaloo, 2013; Rozière et al., 2007) on this topic was based on the size-dependent specific fracture energy, apart from the work of Cifuentes and Karihaloo (2013) who used the model of Hu and Wittmann (2000) and its simplified version proposed by Karihaloo et al. (2003).

It is the aim of the present Chapter to investigate in detail the role of several composition parameters of SCC mixes in their fracture behaviour. In particular, the influence of coarse aggregate volume, paste to solids (p/s) and water to binder (w/cm) ratios on the size-independent fracture energy (G_F) will be studied using the simplified boundary effect approach (SBE) suggested by Abdalla and Karihaloo (2003) and validated by Karihaloo et al. (2003). The corresponding bilinear approximation of the tension softening diagram will then be obtained using the procedure based on the non-linear hinge model proposed by Abdalla and Karihaloo (2004), and Murthy et al. (2013a). In view of the many variables involved, the author joined forces with two other PhD students (Abo Dhaheer, 2016; Alyhya, 2016) to perform a detailed investigation covering all variables in the limited time available.

This chapter has been published in the journal ‘Construction and Building Materials’ (see publication 6 in the list in Chapter 1).

6.2 Theoretical background

The specific fracture energy (G_f), as defined by RILEM technical committee, is the average energy given by dividing the total work of fracture by the projected fracture area (i.e. cross-section of initially un-cracked ligament) based on the load-displacement P - δ curve. Hence, for a specimen of depth W , thickness B and initial notch depth a (as schematically shown later in Figure 6.5) the specific fracture energy (G_f) can be expressed as:

$$G_f = \frac{1}{(W-a)B} \int P d\delta \quad (6.1)$$

If a fictitious crack (Hillerborg, 1983; Hillerborg, 1985) is used to model the concrete fracture, the energy dissipation for crack propagation can be completely characterised

by a cohesive stress – separation curve $\sigma(w)$. The area under this curve is the specific fracture energy, G_F

$$G_F = \int_0^{w_c} \sigma(w) dw \quad (6.2)$$

where w_c is the critical crack opening.

The fracture process zone (FPZ) around the propagating crack can be considered as consisting of two regions, an inner softening zone w_{sf} , and an outer micro-fracture zone, w_f as shown in Figure 6.1 (Karihaloo, 1995; Hu, 1995). The inner softening zone w_{sf} contains interconnected cracks along the aggregate and mortar interfaces. The main open crack plus a few large crack branches along the interfaces can be formed within the softening zone. The formation and complete separation of the softening zone controls the $\sigma(w)$ relationship. The outer microfracture zone contains isolated micro-cracks that are not interconnected. These do not contribute to the concrete softening but to its non-linear response before the peak load. The fracture energy consumed in the outer micro-fracture zone is small, and equations (6.1) and (6.2) should in principle determine the same specific fracture energy.

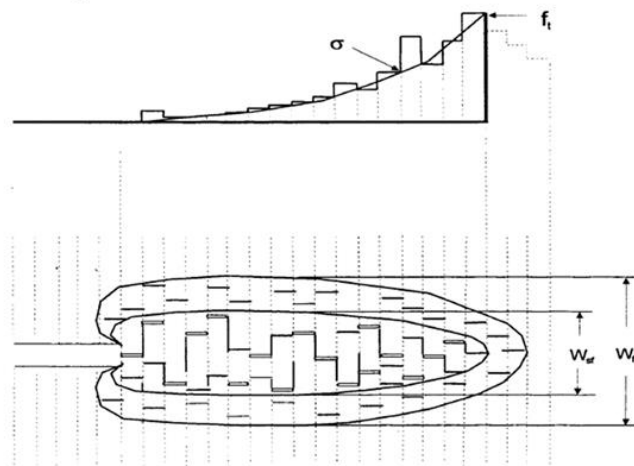


Figure 6. 1 The FPZ and discrete bridging stresses. The FPZ is divided into the inner softening zone and the outer microfracture zone. w_c is related to the width of the inner softening zone w_{sf} (After: Hu, 1995)

During crack propagation the inner and the outer zone widths may vary substantially, depending on the crack tip stress field. Clearly, the critical crack opening w_c is restricted by the inner and the outer zone widths. This restriction becomes more obvious when a FPZ approaches the free boundary of a specimen. Therefore, a smaller w_c and a smaller fracture energy are calculated if Equation (6.2) is used. These variations in w_{sf} , w_f and w_c lead to the conclusion that the fracture energy G_F defined by Equation (6.2) can be dependent on the location of FPZ in relation to the free boundary of the specimen. To distinguish the fracture energy G_F defined by the two equations, (Duan et al., 2003) use symbol g_f for the local fracture energy defined by Equation (6.2).

(Hu and Wittmann, 1992; Hu, 1995) have made the following assumptions:

$$w_{sf}(x) \propto w_f(x)$$

$$w_c(x) \propto w_{sf}(x) \tag{6.3}$$

$$g_f(x) \propto w_c(x)$$

where x denotes a position along a fracture ligament in the FPZ and $g(x)$ represents the local fracture energy. The fracture energy defined by Equation (6.1), which may be size- or ligament-dependent, is denoted by $G_f(\alpha)$, to distinguish it from the size-independent G_F , with $\alpha = a/w$.

The specific fracture energy (G_f) can also be determined using a local energy g_f concept described by Duan et al. (2003, 2007) as follows

$$G_f\left(\frac{a}{W}\right) = \frac{1}{W-a} \int_0^{W-a} g_f(x) dx \tag{6.4}$$

Differentiating Equation (6.4) with respect to the crack length a gives the local fracture energy $g_f(x)$ at the crack tip:

$$g_f(x) = G_f(\alpha) - (W - a) \frac{dG_f(\alpha)}{d\alpha} \tag{6.5}$$

Equations (6.4) and (6.5) above imply that $G_f(\alpha) = \text{constant}$, if $g_f(x) = \text{constant}$. If $g_f(x) \neq \text{constant}$ then $G_f(\alpha) \neq \text{constant}$, i.e. size or ligament effects are observed. Figure (6.2) shows schematically that if $g_f(x)$ decreases when approaching the boundary of the specimen at later stages of fracture, $G_f(x)$ is indeed dependent on the ligament or initial crack length.

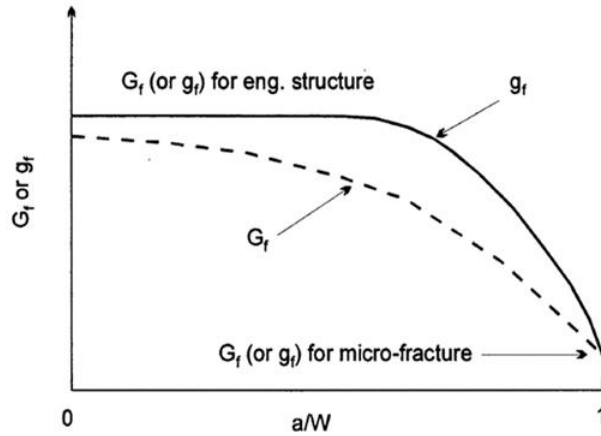


Figure 6. 2 If g_f decreases monotonically along the ligament, G_f has to be dependent on the a/W ratio, as observed in many experiments (After: Hu and Wittmann, 1992)

Hu and Wittman (2000) proposed a bilinear approximation for the local fracture energy variation (g_f) along the crack path (Figure 6.3) with the intersection of the two asymptotes defining a transition ligament size (a_l). The latter, unlike the asymptotic value of specific fracture energy (G_F), varies with the material properties and specimen geometry.

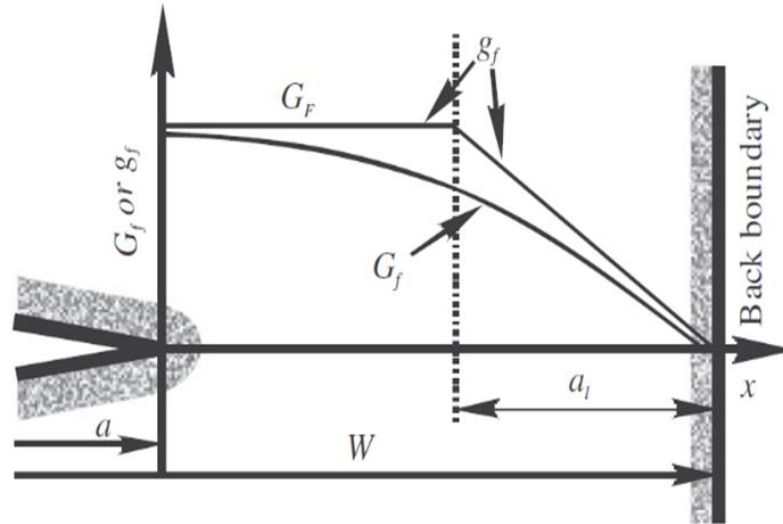


Figure 6. 3 Bilinear local fracture energy $G_f \left(\frac{a}{W} \right)$ variation along the un-notched ligament of a notched specimen (After: Duan et al., 2001)

A relation between the measured size-dependent fracture energy (G_f), the transition length (a_l) and the size-independent fracture energy (G_F) can be obtained by substituting the bilinear approximation for the local fracture energy variation (Figure 6.3) into Equation (6.4)

For a specimen with a ligament size ($W - a$) larger than the transition ligament size a_l , $g_f(x)$ is given by Hu and Wittmann(2000).

$$G_f \left(\frac{a}{W} \right) = \begin{cases} G_F & x < W - a - a_l \\ G_F \left[1 - \frac{x - (W - a - a_l)}{a_l} \right] & x \geq W - a - a_l \end{cases} \quad (6.6)$$

If ($W - a$) is smaller than the ligament transition length a_l , the first function in equation (6.6) disappears. Substituting equation (6.6) into equation (6.4) and introducing the a/W ratio, G_F is obtained

$$G_f \left(\frac{a}{W} \right) = \begin{cases} G_F \left[1 - \frac{\frac{a_l}{W}}{2(1 - \frac{a}{W})} \right] & 1 - \frac{a}{W} > \frac{a_l}{W} \\ G_F \left[\frac{(1 - \frac{a}{W})}{2 \frac{a_l}{W}} \right] & 1 - \frac{a}{W} \leq \frac{a_l}{W} \end{cases} \quad (6.7)$$

The values of G_F and a_l of a concrete mix are obtained once the mean size-dependent specific fracture energy (G_f) of the mix has been measured on specimens of identical

sizes, half of which have a shallow starter notch ($a/W = 0.1$), while the other half have a deep starter notch ($a/W = 0.6$) by the RILEM work-of-fracture method using Equation (6.1). Hu and Duan (2004) showed that although the measured values of G_f depend on W and a/W , the above procedure indeed leads to a G_F value that is essentially independent of the specimen size and relative notch depth.

In recent works, a trilinear approximation of the local fracture energy along the unbroken ligament was proposed by Muralidhara et al. (2010, 2011), and Karihaloo et al. (2013). As has been evidenced by acoustic emission data, the trilinear approximation is closer to how the local fracture energy varies as the crack grows from a notched specimen (Muralidhara, 2010). The local fracture energy (G_f) first rises from the fictitious boundary (notch tip), then remains nearly constant G_F , before reducing again as the crack approaches both the stress-free back face boundary, Figure 6.4.

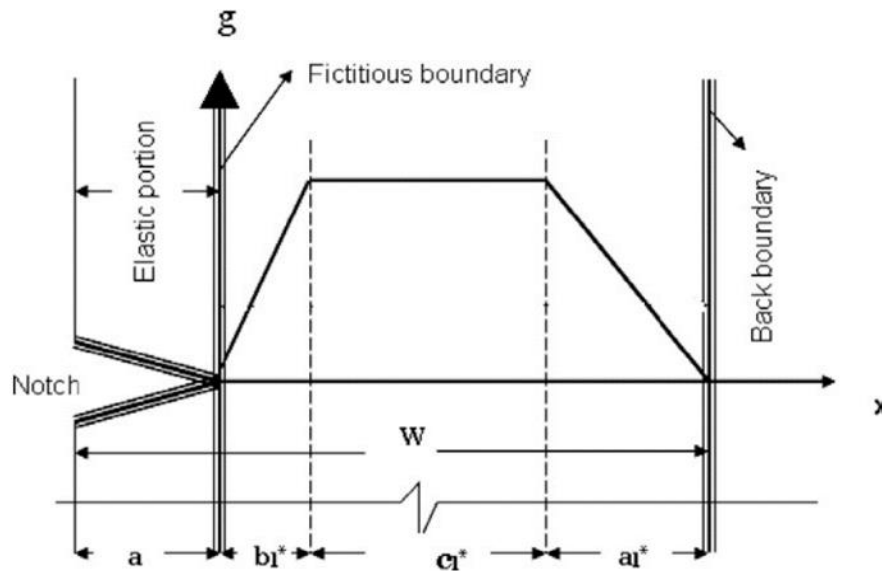


Figure 6. 4 Trilinear approximation of local fracture energy g_f variation over the un-notched ligament length (After: Muralidhara et al., 2011)

The G_f and G_F relationship for the trilinear approximation is given in Equation (6.8):

$$G_f \left(\frac{a}{W} \right) = \begin{cases} G_F \left[\frac{\frac{b_l^*}{W}}{2(1-\frac{a}{W})} \right] & 1 - \frac{a}{W} \leq \frac{b_l^*}{W} \\ G_F \left[1 - \frac{(\frac{a_l^*}{W} + \frac{b_l^*}{W})}{2(1-\frac{a}{W})} \right] & 1 - \frac{a}{W} \geq \frac{a_l^*}{W} \end{cases} \quad (6.8)$$

To obtain the values of G_F , a_l^* and b_l^* of a concrete mix, the G_f of specimens of identical sizes and a range (more than three) of the notch to depth ratios is first determined by the RILEM method. Then Equation (6.8) is applied to the mean values of G_f different notch to depth ratios. This gives an over-determined system of equations which is solved by a least squares method to obtain the best estimates of G_F , a_l^* and b_l^* . It should be noted that the trilinear method proposed by Karihaloo et al. (2013) cannot be applied in the present study because the specimens have been tested with two notch to depth ratios only, as required by the bilinear model of Karihaloo et al. (2003). It is however known (Murthy et al., 2013b) that the bilinear and trilinear approximations give nearly the same values of the size-independent specific fracture energy (G_F).

6.3 Experimental programme

6.3.1 Test geometry and specimens

The test geometry adopted for this study was the three point bend test (TPB) (Figure 6.5). The purpose of this test is to measure the amount of energy absorbed when the specimen is broken into halves, which is equivalent to the total work done (or work-of-fracture). This work is divided by the projected fracture area (the area of the ligament that was intact before the test began), and the resulting value is the specific fracture energy G_f of SCC beam specimens. This test was performed on three series of SCC mixes having 28-day nominal cube compressive strengths of 30, 60 and 80 MPa.

The TPB is loaded at mid-span by a concentrated load, and is simply supported over span S .

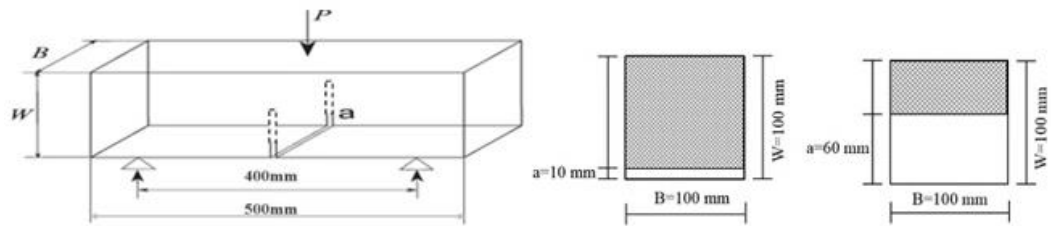


Figure 6. 5 Schematic representation of the three-point bending test

A notch of depth (a) is cut into the cured beam at mid-length. Two notch to depth ratios were selected, so that the notch to depth ratio can vary from the shallow (0.1) to the deep (0.6). The span to depth ratio, S/W was constant and equal to 4 and the beam width, B was kept fixed at 100 mm. The specimen weight can be neglected for the small specimens used in this study.

The hardened concrete beam specimens were demoulded 24 hours after mixing and placed in a water tank at $20 \pm 2 \text{ C}^\circ$ for curing. After 28 days of curing the specimens were removed from the curing tank for testing and notched with a diamond saw (blade thickness = 2mm) as shown in Figure 6.6 and 6.7.



Figure 6. 6 The hardened SCC shallow notched beams



Figure 6. 7 The hardened SCC deep-notched beams

The experimental set up required to test the notched beams is illustrated in Figures 6.8 and 6.9. 108-notched beams of the same depth (100 mm) with a constant span to depth ratio of 4 were tested in three point bending. The testing was carried out using Dartec closed-loop testing machine (capacity = 250 kN). The vertical displacement and the crack mouth opening displacement (CMOD) were measured via LVDT and clip gauge attached to knife edges on the test specimens (Figure 6.9).



Figure 6. 8 The TPB ready for testing

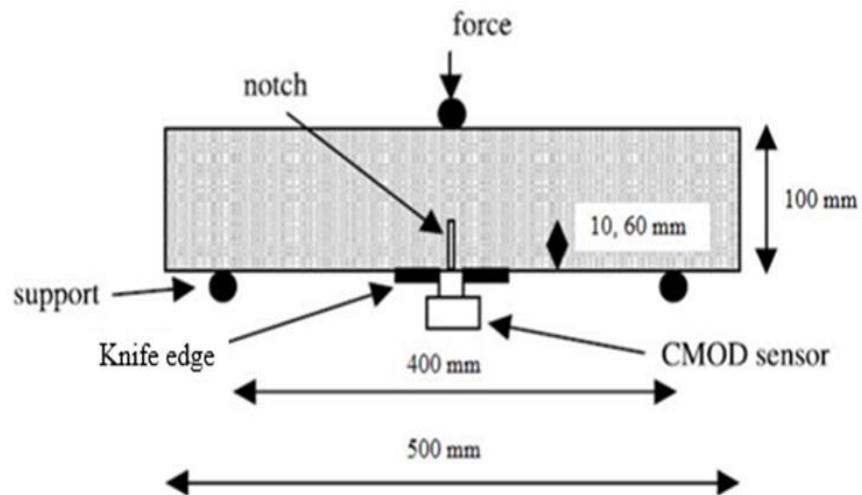


Figure 6. 9 Three point bend (TPB) test specimen

During the testing the load-displacement and load-CMOD curves were recorded by X-Y plotters, as shown in Figure 6.10 and the data were also recorded in a computer disk. The rate of loading was controlled by a crack mouth opening displacement (CMOD) control, and the beams were loaded at a very small CMOD rate (0.0002 mm/sec.), so that a stable crack growth could be achieved.

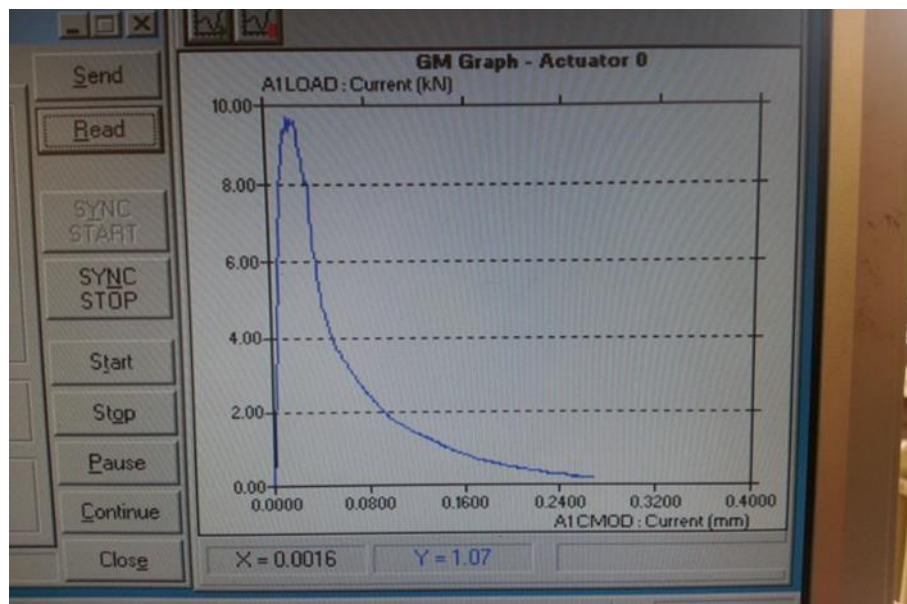


Figure 6. 10 Load- displacement curve on X-Y plotter (also recorded digitally)

6.3.2 Materials

Locally available type II cement (cement II /B-V 32.5 R according to BS EN197-1 (2011)) and ground granulated blast furnace slag (*ggbfs*) with a specific gravity of 2.95 and 2.40, respectively were used. The super-plasticizer used was a polycarboxylic ether-based type with specific gravity of 1.07. Crushed limestone coarse aggregate with a maximum size of 20 mm and a specific gravity of 2.80 was used, while the fine aggregate was river sand having a specific gravity of 2.65. Limestone powder as filler with maximum particle size of 125 μm was used (specific gravity 2.40). A part of the river sand was replaced by an equivalent volume of the coarser fraction of limestone filler in the size range 125 μm - 2 mm.

6.3.3 Mix design

Three series of SCC mixes were designed according to the mix design method and Abo Dhaheer et al. (2016a; 2016b) having 28-day nominal cube compressive strengths of 30, 60 and 80 MPa with *w/cm* ratios of 0.63, 0.47 and 0.35, respectively. Deeb et al. (2012) have also used the same method to design ultra-high strength SCC mixes based on the ultra-high strength vibrated mix CARDIFRC of Benson and Karihaloo (Benson and Karihaloo, 2005). The SCC mixes contained different volume fractions of coarse aggregate and paste to solid ratios. They are designated A, B and C for low, medium and high *p/s* ratios, respectively. In order to get a complete picture of the role of several composition parameters of SCC in their fracture behaviour, the SCC mixes (A) that was studied by Abo Dhaheer (2016), have been combined with the SCC mixes (B) that was studied by Alyhya (2016), and the SCC mixes (C) of the present work. The compositions of all mixes are given in Table 6.1. In order to ensure that all mixes met the flow and passing ability criteria without segregation (SCC requirements), slump flow, J-ring, L-box and V-funnel tests were conducted (Table 6.2) according to EFNARC guidelines (2005).

Table 6. 1 Mix proportions of test SCC mixes, kg/m³

Mix designation	<i>cm</i> ^a		<i>water</i>	<i>SP</i> ^b	<i>w/cm</i>	<i>SP/cm</i>	<i>LP</i> ^c	<i>FA</i> ^d		<i>CA</i> ^e	<i>p/s</i> by vol.
	<i>cement</i>	<i>ggbs</i>						<i>FA</i> ^{**}	<i>FA</i> ^{***}		
30A *	240	80	201.6	1.1	0.63	0.44	109	164	579	924	0.61
30B *	240	80	201.6	1.6	0.63	0.50	156	234	530	840	0.67
30C *	240	80	201.6	2.3	0.63	0.72	194	291	504	756	0.72
60A	315	105	197.5	2.0	0.47	0.48	94	141	536	924	0.69
60B	315	105	197.5	2.4	0.47	0.57	125	188	528	840	0.72
60C	315	105	197.5	2.8	0.47	0.67	172	258	477	756	0.79
80A	367.5	122.5	171.5	2.8	0.35	0.57	94	141	536	924	0.69
80B	367.5	122.5	171.5	3.0	0.35	0.61	125	188	529	840	0.72
80C	367.5	122.5	171.5	3.5	0.35	0.80	172	258	478	756	0.79

*A, B and C denote a decrease in coarse aggregate content and an increase in paste volume for the same strength grade.

a: cementitious material, i.e. binder.

b: super-plasticizer.

c: limestone powder < 125µm.

d: fine aggregate < 2mm (Note: a part of the fine aggregate is the coarser fraction of the limestone powder, FA^{***} refers to natural river sand < 2mm).

e: coarse aggregate < 20mm.

Table 6. 2 Flow and passing ability test results of SCC mixes

Mix designation	Slump flow		V-funnel	J-ring flow test		L-box test		
	Spread mm	t ₅₀₀ s	t _{v-funnel} s	Spread mm	t _{500J} s	t ₂₀₀ s	t ₄₀₀ s	H ₂ / H ₁
30A	685	0.50	2.46	665	0.60	0.47	1.08	0.91
30B	665	0.88	2.47	635	1.04	0.57	1.11	0.84
30C	655	0.81	2.76	650	0.74	0.53	1.10	0.92
60A	665	1.18	3.23	640	1.48	0.77	1.48	0.89
60B	650	1.32	3.54	645	1.43	0.81	1.72	0.84
60C	655	1.40	4.04	630	1.60	0.81	1.65	0.87
80A	730	1.92	6.67	705	2.43	1.45	3.10	0.93
80B	750	2.06	7.34	730	2.70	1.62	3.20	0.90
80C	670	2.09	7.44	655	2.80	1.45	3.07	0.91

6.3.4 Specimen preparation and test procedure

From each of the nine mixes (Table 6.1) 12 beam specimens (Figure 6.5), three cubes (100 mm), and three cylinders (100 x 200 mm) were cast. The specimens were de-moulded after 1 day and cured in water at ambient temperature for 28 days. The cube compressive strength was measured according to BS EN 12390-3 (2009). Six of the beams were notched to a depth of 10 mm (notch to depth ratio $a/W = 0.1$) with a thin (2 mm) diamond saw while the remaining six were notched to a depth of 60 mm ($a/W = 0.6$). The modulus of elasticity (E) and the split cylinder strength (f_{st}) were measured on cylinders according to BS 1881-121, (1983) and BS EN 12390-6, (2009), respectively.

6.4 Results and discussion

Typical recorded load–deflection diagrams of two notched beams (out of twelve) from three of the nine mixes are shown in Figure 6.11. The area under the load-deflection diagram was calculated from which the $G_f(a, W)$ was determined using Equation (6.1).

Table 6.3 shows the results of the measured fracture energy $G_f(a, W)$: the mean value, standard deviation and the coefficient of variation (COV %).

Table 6. 3 Measured fracture energy, $G_f(a, W)$ for different SCC mixes from three point bending test (TPB)

Mix designation	W mm	a/ W	Mean [St. dev.]	COV
			$G_f(a, W)$, N/m	%
30A	100	0.1	96.20 [8.90]	9.20
		0.6	53.50 [5.00]	9.30
30B	100	0.1	85.90 [7.70]	9.00
		0.6	53.00 [4.00]	7.60
30C	100	0.1	73.40 [7.30]	10.0
		0.6	52.30 [4.30]	8.20
60A	100	0.1	108.6 [11.6]	10.7
		0.6	65.80 [1.70]	2.60
60B	100	0.1	91.90 [5.70]	6.20
		0.6	56.50 [5.00]	8.85
60C	100	0.1	83.90 [9.60]	11.4
		0.6	51.90 [3.20]	6.10
80A	100	0.1	105.5 [5.50]	5.30
		0.6	58.50 [5.70]	9.80
80B	100	0.1	100.1 [9.90]	9.90
		0.6	57.00 [4.90]	8.60
80C	100	0.1	97.60 [11.0]	11.3
		0.6	57.70 [2.50]	4.30

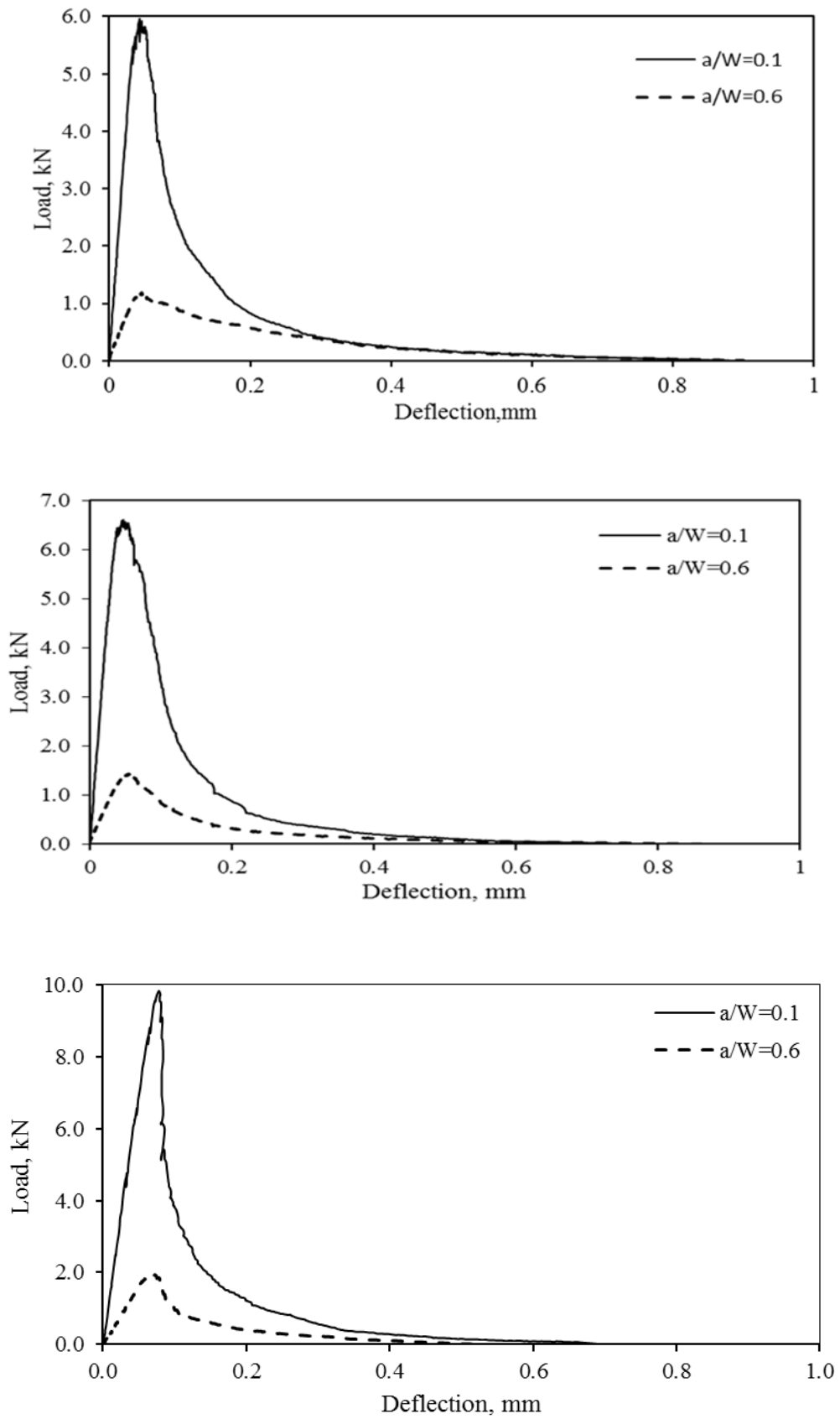


Figure 6. 11 Typical load–displacement diagrams of two notched beams (out of twelve tested) from SCC mixes: 30C (top), 60C (middle), and 80C (bottom)

The specific size-independent fracture energy (G_F) and the transition ligament lengths (a_l) of all mixes are determined from $G_f(0.1)$ and $G_f(0.6)$ of Table 6.3 using the first of the two equalities in Equation (6.7); a MATLAB programme was prepared for this purpose (see Appendix C). In many mixes, however it transpired that the transition ligament length a_l so calculated violated the corresponding inequality for $a/W = 0.6$. In these cases the first of the two equalities was used only for $a/W = 0.1$, while the second equality was used for the deeper notch $a/W = 0.6$. The resulting values of G_F and a_l are reported in Table 6.4 together with the cube compressive strength, split cylinder strength and modulus of elasticity, measured according to the relevant British standards.

Table 6. 4 Results of f_{cu} , f_{st} , E , G_F and a_l of test SCC mixes

Mix designation	f_{cu} , 28 days MPa	f_{st} , 28 days MPa	E , 28 days GPa	G_F N/m	a_l mm
30A	35.4	2.95	33.6	132.8	49.7
30B	37.0	3.04	32.7	112.3	42.4
30C	37.8	3.30	32.0	90.4	33.8
60A	60.5	3.40	36.7	143.2	43.6
60B	62.9	3.52	36.6	120.3	42.6
60C	65.2	3.65	34.5	109.7	42.3
80A	79.8	4.60	42.3	146.9	50.7
80B	81.6	5.00	40.8	136.5	47.9
80C	83.2	5.35	41.0	130.2	45.2

Within the range of coarse aggregate volume fraction (27-33%) investigated in this study, G_F increases with the increase of coarse aggregate fraction as is clear from Table 6.4 and Figure 6.12 because of the increase in the energy dissipation mechanisms (micro-cracking, crack branching, aggregate interlock) in much the same manner as in VC (Karihaloo, 1995; Akcay et al., 2012; Prokopski and Langier, 2000). This

observation is in agreement with previous research on SCC (Beygi et al., 2014b; Beygi et al., 2014c; Nikbin et al., 2014c).

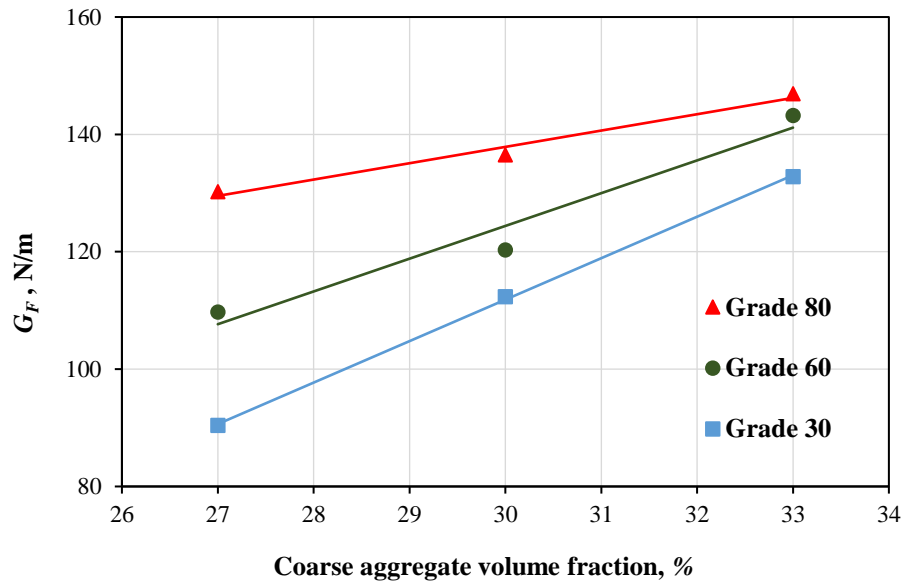


Figure 6. 12 Variation of G_F of SCC mixes of different grades with coarse aggregate volume fraction

Moreover, it can be seen from Figure 6.12 that the increase in G_F with the coarse aggregate volume fraction is less pronounced in the high strength mix (grade 80) than in mix grades 30 and 60. This is may be attributed to the fact that the ITZ (Beygi et al., 2014c) in grade 80 mixes is much denser and therefore more susceptible to cracking because it contains a higher proportion of cementitious materials, as can be seen in Table 6.1.

An increase in the paste to solids (p/s) ratio in all mix grades, as expected, leads to a slight increase in the cube compressive strength f_{cu} but a noticeable decrease in G_F , as shown in Figure 6.13.

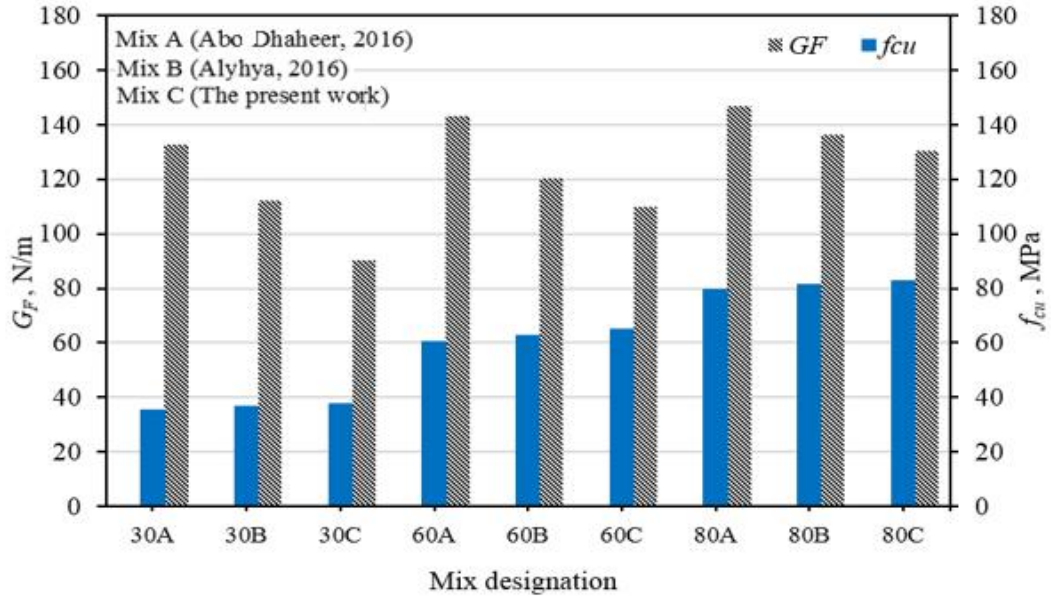


Figure 6. 13 Variation of the G_F and f_{cu} with different p/s ratios

As expected, G_F decreases with increasing water to binder (w/cm) ratio, in much the same manner as in VC (Prokopski and Langier, 2000; Nallathambi et al., 1984) as shown in Figure 6.14. This result is consistent with the recent study on normal strength self-compacting concrete conducted by (Beygi et al., 2013b) who found that fracture energy decreases by 38% as w/cm ratio is increased from 0.4 to 0.7. G_F of high strength self-compacting concrete ($f_{cu} \sim 100$ MPa), on the other hand has been reported by Cifuentes and Karihaloo (2013) to be just 90 N/m for $w/cm = 0.23$. This is a consequence of the densification of ITZ as a result of using a fairly high volume fraction of micro-silica.

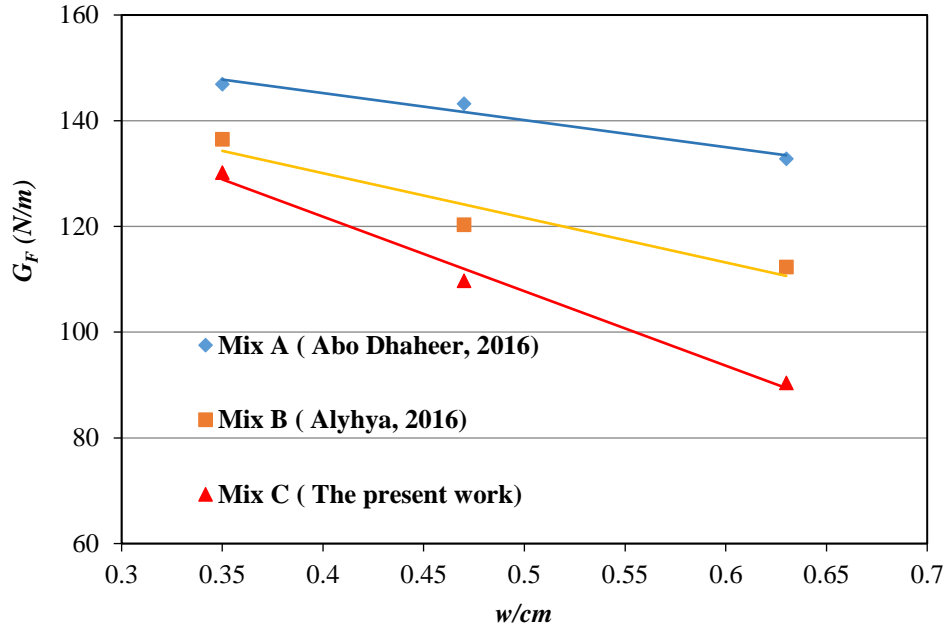


Figure 6. 14 Variation in G_F with w/cm ratio for different coarse aggregate (CA) volume fractions

6.5 Bilinear tension softening diagram

To complete the determination of the fracture properties of the SCC mixes, we now outline briefly an inverse procedure based on the non-linear hinge concept for identifying the parameters of the bilinear tension softening diagrams of the mixes corresponding to their above size-independent values of the specific fracture energy (G_F). The details of the procedure may be found in (Abdalla and Karihaloo, 2004; Murthy et al., 2013a) and Appendix D. It should be mentioned that the popularity of the bilinear approximation of the tension softening diagram (Figure 6.15) stems from the fact that it captures the two major mechanisms responsible for the observed tension softening in a concrete mix, namely micro-cracking and frictional aggregate interlock. The initial linear branch of the bilinear diagram which is steep is a consequence of the micro-cracking, whereas the second linear branch which is shallow is a result of the frictional aggregate interlock.

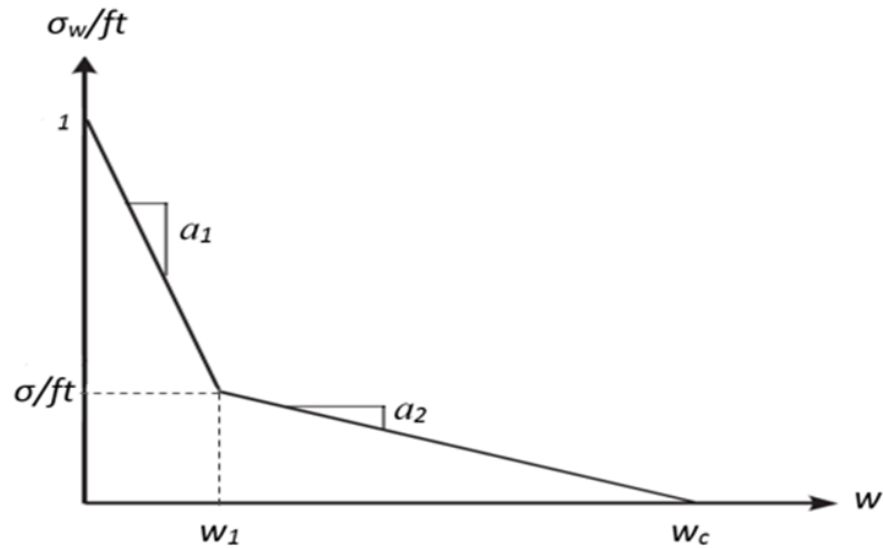
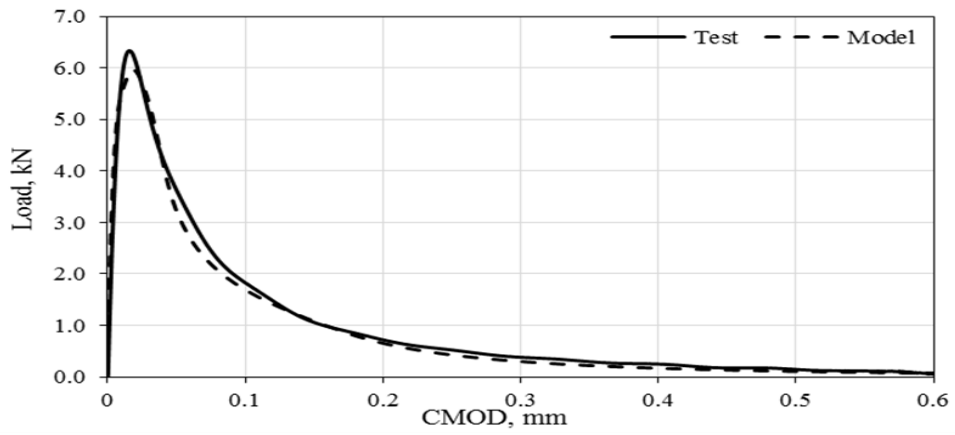
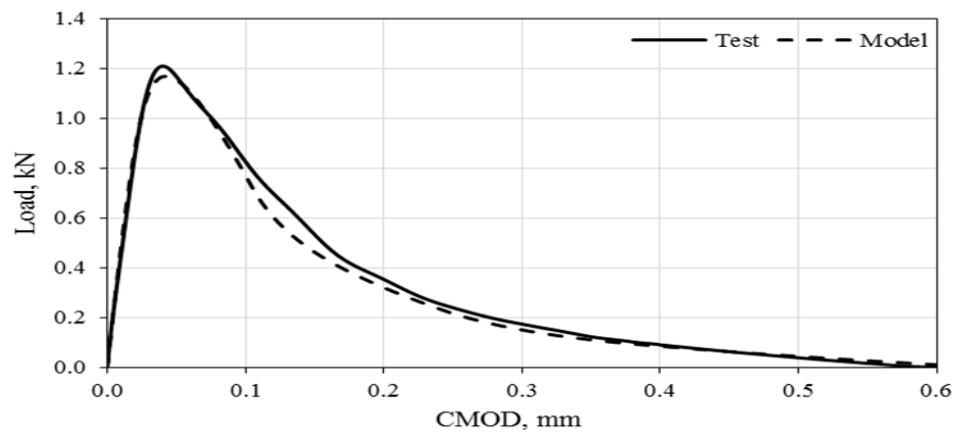


Figure 6. 15 Bilinear softening diagram

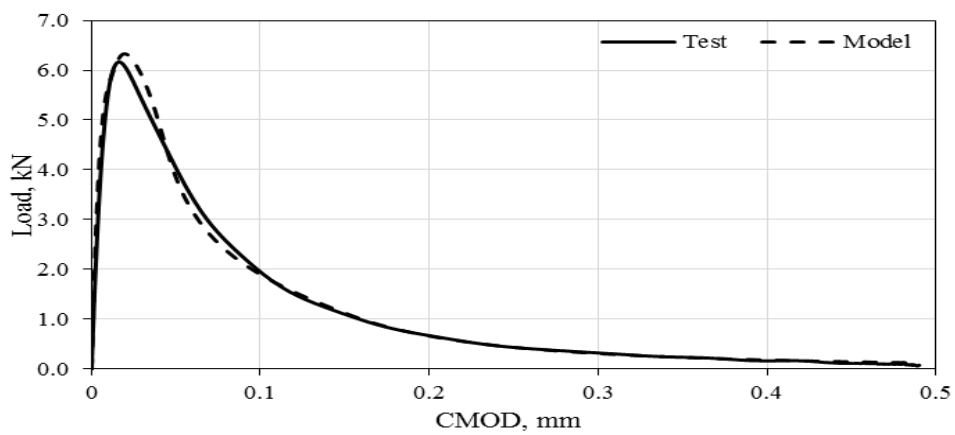
Analytical expressions relating the hinge rotation to the bending moment and crack length in each phase, and in turn to the applied central load on the beam and crack mouth opening displacement (CMOD) are given in Abdalla and Karihaloo (2004). The expressions for CMOD and central load are used to minimize the sum of squares of the errors between the theoretical and experimental values of the load with respect to the three unknown parameters of the bilinear tension softening diagram (Figure 6.15). A MATLAB programme was prepared for determination of the static response of self- compacting concrete beams under three-point bending (Appendix E). The accuracy of this minimization procedure depends on the total number of observations from the recorded load-CMOD diagram used in this procedure and the allowable error (<3%). Typical results of this minimization procedure are shown in Figure 6.16 for some SCC mixes and pre-existing notch depths.



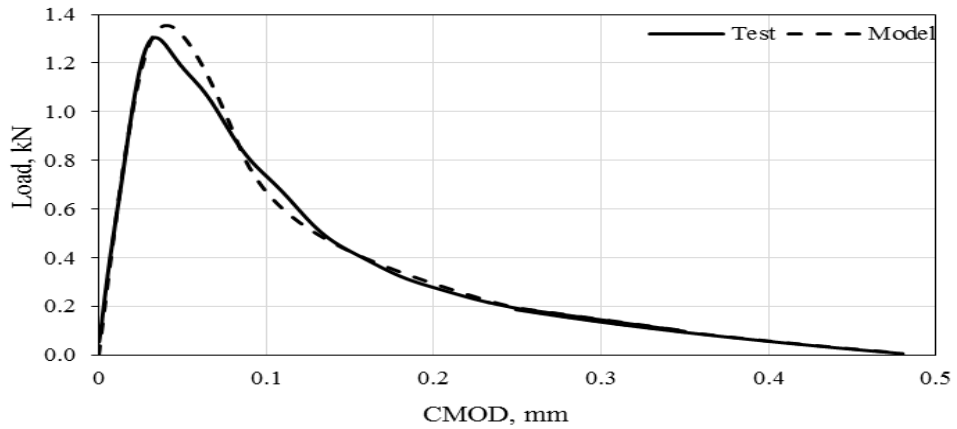
(a) 30C: $a/W = 0.1$



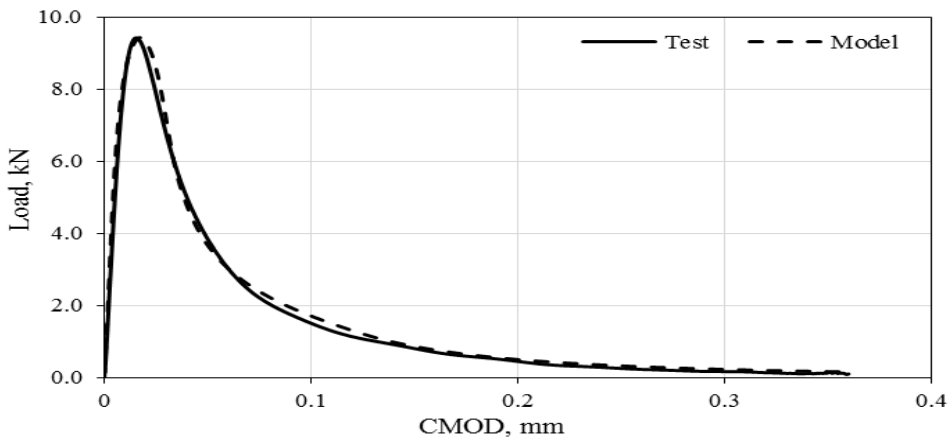
(b) 30C: $a/W = 0.6$



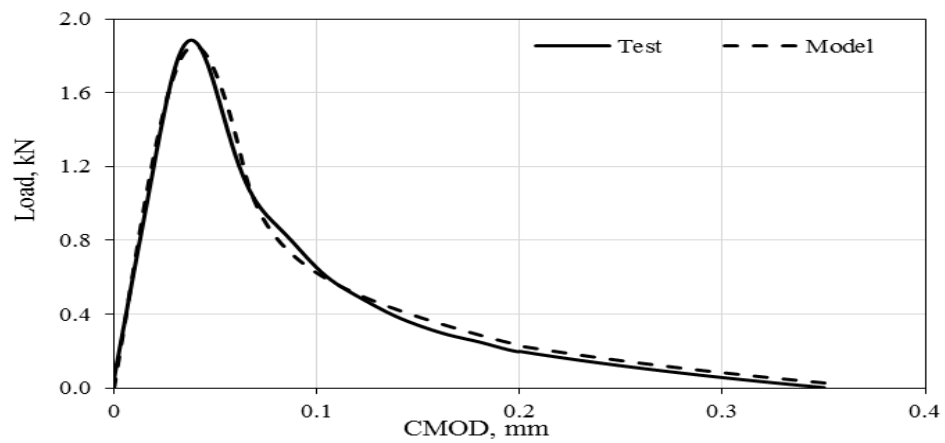
(c) 60C: $a/W = 0.1$



(d) 60C: $a/W = 0.6$



(e) 80C: $a/W = 0.1$



(f) 80C: $a/W = 0.6$

Figure 6. 16 Load-CMOD curves generated by the hinge model and average experimental load-CMOD curves

As the load-CMOD diagrams are recorded on tests on beams with a notch to depth ratio of 0.1 or 0.6, the three unknown parameters of the bilinear tension softening diagram obtained from the above minimization procedure correspond not to the G_F of the SCC mix but to its size-dependent $G_f(0.1)$ and $G_f(0.6)$. These pairs of three parameters need therefore to be appropriately scaled to reflect the size-independent G_F of the mix. The scaling procedure is described in (Abdalla and Karihaloo, 2004). The bilinear tension softening diagrams of all nine SCC mixes corresponding to their size-independent specific fracture energy (G_F) are shown in Figure 6.17 and the parameters tabulated in Table 6.5. The three parameters describing the shape of the bilinear diagram, together with the direct tensile strength (f_{ct}) and the elastic modulus (E) of all SCC mixes are given in Table 6.5. The slope of the initial part of the bilinear softening curve increases with the increasing the p/s ratio, but the influence of p/s decreases as the f_{cu} of the mix increases.

Table 6. 5 Parameters of the bilinear softening diagram corresponding to the size-independent specific fracture energy (G_F)

Mix Designation	a_1 mm	a_2 mm	w_1 mm	w_c mm	$\frac{\sigma}{f_t}$	G_F N/m	E GPa	l_{ch} mm
30A	10.07	1.12	0.078	0.272	0.218	132.8	33.6	1377
30B	13.21	1.05	0.060	0.254	0.203	112.3	32.7	976
30C	18.76	1.20	0.043	0.198	0.186	90.4	32.0	511
60A	10.97	1.14	0.073	0.251	0.203	143.2	36.7	1057
60B	13.17	1.25	0.062	0.213	0.189	120.3	36.6	771
60C	15.38	1.28	0.053	0.198	0.185	109.7	34.5	547
80A	16.19	1.18	0.048	0.238	0.225	146.9	42.3	647
80B	18.51	1.39	0.043	0.194	0.211	136.5	40.8	380
80C	19.75	1.38	0.041	0.177	0.188	130.2	41.0	289

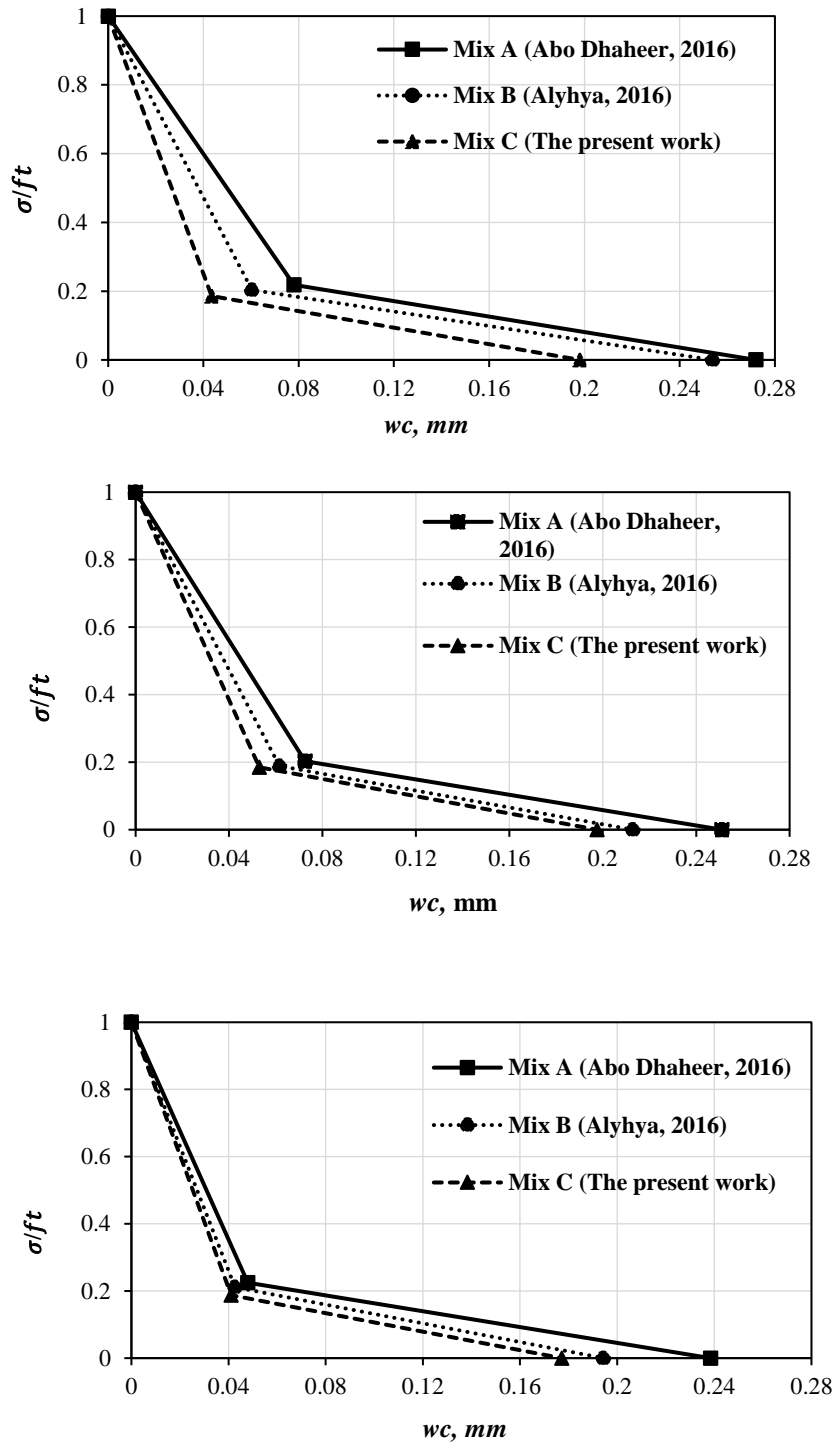


Figure 6. 17 The normalised bilinear stress-crack opening relationship for different SCC grades corresponding to their size-independent fracture energy (G_F) Grade 30 (top), Grade 60 (middle), and Grade 80 (bottom)

It is well documented that the direct tensile strength (f_{ct}) is approximately two thirds of the indirect tensile strength (f_{st}). Although the literature is rich in reporting on SCC, the effect of p/s ratio and mix grade on tensile strength is still not fully addressed. The relationship between the direct tensile strength (determined by the inverse analysis using the non-linear hinge model) and splitting strengths (f_{ct}/f_{st}) of SCC mixes of different p/s ratio and mix grade are summarized in Table 6.6 and Figure 6.18. It is found that f_{ct}/f_{st} is dominated by the p/s in the mix and the mix grade: it increases with both an increase in p/s and mix grade. This might provide a better understanding of the contribution of p/s and strength on the tensile strength of SCC and a useful guide for determining the f_{ct} from the f_{st} in SCC mixes. Note that the ratio (f_{ct}/f_{st}) is slightly different from the conventional 0.65 (Neville, 1995). It depends on the p/s ratio and strength grade (Table 6.6).

Table 6. 6 Relation between f_{ct} and f_{st} of test SCC mixes

Mix Designation	f_{ct} MPa	f_{st} MPa	$\frac{f_{ct}}{f_{st}}$	Mean $\frac{f_{ct}}{f_{st}}$
30A	1.80	2.95	0.61	0.66
30B	1.94	3.04	0.64	
30C	2.38	3.30	0.72	
60A	2.23	3.40	0.66	0.69
60B	2.39	3.52	0.68	
60C	2.63	3.65	0.72	
80A	3.10	4.60	0.67	0.75
80B	3.83	5.00	0.77	
80C	4.30	5.35	0.80	

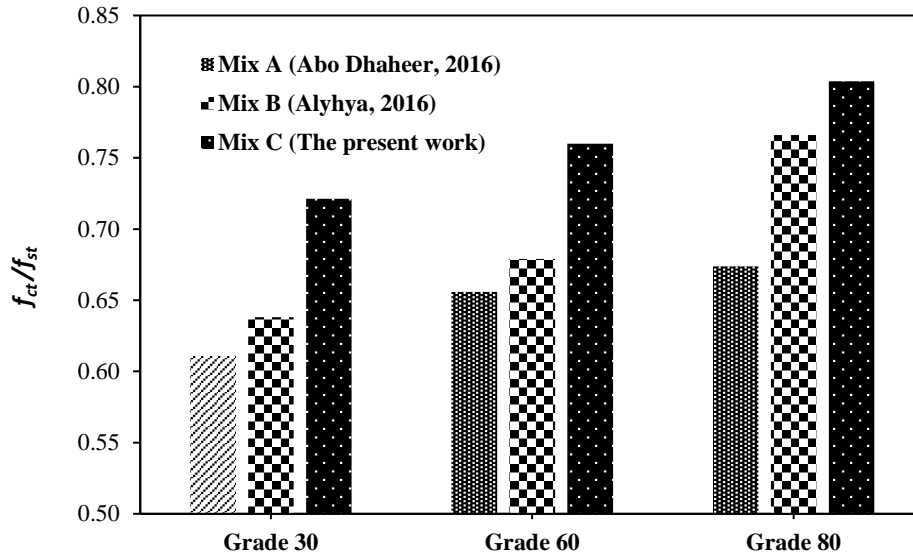


Figure 6. 18 Direct (f_{ct}) and indirect (f_{st}) tensile strengths of different SCC mixes

Also given in Table 6.5 is the characteristic length (l_{ch}) of each mix calculated using the relation:

$$l_{ch} = \frac{E_{GF}}{f_{ct}^2} \quad (6.9)$$

The characteristic length represents the ductility of a mix; the larger the characteristic length, the more ductile the mix. l_{ch} is dominated by the coarse aggregate volume fraction and it decreases with increasing strength grade (Figure 6.19).

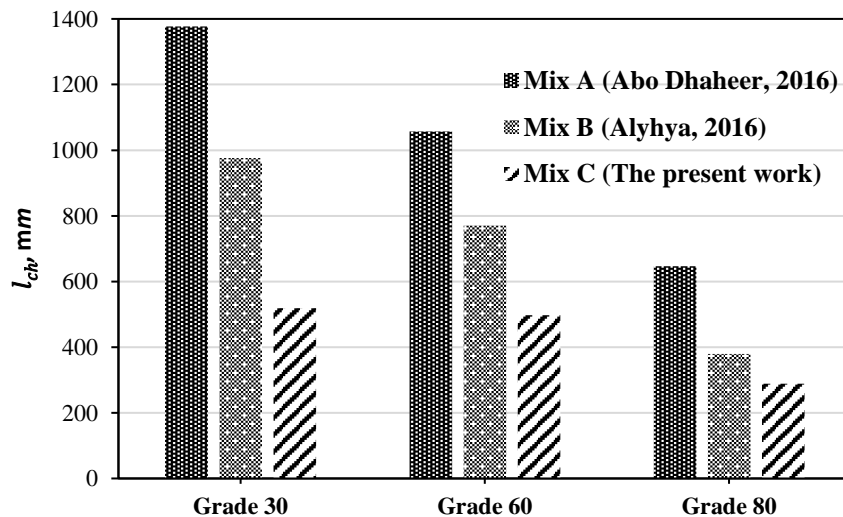


Figure 6. 19 Characteristic length (l_{ch}) of different test SCC mixes

6.6 Concluding remarks

The fracture behaviour of the SCC mixes was investigated in detail with respect to the role of several composition parameters such as coarse aggregate volume, paste to solids (p/s) and water to binder (w/cm) ratios. The results confirm the dependency of the RILEM fracture energy on the notch depth. Besides, it is found that the (G_F) increases with an increase in the coarse aggregate volume fraction, irrespective of the SCC mix grade, although the increase is less pronounced in higher strength mix (grade 80) than in grades 30 and 60 of SCC. Furthermore, within the same nominal strength grade, an increase in the paste to solids (p/s) ratio results in a marginal increase in the strength itself, but a noticeable decrease in G_F .

On the other hand, an increase in the w/cm ratio reduces G_F , the decrease becomes more pronounced with decreasing coarse aggregate volume fraction. Regarding to the critical crack opening w_c , it is dominated by the coarse aggregate volume in the mix and the mix grade. The larger the coarse aggregate volume (or the smaller the paste to solids ratio) the larger is the critical crack opening w_c . However, the higher the mix grade the lower is the critical crack opening (w_c). Similarly, the characteristic length l_{ch} is dominated by the coarse aggregate volume fraction; it increases significantly with an increase in the coarse aggregate volume fraction but decreases with increasing strength grade for the same volume fraction.

Chapter 7

Simulation of the passing and filling abilities of self-compacting concrete (SCC) using L-box and smooth particle hydrodynamics (SPH)

7.1 Introduction

SCC is a special type of concrete with very high flow-ability together with good stability. These two properties allow the concrete to fill every corner of the formwork in which it is placed under its own weight without the need of any external vibration. The passing ability around and between obstacles is another property that is needed for SCC to achieve the filling of heavily congested sections of reinforced concrete structures (Ouchi et al., 1998). Such properties are evaluated through a combination of tests like slump cone flow, J-ring, L-box and V-funnel to determine whether or not a mix can be called self-compacting.

The test using the L-box apparatus has been proposed to assess the filling and passing abilities of an SCC mix (Sonebi and Cevik, 2009). It mimics several phenomena that take place during the casting of concrete: it is a three-dimensional free surface flow of a non-Newtonian fluid between steel bars as obstacles (Nguyen et al., 2006). It consists of an L-shaped apparatus, in which the vertical section is filled with SCC while the gate is closed. The test starts by lifting the gate and the SCC flows through the rebar obstructions into the horizontal section of the apparatus. Measurements consist in recording the flow times of SCC mix at 200 mm and 400 mm from the gate (t_{200} and t_{400}); and the heights of the concrete at the beginning and the end of the horizontal section H_1 and H_2 after the flow has stopped; the ratio (H_2/H_1) represents the filling ability. There is no recommendation for t_{200} and t_{400} values, but longer values represent higher plastic viscosity.

The durability of concrete structures is affected by many problems of compactness. These problems result from incomplete filling of formworks and segregation of aggregates inside the structure. It is therefore important to devise numerical tools for predicting the flow, filling and passing abilities and providing insight into how the coarse aggregates will distribute during the flow in order to save time, effort and materials. Besides, the computational simulation of SCC flow can be a helpful tool for understanding the rheological behaviour of SCC and can allow to identify a lower workability of fresh concrete that could ensure proper filling of formwork (Roussel, et al., 2007). As an SCC mix consists of particles of different sizes and shapes, it is simpler and more convenient to use mesh-free particle-based numerical techniques to

simulate the flow. For this purpose, a three-dimensional Lagrangian particle-based smooth particle hydrodynamics (SPH) method is used in this work to simulate the flow times, the profile of the free surface flow, and to reveal the distribution of coarse aggregate particles larger than or equal to 8 mm in the mix and then to compare the numerical results with the corresponding experimental data. This method is chosen because it allows the heavier coarse aggregates to be distinguished in the homogeneous SCC continuum and tracked during the flow.

An SCC mix can be regarded as a non-Newtonian incompressible fluid whose rheology can be described by Bingham-type constitutive parameters: the yield stress τ_y and the plastic viscosity η . The measurement of τ_y and η by rheometers is inconsistent and fraught with inaccuracies. For one and the same SCC mix different rheometers are known to give vastly different values of τ_y and η (Banfill *et al.*, 2000; Wallevik and Wallevik, 2011). The published results are therefore highly unreliable. It is for this reason that alternative methods of estimating these parameters have been developed which have been used in this study.

Ghanbari and Karihaloo (2009) have proposed a micro-mechanical procedure for estimating the plastic viscosity of a heterogeneous SCC mix knowing the plastic viscosity of the homogeneous paste used in it. In this procedure, SCC is regarded as a two-phase suspension in which the solid phase is suspended in a viscous liquid phase. The yield stress of SCC mixes is very low when compared with normal vibrated concrete mixes and remains nearly constant over a wide range of plastic viscosities (Ghanbari and Karihaloo, 2009). Badry *et al.* (2016a) have confirmed that the yield stress τ_y of SCC mix can be accurately estimated in an inverse manner from the measured t_{500} and t_{stop} times of slump flow test knowing the plastic viscosity of the mix using the SPH simulation methodology.

The modelling of the flow of the SCC mix in the L-box has been undertaken previously (Deeb *et al.*, 2014a). The simulation of flow times (t_{200} and t_{400}) of SCC in the L-box was performed but the comparison between experimental data and simulated results showed some differences. This could be because several factors that influence the flow in L-box were not considered in that first exploratory simulation (Deeb *et al.*, 2014a). Foremost among these is the kinematic friction between the mix and the sides of L-

box and between the mix and the steel bars; only the kinematic friction between the mix and base of the L-box was considered by Deeb *et al.* (2014a). This has been included in the present study. Moreover, the simulated distribution of large coarse aggregate particles has been compared with the distribution in tests performed in the laboratory on two representative SCC mixes using colour-coded aggregates.

In this Chapter we will simulate all mixes developed in Chapter 5 using the SPH methodology. The basic equations solved in SPH are the mass and momentum conservations equations (Equations 3.6 and 3.8) together with the constitutive equation (3.3). The predictor-corrector numerical procedure used to solve these equations was described in Section 3.8. It only remains to explain how the boundary conditions were imposed.

This chapter has been accepted for publication (see publication 1 in the list in Chapter 1).

7.2 Development of SCC mixes

An extensive laboratory study was performed to develop different grades of normal and moderate strength SCC mixes (with nominal 28-day cube compressive strengths of 30, 40, 50, 60, 70, and 80 MPa). These mixes were developed according to the rational mix design method proposed in by Abo Dhaheer *et al.* (2016a, b) which rationalized and simplified the method proposed earlier by Karihaloo and Ghanbari (2012) and Deeb and Karihaloo (2013). The amounts and details of the ingredients used in the SCC test mixes are given in Table 7.1. Locally available type II cement and ground granulated blast furnace slag (ggbs) with specific gravities of 2.95 and 2.40, respectively were used. The super-plasticizer (SP) used was a polycarboxylic ether-based type with specific gravity of 1.07. Crushed limestone coarse aggregate (CA) with a maximum size of 20 mm and a specific gravity of 2.80 was used, while the fine aggregate (FA) was partly river sand having a specific gravity of 2.65. Limestone powder (LP) as filler with maximum particle size of 125 μm was used (specific gravity 2.40). A part of the river sand was replaced by an equivalent volume of the coarser fraction of limestone filler in the size range 125 μm - 2 mm. All mixes were tested in the fresh state using the slump cone, J-ring, L-box, and V-funnel

apparatus (EFNARC, 2005; BS EN 206-9, 2010). They all satisfied the flow-ability and passing ability criteria and showed no visible signs of segregation. The plastic viscosity of each mix was calculated using the micro-mechanical procedure described by Ghanbari and Karihaloo (2009) and the plastic viscosity of the homogeneous paste (Sun et al., 2006). The corresponding yield stress of each mix estimated by Badry *et al.* (2016a) is also given in the table.

Table 7. 1 Mix proportions of test SCC mixes, kg/m³

Constituents		Mix strength grade, MPa					
		30	40	50	60	70	80
Cement		240	262.5	281.2	315	345	367.5
GGBS		80	87.5	93.8	105	115	122.5
cm		320	350	375	420	460	490
Water		201.6	199.5	198.8	197.5	184	171.5
Sp		2.3	2.5	2.8	2.8	3.3	3.9
w/cm		0.63	0.57	0.53	0.47	0.40	0.35
LP		194	194	186	172	170	172
FA*	FA**	291	291	279	258	255	258
	FA***	504	479	478	477	478	478
CA		756	756	756	756	756	756
t ₂₀₀ in L-box, s		0.53	0.67	0.63	0.81	1.15	1.45
t ₄₀₀ in L-box, s		1.10	1.40	1.33	1.65	2.46	3.07
Level-off ratio (H ₂ /H ₁)		0.91	0.92	0.87	0.91	0.89	0.92
Plastic viscosity, Pa s		5.24	7.44	8.52	9.00	10.22	11.52
Yield stress, Pa		175	175	178	180	180	190
Density, kg/m ³		2298.8	2302	2304.8	2310.3	2335.3	2355.4

7.3 Boundary conditions

When solving the mass and momentum conservation equations (3.6) and (3.8), three types of boundary conditions need to be considered;

1. Zero pressure condition (i.e. atmospheric pressure) on the free surface;
2. Dirichlet boundary condition has to be imposed on the normal component of particle velocity at the sides of the L-box;
3. Neumann conditions on the pressure gradient (this additional zero pressure gradient condition is needed only for solving the second-order pressure Poisson equation (3.23)).

In SPH, a number of techniques have been developed in the past to enforce various boundary conditions. Some of these techniques have been mentioned in Chapter 3. In this research, Four arrays of rigid dummy particles placed outside the sides and the base of the L-box were used to implement the boundary conditions as illustrated in Figure 7.1. The coefficient of kinematic friction (c_f) between the SCC mix and steel base and side plates and between the mix and steel rods was chosen to be 0.55 Ns/m, i.e. the same as in Deeb et al. (2014a).

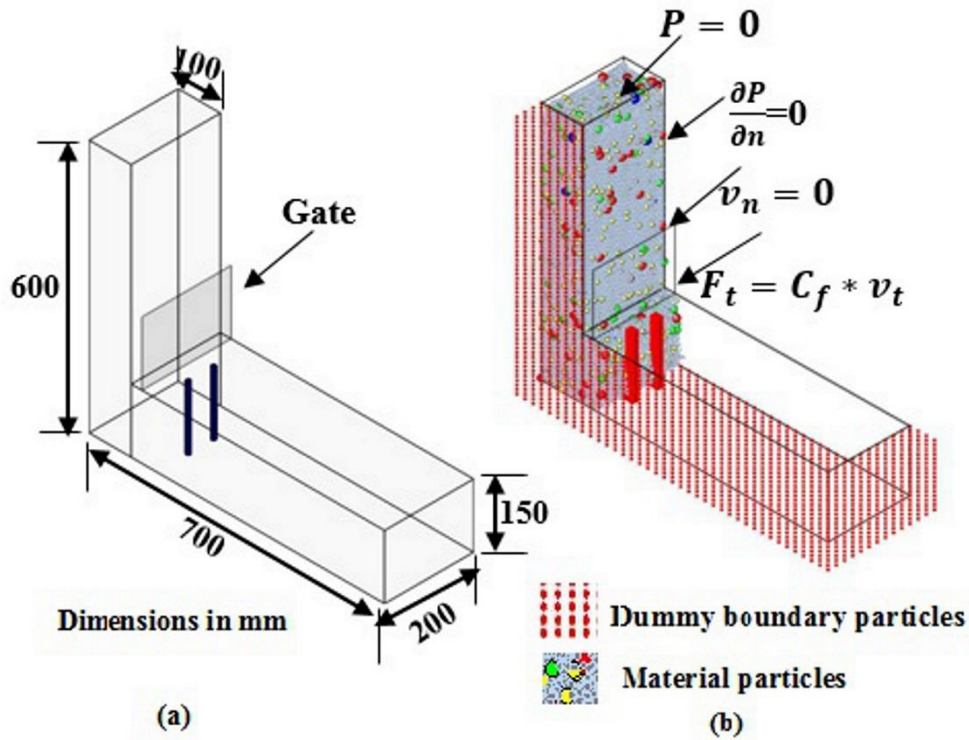


Figure 7. 1 (a) L-box configuration (b) boundary conditions

7.4 Treatment of aggregates

7.4.1 Colour coding of coarse aggregates in the test SCC mixes

Tracking the coarse aggregate particles during the flow of SCC gives an indication if the coarse aggregates are homogeneously distributed in the mix or not. In order to be able to compare the simulated distribution of coarse aggregates equal to or larger than 8 mm in size with the distribution in the actual test specimen after the flow has stopped, the coarse aggregates in the size ranges ($g \geq 20$, $16 \leq g < 20$, $12 \leq g < 16$ and $8 \leq g < 12$ mm) used in the test mixes were colour coded with non-toxic non-water soluble paints (Figure 7.2). As a result, the outlines of the aggregate particles would be clearly visible in the cut sections of the L-box test slab after it had hardened.



Figure 7. 2 Colour coded coarse aggregates; $g \geq 20$ mm (white, bottom right), $16 \leq g < 20$ mm (red, bottom left), $12 \leq g < 16$ mm (green, top left), and $8 \leq g < 12$ mm (yellow, top right)

In order to retrieve the test specimen from the horizontal section of the box, the front end plate of the horizontal section of the L-box was hinged (Figure 7.3a). Two SCC mixes of 40 and 60 MPa were cast with colour coded coarse aggregates and tested in the L-box (Figure 7.3b). When the mix had flowed into the horizontal section of the L-box, the two steel bars were unscrewed and removed. After 24 hours, the hinged end plate was dropped and the solid slab was removed from the L-box and placed in water tank for curing until needed for cutting. It was cut along two longitudinal sections with a diamond saw (Figures 7.4a and 7.5a).



Figure 7. 3 (a) Hinged end plate of L-box apparatus (b) 60C SCC mix with colour coded aggregates

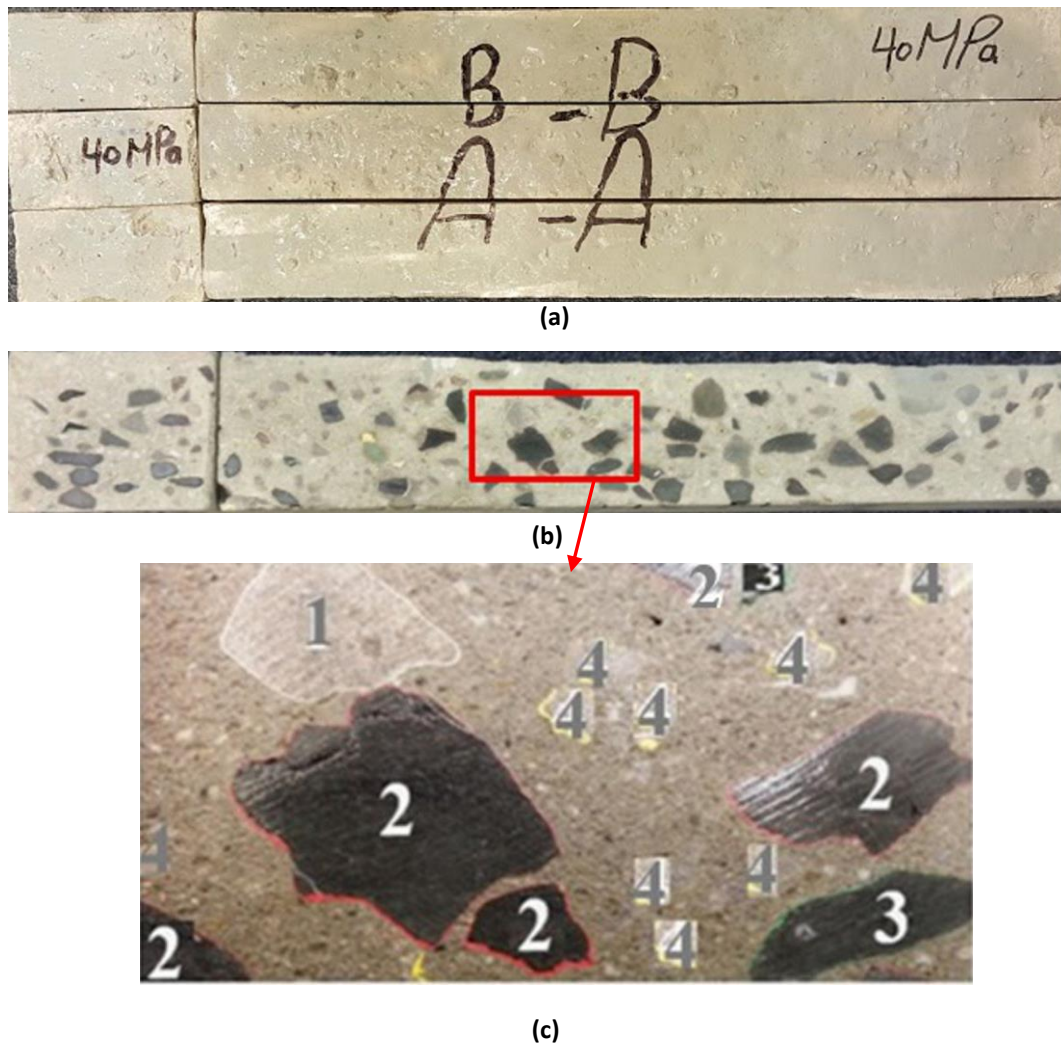
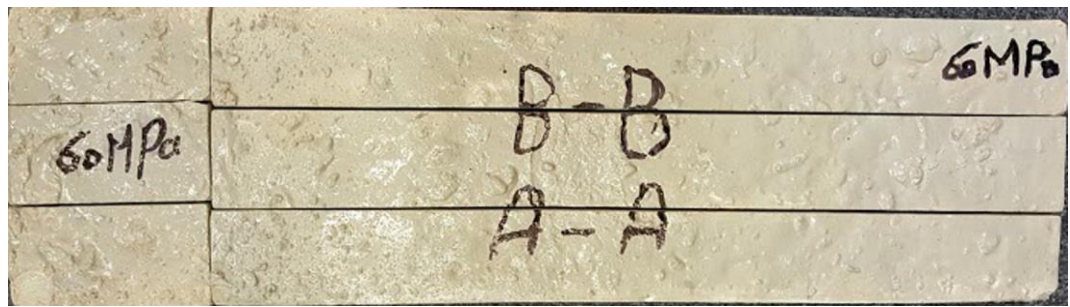


Figure 7. 4 (a) Two longitudinal sections of hardened slab (Mix 40 MPa) (b) one of the two surfaces made by the longitudinal cut, and (c) the outlines of coloured coarse aggregates are clearly visible in the cut surface. Coarse aggregates with white outlines are labelled 1, with red 2, with green 3, and those with yellow 4.



(a)



(b)



(c)

Figure 7.5 (a) Two longitudinal sections of hardened slab (Mix 60 MPa) (b) one of the two surfaces made by the longitudinal cut, and (c) the outlines of coloured coarse aggregates are clearly visible in the cut surface. Coarse aggregates with white outlines are labelled 1, with red 2, with green 3, and those with yellow 4.

The number of aggregates in the different size ranges (according to their different coloured outlines, Figures 7.4c and 7.5c) was counted. Table 7.2 lists the number of different size aggregates counted along the two longitudinal sections of the L-box test specimen in the two test mixes.

Table 7. 2 Average number of coarse aggregate particles in the size ranges $g \geq 20$, $16 \leq g < 20$, $12 \leq g < 16$ and $8 \leq g < 12$ mm in the two longitudinal sections of hardened L- box slab of mixes 40C and 60C

Mix strength grade, MPa	Section	$g \geq 20$ mm	$16 \leq g < 20$ mm	$12 \leq g < 16$ mm	$8 \leq g < 12$ mm
40C	Section A-A	6	30	35	90
	Section B-B	5	34	40	95
60C	Section A-A	6	30	37	95
	Section B-B	5	32	40	102

7.4.2 Treatment of particles in SPH modelling of the L-box test

The coarse aggregates must be homogeneously distributed in the SCC mixes, therefore an important requirement of the SCC mix is that heavier aggregate particles do not segregate from the paste but stay homogeneously distributed during the flow. In order to be able to monitor the velocity vectors and positions of different sizes of aggregates, as well as those of the fluid particles representing the paste, the particles are represented by distinct colours as shown in Figure 7.6.

The total number of particles used in 3D simulation is 59,568 to represent the volume of the SCC mix in the L-box ($129 \times 105 \text{ mm}^3$) giving a resolution of 216.56 mm^3 per particle, if all particles have the same density as the viscous continuum. The resolution will be somewhat different if the particles have different densities (see Tables 7.3). Thus, in all the SCC mixes the large aggregates that can be distinguished from the homogeneous mass must have a volume exceeding this minimum. It is for this reason that only the aggregates of size 8 mm and above could be treated as discrete identities. According to the volume fractions (obtained by sieve analysis), the masses of the SPH particles representing different coarse aggregate particles in the mix were calculated. All particles representing the mix were generated randomly.

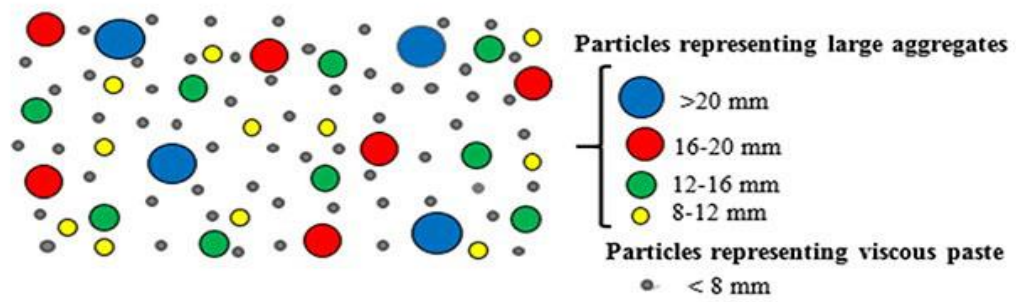


Figure 7. 6 Schematic sketch of particle representation in the simulated mixes

Table 7. 3 Volume fractions and assigned volumes of aggregates particles (Mix 40C)

SCC mix (40C)	Particle range (mm)	Representative particle diameter (mm)	Density (kg/m ³)	Volume fraction (%)	3D L-box test	
					Number of particles N _p	Assigned volume per particle V _a (mm ³)
Aggregates g ≥ 8 mm	g ≥ 20	20.0	2800	1.28	39	5097
	16 ≤ g < 20	18.0	2800	7.20	305	3716
	12 ≤ g < 16	14.0	2800	4.20	373	1748
	8 ≤ g < 12	10.0	2800	7.90	1953	637
Particles < 8 mm	g < 8	8.0	2173	79.0	56898	170
Total			2302	100	59568	

For the purpose of modelling, each aggregate size range was replaced by a single aggregate size that best represented the average of the upper and lower limits of aggregate size range. The assigned volume (V_a) for each particle size which appears in the discrete form of SPH equations is equal to the ratio of its actual mass to the density of the continuum. An example is presented below on how to calculate the assigned volume of the discrete particles in mix 40 MPa.

Firstly, the density of mortar is calculated (i.e. cement + ggbs + LP + FA + water + SP + CA particles < 8 mm in size) whose volume fraction is 0.79 (Table 7.2). It can be calculated as follows using the rule of mixtures. The density of SCC mix = sum of the volume fractions of CA > 8 mm x density of CA + volume fraction of mortar x density of mortar, i.e. $2302 = (0.0128 + 0.072 + 0.042 + 0.079) \times 2800 + 0.79 \times \text{density of mortar}$).

This gives the density of mortar (particles < 8 mm) to be 2173 kg/m^3 .

The number of particles of each size used in the simulation N_p is calculated as follows:

$N_p = \text{volume fraction} \times \text{volume of L-box} / \text{volume of one particle}$

$$N_p (g \geq 20) = 0.0128 \times 12900000 / 4190 = 39$$

$$N_p (16 \leq g < 20) = 0.072 \times 12900000 / 3055 = 305$$

$$N_p (12 \leq g < 16) = 0.042 \times 12900000 / 1437 = 373$$

$$N_p (8 \leq g < 12) = 0.079 \times 12900000 / 524 = 1953$$

$$N_p (< 8) = 59568 - (39 + 3045 + 373 + 1953) = 56898$$

Next, the assigned volume $V_a (\text{mm}^3)$ for each size is = actual average volume x actual density / density of continuum:

$$V_a (g \geq 20) = ((0.0128 \times 12900000) \times 2800 / 2302) / 39 = 5097 \text{ mm}^3$$

$$V_a (16 \leq g < 20) = ((0.072 \times 12900000) \times 2800 / 2302) / 304 = 3716 \text{ mm}^3$$

$$V_a (12 \leq g < 16) = ((0.042 \times 12900000) \times 2800 / 2302) / 373 = 1748 \text{ mm}^3$$

$$V_a (8 \leq g < 12) = ((0.079 \times 12900000) \times 2800 / 2302) / 1953 = 637 \text{ mm}^3$$

$$V_a (< 8) = ((0.79 \times 12900000) \times 2173 / 2302) / 56898 = 170 \text{ mm}^3$$

7.5 Simulation results

7.5.1 Simulation of the flow times of SCC mixes in the L-box

The simulation results of the flow times are given in Table 7.3. It can be observed that there are differences in the flow times needed for the SCC mixes to reach 200 mm and 400 mm (t_{200} and t_{400}) as compared with the times measured in the laboratory test. There are two reasons behind these differences. Firstly, it is difficult to time precisely the moment when the gate is lifted to release the mix. This is perhaps the major reason for the difference. Secondly, there is another minor reason, namely the delay in lifting the gate because of the hydrostatic pressure on it from the SCC mix in the vertical leg. The delay in lifting the gate will therefore be the slightly longer the higher the hydrostatic pressure on the gate (i.e. the higher the density of the SCC mix). This is confirmed by Figure 7.7, which shows the differences in the measured and simulated flow times t_{200} and t_{400} as a function of the mix density. This result is consistent with the study conducted by Thrane et al., (2004) who also found that the simulated flow times are much shorter than the experimental values.

Table 7. 4 Flow times of SCC mixes in the L- box

Mix strength grade, MPa	Experimental flow times, s		Simulated flow times, s	
	t_{200}	t_{400}	t_{200}	t_{400}
30C	0.53	1.10	0.31	0.70
40C	0.67	1.40	0.40	1.10
50C	0.63	1.30	0.45	1.05
60C	0.81	1.65	0.50	1.20
70C	1.15	2.46	0.55	1.38
80C	1.45	3.07	0.66	1.60

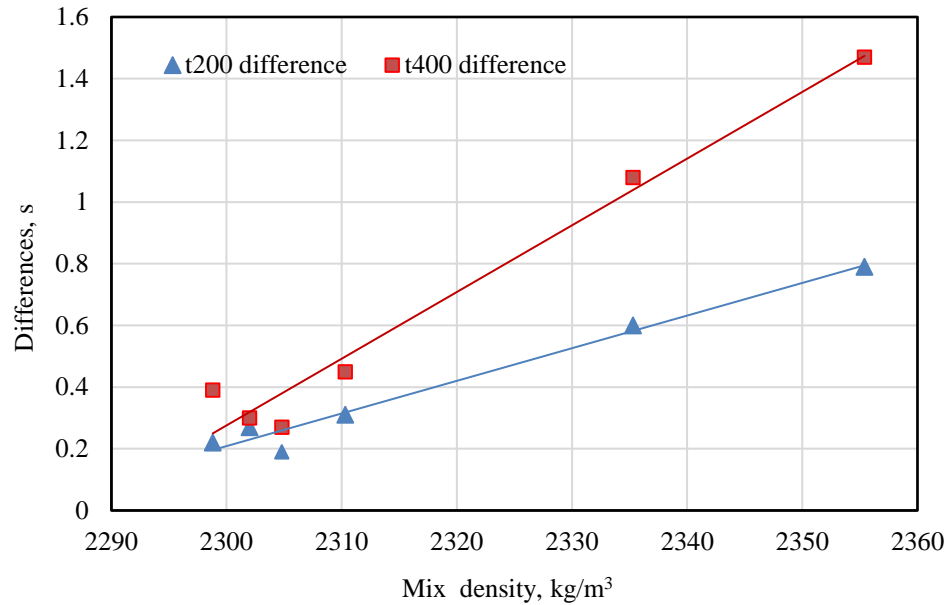


Figure 7.7 Effect of the plastic viscosity of SCC mix on the difference between experimental and simulated flow times

7.5.2 Simulation of the free surface profile of SCC in the L-box

The simulated profiles of the free surface flows at several distances from the gate and the final profile are compared with profiles in test mixes in Figure 7.8 and 7.9. The profile of free surface of the simulated mix looks similar to that observed in the laboratory test. Moreover, it has been found that the ratio of the SCC mix height at the end of the horizontal section of the L-box to the height of the remaining concrete in the vertical section in the simulated flow is more than the minimum recommended value 0.8 (EFNARC, 2005); these results correlate very well with the experimental results.

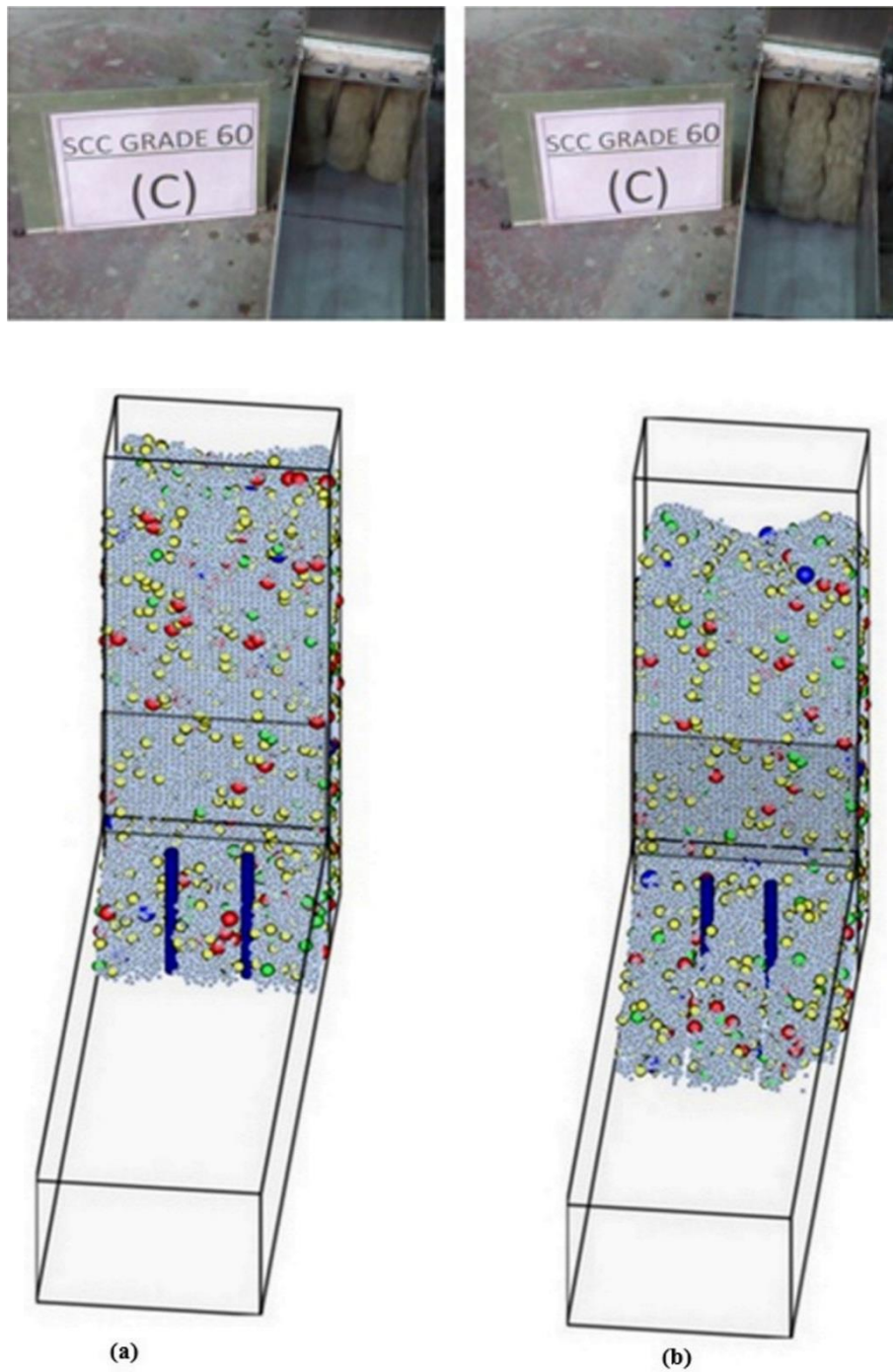


Figure 7. 8 (a) The profiles of free surface of experimental and simulated SCC (Mix 60 MPa) at approximately 75 mm, (b) 200 mm from the gate. Note that here, and in Figures 7.9, 7.10 and 7.11, the size of the spots corresponds to the size range of the aggregate; the smallest spot to $8 \leq g < 12$ mm and the largest to $g \geq 20$ mm.

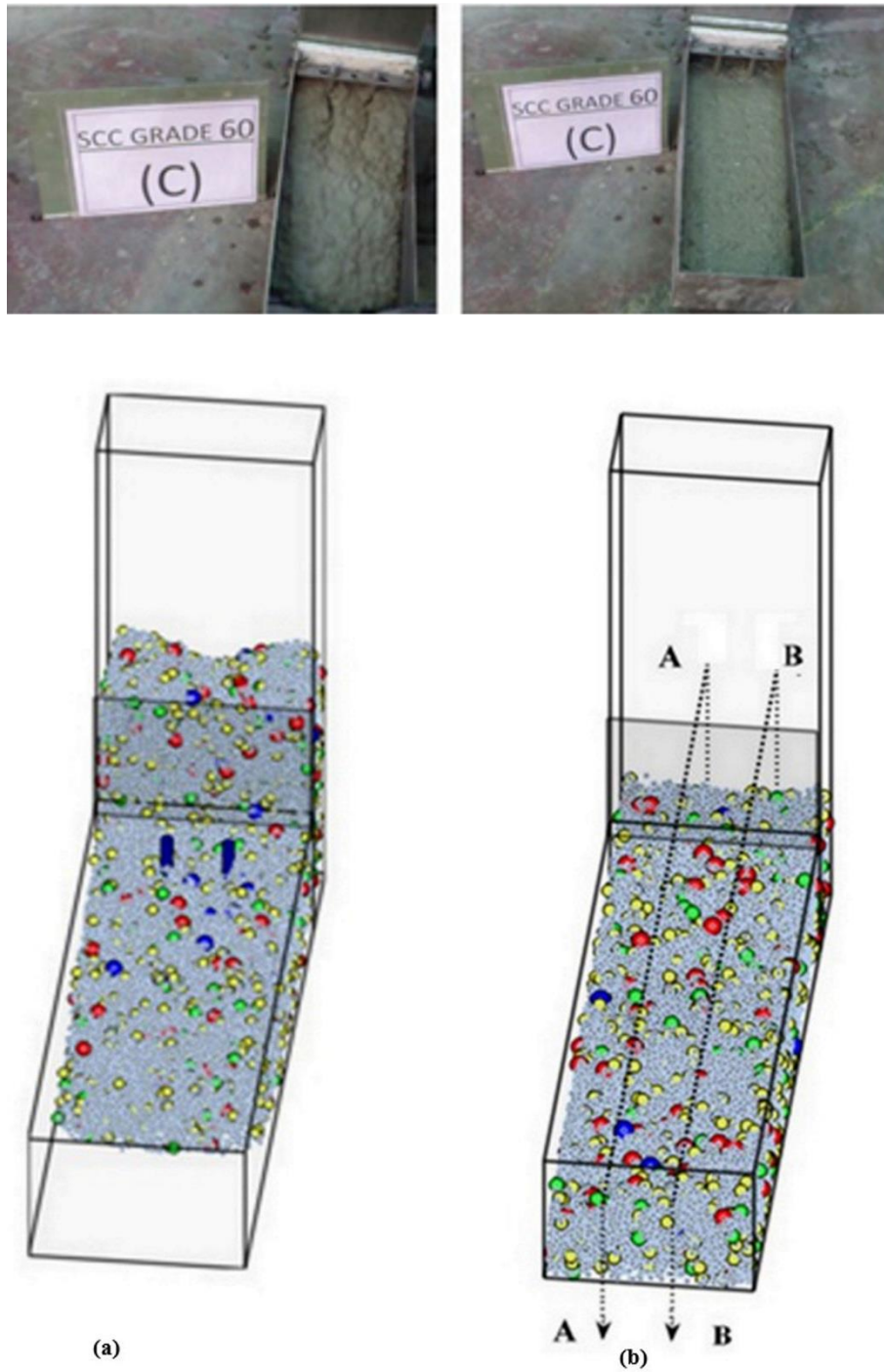


Figure 7. 9 (a) The profiles of free surface of the experimental and simulated SCC (Mix 60 MPa) at approximately 400 mm from the gate. (b) The final profile of free surface flow after the flow has stopped. AA and BB refer to sections along which cuts will be made.

7.5.3 Simulation of the distribution of large aggregates during the SCC flow in the L-box

The distribution of large aggregates (≥ 8 mm) in two simulated SCC mixes 40C and 60C was examined using two approaches and compared with the test results. In the first approach the simulated L-box mix after the flow had stopped was cut along two longitudinal sections (A-A and B-B Figure 7.9 b). One of the two surfaces made by each of the two cuts is shown in Figures 7.10 and 7.11. The number of large aggregates of different size ranges in each of the two surfaces was counted. The average numbers in the two sections are given in Table 7.5.

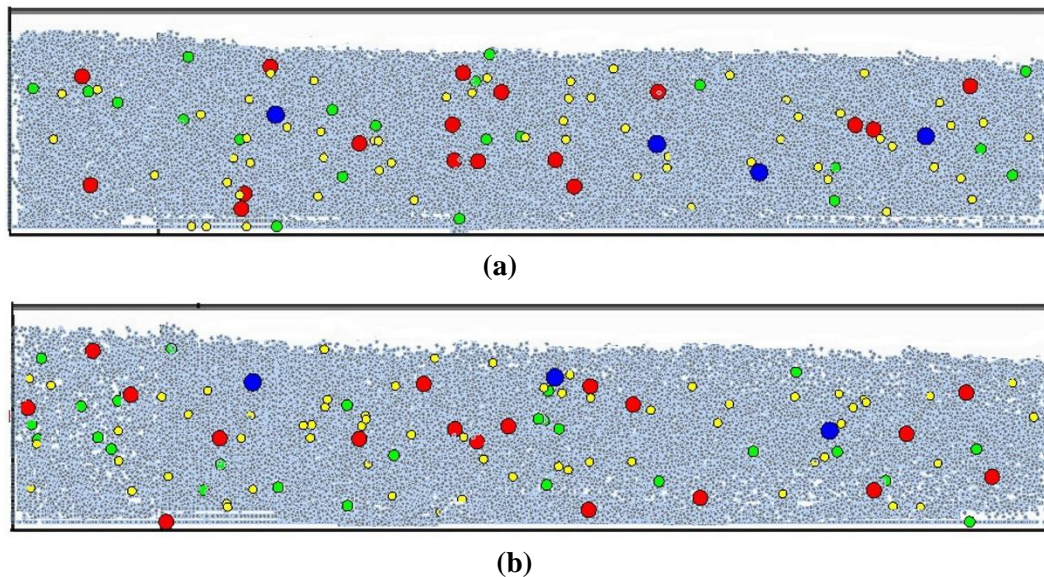


Figure 7. 10 (a) One of the two surfaces made by longitudinal section A-A and (b) by B-B of the simulated SCC (Mix 40C)

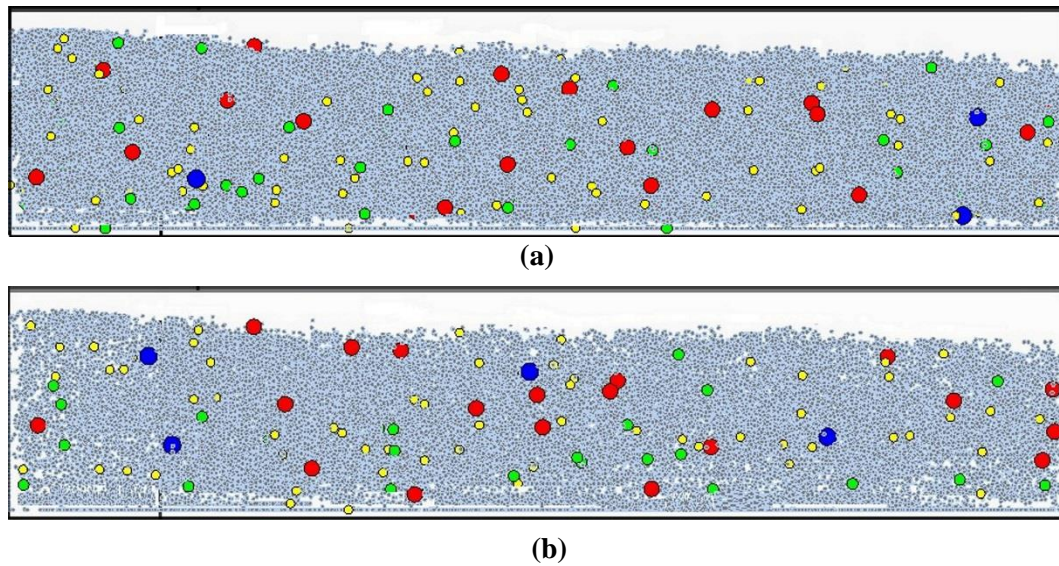


Figure 7. 11 (a) One of the two surfaces made by longitudinal section A-A and (b) by B-B of the simulated SCC (Mix 60C)

Table 7. 5 Average number of coarse aggregate particles in the size ranges $g \geq 20$, $16 \leq g < 20$, $12 \leq g < 16$ and $8 \leq g < 12$ mm in the simulated L-box along two longitudinal sections

Mix strength grade, MPa	Section	$g \geq 20$ mm	$16 \leq g < 20$ mm	$12 \leq g < 16$ mm	$8 \leq g < 12$ mm
40C	A-A	4	17	21	56
	B-B	3	18	25	60
60C	A-A	3	17	24	60
	B-B	4	19	21	58

As the volume fractions of the coarse aggregates of different size ranges (but not their actual numbers) are the same in the test mixes and simulations, their numbers in the cut sections of the L-box test and the simulated L- box flow must necessarily be correlated. This correlation may, for instance, be revealed by considering the ratio of the average number of aggregates of a certain size range to the number of aggregates of the largest size. This has been done for the test and simulated L-box flow and is reported in columns 5 and 6 of Table 7.6 from which it is seen that the relative numbers of aggregates of different size ranges are indeed nearly the same. Further, the larger aggregates are indeed homogeneously distributed along the two sections with no visible settlement of the larger aggregates (≥ 8 mm) as in the actual test. This observation is in a good agreement with recent study conducted by Badry et al., (2016a) who found that the SPH methodology is capable of predicting accurately the distribution of large coarse aggregates in the simulated slump cone test.

Table 7. 6 Average number of coarse aggregates along two longitudinal sections of mixes 40C and 60C

Mix strength grade, MPa	Size range (mm)	Average number in experiment	Average number in simulation	Ratio of average number in experiment to average number of 20 mm	Ratio of average number in simulation to average number of 20 mm
40C	$g \geq 20$	5.5	3.5	1.0	1.0
	$16 \leq g < 20$	32.0	17	5.82	5.0
	$12 \leq g < 16$	37.5	23.5	6.82	6.57
	$8 \leq g < 12$	97.0	58.0	17.6	16.57
60C	$g \geq 20$	5.5	3.5	1.0	1.0
	$16 \leq g < 20$	31.0	18.0	5.64	5.14
	$12 \leq g < 16$	38.5	22.5	7.0	6.43
	$8 \leq g < 12$	98.5	59.0	17.91	16.86

In the second approach, a statistical analysis was performed using the Weibull Cumulative Distribution Function (CDF) to compare the distribution of coarse aggregates in the experimental and simulated L-box specimens along sections A-A and B-B. The histograms in Figures 7.12 and 7.13 revealed that the average number of larger coarse aggregates in simulated sections is almost identical to the average number of larger coarse aggregates in experimental sections for SCC mixes 40C and 60C.

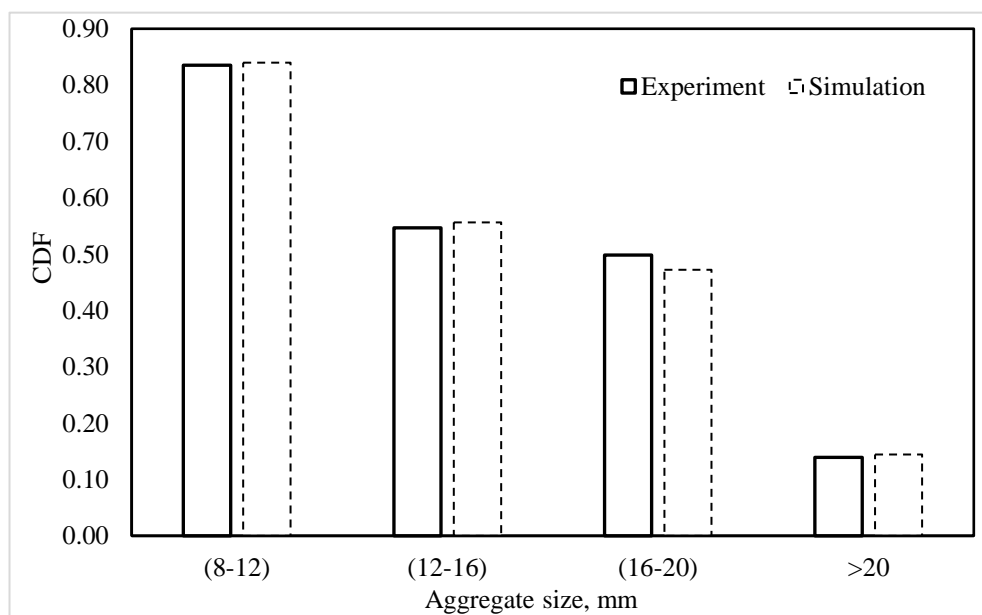


Figure 7. 12 Histogram of the average number of larger coarse aggregates in SCC (Mix 40C)

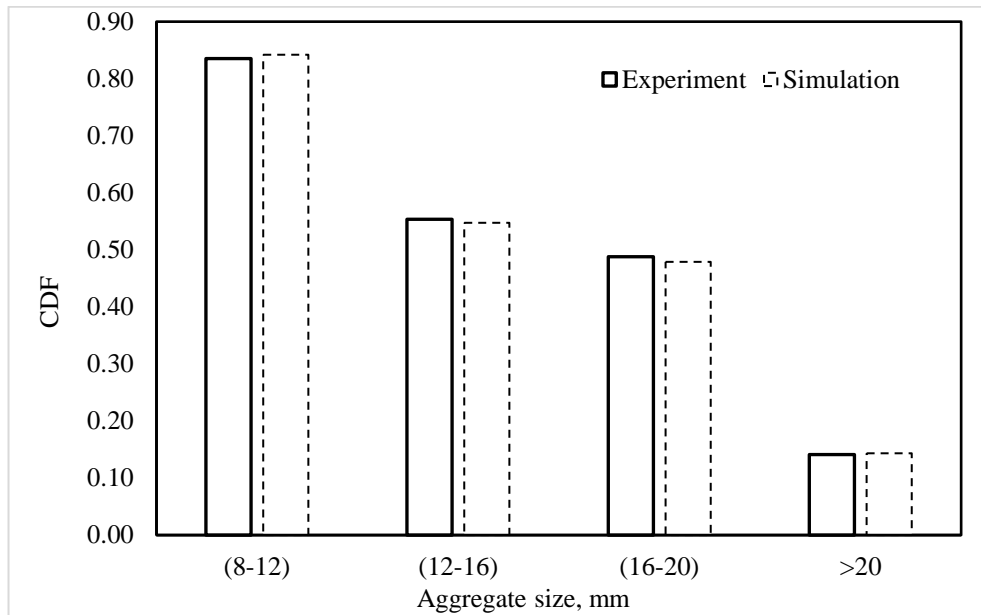


Figure 7.13 Histogram of the average number of larger coarse aggregates in SCC (Mix 60C)

7.6 Concluding remarks

The SPH method is effective in the numerical simulation of SCC flow characteristics in the L-box configuration. The capabilities of this method have been validated by comparing the simulation results with the corresponding experimental data. The SPH methodology is capable of predicting the profile of free surface of SCC mixes and the distribution of the large coarse aggregates during the flow of SCC in the L-box. This distribution is almost identical to that revealed in the cut sections of the hardened slab retrieved from the L-box. The large coarse aggregates in the two test mixes had been colour coded with non-toxic non-water soluble paints. Further, the experiments and numerical simulations also revealed that the coarse aggregates were homogeneously distributed and suspended by the paste without settling to the bottom of the L-box. However, there were differences between the simulated and experimental flow times of the SCC mixes. These are attributed to an unavoidable delay in the lifting of the gate to release the SCC mix, the delay being the greater the higher the hydrostatic pressure on the gate (i.e. the higher the density of the mix). The SPH methodology developed for simulating the passing and filling abilities of the SCC mix in the L-box is particularly relevant to the simulation of real precast self-compacting concrete elements in a factory.

Chapter 8

Conclusions and recommendations for future research

8.1 Conclusions

The main conclusions on the basis of the research work embodied in Chapters 4 to 7, inclusive, are summarised below:

- Designing a self-compacting concrete (SCC) mix necessitates finding the optimum state between flow-ability and non-segregation of constituent materials. The mix design method developed in Chapter 4 produces SCC mix proportions for different strength grades and plastic viscosity through the provision of practical guidelines in the form of design charts.
- The lower target plastic viscosity limit of the SCC mixes that can be proportioned by the method varies between 3.5 and 8 Pa s dependent upon the desired characteristic cubic strength of the mix in the range of 30-80 MPa, while the upper target plastic viscosity is 15 Pa s, irrespective of the compressive strength (Chapter 4).
- Several SCC test mixes designed according to developed method were evaluated in the laboratory through a combination of slump cone flow, J-ring, L-box and V-funnel tests and it is found that SCC mixes meet the self-compatibility criteria of flow- ability, passing ability and stability (Chapter 5).
- Due to the differences of the SCC mix composition from that of VC, the fracture behaviour of the SCC mixes was investigated in detail with respect to the role of several composition parameters such as coarse aggregate volume, paste to solids (p/s) and water to binder (w/cm) ratios. The specific fracture energy and the stress-displacement relationship of a concrete mix are the most important parameters describing its fracture behaviour. It is found that the specific size-independent fracture energy (G_F) increases with an increase in the coarse aggregate volume fraction, irrespective of the SCC mix grade, although the increase is less pronounced in higher strength mix (grade 80) than in grades 30 and 60 of SCC. On the other hand, there is a noticeable decrease in (G_F) with an increase in paste to solids (p/s) ratio and in the w/cm ratio. With reference to critical crack opening (w_c), it is dominated by the coarse aggregate volume in the mix and the mix grade. The larger the coarse aggregate volume

(or the smaller the paste to solids ratio) the larger is the critical crack opening w_c . However, the higher the mix grade the lower is the critical crack opening (w_c) (Chapter 6).

- The mesh-less Lagrangian SPH approach was shown to offer considerable potential as a numerical method for modelling problems involving large deformations. A corrected incompressible SPH method was implemented to simulate the flow characteristics of SCC mixes in the L-box. The simulation of SCC was focused on the flow times, the profile of free surface flow, the distribution of large aggregates (larger than or equal to 8 mm) during the flow (Chapter 7). The capabilities of this methodology were validated by comparing the simulation results with the L-box flow test carried out in the laboratory. The comparison revealed that this methodology is very well suited for predicting the flow behaviour of SCC in terms of passing and filling abilities (Chapter 7).
- The simulation of SCC mixes using the SPH methodology is capable of accurately predicting the distribution of large coarse aggregates in the simulated L-box flow. This distribution was indeed very similar to that revealed in the cut sections of the hardened L-box slab. These large coarse aggregates in the test mixes had been painted with non-toxic non-water soluble paints for making this comparison (Chapter 7).

8.2 Recommendations for future research

- It would be advisable to measure the plastic viscosity of the paste with a viscometer rather than estimating it from published data.
- It would be interesting to develop SCC mixes according to the rational mix design method with a larger replacement of cement by ggbs than the 25% limit placed in the present work in order to achieve SCC mixes with different target plastic viscosity, especially at the lower end.
- Regarding the assumption of the trial superplasticizer (*SP*) dosage in the mix design procedure, it would be advisable to use the full range of the superplasticizer recommended by its manufacturer to change t_{500} or to use a constant

value of t_{500} for the SCC mixes developed with different cube compressive strengths.

- It would be interesting to establish design charts of the mix design method for proportioning SCC mixes with different ratios of steel fibers.
- It would be advisable to study the role of composition parameters (coarse aggregate volume, paste to solids (p/s) and water to binder (w/cm) ratios) of SCC mixes with different ratios of steel fibers on the fracture properties of SCC.
- The lengthy computational time needs to be significantly reduced in order to simulate large real size structural members within a reasonable computational time.
- It would interesting to estimate the plastic viscosity of the SCC mixes in an inverse manner by matching the simulated flow times with the measured values.
- There is need for an alternative method for opening the gate instantaneously in order to avoid delay in manually lifting the gate to release the SCC mix.

References

Abdalla, H.M. and Karihaloo, B.L., 2003. Determination of size-independent specific fracture energy of concrete from three-point bend and wedge splitting tests. *Magazine of Concrete Research*, 55(2), pp.133–141.

Abdalla, H.M. and Karihaloo, B.L., 2004. A method for constructing the bilinear tension softening diagram of concrete corresponding to its true fracture energy. *Magazine of Concrete Research*, 56(10), pp.597–604.

Abo Dhaheer, M.S., Al-Rubaye, M.M., Alyhya, W.S., Karihaloo, B.L. and Kulasegaram, S., 2016a. Proportioning of self-compacting concrete mixes based on target plastic viscosity and compressive strength: mix design procedure. *Journal of Sustainable Cement-Based Materials*, 5(4), pp.199–216.

Abo Dhaheer, M.S., Al-Rubaye, M.M., Alyhya, W.S., Karihaloo, B.L. and Kulasegaram, S., 2016b. Proportioning of self-compacting concrete mixes based on target plastic viscosity and compressive strength: Part II - experimental validation. *Journal of Sustainable Cement-Based Materials*, 5(4), pp.217–232.

Abo Dhaheer, M.S., 2016. Design and properties of self-compacting concrete mixes and their simulation in the J-ring, PhD Thesis, Cardiff University, UK.

ACI 211.1-91, 1991. Standard practice for selecting proportions for normal, heavyweight and mass concrete, A Committee ed., p. 33.

Akçaoğlu, T., Tokyay, M. and Çelik, T., 2004. Effect of coarse aggregate size and matrix quality on ITZ and failure behavior of concrete under uniaxial compression. *Cement and Concrete Composites*, 26, pp.633–638.

Akcay, B., Agar-Ozbek, A.S., Bayramov, F., Atahan, H., N., Sengul, C. and Tasdemir, M., A., 2012. Interpretation of aggregate volume fraction effects on fracture behavior of concrete. *Construction and Building Materials*, 28(1), pp.437–443.

Alyhya, W.S., 2016. Self-compacting concrete: mix proportioning, properties and its flow simulation in the V-funnel, PhD Thesis, Cardiff University, UK.

Amini, Y., Emdad, H. and Farid, M., 2011. A new model to solve fluid--hypo-elastic solid interaction using the smoothed particle hydrodynamics (SPH) method. *European Journal of Mechanics-B/Fluids*, 30(2), pp.184–194.

ASTM C 1621/C 1621M-14, 2008. Standard Test Method for Passing Ability of Self-Consolidating Concrete by J-Ring. Standards and Publications, ASTM International, West Conshohocken, PA, USA.

Badry, F., Kulasegaram, S. and Karihaloo, B.L., 2016a. Estimation of the yield stress and distribution of large aggregates from slump flow test of self-compacting concrete mixes using smooth particle hydrodynamics simulation. *Journal of Sustainable Cement-Based Materials*, 5(3), pp.117–134.

Badry, F., Kulasegaram, S. and Karihaloo, B.L., 2016b. Effect of cone lift rate on the flow time of self-compacting concrete. *Magazine of Concrete Research*, 68(2), pp.80–86.

Baluch, M.H., Rahman, M.K., Mukhtar, F. and Malik, M. a., 2011. A 2-D Computational Fluid Dynamics Simulation of Slump Flow and L-Box Test on SCC Using ANSYS / FLUENT. In: 2nd international Engineering mechanics and materials speciality conference. Ottawa, Canada, pp.1–8.

Banfill, P.B.G., Beaupré, D., Chapdelaine, F., de Larrard, F., Domone, P.L., Nachbaur, L., Sedran, T., Wallevik, J.E. and Wallevik, O., 2000. Comparison of concrete rheometers: International tests at LCPC. In: C.F. Ferraris and L.E. Brower, eds., NISTIR 6819. Nantes, France: National Institute of Standards and Technology.

Banfill, P., 2006. Rheology of fresh cement and concrete. *Rheology Reviews*, pp.61-130.

BASF, 2014. MasterGlenium 499. Technical Data Sheet, pp. 14.

Bažant, Z.P., 1996. Analysis of work-of-fracture method for measuring fracture energy of concrete. *Journal of Engineering Mechanics*, 122, pp.138–144.

Bažant, Z.P. and Kazemi, M.T., 1991. Size dependence of concrete fracture energy determined by RILEM work-of-fracture method. *International Journal of Fracture*, 51(2), pp.121–138.

Bažant, Z.P. and Planas, J., 1998. *Fracture and size effect in concrete and other quasibrittle materials*, CRC press, UK.

Bennenk, I.H.W., 2005. Self-compacting concrete - Five years of experience with SCC in the Netherlands. In: *Proceedings of the 18th BIBM International Congress*. Amsterdam, Netherland, pp.211–218.

Benson, S.D.P. and Karihaloo, B.L., 2005. CARDIFRC® – Development and mechanical properties. Part III: Uniaxial tensile response and other mechanical properties. *Magazine of Concrete Research*, 57(8), pp.433–443.

Beygi, M.H., Berenjian, J., Omran, L.O., Nik, S.A. and Nikbin, I.M., 2013a. An experimental survey on combined effects of fibers and nanosilica on the mechanical, rheological, and durability properties of self-compacting concrete. *Materials and Design*, 50, pp.1019–1029.

Beygi, M.H.A., Kazemi, M. T., Nikbin, I.M. and Amiri, J.V., 2013b. The effect of water to cement ratio on fracture parameters and brittleness of self-compacting concrete. *Materials and Design*, 50, pp.267–276.

Beygi, M.H.A., Kazemi, M.T., Nikbin, I.M. and Amiri, J.V., 2014a. The effect of aging on the fracture characteristics and ductility of self-compacting concrete. *Materials and Design*, 55, pp.937–948.

Beygi, M.H.A., Kazemi, M.T., Nikbin, I.M., Amiri, J.V., Rabbanifar, S. and Rahmani, E., 2014b. The influence of coarse aggregate size and volume on the fracture behavior and brittleness of self-compacting concrete. *Cement and Concrete Research*, 66, pp.75–90.

Beygi, M.H.A., Kazemi, M.T., Amiri, V.J., Nikbin, I.M., Rabbanifar, S. and Rahmani, E., 2014c. Evaluation of the effect of maximum aggregate size on fracture behavior of self-compacting concrete. *Construction and Building Materials*, 55, pp.202–211.

Billberg, P., 1999. Self-compacting concrete for civil engineering structures-the Swedish experience, Report no 2:99. Stockholm: Swedish Cement and Concrete Research Institute.

Billberg, P., Petersson, O., Westerholm, M., Wustholz, T. and Reinhardt, H.W., 2004. Summary report on work package 3.2: Test methods for passing ability.

Bonet, J. and Kulasegaram, S., 2000. Correction and stabilization of smooth particle hydrodynamics methods with applications in metal forming simulations. *International Journal for Numerical Methods in Engineering*, 47, pp.1189–1214.

Bonet, J. and Lok, T.-S.L., 1999. Variational and momentum preservation aspects of Smooth Particle Hydrodynamic formulations. *Computer Methods in Applied Mechanics and Engineering*, 180, pp.97–115.

Bonet, J. and Peraire, J., 1991. An alternating digital tree (ADT) algorithm for 3D geometric searching and intersection problems. *International Journal for Numerical Methods in Engineering*, 31, pp.1–17.

Boukendakdji, O., Kadri., E.-H. and Kenai, S., 2012. Effects of granulated blast furnace slag and superplasticizer type on the fresh properties and compressive strength of self-compacting concrete. *Cement and Concrete Composites*, 34, pp.583–590.

Bouziani, T., 2013. Assessment of fresh properties and compressive strength of self-compacting concrete made with different sand types by mixture design modelling approach. *Construction and Building Materials*, 49, pp.308–314.

Breslar, B. and Wollack, E., 1952. Shear strength of concrete. Report, Department of Civil Engineering. University of California, Berkeley.

BS EN 12350-8, 2010. Testing fresh concrete, Part 8: Self-compacting concrete-Slump test flow, British Standards publication.

BS EN 12350-9, 2010. Self-compacting concrete, Part 9: Self-compacting concrete-V-funnel test, British Standards publication.

BS EN 12350-12, 2010. Testing fresh concrete, Part 12: Self-compacting concrete- J-ring test, British Standards publication.

BS EN 12350-10, 2010. Self-compacting concrete, Part 10: Self-compacting concrete-L-box test, British Standards publication.

BS EN 12390-3, 2009. Testing hardened concrete, Part 3: Compressive strength of test specimens, British Standards publication.

BS EN 12390-6, 2009. Testing hardened concrete, Part 6: Tensile splitting strength of test specimens, British Standards publication.

BS EN 206-9, 2010. Concrete, Part 9: Additional rules for self-compacting concrete (SCC), British Standards publication.

BS 1881- 121, 1983. Method for determination of static modulus of elasticity in compression, British Standards Publication.

BS EN 197-1, 2011. Cement, Part 1: Composition, specifications, and conformity criteria for common cements.

Bui, H.H., Fukagawa, R., Sako, K. and Ohno, S., 2008. Lagrangian meshfree particles method (SPH) for large deformation and failure flows of geomaterial using elastic--plastic soil constitutive model. *International Journal for Numerical and Analytical Methods in Geomechanics*, 32(12), pp.1537–1570.

Bui, V.K., Akkaya, Y. and Shah, S.P., 2002. Rheological model for self-consolidating concrete. *ACI Materials Journal*, 99, pp.549–559.

Carpinteri, A. and Brighenti, R., 2010. Fracture behaviour of plain and fiber-reinforced concrete with different water content under mixed mode loading. *Materials and Design*, 31, pp.2032–2042.

Carpinteri, A. and Chiaia, B., 1996. Size effects on concrete fracture energy: dimensional transition from order to disorder. *Materials and Structures*, 29(5), pp.259–266.

Chanotis, A.K., Poulidakos, D. and Koumoutsakos, P., 2002. Remeshed smoothed particle hydrodynamics for the simulation of viscous and heat conducting flows. *Journal of Computational Physics*, 182(1), pp.67–90.

Chidiac, S.E. and Mahmoodzadeh, F., 2009. Plastic viscosity of fresh concrete - A critical review of predictions methods. *Cement and Concrete Composites*, 31(8), pp.535–544.

Chorin, A.J., 1968. Numerical solutions of the Navier-Stokes equations. *Mathematics of computation*, 22, pp.745–762.

Cifuentes, H. and Karihaloo, B.L., 2013. Determination of size-independent specific fracture energy of normal- and high-strength self-compacting concrete from wedge splitting tests. *Construction and Building Materials*, 48, pp.548–553.

Cleary, P., Ha, J., Alguine, V. and Nguyen, T., 2002. Flow modelling in casting processes. *Applied Mathematical Modelling*, 26(2), pp.171–190.

Colagrossi, A. and Landrini, M., 2003. Numerical simulation of interfacial flows by smoothed particle hydrodynamics. *Journal of Computational Physics*, 191, pp.448–475.

Colleparidi, M., Colleparidi, S. and Troli, R., 2007. Properties of SCC and Flowing Concrete. In: R. Kraus, T. Naik, P. Claisse and H. Sadeghi-Pouya, eds., *Proceedings International Conference: Sustainable construction materials and technologies*. University of Wisconsin Publ, Milwaukee, USA, pp.25–31.

Corinaldesi, V. and Moriconi, G., 2004. Durable fiber reinforced self-compacting concrete. *Cement and Concrete Research*, 34(2), pp.249–254.

Cummins, S.J. and Rudman, M., 1999. An SPH Projection Method. *Journal of Computational Physics*, 152(2), pp.584–607.

Dalrymple, R.. and Knio, O., 2001. SPH Modelling of Water Waves. *Coastal Dynamics*, 1, pp.779–787.

Deeb, R., 2013. Flow of self-compacting concrete. PhD Thesis, Cardiff University, UK.

Deeb, R., Ghanbari, A. and Karihaloo, B.L., 2012. Development of self-compacting high and ultra high performance concretes with and without steel fibres. *Cement and Concrete Composites*, 34(2), pp.185–190.

- Deeb, R. and Karihaloo, B.L., 2013. Mix proportioning of self-compacting normal and high-strength concretes. *Magazine of Concrete Research*, 65(9), pp.546–556.
- Deeb, R., Kulasegaram, S. and Karihaloo, B.L., 2014a. 3D modelling of the flow of self-compacting concrete with or without steel fibres. Part II: L-box test and the assessment of fibre reorientation during the flow. *Computational Particle Mechanics*, 1, pp.391–408.
- Deeb, R., Kulasegaram, S. and Karihaloo, B.L., 2014b. 3D modelling of the flow of self-compacting concrete with or without steel fibres. Part I: slump flow test. *Computational Particle Mechanics*, 1(4), pp.373–389.
- Deeb, R., Karihaloo, B.L. and Kulasegaram, S., 2014c. Reorientation of short steel fibres during the flow of self-compacting concrete mix and determination of the fibre orientation factor. *Cement and Concrete Research*, 56, pp.112–120.
- Dehn, F., Holschemacher, K. and Weiße, D., 2000. Self-Compacting Concrete (SCC) Time Development of the Material Properties and the Bond Behaviour. *LACER*, 5, pp.115–124.
- de Kruif, C.G., van Iersel, E.M.F. and Vrij, A., 1985. Hard sphere colloidal dispersions: Viscosity as a function of shear rate and volume fraction. *The Journal of Chemical*, 83, pp.4717–4725.
- Dilts, G. A., 1999. Moving-least-squares-particle hydrodynamics—I. Consistency and stability. *International Journal for Numerical Methods in Engineering*, 44(8), pp.1115–1155.
- Dilts, G. A., 2000. Moving least-squares particle hydrodynamics II: Conservation and boundaries. *International Journal for Numerical Methods in Engineering*, 48(10), pp.1503–1524.
- Dinakar, P., 2012. Design of self-compacting concrete with fly ash. *Magazine of Concrete Research*, 64(5), pp.401–409.

Dinakar, P., Babu, K.G. and Santhanam, M., 2008. Durability properties of high volume fly ash self- compacting concretes. *Cement and Concrete Composites*, 30(10), pp.880–886.

Dinakar, P., Kartik Reddy, M. and Sharma, M., 2013a. Behaviour of self- compacting concrete using Portland pozzolana cement with different levels of fly ash. *Materials and Design*, 46, pp.609–616.

Dinakar, P., Sethy, K. P. and Sahoo, U.C., 2013b. Design of self-compacting concrete with ground granulated blast furnace slag. *Materials and Design*, 43, pp.161–169.

Domen, P. L., 2000. Self-compacting concrete- state-of-the-art report of RILEM TC 174- SCC. In: Å. Skarendahl and Ö. Petersson, eds. *RILEM Publications SARL (Part VI - Mix design)*, pp.49–65.

Domone, P.L., 2003. Fresh concrete: Advanced Concrete Technology. In: J. Newman and B. Choo, eds. Oxford: Elsevier Ltd, pp.20–30.

Domone, P.L., 2006. Self-compacting concrete: An analysis of 11 years of case studies. *Cement and Concrete Composites*, 28(2), pp.197–208.

Domone, P.L., 2007. A review of the hardened mechanical properties of self-compacting concrete. *Cement and Concrete Composites*, 29, pp.1–12.

Domone, P.L., 2009. Proportioning of self-compacting concrete – the UCL method, Department of Civil, Environmental and Geomatic Engineering. pp.1–30.

Douglas, R.P., 2004. Properties of self-consolidating concrete containing type F fly ash,. M.Sc. Thesis, Northwestern University.Evanston, Illinois.

Dransfield, J., 2003. Admixtures for concrete, mortar and grout: Advanced Concrete Technology. In: J. Newman and B.S. Choo, eds., 1st ed. Oxford: Elsevier, pp.162–195.

Duan, K., Hu, X. and Wittmann, F.H., 2001. Boundary effect on concrete fracture induced by non-constant fracture energy distribution. In: R. de Bordt, J. Mazars, G. Pijaudier-Cabot and J.G.M. Van Mier, eds., *Fracture Mechanics of Concrete Structures*. Balkema Publishers, Rotterdam, pp.49–55.

Duan, K., Hu, X. and Wittmann, F.H., 2003. Boundary effect on concrete fracture and non-constant fracture energy distribution. *Engineering Fracture Mechanics*, 70, pp.2257–2268.

Duan, K., Hu, X. and Wittmann, F.H., 2007. Size effect on specific fracture energy of concrete. *Engineering Fracture Mechanics*, 74, pp.87–96.

Dufour, F. and Pijaudier-Cabot, G., 2005. Numerical modelling of concrete flow: homogeneous approach. *International Journal for Numerical and Analytical Methods in Geomechanics*, 29(4), pp.395–416.

Edamatsu, Y., Nishida, N. and Ouchi, M., 1998. A rational mix-design method for self-compacting concrete considering interaction between aggregate and mortar particles. In: Å. Skarendahl and Ö. Pettersson, eds., 1st International RILEM Symposium on Self-Compacting Concrete. Stockholm, Sweden, pp.309–320.

EFNARC, 2002. Specification and guidelines for self-compacting concrete.

EFNARC, 2005. The European guidelines for self-compacting concrete; specification, production and use.

Esmailkhanian, B., Khayat, K.H., Yahia, A. and Feys, D., 2014. Effects of mix design parameters and rheological properties on dynamic stability of self-consolidating concrete. *Cement and Concrete Composites*, 54, pp.21–28.

Felekoğlu, B., Türkel, S. and Baradan, B., 2007. Effect of water/cement ratio on the fresh and hardened properties of self-compacting concrete. *Building and Environment*, 42(4), pp.1795–1802.

Ferrara, L., Park, Y.D. and Shah, S.P., 2007. A method for mix-design of fiber-reinforced self-compacting concrete. *Cement and Concrete Research*, 37(6), pp.957–971.

Ferraris, C.F., 1999. Measurement of the rheological properties of high performance concrete. State of the art report. *Journal of Research of the National Institute of Standards and Technology*, 104(5), pp. 461-478.

- Feys, D., Heirman, G., De Schutter, G., Verhoeven, R., Vandewalle, L. and Van Germet, D., 2007. Comparison of two concrete rheometers for shear thickening behaviour of SCC. In: G. De Schutter and V. Boel eds. 5th International RILEM Symposium of self-compacting concrete. RILEM Publications S.A.R.L. Ghent, Belgium. pp. 365–370.
- Figueiras, H., Nunes, S., Coutinho, J.S. and Andrade, C., 2014. Linking fresh and durability properties of paste to SCC mortar. *Cement and Concrete Composites*, 45, pp.209–226.
- Fulk, D.A. and Quinn, D.W., 1996. An analysis of 1-D smoothed particle hydrodynamics kernels. *Journal of Computational Physics*, 126, pp.165–180.
- Gao, J. and Fourie, A., 2015. Spread is better: An investigation of the mini-slump test. *Minerals Engineering*, 71, pp.120–132.
- Ghanbari, A., 2011. Self-compacting high and ultra-high performance concretes. PhD Thesis, Cardiff University, UK.
- Ghanbari, A. and Karihaloo, B.L., 2009. Prediction of the plastic viscosity of self-compacting steel fibre reinforced concrete. *Cement and Concrete Research*, 39(12), pp.1209–1216.
- Gingold, R.A. and Monaghan, J.J., 1977. Smoothed particle hydrodynamics: theory and application to non-spherical stars. *Monthly notices of the royal astronomical society*, 181(3), pp.375–389.
- Glucklich, J., 1963. Fracture of plane concrete. *ASCE Journal of engineering mechanics*, 89, pp.127–138.
- Gram, A., 2009. Numerical modelling of self-compacting concrete flow-discrete and continuous Approach. PhD Thesis, Royal Institute of Technology, Sweden.
- Griffith, A.A., 1920. The phenomena of rupture and flow in solids. *Philosophical transaction, royal society of London*, 221, pp.163–198.
- Griffith, A.A., 1924. The theory of rupture. In: *Proceedings 1st International congress on applied physics*. Delft, The Netherlands, pp.55–63.

Grünewald, S., 2004. Performance-based design of self-compacting fibre reinforced concrete. PhD Thesis, Delft University, Netherlands.

Guinea, G. V., Planas, J. and Ellices, M., 1992. Measurement of the fracture energy using three-point bend tests: Part 1-Influence of experimental procedures. *Materials and Design*, 25, pp.212–218.

Guinea, G.V., Planas, J. and Ellices, M., 1994. A general bilinear fit for the softening curve of concrete. *Materials and Structures*, 27(2), pp.99–105.

Han, J., Fang, H. and Wang, K., 2014. Design and control shrinkage behavior of high-strength self-consolidating concrete using shrinkage-reducing admixture and superabsorbent polymer. *Journal of Sustainable Cement-Based Materials*, 3, pp.182–190.

Hassan, K.E., Cabrera, J.G. and Maliehe, R.S., 2000. The effect of mineral admixtures on the properties of high-performance concrete. *Cement and Concrete Composites*, 22(4), pp.267–271.

Hillerborg, A., 1983. Analysis of one single crack, in *Fracture Mechanics of Concrete*, In: F. H. Wittmann, ed, Elsevier, Amsterdam. pp.223–249.

Hillerborg, A., 1985. The theoretical basis of a method to determine the fracture energy G_F of concrete. *Materials and Structures*, 18, pp.291–296.

Hillerborg, A., Modeer, M. and Petersson, P.-E., 1976. Analysis of crack formation and crack growth in concrete by means of fracture mechanics and finite elements. *Cement and Concrete Research*, 6, pp.773–782.

Holschmacher, K. and Klug, Y., 2002. A Database for the evaluation of hardened properties of SCC. *Lacer*, 7, pp.123–134.

Hu, C. and de Larrard, F., 1996. The rheology of fresh high-performance concrete. *Cement and Concrete Research*, 26, pp.283–294.

Hu, J. and Wang, K., 2005. Effects of aggregate on flow properties of mortar. In: *Mid-Continent Transportation Research Symposium*, Ames, Iowa, USA. Iowa State University, pp.1–8.

Hu, X., 1995. Fracture process zone and strain softening in cementitious materials. ETH Building Materials Report No.1, ETH, Switzerland, Aedificatio Publishers, Freiburg.

Hu, X. and Duan, K., 2004. Influence of fracture process zone height on fracture energy of concrete. *Cement and Concrete Research*, 34(8), pp.1321–1330.

Hu, X. and Wittmann, F., 2000. Size effect on toughness induced by crack close to free surface. *Engineering Fracture Mechanics*, 65, pp.209–221.

Hu, X. and Wittmann, F.H., 1992. Fracture energy and fracture process zone. *Materials and Structures*, 25, pp.319–326.

Hwang, C.L. and Tasai, C., 2005. The effect of aggregate packing types on engineering properties of self-consolidating concrete. In: Z. Yu, C. Shi, K.H. Khayat and Y. Xie, eds., 1st International Symposium on Design, Performance and Use of Self-Consolidating Concrete. China: RILEM Publications S.A.R.L.

Irwin, G.R., 1957. Analysis of stresses and strains near the end of a crack traversing. *Journal of Applied Mechanics*, 24, pp.361–364.

Kanadasan, J. and Abdul Razak, H., 2014. Mix design for self-compacting palm oil clinker concrete based on particle packing. *Materials and Design*, 56, pp.9–19.

Kaplan, M.F., 1961. Crack Propagation and the Fracture of Concrete. *Journal of ACI*, 58, pp.591–610.

Karihaloo, B.L., 1995. *Fracture Mechanics and Structural Concrete*, Addison Wesley Longman, UK.

Karihaloo, B.L., Abdalla, H.M. and Imjai, T., 2003. A simple method for determining the true specific fracture energy of concrete. *Magazine of Concrete Research*, 55(5), pp.471–481.

Karihaloo, B.L. and Ghanbari, A., 2012. Mix proportioning of self- compacting high- and ultra- high-performance concretes with and without steel fibres. *Magazine of Concrete Research*, 64, pp.1089–1100.

Karihaloo, B.L., Murthy, A.R. and Iyer, N.R., 2013. Determination of size-independent specific fracture energy of concrete mixes by the tri-linear model. *Cement and Concrete Research*, 49, pp.82–88.

Kelecy, F.J. and Pletcher, R.H., 1997. The development of a free surface capturing approach for multidimensional free surface flows in closed containers. *Journal of computational physics*, 138(2), pp.939–980.

Kesler, C., Naus, D. and Lott, J., 1972. Fracture mechanics- its applicability to concrete. In: *Conference on the Mechanical Behavior of Materials*. Kyoto, Japan, pp.113–124.

Khaleel, O.R. and Abdul Razak, H., 2014. Mix design method for self compacting metakaolin concrete with different properties of coarse aggregate. *Materials and Design*, 53, pp.691–700.

Khaloo, A., Raisi, E.M., Hosseini, P. and Tahsiri, H., 2014. Mechanical performance of self-compacting concrete reinforced with steel fibers. *Construction and Building Materials*, 51, pp.179–186.

Khatri, R.P. and Sirivivatnanon, V., 1995. Effect of different supplementary cementitious materials on mechanical properties of high performance concrete. *Cement and Concrete Research*, 25(1), pp.209–220.

Khayat, K. and Tangtermsirkul, S., 2000. Fresh concrete properties. In: A. Skrendahl and Ö. Petersson, eds., *State-of-the-Art Report (23) of RILEM Technical Committee 174-SCC*. Cachan Cedex, France: RILEM Publications S.A.R.L, pp.17–22.

Khayat, K.H., 1995. Effects of antiwashout admixtures on fresh concrete properties. *ACI Materials Journal*, 92, pp.164–171.

Khayat, K.H., 1999. Workability, testing, and performance of self- consolidating concrete. *ACI Materials Journal*, 96, pp.346–353.

Khayat, K.H., Ghezal, A. and Hadriche, M., 1999a. Factorial design model for proportioning self- consolidating concrete. *Materials and Structures*, 32, pp.679–686.

Khayat, K.H., Ghezal, A. and Hadriche, M., 2000. Utility of statistical models in proportioning self-compacting concrete. *Materials and Structures*, 33, pp.338–344.

Khayat, K.H. and Guizani, Z., 1997. Use of viscosity-modifying admixture to enhance stability of fluid concrete. *ACI Materials Journal*, 94(4), pp.332–339.

Khayat, K.H., Hu, C. and Monty, H., 1999b. Stability of self-consolidating concrete, advantages, and potential applications. In: *First International RILEM Symposium on Self-Compacting Concrete*. Paris, pp.143–152.

Kitaoji, H., Tanigawa, Y., Mori, H., Kurokawa, Y. and Urano, S., 1996. Flow simulation of fresh concrete cast into wall structure by viscoplastic divided space element method. *Transactions of the Japan Concrete Institute*, 16, pp.45–52.

Koehler, E.P. and Fowler, D.W., 2007. Aggregates in self-consolidating concrete. *International Center for Aggregates Research (ICAR) Final Report: The University of Texas at Austin, USA*.

Koehler, E.P., Fowler, D.W., Folet, E.H., Rogers, G.J., Watanachet, S. and Jung, M.J., 2007. *Self-Consolidating Concrete for Precast Structural Applications :Mixture Proportions, Workability, and Early-Age Hardened Properties*, Aggregates Foundation for Technology: Research and Education. University of Texas, Austin, CTR Technical Report: 0-5134-1, pp. 372.

Koshizuka, S., Nobe, A. and Oka, Y., 1998. Numerical analysis of breaking waves using the moving particle semi-implicit method. *International Journal for Numerical Methods in Fluids*, 26(7), pp.751–769.

Koshizuka, S., Oka, Y. and Tamako, H., 1995. A particle method for calculating splashing of incompressible viscous fluid. In: *International Conference on Mathematics and Computations, Reactor Physics and Environmental Analysis*, 2., pp.1514–1521.

Krieger, I.M. and Dougherty, T.J., 1959. A mechanism for Non-Newtonian flow in suspensions of rigid spheres. *Transactions of The Society of Rheology*, 3, pp.137–152.

Kulasegaram, S., Bonet, J., Lewis, R.W. and Profit, M., 2004. A variation formulation based contact algorithm for rigid boundaries in two-dimensional SPH applications. *Computational Mechanics*, 33(4), pp.316–325.

Kulasegaram, S., Karihaloo, B.L. and Ghanbari, A., 2011. Modelling the flow of self-compacting concrete. *International Journal for Numerical and Analytical Methods in Geomechanics*, 35, pp.713–723.

Kulasegaram, S. and Karihaloo, B.L., 2012. Fibre-reinforced, self-compacting concrete flow modelled by smooth particle hydrodynamics. *Engineering and Computational Mechanics*, 166(1), pp.22–31.

Kurokawa, Y., Tanigawa, Y., Mori, H. and Nishinosono, K., 1997. Analytical study on effect of volume fraction of coarse aggregate on Bingham's constants of fresh concrete. *Transactions of the Japan Concrete Institute*, 18, pp.37–44.

Lashkarbolouk, H., Chamani, M.R., Halabian, A.M., Pishehvar., A.R., Chamani, R.M., Halabian, A.M. and Pishehvar., A.R., 2013. Viscosity evaluation of SCC based on flow simulation in the L-box test. *Magazine of Concrete Research*, 65, pp.365–376.

Lee, E.S., Moulinec, C., Xu, R., Violeau, D., Laurence, D. and Stansby, P., 2008. Comparisons of weakly compressible and truly incompressible algorithms for the SPH mesh free particle method. *Journal of Computational Physics*, 227(18), pp.8417–8436.

Leemann, A. and Hoffmann, C., 2005. Properties of self-compacting and conventional concrete – differences and similarities. *Magazine of Concrete Research*, 57(6), pp.315–319.

Li, L.G. and Kwan, A.K.H., 2013. Concrete mix design based on water film thickness and paste film thickness. *Cement and Concrete Composites*, 39, pp.33–42.

Li, L.G. and Kwan, A. K. H., 2011. Mortar design based on water film thickness. *Construction and Building Materials*, 25(5), pp.2381–2390.

Li, S. and Liu, W.K., 2002. Meshfree and particle methods and their applications. *American Society of Mechanical Engineers*, 55(1), pp.1–34.

Liu, G.R. and Liu, M.B., 2003. Smoothed particle hydrodynamics: A Meshfree particle method. Singapore: World Scientific Publishing Co. Pte. Ltd. ISBN 981-238-456-1.

Liu, M.B. and Liu, G.R., 2010. Smoothed particle hydrodynamics (SPH): an overview and recent developments. *Archives of Computational Methods in Engineering*, 17, pp.25–76.

Lucy, L.B., 1977. A numerical approach to the testing of the fission hypothesis. *The Astronomical Journal*, 82, pp.1013–1024.

Martys, N., 2005. Study of a dissipative particle dynamics based approach for modeling suspensions. *Journal of Rheology*, 49(2), pp.401–424.

Martys, N. and Ferraris, C.F., 2002. Simulation of SCC Flow. *First North American Conference on the Design and Use of Self- Consolidating Concrete*, pp.27–30.

Mehta, P.K., 1994. Mineral admixtures for concrete-an overview of recent developments. *Advances in Cement and Concrete*. In: M.W. Grutzeck and S.L. Sarkar, eds., *Proceedings of the Engineering Foundation Conference*. New yourk, USA: American Society of Civil Engineers, pp.243–256.

Mindess, S., 1984. The effect of specimen size on the fracture energy of concrete. *Cement and Concrete Research*, 14, pp.431–436.

Monaghan, J. and Lattanzio, J., 1985. A refined particle method for astrophysical problems. *Astronomy and Astrophysics*, 149, pp.135–143.

Monaghan, J.J., 1994. Simulating free surface flows with SPH. *Journal of Computational Physics*, 110(2), pp.399–406.

Monaghan, J.J., 1996. Gravity currents and solitary waves. *Physica D: Nonlinear Phenomena*, 98(2), pp.523–533.

Monaghan, J.J. and Gingold, R.A., 1983. Shock simulation by the particle method SPH. *Journal of computational physics*, 52(2), pp.374–389.

Monaghan, J.J. and Kocharyan, A., 1995. SPH simulation of multi-phase flow. *Computer Physics Communications*, 87, pp.225–235.

- Mori, H. and Tanigawa, Y., 1992. Simulation methods for fluidity of fresh concrete. Nagoya University, Memoirs of the school of engineering, pp.71–134.
- Morris, J.P., Fox, P.J. and Zhu, Y., 1997. Modeling low Reynolds number incompressible flows using SPH. *Journal of Computational Physics*, 136, pp.214–226.
- Muralidhara, S., Prasad, B.K.R., Eskandari, H. and Karihaloo, B.L., 2010. Fracture process zone size and true fracture energy of concrete using acoustic emission. *Construction and Building Materials*, 24, pp.479–486.
- Muralidhara, S., Prasad, B.K.R., Karihaloo, B.L. and Singh, R.K., 2011. Size-independent fracture energy in plain concrete beams using tri-linear model. *Construction and Building Materials*, 25(7), pp.3051–3058.
- Murthy, A.R., Karihaloo, B.L., Iyer, N.R. and Prasad, B.K.R., 2013a. Bilinear tension softening diagrams of concrete mixes corresponding to their size-independent specific fracture energy. *Construction and Building Materials*, 47, pp.1160–1166.
- Murthy, A.R., Karihaloo, B.L., Iyer, N.R. and Prasad, B.K.R., 2013b. Determination of size-independent specific fracture energy of concrete mixes by two methods. *Cement and Concrete Research*, 50, pp.19–25.
- Nallathambi, P., Karihaloo, B.L. and Heaton, B.S., 1984. Effect of specimen and crack sizes, water/cement ratio and coarse aggregate texture upon fracture toughness of concrete. *Magazine of Concrete Research*, 36(129), pp.227–236.
- Nallathambi, P., Karihaloo, B.L. and Heaton, B.S., 1985. Various size effects in fracture of concrete. *Cement and Concrete Research*, 15(1), pp.117–126.
- Nanthagopalan, P. and Santhanam, M., 2009. Experimental investigations on the influence of paste composition and content on the properties of self-compacting concrete. *Construction and Building Materials*, 23(11), pp.3443–3449.
- Nawa, T., Izumi, T. and Edamatsu, Y., 1998. State-of-the-art report on materials and design of self-compacting concrete. In: *International Workshop on Self-Compacting Concrete*. pp.160–190.

Nehdi, M. and Rahman, M.A., 2004. Estimating rheological properties of cement pastes using various rheological models for different test geometry, gap and surface friction. *Cement and Concrete Research*, 34(11), pp.1993–2007.

Nepomuceno, M.C.S., Oliveira, L.A.P. and Lopes, S.M. R.R., 2014. Methodology for mix design of the mortar phase of self-compacting concrete using different mineral additions in binary blends of powders. *Construction and Building Materials*, 64(1), pp.82–94.

Neville, A.M., 1995. *Properties of Concrete*, 4th ed., Longman Scientific Group Limited, London.

Nguyen, T.L.H., Roussel, N. and Coussot, P., 2006. Correlation between L-box test and rheological parameters of a homogeneous yield stress fluid. *Cement and Concrete Research*, 36(10), pp.1789–1796.

Nikbin, I.M., Beygi, M.H.A., Kazemi, M.T., Vaseghi Amiri, J., Rabbanifar, S., Rahmani, E. and Rahimi, S., 2014a. A comprehensive investigation into the effect of aging and coarse aggregate size and volume on mechanical properties of self-compacting concrete. *Materials and Design*, 59, pp.199-210.

Nikbin, I.M., Beygi, M.H.A., Kazemi, M.T., Vaseghi Amiri, J., Rabbanifar, S., Rahmani, E. and Rahimi, S., 2014b. A comprehensive investigation into the effect of water to cement ratio and powder content on mechanical properties of self-compacting concrete. *Construction and Building Materials*, 57, pp. 69-80.

Nikbin, I.M., Beygi, M.H.A., Kazemi, M.T., Vaseghi Amiri, J., Rahmani, E., Rabbanifar, S. and Eslami, M., 2014c. Effect of coarse aggregate volume on fracture behavior of self-compacting concrete. *Construction and Building Materials*, 52, pp.137–145.

Noguchi, T., Oh, S.G. and Tomosawa, F., 1999. Rheological approach to passing ability between reinforcing bars of self-compacting concrete. In: A. Skrendahl and Ö. Petersson, eds., *Proceeding of the 1st International RILEM Symposium on Self-Compacting Concrete*. France: RILEM Publications S.A.R.L, pp.3–14.

Nuruddin, M.F., Chang, K.Y. and Azmee, N.M., 2014. Workability and compressive strength of ductile self- compacting concrete (DSCC) with various cement replacement materials. *Construction and Building Materials*, 55, pp.153–157.

Okamura, H., 1997. Self-compacting high-performance concrete. *Concrete international*, 19(7), pp.50–54.

Okamura, H. and Ouchi, M., 1999. Self-compacting concrete. development, present use and future. In: Å. Skarendahl and Ö. Petersson, eds., *Proceeding of the 1st International RILEM Symposium on Self-Compacting Concrete*. Stockholm, Sweeden: RILEM Publications S.A.R.L., pp.3–14.

Okamura, H. and Ouchi, M., 2003. Self-compacting concrete. *Journal of Advanced Concrete Technology*, 1(1), pp.5–15.

Okamura, H. and Ozawa, K., 1995. Mix design for self-compacting concrete. *Concrete Library of JSCE*, 25, pp.107–120.

Okamura, H., Ozawa, K. and Ouchi, M., 2000. Self-compacting concrete. *Structural Concrete*, 1, pp.3–17.

Olesen, J.F., 2001. Fictious crack propagation in fiber-reinforced-concrete beams. *Journal of Engineering Fracture Mechanics*, 127(3), pp.272–280.

Orowan, E., 1949. Fracture and strength of solids. *Reports on Progress in Physics*, 12, pp.185–232.

Ouchi, M., Hibino, M., Ozawa, K. and Okamura, H., 1998. A rational mx-design method for mortar in self-compacting concrete. In: Y.-B. Yang. and L.-J. Leu., eds., *Proceedings of the Sixth East-Asia- Pacific Conference on Structural Engineering and Construction*. Taipei, Taiwan, pp.1307–1312.

Ouchi, M., Nakamura, S., Osterberg, T., Hallberg, S.-E. and Lwin, M., 2003. Applications of self-compacting concrete in Japan, Europe and the United States. *ISHPC*, pp.1–20.

- Ozbay, E., Oztas, A., Baykasoglu, A. and Ozbebek, H., 2009. Investigating mix proportions of high strength self- compacting concrete by using Taguchi method. *Construction and Building Materials*, 23, pp.694–702.
- Panesar, D.K. and Shindman, B., 2011. Elastic properties of self- consolidating concrete. *Construction and Building Materials*, 25(8), pp.3334–3344.
- Papanastasiou, T.C., 1987. Flows of materials with yield. *Journal of Rheology*, 31(5), pp.385–404.
- Parra, C., Valcuende, M. and Gómez, F., 2011. Splitting tensile strength and modulus of elasticity of self-compacting concrete. *Construction and Building Materials*, 25, pp.201–207.
- Patzák, B. and Bittnar, Z., 2009. Modeling of fresh concrete flow. *Computers and Structures*, 87, pp.962–969.
- Persson, B., 2001. A comparison between mechanical properties of self-compacting concrete and the corresponding properties of normal concrete. *Cement and Concrete Research*, 31(2), pp.193–198.
- Petersson, Ö. and Billberg, P., 1999. Investigation on blocking of self- compacting concrete with different maximum aggregate size and use of viscosity agent instead filler. In: Å. Skarendahl and Ö. Petersson, eds., *Proceeding of the 1st International RILEM Symposium*. Stockholm, Sweden: RILEM Publications S.A.R.L., pp.333–344.
- Planas, J., Elices, M. and Guinea, G.V., 1992. Measurement of the fracture energy using three-point bend tests: Part 2-Influence of bulk energy dissipation. *Materials and Structures*, 25(5), pp.305–312.
- Prokopski, G. and Langier, B., 2000. Effect of water/cement ratio and silica fume addition on the fracture toughness and morphology of fractured surfaces of gravel concretes. *Cement and Concrete Research*, 30, pp.1427–1433.

Rabehi, M., Mezghiche, B. and Guettala, S., 2013. Correlation between initial absorption of the cover concrete, the compressive strength and carbonation depth. *Construction and Building Materials*, 45, pp.123–129.

RILEM-50FMC, 1985. Determination of the fracture energy of mortar and concrete by means of three-point bend tests on notched beams. *Materials and Structures*, 18, pp.285–290.

RILEM TC 174 SCC, 2000. Self- compacting concrete State-of-the-art report of RILEM technical committee 174-SCC. In: A. Skrendahl and Ö. Petersson, eds. France: RILEM Publications S.A.R.L.

Roussel, N., 2006a. A theoretical frame to study stability of fresh concrete. *Materials and Structures*, 39(1), pp.81–91.

Roussel, N., 2006b. Correlation between yield stress and slump: comparison between numerical simulations and concrete rheometers results. *Materials and Structures*, 39, pp.501–509.

Roussel, N. and Coussot, P., 2005. ‘Fifty-cent rheometer’ for yield stress measurements: from slump to spreading flow. *Journal of Rheology*, 49(3), pp.705–718.

Roussel, N., Geiker, M.R., Dufour, F., Thrane, L.N. and Szabo, P., 2007. Computational modeling of concrete flow: General overview. *Cement and Concrete Research*, 37(9), pp.1298–1307.

Rozière, E., Granger, S., Turcry, P. and Loukili, A., 2007. Influence of paste volume on shrinkage cracking and fracture properties of self-compacting concrete. *Cement and Concrete Composites*, 29(8), pp.626–636.

Saak, A., Jennings, H. M. and Shah, S.P., 2001. New methodology for designing self-compacting concrete. *ACI Materials Journal*, 98, pp.429–439.

Sebaibi, N., Benzerzour, M., Sebaibi, Y. and Abriak, N.-E., 2013. Composition of self compacting concrete (SCC) using the compressible packing model, the Chinese

method and the European standard. *Construction and Building Materials*, 43, pp.382–388.

Sedran, T. and de Larrard, F., 1999. Optimization of self-compacting concrete thanks to packing model packing model. In: Skarendahl A and Ö. Petersson, eds., *Proceeding of the 1st International RILEM Symposium on Self-Compacting Concrete*. Stockholm, Sweeden: RILEM Publications SARL, pp. 321-332.

Shao, S. and Lo, E.Y.M., 2003. Incompressible SPH method for simulating Newtonian and non-Newtonian flows with a free surface. *Advances in Water Resources*, 26(7), pp.787–800.

Shi, C., Wu, Z., Lv, K. and Wu, L., 2015. A review on mixture design methods for self-compacting concrete. *Construction and Building Materials*, 84, pp.387–398.

Shilstone, Sr., J.M., 1990. Concrete mixture optimization. *Concrete International*, 12, pp.33–39.

Siddique, R., Aggarwal, P. and Aggarwal, Y., 2012. Mechanical and durability properties of self- compacting concrete containing fly ash and bottom ash. *Journal of Sustainable Cement-Based Materials*, 1, pp.67–82.

Solenthaler, B. and Pajarola, R., 2009. Predictive-corrective incompressible SPH. *ACM Transactions on Graphics*, 28, pp.402–406.

Sonebi, M., 2004. Medium strength self-compacting concrete containing fly ash: Modelling using factorial experimental plans. *Cement and Concrete Research*, 34, pp.1199–1208.

Sonebi, M. and Cevik, A., 2009. Genetic programming based formulation for fresh and hardened properties of self-compacting concrete containing pulverised fuel ash. *Construction and Building Materials*, 23(7), pp.2614–2622.

Stang, H. and Olesen, J.F. 1998. On interpretation of bending Frc-materials. In: *FRAMCOS-3. Fracture mechanics of concrete structures*. Freiburg, Germany: Aedificatio Publishers, pp. 511–520.

- Struble, L. and Sun, G.K., 1995. Viscosity of portland cement paste as a function of concentration. *Advanced Cement Based Materials*, 2, pp.62–69.
- Su, J.K., Cho, S.W., Yang, C.C. and Huang, R., 2002. Effect of sand ratio on the elastic modulus of self-compacting concrete. *Journal of Marine Science and Technology*, 10, pp.8–13.
- Su, N., Hsu, K.-C. and Chai, H.-W., 2001. A simple mix design method for self-compacting concrete. *Cement and Concrete Research*, 31, pp.1799–1807.
- Su, N. and Miao, B., 2003. A new method for the mix design of medium strength flowing concrete with low cement content. *Cement and Concrete Composites*, 25(2), pp.215–222.
- Sun, Z., Voigt, T. and Shah, S.P., 2006. Rheometric and ultrasonic investigations of viscoelastic properties of fresh Portland cement pastes. *Cement and Concrete Research*, 36(2), pp.278–287.
- Švec, O., Skoček, J., Stang, H., Geiker, M.R. and Roussel, N., 2012. Free surface flow of a suspension of rigid particles in a non-Newtonian fluid: A lattice Boltzmann approach. *Journal of Non-Newtonian Fluid Mechanics*, 179–180, pp.32–42.
- Tada, H., Paris, P.C. and Irwin, G.R., 1985. *The stress analysis of cracks handbook*. St. Louis MO: Paris Productions.
- Takada, K. and Tangtermsirikul., S., 2000. Testing of Fresh Concrete. In: A. Skarendahl and Ö. Petersson, eds., *Self-compacting concrete: state-of-the-art report of RILEM Technical Committee, 174-SCC*. Cachan Cedex, France: RILEM Publications S.A.R.L., pp.25–39.
- Takeda, H., Miyama, S.M. and Sekiya, M., 1994. Numerical simulation of viscous flow by smoothed particle hydrodynamics. *Progress of Theoretical Physics*, 92(5), pp.939–960.
- Tattersall, G.H. and Banfill, P.F.G., 1983. *The rheology of fresh concrete*. Pitman Advanced Publishing Program, Boston. London: Melbourne.

Tattersall, H., 1991. Workability and quality control of concrete. London: Taylor & Francis Publication. ISBN: 0419148604.

Thrane, L.N., 2007. Form filling with self-compacting concrete. Ph.D. Thesis. Technical University of Denmark.

Thrane, L.N., Szabo, P., Geiker, M., Glavind, M. and Stang, H., 2004. Simulation of the test method ' L-Box ' for self-compacting concrete. Annual Transactions of the Nordic Rheology Society, 12, pp.47–54.

Tregger, N., Ferrara, L. and Shah, S.P., 2007. Empirical relationships between viscosity and flow time measurements from mini-slump tests for cement pastes formulated from SCC. In: G. De Schutter and V. Boel, eds., Proceeding of the 5th International RILEM Symposium-SCC. Ghent, Belgium: RILEM Publications S.A,R,L, pp.273–278.

Tregger, N., Gregori, A., Ferrara, L. and Shah, S.P., 2012. Correlating dynamic segregation of self-consolidating concrete to the slump-flow test. Construction and Building Materials, 28(1), pp.499–505.

Ulfkjær, J.P., Krenk, S. and Brincker, R., 1995. Analytical model for fictitious crack propagation in concrete beams. Journal of Engineering Mechanics, 121(1), pp.7–15.

Utsi, S., Emborg, M. and Carlsward, J., 2003. Relation between workability and rheological parameters. In: O. Wallevik and I. Nielsson, eds., Proceeding of the 3rd International RILEM Symposium on Self-compacting concrete. Cachan, France: RILEM Publications S.A.R.L, pp.311-322.

Vasilic, K., Roussel, N., Meng, B. and Kühne, H.C., 2010. Computational modeling of SCC flow through reinforced sections in self-compacting concrete (SCC). In: K.H. Khayat and D. Feys, eds., Proceedings of the International RILEM Symposium on Self-Compacting Concrete. Design, Production and Placement of Self-Consolidating Concrete. Canada, pp.187–195.

Vesenjak, M. and Ren, Z., 2007. Application aspects of the meshless SPH method. Journal of the Serbian Society for Computational Mechanics, 1(1), pp.74–86.

Wallevik, J.E., 2003. Rheology of particle suspension: fresh concrete, mortar and cement paste with various types of lignosulfates. The Norwegian University of Science and Technology (NTUN), Norway.

Wallevik, O.H. and Wallevik, J.E., 2011. Rheology as a tool in concrete science: The use of rheographs and workability boxes. *Cement and Concrete Research*, 41, pp.1279–1288.

Wang, X., Wang, K., Taylor, P. and Morcous, G., 2014. Assessing particle packing based self-consolidating concrete mix design method. *Construction and Building Materials*, 70, pp.439–452.

Welton, W., 1998. Two-dimensional PDF/SPH simulations of compressible turbulent flows. *Journal of Computational Physics*, 139(2), pp.410–443.

Wróblewski, P., Boryczko, K. and Kopeć, M., 2007. SPH-A comparison of neighbor search methods based on constant number of neighbors and constant cut-off radius. *Task Quarterly*, 11, pp.273–283.

Wu, Q. and An, X., 2014. Development of a mix design method for SCC based on the rheological characteristics of paste. *Construction and Building Materials*, 53, pp.642–651.

Xie, Y., Liu, B., Yin, J. and Zhou, S., 2002. Optimum mix parameters of high-strength self-compacting concrete with ultrapulverized fly ash. *Cement and Concrete Research*, 32, pp.477–480.

Yahia, A., Tanimura, M. and Shimoyama, Y., 2005. Rheological properties of highly flowable mortar containing limestone filler-effect of powder content and W/C ratio. *Cement and Concrete Research*, 35, pp.532–539.

Ye, G., Liu, X., De Schutter, G., Poppe, A.-M. and Taerwe, L., 2007. Influence of limestone powder used as filler in SCC on hydration and microstructure of cement pastes. *Cement and Concrete Composites*, 29, pp.94–102.

Yen, T., Tang, C., Chang, C. and Chen, K., 1999. Flow behaviour of high strength high-performance concrete. *Cement and Concrete Composites*, 21, pp.413–424.

Zhu, W. and Gibbs, J.C., 2005. Use of different limestone and chalk powders in self-compacting concrete. *Cement and Concrete Research*, 35(8), pp.1457–1462.

Zhu, Y., Fox, P.J. and Morris, J.P., 1999. A pore-scale numerical model for flow through porous media. *International Journal for numerical and analytical methods in geomechanics*, 23(9), pp.881–904.

Appendix A

**A MATLAB code for designing SCC
mixes**

A MATLAB code for designing Self-Compacting Concrete mixes 2014- 2015

according to its target compressive strength and plastic viscosity

```

%*****
***
%      List of variables
%      Name          Description
%      -----      -
%      WCM           Water to cementitious materials (binder) ratio
%      PV            Paste viscosity (values based on w/cm and sp dosage)
%      TMV           Target mix viscosity
%      Z, U and X    Random names are used to solve equations
%      t1, t2 and t3 Factors are chosen arbitrarily such that
t1*t2*t3=1
%      H            Unity factor (H=t1*t2*t3)
%      CM           Cementitious materials
%      WTR          Water content (kg)
%      CEM          Cement content (kg)
%      G            Cement replacement materials (kg) e.g. GGBS
%      SP           Superplasticizer dosage (kg)
%      VPS          Volume of paste per cubic meter
%      FLP          Volume fraction of filler (materials < 125µm)
%      FS           Volume fraction of fine aggregate
%      FG           Volume fraction of coarse aggregate
%      WLP          Mass of filler
%      WS           Mass of fine aggregate
%      WG           Mass of coarse aggregate
%      VLP          Volume of filler per cubic meter
%      VS           Volume of fine aggregate per cubic meter
%      VG           Volume of coarse aggregate per cubic meter
%      TV           Total volume of the mix (m³)
%      PSRATIO      Paste to solid ratio
%      FFLP         A factor larger than unity that predicts the
%                  increase in the plastic viscosity induced by
%                  addition of filler
%      FFS          A factor larger than unity that predicts the
%                  increase in the plastic viscosity induced by
%                  addition of fine aggregate
%      FFG          A factor larger than unity that predicts the
%                  increase in the plastic viscosity induced by
%                  addition of coarse aggregate
%      AMV          Actual mix plastic viscosity calculated by
%                  micromechanical procedure
%      ERR          Percentage difference between target (TMV) and
%                  actual mix viscosity (AMV)
%      PWDR         Powder content (Any materials<=125µm i.e.
%                  (cementitious materials and filler))
%      WTPR         Water to powder ratio
%      FIRSTLINE    Normalized cementitious materials content
%      SECONDLINE   Normalized cementitious materials and filler
%                  contents
%      THIRDLIN     Normalized cementitious materials, filler and fine
%                  aggregate contents
%      FOURTHLINE   Normalized cementitious materials, filler, fine
%                  aggregate and coarse aggregate contents
%*****
***
%*****
***

```

```

clear
clc
% Input the water to binder (cementitious materials) ratio from Eq.
3.1
WCM=0.63;
% Input the paste viscosity from Table 3.1
PV=0.11;
%*****
***
s=0;
p=0;
for TMV=3.5:0.05:15
Z=0.524^ (-1.9)*0.63^ (-1.9)*0.74^ (-1.9);
U= (Z*TMV/PV) ^ (-1/1.9);
X=U^ (1/3) ;
t1=0.424/X ;
t2=0.53/X ;
t3=0.64/X ;
a=linspace (0, t1, 200) ;
b=linspace (0, t2, 200) ;
c=linspace (0, t3, 200) ;
for i= 1:200
for j= 1:200
for k= 1:200

H=a (i)*b (j)*c (k);
if (H<=1.0001 && H>=0.9999)
s=s+1;
% input the cementitious materials contents limits
for CM=230:5:350
WTR(s) =CM*WCM;
CEM(s) =0.75*CM;
GG(s) =0.25*CM;
SP(s) =0.005*CM;
VPS(s) =CEM(s)/2950+GG(s)/2400+WTR(s)/1000+SP(s)/1070+0.02;

FLP(s) =0.524-a (i)*X;
FS(s) =0.63-b (j)*X;
FG(s) =0.74-c (k)*X;
WLP(s) =2400*FLP(s)*VPS(s)/ (1-FLP(s));
WS(s) =2650*FS(s)*(VPS(s) + (WLP(s)/2400))/ (1-FS(s));
WG(s) =2800*FG(s)*(VPS(s) + (WLP(s)/2400) + (WS(s)/2650))/ (1-
FG(s));

VLP(s) =WLP(s)/2400;
VS(s) =WS(s)/2650;
VG(s) =WG(s)/2800;
TV(s) =VLP(s) +VS(s) +VG(s) +VPS(s)-0.02;

WCEMnew(s) =CEM(s)*0.98/TV(s);
WGGnew(s) =GG(s)*0.98/TV(s);
WWTRnew(s) =WTR(s)*0.98/TV(s);
WSPnew(s) =SP(s)*0.98/TV(s);
WLPnew(s) =WLP(s)*0.98/TV(s);
WSnew(s) =WS(s)*0.98/TV(s);
WGnew(s) =WG(s)*0.98/TV(s);

VCEMnew(s) =WCEMnew(s)/2950;
VGGnew(s) =WGGnew(s)/2400;
VWTRnew(s) =WWTRnew(s)/1000;

```

```

VSPnew(s) =WSPnew(s)/1070;
VLPnew(s) =WLPnew(s)/2400;
VSnew(s) =WSnew(s)/2650;
VGnew(s) =WGnew(s)/2800;
TVnew(s) =VCEMnew(s) +VGGnew(s) +VWTRnew(s) +VSPnew(s)
+VLPnew(s)+VSnew(s) +VGnew(s) +0.02;

WCMnew(s) =WCEMnew(s) +WGGnew(s);
STAG(s) =VSnew(s)/ (VSnew(s) +VGnew(s))*100;
GTAG(s) =VGnew(s)/ (VSnew(s) +VGnew(s))*100;
VPSnew(s) =VCEMnew(s) +VGGnew(s) +VWTRnew(s) +VSPnew(s) +0.02;
PSRATIO(s) = (VPSnew(s) +VLPnew(s))/ (VSnew(s) +VGnew(s));
FLPnew(s) =VLPnew(s)/ (VLPnew(s) +VPSnew(s));
FSnew(s) =VSnew(s)/ (VSnew(s) +VLPnew(s) +VPSnew(s));
FGnew(s) =VGnew(s)/ (VGnew(s) +VSnew(s) +VLPnew(s) +VPSnew(s));
FFLP(s) = (1-FLPnew(s)/0.524) ^ (-1.9);
FFS(s) = (1-FSnew(s)/0.63) ^ (-1.9);
FFG(s) = (1-FGnew(s)/0.74) ^ (-1.9);
AMV(s) =PV*FFLP(s)*FFS(s)*FFG(s);
ERR(s) = (AMV(s)-TMV)/TMV*100;
PWDR=WCMnew(s) +WLPnew(s);
WTPR(s) =VWTRnew(s)/ (VLPnew(s) +VCEMnew(s) +VGGnew(s))*100;

A=TVnew(s);
B=WLPnew(s);
C=WSnew(s);
D=WGnew(s);
E=STAG(s);
F=GTAG(s);
G=PSRATIO(s);
I=AMV(s);
L=ERR(s);
J=WTPR(s);
K=WCMnew(s);
R=WSPnew(s);
WCMRnew(s) =WWTRnew(s)/WCMnew(s);
EEE=WCMRnew(s);
WWTR=WWTRnew(s);

% Check the typical range of SCC mix compositions according to
EFNARC
if (PWDR>=380 && PWDR<=600)
if (WWTR>=150 && WWTR<=210)
if (D>=750 && D<=1000)
if (J>=85 && J<=130)
if (E>=48 && E<=55)
% Check the percentage difference between (TMV) and (AMV)
if (L>=-5 && L<=5)

p=p+1;
AA (p) =K/I;
BB (p) = (K+B)/I;
CC (p) = (K+B+C)/I;
DD (p) = (K+B+C+D)/I;
EE (p) =C/I;
FF (p) =D/I;
RR (p) =B/I;
TT (p) =(C+D)/I;
StoTOTAL (p) =E/I;

```

```

SANDplusLP (p) = (B+C)/I;
CMplusSAND (p) = (K+C)/I;

AAA=AA (p);
BBB=BB (p);
CCC=CC (p);
DDD=DD (p);

GGG=EE (p);
FFF=FF (p);
RRR=RR (p);
TTT=TT (p);
STST=StoTOTAL (p);
SLP=SANDplusLP (p);
CMSAND=CMplusSAND (p);

TotalVolume (p) =A;
Limestone (p) =B;
Sand (p) =C;
CoarseAGG (p) =D;
StoTAG (p) =E;
GtoTAG (p) =F;
PtoSRATIO (p) =G;
Viscosity (p) =I;
ERROR (p) =L;
SUPER (p) =R;
WATER (p) =WWTR;
CMmaterials (p) =K;
WtoPRatio (p) =J;
FIRSTLINE (p) =AAA;
SECONDLINE (p) =BBB;
THIRDLINE (p) =CCC;
FOURTHLINE (p) =DDD;

WATERtoCM (p) =EEE;
SANDtoVISCOSITY (p) =GGG;
GRAVELtoVISCOSITY (p) =FFF;
LIMEtoVISCOSITY (p) =RRR;
CplusFA (p) =TTT;
StoTOTALAGG (p) =STST;
LPplusLSAND (p) =SLP;
CMandSAND (p) =CMSAND;

end
end
end
end
end
end

end
end
end
end
end

%*****
***

```

```

% print the results in order to plot the graphs
GtoTAG = round (GtoTAG);
Limestone = round (Limestone);
Sand = round (Sand);
CoarseAGG = round (CoarseAGG);
StoTAG = round (StoTAG);
TotalVolume = round (TotalVolume*1000)/1000;
ERR = round (ERR);
PSRATIO = round (PSRATIO);

%*****
***

% desired parameters to be printed in the output sheet

myMatrix =
[CMmaterials;Limestone;Sand;CoarseAGG;WATER;SUPER;TotalVolume;WATERtoCM;WtoPRatio;StoTAG;GtoTAG;PtoSRATIO;ERROR;Viscosity;FIRSTLINE;SECONDLINE;THIRDLINE;FOURTHLINE]';

HeaderNames='CMmaterials,Limestone,Sand,CoarseAGG,WATER,SUPER,TotalVolume,WATERtoCM,WtoPRatio,StoTAG,GtoTAG,PtoSRATIO,ERROR,Viscosity,FIRSTLINE,SECONDLINE,THIRDLINE,FOURTHLINE';
%*****
***

% preferable output sheet name printed here (change the underline text)

fileName ='choose output file name here.csv';
outid = fopen (fileName, 'w+');
fprintf (outid, '%s', HeaderNames);
fclose (outid);

dlmwrite(fileName,myMatrix,'roffset',1,'-append', 'precision', 4);
% you may need to increase precision to allow all digits to be saved
disp (strcat ('Generated report ''', fileName, '''))
%*****
***

%*****
***

%*****
***

%*****
***

```

Appendix B

**The constituents of the SCC mixes
according to their plastic viscosities**

Table B.1. The constituents of SCC mixes according to their plastic viscosities (30 MPa)

<i>cm</i> kg/m ³	<i>W</i> kg/m ³	<i>SP</i> kg/m ³	<i>w/cm</i>	<i>LP</i> kg/m ³	<i>FA</i> kg/m ³	<i>CA</i> kg/m ³	<i>Vol.</i> m ³	<i>p/s</i>	<i>Viscosity</i> Pa s
338.9	213.5	1.694	0.63	217	704	804	1	0.8086	3.88
336.3	211.9	1.682	0.63	222	705	805	1	0.8068	4.012
336.1	211.7	1.68	0.63	180	800	754	1	0.7503	4.267
325.1	204.8	1.626	0.63	187	740	840	1	0.7263	4.546
321.7	202.6	1.608	0.63	188	744	844	1	0.7173	4.754
320.5	201.9	1.603	0.63	202	767	807	1	0.732	4.992
320.5	201.9	1.602	0.63	270	727	769	1	0.8213	5.201
313	197.2	1.565	0.63	216	752	827	1	0.7267	5.442
311.7	196.4	1.558	0.63	245	744	805	1	0.7598	5.673
310.3	195.5	1.552	0.63	232	781	785	1	0.7387	5.901
310.3	195.5	1.552	0.63	275	766	751	1	0.7948	6.139
304.1	191.6	1.52	0.63	184	812	827	1	0.6625	6.366
300.4	189.3	1.502	0.63	240	760	826	1	0.7188	6.599
296	186.5	1.48	0.63	224	755	861	1	0.6876	6.831
300.5	189.3	1.502	0.63	173	854	803	1	0.641	7.063
299.6	188.8	1.498	0.63	199	861	769	1	0.668	7.299
297.6	187.5	1.488	0.63	200	864	771	1	0.6631	7.531
290.9	183.3	1.455	0.63	220	809	824	1	0.6684	7.765
293.8	185.1	1.469	0.63	189	872	785	1	0.6408	8.001
294.1	185.3	1.471	0.63	166	895	787	1	0.6164	8.228
287.4	181	1.437	0.63	215	839	808	1	0.6522	8.467
287.9	181.4	1.439	0.63	151	874	844	1	0.584	8.7
280.1	176.5	1.401	0.63	242	782	857	1	0.6638	8.939
277.6	174.9	1.388	0.63	191	808	896	1	0.6003	9.16
283.7	178.7	1.418	0.63	206	876	789	1	0.6328	9.396
280.5	176.7	1.403	0.63	162	869	857	1	0.5772	9.634
278.3	175.3	1.391	0.63	187	862	842	1	0.5976	9.868
273.9	172.6	1.37	0.63	247	804	844	1	0.6532	10.15
281.4	177.3	1.407	0.63	167	913	802	1	0.5843	10.33
274.1	172.7	1.371	0.63	150	864	894	1	0.5498	10.56
268.7	169.3	1.344	0.63	161	830	932	1	0.5483	10.79
272.5	171.7	1.362	0.63	159	874	877	1	0.5549	11.03
270.6	170.4	1.353	0.63	175	880	858	1	0.5665	11.49
267.3	168.4	1.337	0.63	198	862	859	1	0.582	11.77
269	169.5	1.345	0.63	188	888	839	1	0.5758	11.96
263.2	165.8	1.316	0.63	194	845	894	1	0.5676	12.19
261.3	164.6	1.306	0.63	236	805	892	1	0.6071	12.19
267.3	168.4	1.336	0.63	200	891	826	1	0.5843	12.43
259.2	163.3	1.296	0.63	237	807	895	1	0.6025	12.66
257.8	162.4	1.289	0.63	218	816	910	1	0.5794	12.89
259.2	163.3	1.296	0.63	195	849	899	1	0.5592	13.12

260.5	164.1	1.303	0.63	236	858	838	1	0.605	13.4
262	165.1	1.31	0.63	218	888	823	1	0.5904	13.59
258.8	163.1	1.294	0.63	236	860	840	1	0.6012	13.84
257.9	162.5	1.29	0.63	178	875	895	1	0.5387	14.07
260.1	163.9	1.301	0.63	179	902	859	1	0.5454	14.3
256.7	161.7	1.283	0.63	234	869	840	1	0.593	14.55
255.1	160.7	1.276	0.63	234	871	841	1	0.5897	14.99
253.5	159.7	1.267	0.63	145	870	951	1	0.4974	15.26

Table B.2. The constituents of SCC mixes according to their plastic viscosities (40 MPa)

<i>Cm</i> kg/m ³	<i>W</i> kg/m ³	<i>SP</i> kg/m ³	<i>w/cm</i>	<i>LP</i> kg/m ³	<i>FA</i> kg/m ³	<i>CA</i> kg/m ³	<i>Vol.</i> m ³	<i>p/s</i>	<i>Viscosity</i> Pa s
383.3	218.5	1.917	0.57	164	709	801	1	0.8057	4.908
383	218.3	1.915	0.57	136	765	776	1	0.7673	5.116
379.3	216.2	1.897	0.57	137	770	780	1	0.7577	5.321
375.6	214.1	1.878	0.57	209	724	754	1	0.8433	5.537
373.7	213	1.869	0.57	109	796	799	1	0.7072	5.744
369.5	210.6	1.848	0.57	212	736	754	1	0.8288	5.955
366.4	208.9	1.832	0.57	213	739	757	1	0.8205	6.163
367.8	209.6	1.839	0.57	132	828	755	1	0.7187	6.372
359.8	205.1	1.799	0.57	235	714	775	1	0.8303	6.588
357.1	203.6	1.786	0.57	227	728	777	1	0.8112	6.795
353	201.2	1.765	0.57	92	782	888	1	0.6331	7.006
350.6	199.9	1.753	0.57	92	785	891	1	0.6275	7.22
355.5	202.6	1.778	0.57	123	845	779	1	0.6744	7.424
346.2	197.4	1.731	0.57	93	790	897	1	0.6173	7.634
347.5	198.1	1.738	0.57	241	760	752	1	0.8008	7.869
345.9	197.2	1.73	0.57	242	762	754	1	0.7966	8.027
347.5	198	1.737	0.57	131	857	778	1	0.6634	8.266
345.6	197	1.728	0.57	131	859	780	1	0.659	8.474
337.1	192.1	1.685	0.57	250	732	799	1	0.7814	8.683
339.6	193.6	1.698	0.57	89	840	866	1	0.5969	8.907
336.4	191.8	1.682	0.57	100	832	870	1	0.6011	9.101
330.1	188.2	1.651	0.57	108	798	912	1	0.5947	9.311
334	190.4	1.67	0.57	155	845	798	1	0.6557	9.527
330.2	188.2	1.651	0.57	221	797	781	1	0.7253	9.733
332.3	189.4	1.661	0.57	105	856	849	1	0.5967	9.94
329.4	187.8	1.647	0.57	156	851	803	1	0.6451	10.16
324.1	184.7	1.62	0.57	154	821	850	1	0.6303	10.37
318.7	181.7	1.594	0.57	166	784	890	1	0.6303	10.57
325.8	185.7	1.629	0.57	182	856	776	1	0.6661	10.78
324.4	184.9	1.622	0.57	182	857	778	1	0.663	10.99
316.1	180.2	1.58	0.57	211	780	847	1	0.6747	11.2
317.4	180.9	1.587	0.57	148	829	867	1	0.6068	11.41
316	180.1	1.58	0.57	110	826	917	1	0.5645	11.63
314.9	179.5	1.575	0.57	148	832	869	1	0.6013	11.84
309.6	176.5	1.548	0.57	155	797	911	1	0.5964	12.04
319.5	182.1	1.598	0.57	99	878	866	1	0.561	12.25
316.9	180.6	1.585	0.57	125	876	844	1	0.5818	12.47
315.9	180.1	1.579	0.57	125	878	845	1	0.5796	12.67
314.9	179.5	1.575	0.57	183	882	777	1	0.6392	12.88
313.9	178.9	1.569	0.57	183	883	778	1	0.6368	13.09

Appendix B : The constituents SCC mixes

311.5	177.6	1.558	0.57	120	870	871	1	0.5637	13.31
308.5	175.8	1.542	0.57	135	859	872	1	0.573	13.52
305.9	174.4	1.529	0.57	134	848	893	1	0.5651	13.74
304.8	173.7	1.524	0.57	134	849	895	1	0.5628	13.98
301.8	172	1.509	0.57	140	833	911	1	0.5628	14.16
300.8	171.5	1.504	0.57	141	834	913	1	0.5607	14.38
299.6	170.8	1.498	0.57	141	836	914	1	0.5583	14.65
310.1	176.8	1.551	0.57	124	914	824	1	0.5646	14.77
298.3	170	1.491	0.57	141	837	916	1	0.5554	14.98

Table B.3. The constituents of SCC mixes according to their plastic viscosities (50 MPa)

<i>Cm</i> kg/m ³	<i>W</i> kg/m ³	<i>SP</i> kg/m ³	<i>w/cm</i>	<i>LP</i> kg/m ³	<i>FA</i> kg/m ³	<i>CA</i> kg/m ³	<i>Vol.</i> <i>m</i> ³	<i>P/s</i>	<i>Viscosity</i> <i>Pa s</i>
412.8	218.8	2.064	0.53	125	727	798	1	0.7879	5.604
410	217.3	2.05	0.53	123	738	795	1	0.7774	5.797
405.2	214.8	2.026	0.53	153	713	799	1	0.8038	5.992
402.1	213.1	2.01	0.53	154	716	803	1	0.7955	6.181
403.3	213.8	2.017	0.53	100	805	768	1	0.7292	6.57
403	213.6	2.015	0.53	100	806	769	1	0.7285	6.592
398.1	211	1.99	0.53	134	778	770	1	0.7585	6.744
393.3	208.4	1.966	0.53	200	718	769	1	0.8337	6.931
390.5	207	1.952	0.53	201	721	772	1	0.8264	7.133
386.9	205.1	1.935	0.53	202	724	776	1	0.8173	7.4
385.4	204.3	1.927	0.53	202	726	777	1	0.8135	7.517
390.1	206.8	1.951	0.53	113	839	750	1	0.7109	7.772
383.6	203.3	1.918	0.53	193	765	751	1	0.7958	7.88
384.6	203.9	1.923	0.53	96	827	797	1	0.6765	8.076
378	200.4	1.89	0.53	144	786	800	1	0.7166	8.266
372.7	197.5	1.863	0.53	107	768	876	1	0.6592	8.453
377.2	199.9	1.886	0.53	167	810	751	1	0.7434	8.649
372.3	197.3	1.862	0.53	200	765	772	1	0.7726	8.834
370.9	196.6	1.854	0.53	153	797	796	1	0.7095	9.022
366.9	194.4	1.834	0.53	198	755	798	1	0.7542	9.223
365.6	193.8	1.828	0.53	178	775	804	1	0.7257	9.4
364.5	193.2	1.823	0.53	180	782	796	1	0.7255	9.599
366.5	194.2	1.832	0.53	111	829	822	1	0.6486	9.78
364.8	193.3	1.824	0.53	111	831	824	1	0.6448	9.987
364.1	193	1.821	0.53	111	832	825	1	0.6432	10.07
359.5	190.5	1.798	0.53	216	778	771	1	0.7578	10.36
358	189.8	1.79	0.53	216	780	772	1	0.7542	10.54
353.5	187.4	1.768	0.53	101	797	900	1	0.607	10.78
355.1	188.2	1.776	0.53	121	820	849	1	0.6325	10.92
353.8	187.5	1.769	0.53	121	821	851	1	0.6295	11.11
352.1	186.6	1.761	0.53	121	823	853	1	0.6259	11.34
351.1	186.1	1.756	0.53	121	824	854	1	0.6238	11.49
347.3	184.1	1.736	0.53	102	804	908	1	0.5936	11.68
352.8	187	1.764	0.53	153	865	770	1	0.663	11.99
343.3	181.9	1.716	0.53	149	793	873	1	0.6357	12.07
351.3	186.2	1.756	0.53	153	867	771	1	0.6595	12.25
345.4	183	1.727	0.53	130	833	848	1	0.6198	12.44
344.1	182.4	1.721	0.53	130	834	850	1	0.6171	12.65
347.8	184.3	1.739	0.53	154	871	775	1	0.6518	12.82
340.9	180.7	1.705	0.53	118	827	880	1	0.5966	13.01
343.8	182.2	1.719	0.53	93	852	876	1	0.5766	13.2

Appendix B : The constituents SCC mixes

347.4	184.1	1.737	0.53	114	890	802	1	0.6068	13.39
337	178.6	1.685	0.53	188	815	822	1	0.6644	13.58
337.7	179	1.689	0.53	191	830	800	1	0.6702	13.77
333.6	176.8	1.668	0.53	212	791	827	1	0.6843	13.96
345.2	183	1.726	0.53	107	904	801	1	0.5941	14.15
337.4	178.8	1.687	0.53	186	858	777	1	0.6632	14.34
329.9	174.9	1.65	0.53	133	814	904	1	0.5871	14.54
335.4	177.8	1.677	0.53	192	857	776	1	0.6648	14.72
339.5	180	1.698	0.53	105	893	828	1	0.5801	14.91

Table B.4. The constituents of SCC mixes according to their plastic viscosities (60 MPa)

<i>Cm</i> kg/m ³	<i>W</i> kg/m ³	<i>SP</i> kg/m ³	<i>w/cm</i>	<i>LP</i> kg/m ³	<i>FA</i> kg/m ³	<i>CA</i> kg/m ³	<i>Vol.</i> m ³	<i>p/s</i>	<i>Viscosity</i> Pa s
453	212.9	2.265	0.47	124	727	775	1	0.8147	6.504
449.9	211.5	2.25	0.47	137	716	778	1	0.8247	6.641
447	210.1	2.235	0.47	138	719	781	1	0.8174	6.812
444.2	208.8	2.221	0.47	116	732	799	1	0.7801	6.98
442.4	207.9	2.212	0.47	109	744	799	1	0.7663	7.15
437.5	205.6	2.188	0.47	109	728	826	1	0.7546	7.32
435.6	204.7	2.178	0.47	145	719	799	1	0.7965	7.491
434.8	204.4	2.174	0.47	110	752	807	1	0.7483	7.668
431.4	202.8	2.157	0.47	133	737	804	1	0.7696	7.835
428.3	201.3	2.142	0.47	147	726	806	1	0.779	8.012
426.7	200.5	2.133	0.47	149	733	800	1	0.7783	8.19
428.4	201.3	2.142	0.47	162	760	752	1	0.7997	8.348
422.4	198.5	2.112	0.47	150	737	804	1	0.7683	8.528
424.3	199.4	2.121	0.47	163	765	757	1	0.7899	8.682
422.3	198.5	2.112	0.47	163	767	758	1	0.7853	8.85
422.8	198.7	2.114	0.47	111	806	777	1	0.7192	9.021
419.1	197	2.096	0.47	161	778	757	1	0.774	9.191
415	195	2.075	0.47	110	778	826	1	0.6991	9.362
412.3	193.8	2.062	0.47	157	757	799	1	0.7509	9.531
408.4	191.9	2.042	0.47	167	735	820	1	0.7543	9.704
413.5	194.4	2.068	0.47	152	802	755	1	0.7473	9.874
404.1	189.9	2.021	0.47	153	739	842	1	0.7253	10.04
408.2	191.8	2.041	0.47	192	766	758	1	0.7855	10.21
400.8	188.4	2.004	0.47	154	742	846	1	0.7181	10.38
407	191.3	2.035	0.47	158	806	759	1	0.7388	10.55
397.7	186.9	1.988	0.47	154	745	849	1	0.7111	10.72
397.4	186.8	1.987	0.47	189	735	820	1	0.7541	10.89
397.8	187	1.989	0.47	142	779	827	1	0.6965	11.07
397.1	186.6	1.985	0.47	144	785	820	1	0.6976	11.23
393.1	184.8	1.966	0.47	195	736	821	1	0.7507	11.4
391.6	184.1	1.958	0.47	191	740	826	1	0.7413	11.57
398	187.1	1.99	0.47	95	830	828	1	0.6423	11.75
389	182.8	1.945	0.47	196	740	826	1	0.7416	11.91
388.7	182.7	1.943	0.47	102	784	890	1	0.6294	12.08
386.4	181.6	1.932	0.47	197	743	828	1	0.7358	12.25
385.2	181.1	1.926	0.47	161	767	847	1	0.689	12.42
384	180.5	1.92	0.47	161	769	848	1	0.6864	12.6
385.1	181	1.926	0.47	109	799	874	1	0.6293	12.79
381.4	179.2	1.907	0.47	162	771	851	1	0.6809	12.96
384.6	180.8	1.923	0.47	146	810	820	1	0.6703	13.1
386.1	181.5	1.931	0.47	141	833	799	1	0.668	13.29

385	180.9	1.925	0.47	141	834	800	1	0.6656	13.46
384	180.5	1.92	0.47	142	835	801	1	0.6636	13.62
380.2	178.7	1.901	0.47	147	815	825	1	0.6611	13.78
374.4	176	1.872	0.47	199	752	844	1	0.709	13.95
375.4	176.4	1.877	0.47	199	772	820	1	0.7113	14.12
381	179.1	1.905	0.47	159	845	778	1	0.6764	14.29
373.3	175.4	1.866	0.47	116	799	894	1	0.6109	14.46
372.3	175	1.861	0.47	116	800	895	1	0.6089	14.63
369.2	173.5	1.846	0.47	200	757	849	1	0.698	14.8

Table B.5. The constituents of SCC mixes according to their plastic viscosities (70 MPa)

<i>Cm</i> kg/m ³	<i>W</i> kg/m ³	<i>SP</i> kg/m ³	<i>w/cm</i>	<i>LP</i> kg/m ³	<i>FA</i> kg/m ³	<i>CA</i> kg/m ³	<i>Vol.</i> m ³	<i>p/s</i>	<i>Viscosity</i> <i>Pa s</i>
496	198.4	2.48	0.4	128	704	791	1	0.8249	7.414
491.3	196.5	2.456	0.4	130	718	784	1	0.8147	7.769
490.6	196.2	2.453	0.4	130	719	785	1	0.8132	7.811
490.1	196	2.451	0.4	130	719	785	1	0.8121	7.841
487.1	194.8	2.435	0.4	130	722	788	1	0.8051	8.036
485	194	2.425	0.4	131	724	790	1	0.8005	8.172
488.1	195.2	2.441	0.4	110	777	752	1	0.7805	8.345
483	193.2	2.415	0.4	108	759	784	1	0.765	8.503
480.8	192.3	2.404	0.4	161	735	752	1	0.8314	8.655
480.4	192.2	2.402	0.4	130	769	754	1	0.7877	8.822
476.5	190.6	2.383	0.4	162	739	756	1	0.8216	8.972
471.6	188.7	2.358	0.4	130	742	801	1	0.7665	9.17
470	188	2.35	0.4	130	743	803	1	0.7629	9.3
468.2	187.3	2.341	0.4	130	745	805	1	0.7591	9.444
466.4	186.5	2.332	0.4	130	746	807	1	0.7551	9.598
464	185.6	2.32	0.4	131	749	809	1	0.75	9.797
465.6	186.2	2.328	0.4	141	771	771	1	0.7664	9.943
463.7	185.5	2.318	0.4	141	772	773	1	0.7623	10.11
452	180.8	2.26	0.4	139	738	837	1	0.7324	10.69
450.1	180	2.25	0.4	139	739	839	1	0.7285	10.88
447.2	178.9	2.236	0.4	140	742	842	1	0.7225	11.17
445.4	178.2	2.227	0.4	140	743	844	1	0.7189	11.35
444.5	177.8	2.222	0.4	140	744	845	1	0.7169	11.45
446.2	178.5	2.231	0.4	148	772	802	1	0.7302	11.68
449.3	179.7	2.246	0.4	124	810	784	1	0.7078	11.8
441.1	176.4	2.205	0.4	137	760	839	1	0.7053	11.96
448.8	179.5	2.244	0.4	124	828	766	1	0.7068	12.11
445.2	178.1	2.226	0.4	125	814	788	1	0.6995	12.27
446.1	178.4	2.231	0.4	124	830	769	1	0.7013	12.43
443	177.2	2.215	0.4	127	820	784	1	0.6976	12.6
443.7	177.5	2.218	0.4	125	833	771	1	0.6963	12.74
439.2	175.7	2.196	0.4	145	808	783	1	0.7107	12.9
436	174.4	2.18	0.4	93	801	857	1	0.6437	13.06
436.8	174.7	2.184	0.4	145	811	785	1	0.7058	13.21
433.7	173.5	2.168	0.4	94	803	859	1	0.6392	13.37
435.9	174.4	2.18	0.4	128	826	790	1	0.6834	13.53
434.8	173.9	2.174	0.4	128	828	791	1	0.6811	13.69
429.4	171.8	2.147	0.4	139	797	822	1	0.6819	13.84
428.3	171.3	2.141	0.4	139	798	823	1	0.6797	14
425	170	2.125	0.4	139	784	845	1	0.6733	14.16

Appendix B : The constituents SCC mixes

429.2	171.7	2.146	0.4	118	824	819	1	0.6575	14.31
424.8	169.9	2.124	0.4	143	800	824	1	0.6773	14.47
421.3	168.5	2.106	0.4	100	788	895	1	0.6208	14.65
426.2	170.5	2.131	0.4	115	829	824	1	0.6476	14.8
418.1	167.3	2.091	0.4	123	780	882	1	0.6407	14.94
424.4	169.8	2.122	0.4	115	831	825	1	0.6441	15.1

Table B.6. The constituents of SCC mixes according to their plastic viscosities (80 MPa)

<i>cm</i> kg/m ³	<i>W</i> kg/m ³	<i>SP</i> kg/m ³	<i>w/cm</i>	<i>LP</i> kg/m ³	<i>FA</i> kg/m ³	<i>CA</i> kg/m ³	<i>Vol.</i> m ³	<i>p/s</i>	<i>Viscosity</i> <i>Pa s</i>
528.2	184.9	2.641	0.35	117	723	789	1	0.8028	8.304
521.2	182.4	2.606	0.35	114	691	840	1	0.7832	8.445
519.3	181.7	2.596	0.35	114	692	842	1	0.7792	8.566
522.2	182.8	2.611	0.35	104	734	804	1	0.7726	8.692
520.3	182.1	2.601	0.35	105	736	806	1	0.7686	8.821
518.3	181.4	2.592	0.35	105	737	808	1	0.7645	8.957
510.9	178.8	2.554	0.35	112	695	859	1	0.7577	9.08
510.9	178.8	2.555	0.35	116	709	839	1	0.7631	9.215
517	181	2.585	0.35	113	768	768	1	0.7727	9.345
507.3	177.6	2.537	0.35	117	712	842	1	0.7559	9.473
502.2	175.8	2.511	0.35	116	689	878	1	0.7431	9.611
511.2	178.9	2.556	0.35	107	770	785	1	0.7515	9.736
505	176.8	2.525	0.35	116	737	822	1	0.7492	9.86
503.4	176.2	2.517	0.35	116	738	823	1	0.7459	9.987
503.5	176.2	2.518	0.35	101	757	822	1	0.7271	10.13
502	175.7	2.51	0.35	101	758	823	1	0.724	10.26
500.5	175.2	2.503	0.35	101	759	824	1	0.7211	10.38
498.8	174.6	2.494	0.35	105	759	824	1	0.7228	10.51
497.2	174	2.486	0.35	105	760	825	1	0.7197	10.65
495.9	173.6	2.479	0.35	106	761	826	1	0.7169	10.77
500.2	175.1	2.501	0.35	115	799	768	1	0.7374	10.91
498.9	174.6	2.494	0.35	115	800	769	1	0.7348	11.03
487.5	170.6	2.437	0.35	103	746	862	1	0.697	11.27
487.9	170.8	2.439	0.35	111	759	838	1	0.7073	11.42
490.2	171.6	2.451	0.35	98	786	821	1	0.6958	11.55
485.2	169.8	2.426	0.35	112	761	841	1	0.7022	11.68
490	171.5	2.45	0.35	113	802	787	1	0.7134	11.81
488.5	171	2.442	0.35	102	802	802	1	0.6972	11.94
487.2	170.5	2.436	0.35	102	804	803	1	0.6947	12.08
484.8	169.7	2.424	0.35	97	796	821	1	0.6838	12.2
483.6	169.2	2.418	0.35	97	798	822	1	0.6814	12.33
474.7	166.1	2.373	0.35	95	749	894	1	0.6616	12.46
481.3	168.5	2.406	0.35	97	800	825	1	0.6772	12.59
479.9	168	2.4	0.35	98	801	826	1	0.6746	12.74
471.2	164.9	2.356	0.35	96	751	898	1	0.6553	12.85
471.9	165.2	2.36	0.35	103	764	874	1	0.6653	12.98
470.8	164.8	2.354	0.35	103	765	875	1	0.6633	13.11
469.6	164.3	2.348	0.35	103	766	877	1	0.661	13.26
478.7	167.5	2.394	0.35	109	830	784	1	0.6859	13.37
480.5	168.2	2.403	0.35	105	848	766	1	0.6846	13.5

Appendix B : The constituents SCC mixes

468.6	164	2.343	0.35	107	782	857	1	0.6635	13.63
460.3	161.1	2.302	0.35	101	734	931	1	0.6407	13.76
477.5	167.1	2.388	0.35	105	851	769	1	0.679	13.89
472.3	165.3	2.362	0.35	105	826	806	1	0.6677	14.02
475.5	166.4	2.378	0.35	106	853	770	1	0.6753	14.15
475.9	166.6	2.379	0.35	100	860	768	1	0.6696	14.28
476.2	166.7	2.381	0.35	95	868	766	1	0.6641	14.41
462.6	161.9	2.313	0.35	92	793	875	1	0.6349	14.54
464.5	162.6	2.323	0.35	99	812	843	1	0.6458	14.67
463.6	162.3	2.318	0.35	99	813	844	1	0.6441	14.81

Appendix C

**A MATLAB programme for
determining the size-independent
specific fracture energy**

A MATLAB programme for determining the size-independent specific fracture energy 2014-2015 using the simplified boundary effect method (SBE)

```

%*****
***%
% List of variables
% Name Description
% -----
% A01 Area of the shallow notch under load-deflection
% curve, kN/mm
% A06 Area of the deep notch under load-deflection
% curve, kN/mm
% WOF01 Work of fracture of the shallow beams according
to
% RILEM FCM-50 (Size-dependent fracture energy,
N/m)
% WOF06 Work of fracture of the deep beams according to
% RILEM FCM-50 (Size-dependent fracture energy,
N/m)
% mean (WOF01) The mean values of work of fracture of shallow
% notches
% mean (WOF06) The mean values of work of fracture of deep
% notches
% std (WOF01) The standard deviation values of work of
fracture
% of shallow notches
% std(WOF06) The standard deviation values of work of
fracture
% of deep notches
% COV01 The coefficient of variation values of work of
% fracture of shallow notches
% COV06 The coefficient of variation values of work of
% fracture of deep notches
% q1 Shallow notch to depth ratio
% q2 Deep notch to depth ratio
% w Depth of beam, m
% B width of beam, m
% GF Specific size-independent fracture energy, N/m
% ALIGNMENT The transition ligament length, mm
%*****
***
clear
clc
%*****
***
% input beam dimension details
q1=0.1;
q2=0.6;
w=0.1;
B=0.1;
%*****
***
% calculate notch depth, m
a1=q1*w;
a2=q2*w;
%*****
***
% Input load-deflection curves areas for shallow and deep notches
beams

```

```

A01 = [0.80 0.85 0.86 0.82 0.79]; % Input the shallow values here
A06 = [0.20 0.21 0.25 0.19 0.23]; % Input the deep values here
% Determining the size dependent work of fracture based on RILEM
FMC-50
WOF01=A01/ (w-a1)/B;
WOF06= [A06/ (w-a2)/B];
mean (WOF01);
mean (WOF06);
std (WOF01);
std (WOF06);
COV01=std (WOF01)/mean (WOF01);
COV06=std (WOF06)/mean (WOF06);
c1=mean (WOF01);
c2=mean (WOF06);
% Determining the size independent specific fracture energy
according
%           to the simplified boundary effect method
z1=w-a1;
z2=w-a2;
r=z1*c2;
x=(2*z1*z2*(c2-c1))/(c2*z2-c1*z1);
y=c1/(1-x/(2*z1));
m=1-q2;
f= 1-q1;
n= x/w;
if ( m > n && f > n )
GFF=y
Aligment=x
end
if (m <= n)
x1=(2*r+((2*r)^2-4*r*c1*z2)^0.5)/(2*c2);
x2=(2*r-((2*r)^2-4*r*c1*z2)^0.5)/(2*c2);
y1=c1/ (1-x1/(2*z1));
y2=c1/ (1-x2/(2*z1));

if ( x1 < w)
GFF=y1;
Aligment=x1;
end
if ( x2 < w)
GFF=y2;
Aligment=x2;
end
end
%*****
***
GF=GFF
ALIGMENT=Aligment*1000
%*****
***
cov01Percent=COV01*100;
cov06Percent=COV06*100;

COVAR01=cov01Percent;
COVAR06=cov06Percent;

COVGf01=COVAR01;
COVGf06=COVAR06;

meanGf01=mean (WOF01);

```

```
meanGf06=mean (WOF06);
%*****
***
% Desired parameters to be printed in the output sheet
MyMatrix = [meanGf01; COVGf01; meanGf06; COVGf06; GF; ALIGMENT]';
HeaderNames='meanGf01, COVGf01, meanGf06, COVGf06, GF, ALIGMENT';
%*****
***
% preferable output sheet name printed here
fileName = 'choose output file name here.csv';
outid = fopen(fileName, 'w+');
fprintf(outid, '%s', HeaderNames);
fclose(outid);

dlmwrite(fileName,myMatrix,'roffset',1,'-append', 'precision', 4); %
increased precision to allow all digits to be saved
disp(strcat('Generated report ',fileName, ''))
%*****
***
%*****
***
```

Appendix D

The non-linear hinge model of a pre-notched beam

D.1 Hinge model

The basic idea of the non-linear cracked hinge model is to isolate the part of the beam close to the propagating crack (i.e. the part under maximum bending moment) as a short beam segment subjected to a bending moment and normal force. Figure D.1 shows a typical three point bend beam and deformation of the hinge element.

In the non-linear hinge model the crack is viewed as a local change in the overall stress and strain field. This change is assumed to vanish outside a certain band of width s (see Figure D.1). Thus, outside of this band the structural element is modelled using the elastic beam theory.

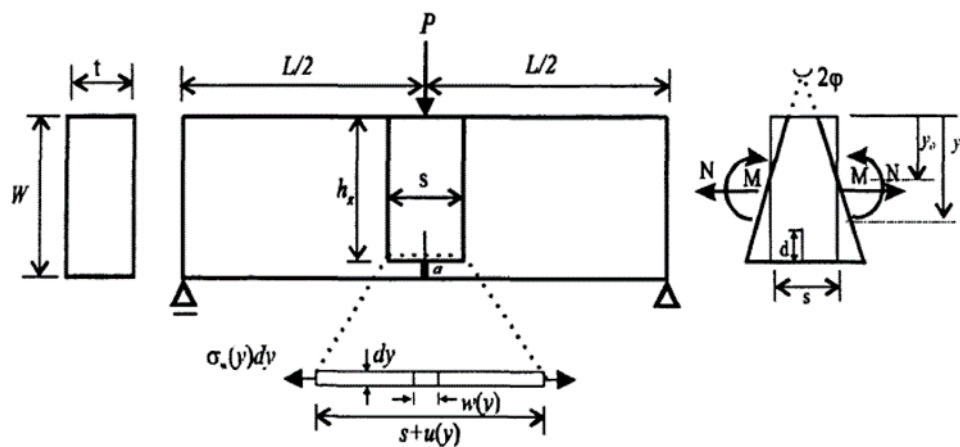


Figure D. 1 Three-point notched bend beam with a non-linear hinge modeling the propagation of a crack at mid-section, with the illustration of an increment horizontal layer of the hinge shown below the right: geometry of the hinge deformation (After: Olesen, 2011)

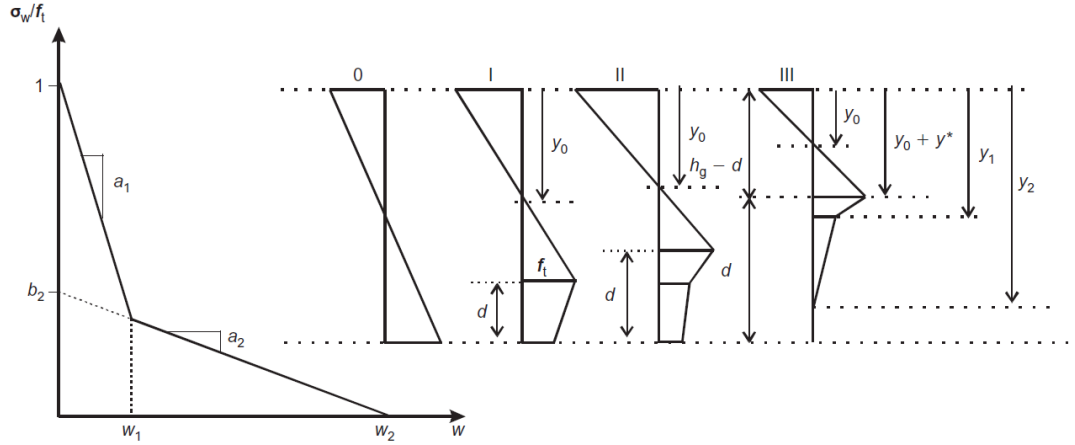


Figure D. 2 Definition of a bi-linear stress-crack opening relationship and the four different phases of crack propagation. Phase 0 = State of stress prior to cracking; Phases I-III = States of stress during crack propagation (After: Olesen, 2011)

The constitutive relationship for each segment inside the hinge is assumed to be linear elastic in the pre-cracked state (phase 0), while the cracked state is approximated by a bilinear softening curve as shown in Figure (D.2)

$$\sigma = \begin{cases} E\varepsilon & \text{pre - cracked state} \\ \sigma_w(w) = \mathbf{g}(w)f_t & \text{cracked state} \end{cases} \quad (\text{D. 1})$$

where E =elastic modulus; ε = elastic strain; w = crack opening; $\sigma_w(w)$ = stress-crack opening relationship; and f_t = uniaxial tensile strength . The shape of the stress-crack opening relationship is defined by the function $\mathbf{g}(w)$ of the crack opening w , normalised so that $\mathbf{g}(0) = 1$. For the assumed bilinear shape (Figure D.2), we have

$$\mathbf{g}(w) = b_i - a_i w = \begin{cases} b_1 - a_1 w & 0 \leq w < w_1 \\ b_2 - a_2 w & w_1 \leq w < w_2 \end{cases} \quad (\text{D. 2})$$

$$w_1 = \frac{1-b_2}{a_1-a_2} ; w_2 = \frac{b_2}{a_2} \quad (\text{D. 3})$$

where $b_1 \equiv 1$; and the limits w_1 and w_2 are given by the intersection of the two line segments, and the intersection of the second line segment and the abscissa, respectively, a_1 and a_2 represent the slopes of the first and the second line segments of the bilinear curve, respectively (see Figure D.2) .

An analysis of the hinge element allows the determination of the axial load \mathbf{N} and bending moment \mathbf{M} for any given angular hinge rotation $2\varnothing$ (Figure D.1). The problem now is solved in four stages, one for each phase of the crack propagation. Phase 0

represents the elastic state, when no crack has formed from the initial notch, while phases I, II and III represent different stages of crack propagation (Figure D.2). In phase I, the fictitious crack of length d is such that the maximum crack opening is less than w_1 . In phase II, a part of the fictitious crack of length d has a crack opening in excess of w_1 but in the remaining part it is less than w_1 . In phase III, a part of the crack has opened more than w_2 and thus become traction-free, while the opening of the remaining part is still less w_2 or even less than w_1 .

When the complete stress distribution is established for the non-linear hinge, a relation between the normal force \mathbf{N} , the moment, \mathbf{M} and the hinge rotation, φ may be obtained in each phase of the crack propagation. The following normalised parameters are introduced

$$\mu = \frac{6}{f_t h_g^2 t} M; \quad \rho = \frac{1}{f_t h_g t} N; \quad \theta = \frac{h_g E}{s f_t} \varphi; \quad \alpha_h = \frac{d}{h_g} \quad (\text{D. 4 a, b, c, d})$$

where t = width of the hinge in the direction normal to the paper; and d = depth of the fictitious crack. Given these normalisations the pre-crack elastic behaviour of the hinge is described by $\alpha_h = 0$ and $\mu = \theta$, where $0 \leq \theta \leq 1 - \rho$, and where the onset of cracking is given by $\theta = 1 - \rho$. The solutions covering each of the cracked Phases I, II, and III are given in (D.5-D.10) respectively.

Phase I

$$\alpha = 1 - \beta_1 - \sqrt{(1 - \beta_1) \left(\frac{1 - \rho}{\theta} - \beta_1 \right)} \quad (\text{D. 5})$$

$$\mu = 4 \left(1 - 3\alpha + 3\alpha^2 - \frac{\alpha^3}{1 - \beta_1} \right) \theta + (6\alpha - 3)(1 - \rho) \quad (\text{D. 6})$$

Phase II

$$\alpha = 1 - \beta_2 - \frac{1 - b_2}{2\theta} \sqrt{(1 - \beta_2) \left(\frac{(1 - b_2)^2}{4\theta^2(\beta_1 - \beta_2)} - \beta_2 + \frac{b_2 - \rho}{\theta} \right)} \quad (\text{D. 7})$$

$$\mu = 4 \left(1 - 3\alpha + 3\alpha^2 - \frac{\alpha^3}{1 - \beta_2} \right) \theta + (6\alpha - 3)(1 - \rho) - \frac{(1 - b_2) \left(3\alpha^2 - \left(\frac{c}{2\theta} \right)^2 \right)}{1 - \beta_2} \quad (\text{D. 8})$$

Phase III

$$\alpha = 1 - \frac{1}{2\theta} \left(1 + \sqrt{\frac{(1-b_2)^2}{\beta_1-\beta_2} + \frac{(b_2)^2}{\beta_2} - 4\rho\theta} \right) \quad (\text{D. 9})$$

$$\mu = 4(1 - 3\alpha + 3\alpha^2 - \alpha^2)\theta + (6\alpha - 3)(1 - \rho) - 3\alpha^2 + \frac{1}{4\theta^2} \left(1 - \frac{b_2}{\beta_1} \right) + \left(1 + \frac{\beta_c}{1-\beta_1} \right) + \left(\frac{c}{2\theta} \right)^2 \quad (\text{D. 10})$$

Here the constant c has been introduced as

$$c = (1 - b_2)(1 - \beta_1)/(\beta_2 - \beta_1) \quad (\text{D. 11})$$

In terms of θ the point of transition from Phase I to Phase II, θ_{I-II} , may be found from the condition that $y_1 = h_g$, and the point of transition from Phase II to Phase III, θ_{II-III} , may similarly be found from $y_2 = h_g$. These transition points, together with the point of transition between Phase 0 and Phase I, θ_{0-1} are given by:

$$\theta_{0-1} = 1 - \rho \quad (\text{D. 12})$$

$$\theta_{I-II} = \frac{1}{2} \left(1 - \rho - c + \sqrt{(1 - \rho - c)^2 + \frac{c^2}{\beta_1 - 1}} \right) \quad (\text{D. 13})$$

$$\theta_{II-III} = \frac{1}{2} \left(\rho(\beta_2 - 1) + \frac{b_2}{\beta_2} + \sqrt{\rho^2(\beta_2 - 1)^2 + 2\rho(\beta_2 - 1) \frac{b_2}{\beta_2} + \frac{(1-b_2)^2}{\beta_1-\beta_2} + \frac{b_2^2}{\beta_2}} \right) \quad (\text{D. 14})$$

D.2 Application to a three-point bend beam

The crack mouth opening displacement (CMOD) in a TPB specimen consists of three contributions. These are the opening due to the crack emanating from the starter crack, δ_{COD} , the opening due to elastic deformation, δ_e and the opening due to geometrical considerations because the line of application of the load is shifted relative to the mouth of the starter crack, δ_g

$$CMOD = \delta_{COD} + \delta_e + \delta_g \quad (\text{D. 15})$$

δ_{COD} is the crack opening at the bottom of the hinge, that is, at $y = h_g$, and may be determined from eq. (D.16)

$$\delta_{COD} = \frac{sf_t}{E} \frac{(1-b_i+2\alpha_h\theta)}{(1-\beta_i)} \quad (\text{D. 16})$$

$$\beta_i = \frac{s a_i f_t}{E} \quad (\text{D. 17})$$

$$(\mathbf{b}_i, \boldsymbol{\beta}_i) = \begin{cases} (\mathbf{1}, \boldsymbol{\beta}_1) & \text{for } \theta_{0-I} < \theta \leq \theta_{1-II} \\ (\mathbf{b}_2, \boldsymbol{\beta}_2) & \text{for } \theta_{1-II} < \theta \leq \theta_{II-III} \\ (\mathbf{0}, \mathbf{0}) & \text{for } \theta_{II-III} < \theta \end{cases} \quad (\text{D. 18})$$

δ_e can be found from handbooks, e.g. Tada et al. (1985) and is given by:

$$\delta_e = \frac{4\sigma\alpha}{E} \left(0.76 - 2.28\alpha + 2.87\alpha^2 - 2.04\alpha^3 + \frac{0.66}{(1-\alpha)^2} \right) \quad (\text{D. 19})$$

where, $\sigma = \frac{6M}{(W^2t)}$, $M = \frac{PL}{4}$, and a is the initial crack length such that $\alpha = a/W$.

The contribution from δ_g has been found to be negligible for the specimen geometries tested.

The load on the beam is related to the normalised moment through the following relation

$$P(\theta) = \frac{2f_t h_g^2 t}{3L} \mu(\theta) \quad (\text{D. 20})$$

where L is the total length of the beam.

The optimization was performed by minimising the area between the theoretical curve obtained from the hinge model and the experiment load-CMOD curve i.e. by minimising the difference between the theoretical load $P(\theta)$ in equation (D.20) and the experimental load P_{exp}

The value of θ corresponding to each phase is calculated from the analytical expression (Stang and Olesen, 1998). Then for this value of θ the normalised moment and the crack length, α_h are calculated, followed by the theoretical CMOD and load $P(\theta)$ (from equation (D.21)). Next the sum of squares of the errors between the theoretical and experimental values of the load is minimised with respect to the three unknown parameters of the bilinear stress-crack relationship

$$\min(\mathbf{a}_1, \mathbf{a}_2, \mathbf{a}_3) \frac{1}{n} \sum_0^n (P(\theta) - P_{exp})^2 \quad (\text{D. 21})$$

where n is the total number of the observations representing the selected entries of θ that is, the selected values of $P(\theta)$ on the experimentally recorded load–CMOD diagram.

D.3 Parameters of bilinear the stress-crack relationship corresponding to G_F

The area under the softening curve (Figure D.3) obtained using the hinge model is not equal to G_F but to the measured G_f (α, W).

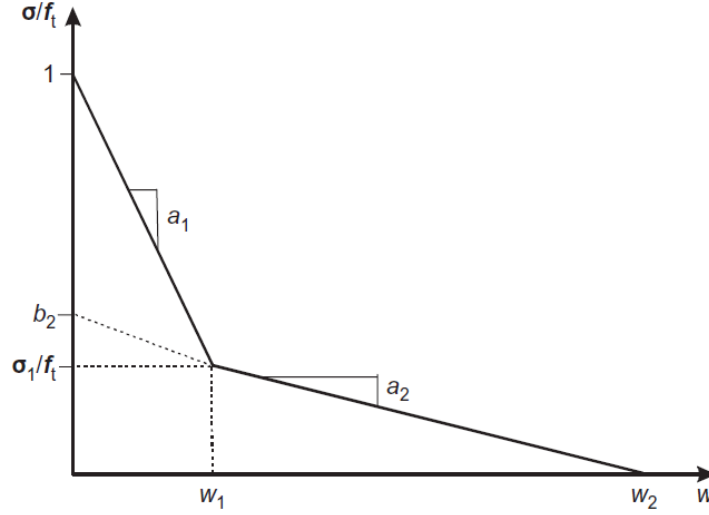


Figure D. 3 Bilinear tension softening diagram

The size-dependent fracture energy (i.e. the area under the bilinear tension diagram) obtained from the hinge model is given by

$$G_f^*(\alpha, W) = \frac{1}{2} f_t^* (w_1^* + \frac{\sigma_1^*}{f_t^*} w_2^*) \quad (\text{D.22})$$

where the superscript * denotes the average parameters of the bilinear diagram obtained from the hinge model.

The size-independent specific fracture energy (i.e. the area under the bilinear stress-crack relationship corresponding to G_F) can be similarly written as

$$G_F = \frac{1}{2} f_t (w_1 + \frac{\sigma_1}{f_t} w_2) \quad (\text{D.23})$$

where w_1 , w_2 and σ_1 , which are to be determined, are the bilinear diagram parameters corresponding to the true fracture energy G_F , and f_t is the direct tensile strength of the mix obtained from an independent test, say a split cylinder test, f_{st} . It is assumed that

$$f_t = 0.65 f_{st} \quad (\text{D.24})$$

The hinge model parameters corresponding to G_f (α, W) can be scaled to the size independent specific fracture energy G_F as

$$\frac{1}{2} f_t \left(w_1 + \frac{\sigma_1}{f_t} w_2 \right) = \frac{1}{2} f_t^* \left(w_1^* + \frac{\sigma_t^*}{f_t^*} w_2^* \right) \frac{G_F}{G^* f(\alpha, w)} \quad (\text{D.25})$$

The coordinates of the knee of the bilinear diagram predicted by the hinge model are related as follows (Figure D.3)

$$\frac{\sigma_t^*}{f_t} = 1 - a_1^* \quad (\text{D.26})$$

From Figure D.3 we obtain an additional equation for the slope a_2 of the true bilinear diagram

$$\frac{\sigma_1}{f_t} = (w_2 - w_1) a_2 \quad (\text{D.27})$$

By using the Equations (D.25- D.27), the parameters w_1 and w_2 can be determined.

Appendix E

A MATLAB code for determining the static response of SCC beams

Appendix E: A MATLAB code for Determining the static response of self- compacting concrete beams based on the fictitious crack model

```

*****
% A MATLAB code for Determination of the static response of self-
% compacting concrete beams under three-point bending, using a
% bilinear tension-softening (stress-crack opening) relationship
% based on the fictitious crack model
*****
%
% References
%
% 1. Hillerborg A. (1980). Analysis of fracture by means of the
% fictitious crack model, particularly for fibre-reinforced
% concrete, Int J Cement Composites, 2, 177-184.
%
% 2. Hillerborg A., Modeer M. and Petersson P. (1976). Analysis of
% crack formation and crack growth in concrete by means of
% fracture mechanics and finite elements, Cement Concrete
% Research, 6, 773-782.
%
% 3. Olesen J.F. (2001). Fictitious crack propagation in fibre-
% reinforced concrete beams, J Engineering Mechanics, 127, 272-80
*****
%
% List of variables
%
% Name Description
% -----
% alp0 Initial notch depth to beam depth ratio
% db beam depth, mm
% h Height of the hinge, mm
% L Span length of the TPB, mm
% t Thickness of the hinge, mm
% S Width of the hinge, mm
% al, a2, b1 & b2 Parameters for the bilinear relation
% a1 & a2 1/mm
% b1 & b2 Dimensionless
% E Young modulus, GPa
% ft Splitting tensile strength, GPa
% GF Specific size-independent fracture energy
*****
%
% Part one for calculation the shallow notch parameters
*****
clc
clear all
close all
polyfitOrder = 30;
% Enter the path of the experimental results Excel files of load-
% CMOD curves
v_matpath='C: \Users\Wajde1975\Desktop\ Fracture\80B';
% Enter the maximum displacement of the shallow and deep notches
MaxDisplacement01=0.42;
MaxDisplacement06=0.30;
% Enter the beam dimensions details
L=400;
t=100;
db=100;
a0shallow=10;
a0deep=60;

```

Appendix E: A MATLAB code for Determining the static response of self- compacting concrete beams based on the fictitious crack model

```

% Enter the rho value (use 0 for plain concrete or 0.045 for fibre
reinforced concrete)
rho=0;
% Enter the selected sheets numbers for shallow samples
SheetNo1 = [1 2 3 4 5];
% Enter the selected sheets numbers for deep samples
SheetNo6 = [7 8 9 10 11];
% Enter a proposed values of minimum and maximum theta
themin=0;
themax=200;
increment=themax/499;
incrementxq=MaxDisplacement01/499;
% xq is a constant increments in the x-direction of the average
experimental load-CMOD curves
xq = 0: incrementxq:MaxDisplacement01;
% Change the path to the file location
cd(v_matpath)
% Find the excel files in the folder
files = dir ('*.xlsx');
% [status, sheets] = xlsfinfo (filename)
filename = files(1).name;
[AA BB] = size(SheetNo1);
for n=1:BB
% Read Microsoft Excel spreadsheet file
clear subsetA
sheet = SheetNo1(1,n);
% Enter column range of the Excel sheets
xlRange = 'A:E';
subsetA = xlsread(filename,sheet,xlRange);
%*****
% Fit curve or surface to data
%*****
% Enter the column number of the x value (CMOD column in the excel
sheet)
x = subsetA (:, 5);
% Enter the column number of the y value (load column in the excel
sheet)
y = subsetA (:, 3);
hold on
plot(x,y);
p = polyfit(x,y, polyfitOrder);
f = polyval(p,x);
ff = polyval(p,xq);
% save all the results in one matrix (each column is a excel file)
Final_results(:,n)= ff(1,:);
hold on
end
% find the average of the final matrix
[m z] = size(Final_results);
for i = 1:m
    C(i,1) = mean(Final_results(i,1:z));
end
    plot(xq,C, 'o');
    hold on
    plot(x,y, 'o');
%*****
%Except parameters that can be used later on
%*****

```

Appendix E: A MATLAB code for Determining the static response of self- compacting concrete beams based on the fictitious crack model

```

clearvars -except xq C polyfitOrder a0shallow a0deep db L t rho
SheetNo6 v_matpath MaxDisplacement06 themin increment themax
%*****
a0=a0shallow;
alp0=a0/db;
h=(1-alp0)*db;
s=0.5*h;
%*****
% Enter a1, a2, b2, ft, E limits values
%*****
count = 1;
for a1=1:0.5:50
for a2=0.1:0.05:1.5
for b2=0.1:0.05:0.9
for ft=0.0018:0.0001:0.0048
for E=25:0.5:40
bet1=ft*a1*s/E;
bet2=ft*a2*s/E;
c = (1-b2)*(1-bet1)/(bet2-bet1);
rho=0;
the01=1-rho ;
the12=.5*(1-rho-c+((1-rho-c)^2+c^2/(bet1-1))^0.5);
the23=.5*(rho*(bet2-1)+b2/bet2+(rho^2*(bet2-1)^2+2*rho*(bet2-1)*b2/bet2+(1-b2)^2/(bet1 -bet2)+b2^2/bet2)^.5);
k=0;
for the=themin :increment: themax
%*****
% Alpha & Mu Calculation
%*****
% For phase 0
if (0<=the & the<=the01)
alp = 0;
mu = the;
cod = 0;
% For phase I
elseif(the01<the & the<=the12)
bi= 1;
beti = bet1;
alp = 1-bet1-((1-bet1)*((1-rho)/the-bet1))^0.5;
mu = 4*(1-3*alp+3*alp^2-alp^3/(1-bet1))*the+(6*alp-3)*(1-rho);
cod = s*ft/E*(1-bi+2*alp*the)/(1-beti);
% For phase II
elseif(the12<the & the<=the23)
bi = b2;
beti = bet2;
alp =1-bet2-(1-b2)/(2*the)-(((1-bet2)*((1-b2)^2/(4*the^2)/(bet1 -bet2)-bet2+(b2-rho)/the))^0.5;
mu = 4*(1-3*alp+3*alp^2-alp^3/(1-bet2))*the+(6*alp-3)*(1-rho)-(((1-b2)*(3*alp^2-(c/(2*the))^2))/(1-bet2));
cod = s*ft/E*(1-bi+2*alp*the)/(1-beti);
% For phase III
elseif(the23<the)
bi =0;
beti = 0;
alp = 1 -1 / (2*the)*(1+((1-b2)^2/(bet1-bet2)+b2^2/bet2-4*rho*the)^.5);
mu = 4*(1-3*alp+3*alp^2-alp^3)*the+(6*alp-3)*(1-rho)-3*alp^2+1/(4*the^2)*(1-b2/bet2)*(1-b2/bet2+c)*(1+bet1*c/(1-bet1))+c/(2*the))^2;
cod = s*ft/E*(1-bi+2*alp*the)/(1-beti);
end

```

Appendix E: A MATLAB code for Determining the static response of self- compacting concrete beams based on the fictitious crack model

```

k=k+1;
pp(k) = 2/3*ft*h^2*t/L*mu;
m = pp(k)*L/4;
sigm = 6*m/(t*db^2);
cod0 = 4*sigm*a0/E*(0.76-2.28*alp0+3.87*alp0^2-2.04*alp0^3+0.66/(1-
alp0)^2);
CMOD(k) = cod + cod0;
end
AA = [CMOD;pp]';
x = AA(:,1); % the x value
y = AA(:,2); % the y value

% select eitherspline fit or polyfit (choose one option as shown
here)
%*****
% spline fit option
ff=interp1(x,y,xq,'spline');
%*****
% poly fit option
% p = polyfit(x,y, polyfitOrder);
% f = polyval(p,x);
% ff = polyval(p,xq);
%*****
clear Error
[mm nn]= size(xq);
for ii = 1:nn
Error(ii,2) = (ff(1,ii)-C(ii,1))^2;
Error(ii,1) = xq(1,ii);
end
SumError (count,1) = sum (Error(:,2))/nn;
SumError (count,2) = a1;
SumError (count,3) = a2;
SumError (count,4) = b2;
SumError (count,5) = ft;
SumError (count,6) = E;
count = count +1;
end
end
end
end
end
EE=sortrows(SumError,[1 6]);
MinERR=EE(1,1);
a1=EE(1,2);
a2=EE(1,3);
b2=EE(1,4);
ft=EE(1,5);
E=EE(1,6);
w1=(1-b2)/(a1-a2);
w2=b2/a2;
sigmaft=a2*(w2-w1);
Gf01=0.5*ft*1000*(w1+sigmaft*w2);
D=[0 w1 w2];
EEE=[1 sigmaft 0];
KneeCoordinatesSHallow= [D; EEE]';
%*****
%Except parameters that can be used later on

```

Appendix E: A MATLAB code for Determining the static response of self- compacting concrete beams based on the fictitious crack model

```

%*****
clearvars -except sigmaft C xq alp0 E ft db h L t s rho a1 a2 b2
themin increment themax KneeCoordinatesSHallow w1 w2 Gf01 MinERR
SumError polyfitOrder a0 a0deep SheetNo6 v_matpath MaxDisplacement06
B1
%*****
bet1=ft*a1*s/E;
bet2=ft*a2*s/E;
c=(1-b2)*(1-bet1)/(bet2-bet1);
rho=0;
the01=1-rho ;
the12=0.5*(1-rho-c+((1-rho-c)^2+c^2/(bet1-1))^0.5);
the23=0.5*(rho*(bet2-1)+b2/bet2+(rho^2*(bet2-1)^2+2*rho*(bet2-
1)*b2/bet2+(1-b2)^2/(bet1-bet2)+b2^2/bet2)^.5);
k=0;
%*****
%*****
% Alpha & MU Calculation
%*****
%*****
% input theta values
for the=themin :increment:themax
% For phase 0
if (0<=the & the<=the01)
alp = 0;
mu = the;
cod = 0;
% For phase I
elseif(the01<the & the<=the12)
bi= 1;
beti = bet1;
alp = 1-bet1-((1-bet1)*((1-rho)/the-bet1))^0.5;
mu = 4*(1-3*alp+3*alp^2-alp^3/(1-bet1))*the+(6*alp-3)*(1-rho);
cod = s*ft/E*(1-bi+2*alp*the)/(1-beti);
% For phase II
elseif(the12<the & the<=the23)
bi = b2;
beti = bet2;
alp =1-bet2-(1-b2)/(2*the)-((1-bet2)*((1-b2)^2/(4*the^2)/(bet1-bet2)-bet2+(b2-rho)/the))^0.5;
mu = 4*(1-3*alp+3*alp^2-alp^3/(1-bet2))*the+(6*alp-3)*(1-rho)-((1-b2)*(3*alp^2-(c/(2*the))^2))/(1-bet2));
cod = s*ft/E*(1-bi+2*alp*the)/(1-beti);
% For phase III
elseif(the23<the)
bi =0;
beti = 0;
alp = 1 -1 / (2*the) * (1+((1-b2)^2/(bet1-bet2)+b2^2/bet2-4*rho*the)^0.5);
mu = 4*(1-3*alp+3*alp^2-alp^3)*the+(6*alp-3)*(1-rho)-3*alp^2+1/(4*the^2)*(1-b2/bet2)*(1-b2/bet2+c)*(1+bet1*c/(1-bet1))+c/(2*the)^2;
cod = s*ft/E*(1-bi+2*alp*the)/(1-beti);
end
k=k+1;
pp(k) = 2/3*ft*h^2*t/L*mu;
m = pp(k)*L/4;
sigm = 6*m/(t*db^2);
cod0 = 4*sigm*a0/E*(0.76-2.28*alp0+3.87*alp0^2-2.04*alp0^3+0.66/(1-alp0)^2);
CMOD(k) = cod + cod0;

```

Appendix E: A MATLAB code for Determining the static response of self- compacting concrete beams based on the fictitious crack model

```

end
AA = [CMOD;pp]';
x = AA(:,1); % the x value
y = AA(:,2); % the y value
% select either spline fit or polyfit (choose one option as shown
here)
%*****
% spline fit option
ff=interp1(x,y,xq,'spline');
%*****
% poly fit option
% p = polyfit(x,y,polyfitOrder);
% f = polyval(p,x);
% ff = polyval(p,xq);
%*****
W1(:,1)=xq;
W2(:,1)=C;
W3(:,1)=ff;
ModelCurve = [xq;ff]';
TestCurve=[W1,W2];
ModelTestCurveShallow = [W1';W2';W3']';
HeaderNames1='xq,PTest,PModel';
% Preferable output sheet name printed here
fileName1 = 'ModelTest01.csv';
outid = fopen(fileName1, 'w+');
fprintf(outid, '%s', HeaderNames1);
fclose(outid);
dlmwrite(fileName1,ModelTestCurveShallow,'roffset',1,'-append',
'precision', 4);
disp(strcat('Generated report ''',fileName1,''''))
% Preferable output sheet name printed here
filename = 'Parameters.xlsx';
% Desired parameters to be printed in the output sheet
A =
{'a1','a2','b2','w1','w2','Gf01','ft01','E','MinERR';a1,a2,b2,w1,w2,
Gf01,ft,E,MinERR};
B1=[a1,a2,b2,Gf01,ft,E,MinERR];
sheet = 1;
xlRange = 'A';
xlswrite(filename,A,sheet,xlRange)
filename = 'Parameters.xlsx';
A = {'Xknee','Yknee';0,1;w1,sigmaft;w2,0};
sheet = 1;
xlRange = 'J';
xlswrite(filename,A,sheet,xlRange)
%*****
%*****
%*****
%*****
% Part two for calculation the deep notch parameters
%*****
clearvars -except polyfitOrder MaxDisplacement06 SheetNo6 a0deep db
L t s rho themin increment themax KneeCoordinatesSHallow v_matpath
B1
%*****
incrementxq = MaxDisplacement06/499;
xq = 0:incrementxq:MaxDisplacement06;
% change the path to the file location automatically
cd(v_matpath)
% find the excel files in the folder

```

Appendix E: A MATLAB code for Determining the static response of self- compacting concrete beams based on the fictitious crack model

```

files = dir('*\.xlsx');
filename = files(1).name;
[AA BB] = size(SheetNo6);
for n=1:BB
% Read Microsoft Excel spreadsheet file
clear subsetA
sheet = SheetNo6(1,n);
xlRange = 'A:E';
subsetA = xlsread(filename,sheet,xlRange);
%*****
% Fit curve or surface to data
%*****
% Enter the column number of the x value (CMOD column in the excel
% sheet)
x = subsetA(:,5);
% Enter the column number of the y value (load column in the excel
% sheet)
y = subsetA(:,3);
hold on
plot(x,y);
p = polyfit(x,y,polyfitOrder);
f = polyval(p,x);
ff = polyval(p,xq);
% save all the results in one matrix (each column is a excel file)
Final_results(:,n)= ff(1,:);
hold on
end
% find the avearge of the final matrix
[m z] = size(Final_results);
for i = 1:m
C(i,1) = mean(Final_results(i,1:z));
end
plot(xq,C,':.');
clearvars -except xq C polyfitOrder L t s rho db themin increment
themax KneeCoordinatesSHallow a0deep B1
%*****
% Enter constant values
%*****
a0=a0deep;
alp0=a0/db;
h=(1-alp0)*db;
% Enter a1, a2, b2, ft, E limits values
count = 1;
for a1=1:0.5:50
for a2=0.1:0.05:1.5
for b2=0.1:0.05:0.9
for ft=0.0018:0.0001:0.0048
for E=25:0.5:40
bet1=ft*a1*s/E;
bet2=ft*a2*s/E;
c = (1-b2)*(1-bet1)/(bet2-bet1);
rho=0;
the01=1-rho ;
the12=.5*(1-rho-c+((1-rho-c)^2+c^2/(bet1-1))^0.5);
the23=.5*(rho*(bet2-1)+b2/bet2+(rho^2*(bet2-1)^2+2*rho*(bet2-
1)*b2/bet2+(1-b2)^2/(bet1 -bet2)+b2^2/bet2)^.5);
k=0;
for the=themin :increment:themax
%*****
% Alpha & Mu Calculation

```

Appendix E: A MATLAB code for Determining the static response of self- compacting concrete beams based on the fictitious crack model

```

%*****
%*****
% For phase 0
if (0<=the & the<=the01)
alp = 0;
mu = the;
cod = 0;
% For phase I
elseif(the01<the & the<=the12)
bi= 1;
beti = bet1;
alp = 1-bet1-((1-bet1)*((1-rho)/the-bet1))^0.5;
mu = 4*(1-3*alp+3*alp^2-alp^3/(1-bet1))*the+(6*alp-3)*(1-rho);
cod = s*ft/E*(1-bi+2*alp*the)/(1-beti);
% For phase II
elseif(the12<the & the<=the23)
bi = b2;
beti = bet2;
alp =1-bet2-(1-b2)/(2*the)-((1-bet2)*((1-b2)^2/(4*the^2)/(bet1 -
bet2)-bet2+(b2-rho)/the))^0.5;
mu = 4*(1-3*alp+3*alp^2-alp^3/(1-bet2))*the+(6*alp-3)*(1-rho)-((1-
b2)*(3*alp^2-(c/(2*the))^2))/(1-bet2));
cod = s*ft/E*(1-bi+2*alp*the)/(1-beti);
% For phase III
elseif(the23<the)
bi =0;
beti = 0;
alp = 1 -1 / (2*the)*(1+((1-b2)^2/(bet1-bet2)+b2^2/bet2-
4*rho*the)^0.5);
mu = 4*(1-3*alp+3*alp^2-alp^3)*the+(6*alp-3)*(1-rho)-
3*alp^2+1/(4*the^2)*(1-b2/bet2)*(1-b2/bet2+c)*(1+bet1*c/(1-
bet1))+c/(2*the))^2;
cod = s*ft/E*(1-bi+2*alp*the)/(1-beti);
end
k=k+1;
pp(k) = 2/3*ft*h^2*t/L*mu;
m = pp(k)*L/4;
sigm = 6*m/(t*db^2);
cod0 = 4*sigm*a0/E*(0.76-2.28*alp0+3.87*alp0^2-2.04*alp0^3+0.66/(1-
alp0)^2);
CMOD(k) = cod + cod0;
end
AA = [CMOD;pp]';
x = AA(:,1); % the x value
y = AA(:,2); % the y value
% select either spline fit or polyfit (choose one option as shown)
%*****
% spline fit option
ff=interp1(x,y,xq,'spline');
%*****
% poly fit option
% p = polyfit(x,y,polyfitOrder);
% f = polyval(p,x);
% ff = polyval(p,xq);
%*****
clear Error
[mm nn]= size(xq);
for ii = 1:nn
Error(ii,2) = (ff(1,ii)-C(ii,1))^2;
Error(ii,1) = xq(1,ii);
end

```

Appendix E: A MATLAB code for Determining the static response of self- compacting concrete beams based on the fictitious crack model

```

SumError(count,1) = sum (Error(:,2))/nn;
SumError(count,2) = a1;
SumError(count,3) = a2;
SumError(count,4) = b2;
SumError(count,5) = ft;
SumError(count,6) = E;
count = count +1;
end
end
end
end
end
EE=sortrows(SumError,[1 6]);
MinERR=EE(1,1);
a1=EE(1,2);
a2=EE(1,3);
b2=EE(1,4);
ft=EE(1,5);
E=EE(1,6);
w1=(1-b2)/(a1-a2);
w2=b2/a2;
sigmaft=a2*(w2-w1);
Gf06=0.5*ft*1000*(w1+sigmaft*w2);
D=[0 w1 w2];
EEE=[1 sigmaft 0];
KneeCoordinatesSHallow=[D;EEE]';
%*****
clearvars -except sigmaft C xq alp0 E ft db h L t s rho a1 a2 b2
themin increment themax KneeCoordinatesDeep w1 w2 Gf01 Gf06 MinERR
SumError polyfitOrder a0deep KneeCoordinatesSHallow B1
%*****
% input a1, a2, b2 values
a0=a0deep;
bet1=ft*a1*s/E;
bet2=ft*a2*s/E;
c = (1-b2)*(1-bet1)/(bet2-bet1);
rho=0;
the01=1-rho ;
the12=.5*(1-rho-c+((1-rho-c)^2+c^2/(bet1-1))^0.5);
the23=.5*(rho*(bet2-1)+b2/bet2+(rho^2*(bet2-1)^2+2*rho*(bet2-1)*b2/bet2+(1-b2)^2/(bet1 -bet2)+b2^2/bet2)^.5);
k=0;
% input theta values
for the=themin :increment:themax
%*****
% Alpha & Mu Calculation
%*****
% For phase 0
if (0<=the & the<=the01)
alp = 0;
mu = the;
cod = 0;
% For phase I
elseif(the01<the & the<=the12)
bi= 1;
beti = bet1;
alp = 1-bet1-((1-bet1)*((1-rho)/the-bet1))^0.5;
mu = 4*(1-3*alp+3*alp^2-alp^3/(1-bet1))*the+(6*alp-3)*(1-rho);
cod = s*ft/E*(1-bi+2*alp*the)/(1-beti);
% For phase II
elseif(the12<the & the<=the23)

```

Appendix E: A MATLAB code for Determining the static response of self- compacting concrete beams based on the fictitious crack model

```

bi = b2;
beti = bet2;
alp = 1 - bet2 - (1 - b2) / (2 * the) - ((1 - bet2) * ((1 - b2) ^ 2 / (4 * the ^ 2) / (bet1 -
bet2) - bet2 + (b2 - rho) / the)) ^ .5;
mu = 4 * (1 - 3 * alp + 3 * alp ^ 2 - alp ^ 3 / (1 - bet2)) * the + (6 * alp - 3) * (1 - rho) - (((1 -
b2) * (3 * alp ^ 2 - (c / (2 * the)) ^ 2)) / (1 - bet2));
cod = s * ft / E * (1 - bi + 2 * alp * the) / (1 - beti);
% For phase III
elseif(the23 < the)
bi = 0;
beti = 0;
alp = 1 - 1 / (2 * the) * (1 + ((1 - b2) ^ 2 / (bet1 - bet2) + b2 ^ 2 / bet2 -
4 * rho * the) ^ .5);
mu = 4 * (1 - 3 * alp + 3 * alp ^ 2 - alp ^ 3) * the + (6 * alp - 3) * (1 - rho) -
3 * alp ^ 2 + 1 / (4 * the ^ 2) * (1 - b2 / bet2) * (1 - b2 / bet2 + c) * (1 + bet1 * c / (1 -
bet1)) + (c / (2 * the)) ^ 2;
cod = s * ft / E * (1 - bi + 2 * alp * the) / (1 - beti);
end
k = k + 1;
pp(k) = 2 / 3 * ft * h ^ 2 * t / L * mu;
m = pp(k) * L / 4;
sigm = 6 * m / (t * db ^ 2);
cod0 = 4 * sigm * a0 / E * (0.76 - 2.28 * alp0 + 3.87 * alp0 ^ 2 - 2.04 * alp0 ^ 3 + 0.66 / (1 -
alp0) ^ 2);
CMOD(k) = cod + cod0;
end
AA = [CMOD; pp]';
x = AA(:, 1); % the x value
y = AA(:, 2); % the y value
% select either spline fit or polyfit (choose one option as shown)
%*****
% spline fit option
ff = interp1(x, y, xq, 'spline');
%*****
% poly fit option
% p = polyfit(x, y, polyfitOrder);
% f = polyval(p, x);
% ff = polyval(p, xq);
%*****
W1(:, 1) = xq;
W2(:, 1) = C;
W3(:, 1) = ff;
ModelCurve = [xq; ff]';
TestCurve = [W1, W2];
ModelTestCurveDeep = [W1'; W2'; W3']';
HeaderNames1 = 'xq, PTest, PModel';
% Preferable output sheet name printed here
fileName1 = 'ModelTest06.csv';
outid = fopen(fileName1, 'w+');
fprintf(outid, '%s', HeaderNames1);
fclose(outid);
dlmwrite(fileName1, ModelTestCurveDeep, 'roffset', 1, '-append',
'precision', 4); % increased precision to allow all digits to be
saved
disp(strcat('Generated report ', fileName1, ''))
% Preferable output sheet name printed here
filename = 'Parameters.xlsx';
% Desired parameters to be printed in the output sheet

```

Appendix E: A MATLAB code for Determining the static response of self- compacting concrete beams based on the fictitious crack model

```

A =
{'a1','a2','b2','w1','w2','Gf06','ft06','E','MinERR';a1,a2,b2,w1,w2,
Gf06,ft,E,MinERR};
sheet = 1;
xlRange = 'L';
xlswrite(filename,A,sheet,xlRange)
filename = 'Parameters.xlsx';
A = {'Xknee','Yknee';0,1;w1,sigmaft;w2,0};
B2=[a1,a2,b2,Gf01,ft,E,MinERR];
parametersstar=(B1+B2)/2;
sheet = 1;
xlRange = 'U';
xlswrite(filename,A,sheet,xlRange)
%*****
%*****
%*****
% This part is to find the unique parameters of hinge model
%*****
% Enter constant values
%*****
% Input the specific size-independent fracture energy, GF and
% splitting tensile strength, ft values
%*****
GF=0.1469; % Experimental simplified boundary effect method, N/m
ft=3.12;% Experimental of splitting tensile strength, MPa
%*****
alstar=parametersstar (1);
a2star=parametersstar (2);
b2star=parametersstar (3);
Gfstar=parametersstar (4);
ftstar=parametersstar(5)*1000;
w1star=(1-b2star)/(alstar-a2star)
w2star=b2star/a2star
w1=w1star*GF*ftstar/(Gfstar*ft);
sigmaftstar=(w2star-w1star)*a2star;
sigmaftstar2=1-alstar*w1star;
sigmastar=ftstar*sigmaftstar;
secondside=GF*sigmastar*w2star/(a2star*Gfstar*ft);
w2one=(w1+(w1^2+4*secondside)^0.5)/2
w2two=(w1-(w1^2+4*secondside)^0.5)/2
if(w2one>0)
    w2=w2one
end
if(w2two>0)
    w2=w2two
end
a2=a2star
sigmaft=(w2-w1)*a2;
a1=(1-sigmaft)/w1;
% Desired parameters to be printed in the output sheet
myMatrix=[alstar;a2star;ftstar;Gfstar;w1star;w2star;sigmaftstar;a1;a
2;ft;GF;w1;w2;sigmaft]';
% Preferable output sheet name printed here
fileName = 'Uniqueparameters.csv';
dlmwrite(fileName,myMatrix,'roffset',1,'-append', 'precision', 8);
disp(strcat('Generated report ''',fileName,''''))
%*****
%*****

```

